# Thermal Transport Phenomena in Carbonate Particles Undergoing Chemical Looping

**Lindsey Dat Kay Yue**

A thesis submitted for the degree of
Doctor of Philosophy of
The Australian National University

Supervised by Prof. Wojciech Lipiński

October 2018

© Copyright by Lindsey Dat Kay Yue 2018
All Rights Reserved

Typeset in Palatino by TEX and LATEX 2ε.
Word count: 56,300

Dr. Vincent M. Wheeler of the Australian National University, Canberra, provided collaboration and guidance on the work presented in Section 5.2.

Dr. Alicia Bayon of CSIRO Energy, Newcastle, provided collaboration and guidance on the work presented in Chapter 7.

Dr. Mihaela Grigore of CSIRO Energy, North Ryde, assisted with the XRD patterns and analysis in Section 7.2; Paul Marvig of CSIRO Energy, Newcastle, assisted with the SEM–BSE images and EDX map in Section 7.2; and Dr. Rene Olivares of CSIRO Energy, Newcastle, assisted with TGA–DSC experimental runs in Section 7.3.

Except where otherwise indicated, this thesis is my own original work. I certify the material in this thesis has not been previously submitted by the student for the purpose of obtaining a degree from any university or other tertiary educational institution.

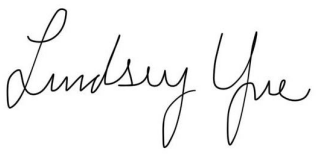

Lindsey Dat Kay Yue
29 October 2018

I dedicate this thesis to all the beautiful people whose actions and beings help me believe that humanity is worth saving.

# Acknowledgments

Financial support from the Australian Renewable Energy Agency (ARENA) through the Australian Solar Thermal Research Initiative (ASTRI) throughout my PhD program is gratefully acknowledged.

Thank you to my supervisors and colleagues: your support and guidance have made me the researcher I am today, have helped me grow more every day into the person I feel I was meant to be.

Thank you to my friends and family, old and new, for your presence and companionship, for the joy you bring to my life. You are my village.

Thank you and so much love to my parents who have supported my decisions all along and who have loved me for me from the beginning.

To my partner in life and co-author of our great adventure: we did this together. I love you.

# Abstract

Thermochemical processes, and specifically those processes which involve heterogeneous solid–gas thermochemical looping of metal oxides, are important technologies with applicability to many research fields and industries. Applications include fuel production, upgrading, and decarbonization, as well as chemical commodity production and processing. One emerging field is solar thermochemistry, in which concentrated solar thermal energy is used to drive thermochemical reactions. Realization of a solar thermochemical technology requires understanding of heat and mass transfer characteristics and chemical kinetics of the reacting system.

In this thesis, intra-particle thermal transport phenomena in particles undergoing cyclic chemical transformations are studied, with the goals of (1) advancing understanding of intra-particle thermal transport phenomena inhibiting chemical reactions and (2) guiding process and reactor design. Intra-particle thermal transport phenomena are studied by developing a detailed numerical model of heat and mass transfer in a single particle undergoing thermochemical looping in Part I of this thesis and using the model to investigate the transient rate and extent of reactions in particles undergoing thermochemical cycling in Part II. Understanding these intra-particle thermal transport phenomena supports the design and operation of better chemical reactors and advances the fields of thermochemical looping and solar thermochemistry.

Calcium oxide looping is chosen as the model reaction cycle. The cycle consists of the endothermic calcination of calcium carbonate into calcium oxide and carbon dioxide, and the exothermic carbonation of calcium oxide with carbon dioxide to form calcium carbonate. In Part I, chemical thermodynamics and kinetics of the model cycle are reviewed, a reaction rate expression describing the reversible reaction system is developed, and a numerical model of intra-particle thermal transport phenomena, linking reversible chemical kinetics to heat and mass transfer, is presented.

The analyzed system is a single, porous particle undergoing thermochemical cycling in an idealized, reactor-like environment. Transient changes in spatial gradients of temperature and composition of the solid and fluid phases are considered. For heat transfer, the following phenomena are considered: conduction in the solid and fluid phases, intra-particle radiative heat transfer, and convection and radiation at the particle surface. For mass transfer, the following phenomena are considered: chemistry, fluid species diffusion, bulk fluid advection, and convective mass transfer at the particle surface.

Two applications are considered in Part II: the first featuring directly irradiated particles for carbon dioxide capture and the second featuring furnace heated particles for carbon dioxide capture or thermochemical energy storage. In the directly irradiated application, two cases with varying period lengths are considered: a full-calcination case with longer calcination and carbonation period times and a full-carbonation case with shorter calcination and carbonation period times. The full-calcination case results in higher sorbent utilization, because the longer period times allow more particle volume to

undergo reaction. The full-carbonation case results in higher energetic efficiency, because the shorter calcination period results in lower solar energy input.

The effects of irradiation, particle size, and ambient gas temperature on thermochemical conversion are next investigated. Sorbent utilization and energetic efficiency are evaluated for each considered case and used to undertake quantitative and qualitative comparisons. Increasing particle size leads to a tradeoff between increased energetic efficiency and decreased sorbent utilization, while increasing irradiation or ambient gas temperature does not result in significant increases in either sorbent utilization or energetic efficiency. Evaluation metrics for the considered parameter ranges indicate parameter values which result in slight increases to both metrics. The metrics also indicate values which maximize a single metric, at the expense of the other in some cases.

In the furnace heated, carbon dioxide capture and thermochemical energy storage application, the effects of particle size and ambient carbon dioxide concentration on thermochemical conversion are investigated experimentally and numerically. Single particles are thermochemically cycled three times in a furnace under different constant carbon dioxide atmospheres. In the numerical model, conditions surrounding the particle are modified to match the furnace conditions as closely as possible, and adjustments are made to selected medium characteristics of the internal particle morphology. After modifications and adjustments, numerical results match the first cycles of equivalent experimental results. Spatial variations in particle composition predicted numerically show similar trends as those observed experimentally: calcium carbonate occupies the outer portions of the particle while calcium oxide occupies the inner region with a sharp gradient separating the two regions.

In this work, model predictions are used to assess the relative importance of operational parameters via evaluation metrics. These metric trends can be extrapolated to help address particle-based reacting medium level practical considerations and choice of compromises when designing a reacting medium and system process.

# Contents

# List of Figures

# List of Tables

# Nomenclature

| | |
|---|---|
| $A$ | area ($m^2$) |
| $A_{eq}$ | equilibrium partial pressure pre-exponential factor ($A_{eq} = 4.137 \times 10^{12}$ Pa) |
| $a$ | power of temperature to which diffusivity is proportional |
| $B_{eq}$ | equilibrium partial pressure constant ($B_{eq} = 2.0474 \times 10^4$ K) |
| $C$ | unit conversion factor in Eq. (5.30) ($C = 1.01325 \times 10^{-2}\,m^2\ kg^{1.5}\ s^{-4}\ K^{-1.75}\ mol^{-0.5}$ |
| $c$ | adsorption constant ($Pa^{-1/2}$) |
| $c_0$ | adsorption constant pre-exponential factor ($Pa^{-1/2}$) |
| $\bar{c}_p$ | molar-specific heat (J $mol^{-1}$ $K^{-1}$) |
| $D$ | diffusivity ($m^2$ $s^{-1}$) |
| $d$ | diameter (m) |
| $E_{b\lambda}$ | spectral blackbody emissive power (W $m^{-2}$ $\mu m^{-1}$) |
| $\overline{E}_a$ | Arrhenius reaction rate constant molar-specific activation energy (J $mol^{-1}$) |
| $\overline{E}_c$ | molar-specific energy in adsorption constant (J $mol^{-1}$) |
| $f(n\lambda T)$ | blackbody fractional function ($f(n\lambda T) = \int_0^{\lambda} E_{b\lambda} d\lambda / \int_0^{\infty} E_{b\lambda} d\lambda$) |
| $f_{CO_2}$ | $CO_2$ partial pressure dependence function (units vary) |
| $f_{morph}$ | function describing morphology dependence (units vary) |
| $f_{T_\infty}(t)$ | transient program for ambient gas temperature (K) |
| $G$ | total incident radiation (W $m^{-3}$) |
| $G_\lambda$ | spectral incident radiation (W $m^{-3}$ $\mu m^{-1}$) |
| $g$ | asymmetry factor of scattering |
| $h$ | heat transfer coefficient (W $m^{-2}$ $K^{-1}$) |
| $h_m$ | mass transfer coefficient (m $s^{-1}$) |
| $\overline{h}$ | molar-specific enthalpy (J $mol^{-1}$) |
| $\Delta\overline{h}^{\circ}_{298\,K}$ | standard molar-specific enthalpy of reaction (J $mol^{-1}$) |

| | |
|---|---|
| $I_\lambda$ | spectral radiative intensity (W m$^{-2}$ μm$^{-1}$ sr$^{-1}$) |
| $i$ | species, time interval, or volume element index |
| $j$ | thermochemical cycle index |
| $\bar{j}''$ | molar flux (mol m$^{-2}$ s$^{-1}$) |
| $K$ | permeability (m$^2$) |
| Kn | Knudsen number |
| $k$ | gray band index |
| $k$ | imaginary part of the complex refractive index |
| $k$ | reaction rate constant (units vary) |
| $k$ | thermal conductivity (W m$^{-1}$ K$^{-1}$) |
| $k_\mathrm{B}$ | Boltzmann constant ($k_\mathrm{B} = 1.3806 \times 10^{-23}$ J K$^{-1}$) |
| $k_0$ | Arrhenius reaction rate constant pre-exponential factor (units vary) |
| $l$ | length (m) |
| $\overline{M}$ | molar mass (kg mol$^{-1}$) |
| $m$ | complex refractive index ($m = n + ik$) |
| $m$ | mass (kg) |
| $m$ | reaction order |
| $m/z$ | mass spectrometry mass-to-charge ratio |
| $N$ | amount of substance (mol) |
| $N$ | number of volume elements |
| $N_\mathrm{band}$ | number of gray bands |
| Nu | Nusselt number |
| $n$ | real part of the complex refractive index |
| $\hat{\mathbf{n}}$ | normal unit vector |
| Pr | Prandtl number |
| $p$ | pressure (Pa) |
| $Q$ | heat (J) |
| $q_\mathrm{rad}$ | radiative heat rate (W) |
| $q''$ | heat flux (W m$^{-2}$) |

| | |
|---|---|
| $\overline{R}$ | ideal gas constant ($\overline{R} = 8.314\,\mathrm{J\ mol^{-1}\ K^{-1}}$) |
| Re | Reynolds number |
| $r$ | radius or radial direction (m) |
| $\bar{r}'''$ | volumetric reaction rate (mol $\mathrm{m^{-3}\ s^{-1}}$) |
| $S$ | surface area ($\mathrm{m^2}$) |
| Sc | Schmidt number |
| Sh | Sherwood number |
| $s$ | mass-specific reaction surface area ($\mathrm{m^2\ kg^{-1}}$) |
| $s'''$ | volume-specific reaction surface area ($\mathrm{m^{-1}}$) |
| $s'''_{\mathrm{phase}}$ | volume-specific interphase surface area ($\mathrm{m^{-1}}$) |
| $\hat{\mathbf{s}}$ | direction unit vector |
| $T$ | temperature (K) |
| $t$ | time (s) |
| $u$ | velocity ($\mathrm{m\ s^{-1}}$) |
| $V$ | volume ($\mathrm{m^3}$) |
| $X$ | reaction extent |
| $\bar{y}$ | molar concentration |
| $\nabla$ | Nabla operator |

## Greek symbols

| | |
|---|---|
| $\alpha$ | absorptivity |
| $\alpha$ | number of sub-volume elements in each volume element |
| $\beta$ | extinction coefficient ($\mathrm{m^{-1}}$) |
| $\gamma$ | Gauss-Seidel overrelaxation coefficient |
| $\delta$ | relative percent error (%) |
| $\bar{\delta}$ | average relative percent error (%) |
| $\varepsilon$ | emissivity |
| $\eta_{\mathrm{e}}$ | energetic efficiency |
| $\theta$ | fraction of occupied active sites |
| $\theta$ | polar or incidence angle (rad) |

| | |
|---|---|
| $\kappa$ | absorption coefficient ($m^{-1}$) |
| $\lambda$ | wavelength ($\mu$m) |
| $\mu$ | viscosity (N s $m^{-2}$) |
| $\xi_c$ | capture capacity |
| $\bar{\xi}$ | sorbent utilization |
| $\pi$ | mathematical constant ($\pi = 3.14159$) |
| $\rho$ | density (kg $m^{-3}$) |
| $\rho$ | reflectivity |
| $\bar{\rho}$ | molar density (mol $m^{-3}$) |
| $(\Sigma\nu)$ | diffusion volume ($m^3$) |
| $\sigma$ | Stefan–Boltzmann constant ($\sigma = 5.6704 \times 10^{-8}$ W $m^{-2}$ $K^{-4}$) |
| $\sigma_s$ | scattering coefficient ($m^{-1}$) |
| $\tau$ | time normalized by cycle length |
| $\tau$ | tortuosity |
| $\phi$ | porosity |
| $\Omega$ | solid angle (sr) |
| $\omega$ | single scattering albedo |

### Subscripts

| | |
|---|---|
| b | blackbody |
| Ca | calcium |
| $CaCO_3$ | calcium carbonate |
| CaO | calcium oxide |
| $CO_2$ | carbon dioxide |
| c | characteristic |
| calc | calcination |
| carb | carbonation |
| col | collision |
| diff | diffusion |
| eff | effective |

| | |
|---|---|
| eq | equilibrium |
| f | fluid |
| g | grain |
| init | initial heating |
| K | Knudsen |
| mol | molecular |
| $N_2$ | nitrogen |
| $O_2$ | oxygen |
| p | particle |
| path | mean free path |
| R | Rosseland |
| rad | radiative |
| s | solid |
| src | source |
| sub | sub-volume element |
| surf | surface |
| w | wall |
| 0 | initial |
| $\lambda$ | spectral |
| $\infty$ | surrounding |

### Superscripts

| | |
|---|---|
| f | fluid phase |
| s | solid phase |
| tr | transport-approximate |
| $\sphericalangle$ | hemispherical |
| $'$ | directional |

### Abbreviations

ARENA Australian Renewable Energy Agency

| | |
|---|---|
| ASTRI | Australian Solar Thermal Research Initiative |
| a.u. | arbitrary unit |
| BSE | back-scattered electron detector |
| CCS | carbon capture and storage |
| CCUS | carbon capture, utilization, and storage |
| CSP | concentrated solar power |
| CST | concentrated solar thermal |
| def | definition |
| DSC | differential scanning calorimetry |
| EDX | energy-dispersive X-ray spectroscopy |
| exp | experimental |
| JCPDS | International Centre for Diffraction Data database standard designation |
| MD$P_0$ | modified differential approximation |
| MEA | monoethanolamine |
| MS | mass spectrometry/spectrometer |
| num | numerical |
| $P_1$ | first order approximation of the method of spherical harmonics |
| PRE | percent relative error |
| ppm | parts per million |
| redox | reduction and oxidation |
| SEM | scanning electron microscopy |
| TES | thermal energy storage |
| TGA | thermogravimetric analysis/analyzer |
| XRD | X-ray diffraction |
| 1D | one dimensional |
| 3D | three dimensional |

Chapter 1

# Introduction

Thermochemical processes, and specifically those processes which involve heterogeneous solid–gas thermochemical looping of metal oxides, are important technologies with applicability to many research fields and industries. Thermochemical reactions are characterized by a significant change in enthalpy and high thermal effects accompanying the reaction. Chemical processing and commodity production industries feature many heterogeneous thermochemical reactions. Thermochemical looping or cycling refers to processes featuring multiple thermochemical reactions occurring sequentially and the cyclic production and reaction of intermediary compounds. The combination of reactions sequentially results in a desired overall reaction. Thermochemical looping systems have the potential to drive the overall reaction more energy efficiently and with less irreversibility than other industrial methods, leading to higher exergy efficiencies and more economical processes [Fan et al., 2015].

One emerging field of thermochemical processing is concentrated solar thermochemistry, in which concentrated solar thermal energy is used to drive thermochemical processes. Calcium oxide-based thermochemical looping is a two step thermochemical looping system being investigated for use with concentrated solar thermal energy for the applications of carbon dioxide ($CO_2$) capture and high-temperature thermal energy storage (TES).

Calcium oxide-based thermochemical looping is commonly referred to as CaO looping, a convention adopted in this thesis. The CaO looping process is comprised of two reactions: (1) the thermal decomposition of calcium carbonate ($CaCO_3$) and (2) the carbonation of calcium oxide (CaO) with $CO_2$, known as the calcination and carbonation reactions, respectively. The intermediaries of the cycle are solid $CaCO_3$ and CaO. CaO looping, as envisioned with solar energy and demonstrated with conventional sources of process heat, features a reacting medium of $CaCO_3$/CaO particles. Many heterogeneous reaction systems in the chemical processing and commodity production industries, including those being investigated for use with concentrated solar thermal energy, feature particle-based, heterogeneous reacting media [Jakobsen, 2014].

This research investigates intra-particle thermal transport phenomena in particles undergoing CaO looping. Thermal transport phenomena in this work is used to describe phenomena related to the exchange of mass, momentum, and energy in thermal energy

systems; it does not include ionic or charge transport. In particles undergoing CaO looping, heat transfer, mass transfer, and chemical kinetics are all important considerations. For many solid–gas thermochemical reactions, intra-particle heat and mass transfer can substantially influence apparent chemical kinetics of reacting particles [House, 2007]. The work presented in this thesis strives to advance the understanding of intra-particle thermal transport phenomena inhibiting chemical reactions in order to improve reactor designs. Improved reactor designs support the commercial viability of thermochemical looping processes and solar thermochemistry.

Particle physical attributes and conditions considered in this work are based on those expected in thermochemical reactors with conventional or solar sources of process heat and for the applications of $CO_2$ capture or high-temperature TES. The aim is to show how such attributes and conditions surrounding particles undergoing CaO looping influence the rate and extent of each of the two reactions that make up the cycle. Understanding these particle level phenomena supports the design and operation of better chemical reactors and advances the fields of thermochemical looping and solar thermochemistry.

## 1.1 Motivation

This research is motivated by the transformative potential of thermochemical looping and solar thermochemistry, as well as the importance of the applications of $CO_2$ capture and high-temperature TES.

### Thermochemical looping

Of multiphase thermochemical processes, an important subset are those involving reactions between solid and gas phases. Solid–gas thermochemical processes are found in several industrial and scientific applications including thermochemical energy storage [Pardo et al., 2014], thermal decomposition of natural carbonates [Oates, 1998], metallurgic refining [Cottrell, 1997], chemical looping combustion [Fan, 2010], the production of commodity materials [Levenspiel, 1999], chemical processing [Levenspiel, 1999], and some atmospheric and aerosol sciences [Kolb and Worsnop, 2012]. An example of a solid–gas thermochemical process in the electricity industry is the gasification of coal into combustible gaseous mixtures [Jakobsen, 2014]. Examples in metallurgy include ore processing by oxidation, volatization, chloridization, sulfation, magnetization, or reduction [Jakobsen, 2014]. An example in the food and beverage industry is the roasting of coffee beans [Jakobsen, 2014].

Thermochemical looping systems, featuring multiple thermochemical reactions, are an attractive subset of thermochemical processes, because of their potential to improve the energy and exergy efficiencies of chemical processes [Fan et al., 2015]. Examples of processes that have the potential to be improved with thermochemical looping systems include combustion and the production of chemical commodities, which are integral to

the energy and chemical industries. Heterogeneous thermochemical looping systems are particularly attractive because of their potential to integrate gas separation into processes with minimal or no additional energy penalties [Fan, 2010]. Examples of processes in which gas separation is pertinent include $CO_2$ separation from product gases in combustion processes and hydrogen ($H_2$) separation from oxygen ($O_2$) in water ($H_2O$) splitting for $H_2$ production. Processes such as these, in which gas separation is desired, have the potential to be improved with thermochemical looping systems.

Desired attributes of a thermochemical looping system include (1) rapid and full conversion of reactants in each reaction, (2) moderate reaction temperatures and pressures for all reactions, (3) similar reaction conditions for all reactions, (4) sustained intermediary reactivity over several cycles, and (5) cheap intermediary feedstock materials. Research and demonstration of thermochemical looping systems have revealed that conversion limitations and declines in reactivity with cycling exist in many attractive reaction systems [Fan, 2010]. However, maximum conversion and sustained reactivity with cycling can generally be improved by feedstock material manufacturing and modification at the expensive of feedstock material cost [Phalak et al., 2013]. Pilot plant-scale demonstrations also suggest reactor design has the potential to be improved to make the processes more efficient and economical [Fan et al., 2015].

### Solar energy

As world energy demand increases, sustainable energy sources, such as solar energy, become more attractive and important to meeting future energy demands. The amount of solar energy being used to generate electricity has increased exponentially [International Energy Agency, 2017], however electricity is only one of the many forms of consumed energy. Many industrial processes, such as cement manufacturing and metal refining, require energy in the form of high-temperature process heat, often to drive thermochemical reactions [Jakobsen, 2014], while consumers and the transportation industry require portable fuel for locomotion. High-temperature process heat is traditionally derived from the combustion of fossil fuels [International Energy Agency, 2017], while transportation fuels are traditionally long-chain hydrocarbons also derived from fossil fuels.

Solar energy can address these non-electrical energy needs by supplying high-temperature process heat with concentrated solar thermal facilities [Bader and Lipiński, 2016]. Additionly, solar energy has the potential to be used to produce synthetic hydrocarbon fuels from $CO_2$ and $H_2O$ [Kim et al., 2013]. Synthetic fuels can be used analogously to current transportation fuels in personal automobiles or other transportation applications [Steynberg, 2004]. Synthetic fuels are an important piece of the future energy market for applications where electrical motors cannot yet replace combustion engines such as in the aviation industry.

Using solar energy to supply industrial process heat for driving thermochemical reactions and produce synthetic fuels converts solar energy to chemical potential. Solar

synthetic fuels are a stable and high-energy density form of solar energy with the benefits of long term storability and long range transportability [Gray, 2009]. Solar thermochemistry therefore has the potential to address two major industrial energy demands that cannot currently be met with renewable electricity: process heat for industrial thermochemical reactions and transportation fuels.

### Carbon dioxide capture

Carbon capture, storage and utilization is an important suite of technologies for addressing increasing anthropogenic greenhouse gas emissions and atmospheric greenhouse gas levels [Wilcox, 2012]. These technologies are commonly referred to as CCS (carbon capture and storage) or CCUS (carbon capture, utilization, and storage). For the carbon capture aspect of CCUS, the three categories of technology are pre-combustion, oxy-combustion, and post-combustion $CO_2$ capture.

In post-combustion $CO_2$ capture, fuel is consumed in its usual manner, and $CO_2$ is separated either directly from the output gas stream, where typical $CO_2$ concentrations are approximately 15%, or from the atmosphere, where the $CO_2$ concentration is approximately 400 ppm [Herzog, 2009; Rackley, 2010]. There is always an energy penalty associated with gas mixture separation, and the minimum theoretical energy required to separate $CO_2$ from a gas mixture increases logarithmically with decreasing $CO_2$ concentration [Kalafati, 1991]. Methods for $CO_2$ separation used for post-combustion $CO_2$ capture include physical or chemical absorption, adsorption, membrane separation, and cryogenic separation [Rackley, 2010]. CaO looping is a form of chemical absorption $CO_2$ capture. The most common commercial process is solvent adsorption with monoethanolamine (MEA) [Dutcher et al., 2015; Rochelle, 2009].

$CO_2$ separation technologies are relevant to CCUS, as well as commodity $CO_2$ production. The separation or production of $CO_2$ is used in the following applications: the production of commodity $CO_2$ from carbonaceous fuel sources, the production of $H_2$ by removal of $CO_2$ from a processes to enhance the water gas shift reaction, and carbon capture by removal of $CO_2$ from a combustion process exhaust gas. Concentrated $CO_2$ is a commodity with applications in the pharmaceutical, medical, environmental, food and beverage, petrochemical, oil recovery, metallurgy, and manufacturing industries [Stalkup, 1978; Pierantozzi, 2003].

An emerging use of $CO_2$ is as a feedstock for the production of synthesis gas and synthetic fuels [Kim et al., 2012, 2013]. Synthesis gas is a mixture of $H_2$ and carbon monoxide (CO), which is in turn the feedstock for the production of methanol, ammonia, and synthetic hydrocarbon fuels via catalysis, the Haber–Bosch process, and the Fischer–Tropsch process, respectively. Using solar energy for post-combustion $CO_2$ capture and then using the captured $CO_2$ to produce synthetic fuels with solar energy results in a closed carbon energy loop with solar energy as the primary driver.

The largest barriers to the implementation of $CO_2$ capture technologies are economic

and political: there will always be an energy penalty associated with separating gas streams and widespread incentives to outweigh paying that penalty for $CO_2$ capture do not yet exist [Eckaus et al., 1996]. Improving the efficiency, cost, and sustainability of $CO_2$ capture technologies supports the adoption of such technologies, because as cost decreases, smaller policy and/or economic factors will be needed to incentivize implementation.

### High-temperature thermal energy storage

Energy storage is playing a crucial role for the integration of large-capacity renewable energy sources into the current energy market. Energy storage provides reliability and continuous performance of intermittent renewable energy sources [Pardo et al., 2014]. When implemented with TES systems, concentrated solar thermal electricity production is a renewable energy technology capable of operating continuously regardless of the intermittence of solar resources [Burgaleta et al., 2011; Guédez et al., 2014].

Higher temperature operation of concentrated solar thermal systems increases the thermodynamic efficiency limits of the associated power cycle. While increasing temperature of the radiation receiver/absorber, or simply solar receiver, decreases the receiver efficiency, improvements to the power cycle efficiency have the potential to outweigh this decrease. Novel high-temperature solar receivers and power cycles are being developed for use in concentrated solar thermal electricity plants [Ho and Iverson, 2014]. A particular power cycle of interest is the supercritical $CO_2$ power cycle, which promises higher theoretical efficiencies and smaller footprints over current steam Rankine cycles [Ma and Turchi, 2011; Ahn et al., 2015]. Current steam Rankine power cycles achieve efficiencies of around 42%. It is generally agreed that supercritical $CO_2$ power cycles have the potential to achieve thermal to electrical energy efficiency of around 50% when operating at temperatures above 600 °C [Iverson et al., 2013].

To maintain the ability to operate continuously, novel high-temperature TES systems for use with high-temperature solar receivers and power cycles are also needed. Sensible and latent heat TES systems are currently in use in commercial concentrated solar thermal plants [Burgaleta et al., 2011; U.S. Department of Energy, 2014]. Commercially available nitrite-based salts used for sensible heat TES decompose at temperatures over 600 °C, limiting their potential for use with high-temperature power cycles. Some sensible heat TES materials are under development for high-temperature operation such as solid cast steel, silica, or magnesia bricks and lithium liquid salt [Kuravi et al., 2013]. Latent heat TES systems using various states of pressurized or saturated water are currently available, with a maximum reported storage temperature of 350 °C [Kuravi et al., 2013]. Some latent heat TES systems under development for high-temperature operation utilize aluminum and magnesium chloride [Kuravi et al., 2013]. However, materials for high-temperature sensible or latent heat TES are limited.

Thermochemical TES is an alternative to sensible or latent heat TES with the potential

to provide discharge temperatures compatible with supercritical $CO_2$ power cycles. Storing solar thermal energy by means of thermochemical reactions has been under development since the 1970's [Wentworth and Chen, 1976; Ervin, 1977], but recently, investigation into high-temperature systems has followed the development of other high-temperature components. High-temperature solar receivers, power cycles, and TES systems have the potential to improve the efficiency and reduce the cost of concentrated solar thermal electricity plants to the extent that wide spread adoption of solar electricity could become the electricity industry utility scale standard [Müller-Steinhagen and Trieb, 2004].

In this section, the importance of $CO_2$ capture technologies and high-temperature TES was highlighted. The research presented in this thesis considers conditions expected in solar and conventional CaO looping thermochemical reactors configured for $CO_2$ capture or high-temperature TES.

## 1.2 Objectives

The goals of this research are to advance (1) understanding of thermal transport phenomena in particles undergoing CaO looping and (2) improve solar $CO_2$ capture and thermochemical TES technologies. Past studies of particles undergoing thermochemical cycling indicate that the interaction between reversible, intrinsic chemical kinetics and intra-particle heat and mass transfer influences apparent kinetics and overall particle conversion. Reaction limitations due to intra-particle heat and mass transfer become more significant in larger sized particles being considered for CaO looping. Current numerical studies of intra-particle thermal transport phenomena in particles undergoing CaO looping are limited to either the calcination or carbonation steps and are not comprehensive in the treatment of all coupled physical phenomena. These limitations and numerical studies will be elaborated in Chapter 2.

Understanding intra-particle thermal transport phenomena will help bring solar thermochemical technology closer to the commercial level by guiding reacting medium and reactor design. In order to support the design of a reacting medium and reactor, heat and mass transfer coupled to reversible chemical kinetics in reacting particles must be properly modeled. Accurate numerical results of intra-particle thermal transport phenomena can then be extrapolated to apparent thermal transport phenomena in a reacting medium of particles. In the realization of any solar thermochemical technology, successful reactor design depends on matching the reaction chemical kinetics to the heat transfer processes of the reacting medium in order to maximize the solar to chemical energy conversion [Palumbo et al., 2004] or other desired outputs determined by reactor level considerations and priorities.

The tasks of this research to achieve these goals include:

(1) Fundamental study of heat and mass transfer phenomena pertinent to porous

sorbent particles undergoing thermochemical looping. Phenomena and length scales considered are those pertinent to CaO looping in millimeter sized particles.

(2) Development of a robust numerical model linking the intrinsic chemical kinetics of the calcination and carbonation reactions to intra-particle heat and mass transfer in a particle undergoing CaO looping driven by time-periodic boundary conditions.

(3) Investigations using the model to identify trade-offs between efficient use of input thermal energy and material utilization for different conditions. The conditions are chosen to reflect potential reactor designs or operating conditions being considered for conventional or solar thermochemical reactors.

## 1.3 Overview

In this thesis, background information about thermochemical looping and solar energy will first be given in Chapter 2. The remainder of the thesis contains two parts.

In Part I, Chapters 3 to 5 contain the development of a numerical model of transient thermal transport phenomena in a carbonate particle undergoing CaO looping. In Chapter 3, chemical thermodynamics and kinetics of the calcination and carbonation reactions are presented, and a single, reversible, intrinsic reaction rate expression is developed. The expression describes both the direction of the reversible reaction system and magnitude of the reaction rate. In Chapter 4, the governing equations, closure models, initial conditions, boundary conditions, and numerical solution of a numerical model of a particle undergoing CaO looping are presented. In the model, CaO looping of the particle is driven by time-periodic conditions at the particle boundary. Concluding Part I, in Chapter 5, the evaluation of two flux terms in the numerical model are further considered. First, two methods for approximating heat flux due to radiative heat transfer in the particle are presented, and heat transfer results using the methods are compared. Then, three models for approximating diffusive flux of gas species in the particle pore space are presented, and effective diffusivity values predicted using the presented models for conditions expected in CaO looping particles are compared.

In Part II, the model developed in Part I is used to compare the relative magnitude of influence of selected parameters on intra-particle thermal transport phenomena and thermochemical conversion. Two different configurations are considered: directly irradiated particles configured for $CO_2$ capture in Chapter 6 and furnace heated particles configured for $CO_2$ or thermochemical TES in Chapter 7.

In Chapter 6, the $CO_2$ concentration during carbonation is fixed at 15%, similar to the concentration in flue gas, while the calcination $CO_2$ concentration is 100%. The effect of calcination and carbonation period lengths on intra-particle reaction extent and temperature profiles is first investigated. Two cases are considered, and the sorbent utilization and energetic efficiency are evaluated for each case and compared. Then

the effect of varying irradiation, particle size, and ambient gas temperature on overall reaction extent, sorbent utilization, and energetic efficiency is investigated.

In Chapter 7, the effect of particle size and $CO_2$ concentration on overall reaction extent in particles undergoing CaO looping is experimentally and numerically investigated. In the experimental sections, sorbent particles are obtained and characterized. Then, particles from different size groups are thermochemically cycled three times in a furnace in different $CO_2$ atmospheres where the $CO_2$ concentration is kept the same during calcination and carbonation. The results are discussed, then reproduced using the numerical model, with good agreement between numerical and experimental results, particularly during the first cycle. Lastly, conclusions from the presented work and outlook related to thermochemical looping and solar thermochemical technologies are discussed in Chapter 8.

Chapter 2

# Background on thermochemical looping and solar energy

## 2.1 Introduction

In this chapter, background information on thermochemical looping and solar energy and the current state of research related to CaO looping in both fields are given. Thermochemical looping is used interchangeably with thermochemical cycling and refers to systems in which a sequence of thermochemical reactions produces the desired overall process. Thermochemical looping systems are investigated because of their potential to improve energy and exergy efficiencies of the overall process.

While photovoltaic and concentrated solar thermal electricity technologies have been commercialized and are currently competing with conventional sources of electricity, solar thermochemistry, including solar driven thermochemical looping, is an emerging field. The importance and maturity of conventional thermochemical processing and concentrated solar thermal electricity make solar thermochemistry an attractive and promising area of research.

## 2.2 Thermochemical looping

Thermochemical looping systems involve multiple thermochemical reactions conducted sequentially in a cycle. The term thermochemical looping is used in this work to describe systems in which two or more thermochemical reactions result in (1) a single, desired overall process and (2) regenerated chemical intermediaries. The following background is limited to thermochemical looping systems based on heterogeneous solid–gas reactions.

Most thermochemical looping systems involve metal or metal compound intermediaries [Fan et al., 2015]. Metal-based thermochemical looping systems are generally divided into two categories: those involving carbon dioxide ($CO_2$) separation or production as a commodity and those involving the production of substances other than $CO_2$, such as $H_2$ or synthesis gas. Reduction and oxidation (redox) reaction systems used in the non-$CO_2$ generating category typically involve the partial or complete reduction and

oxidation of a metal oxide [Fan et al., 2015].

Examples include iron(II,III) oxide ($Fe_3O_4$)/iron (Fe) looping for $H_2$ production from CO and $H_2O$ [Fan et al., 2015], zinc oxide (ZnO)/zinc (Zn) looping for $H_2$ production from $H_2O$ [Bader and Lipiński, 2016], and the partial reduction and oxidation of cerium dioxide ($CeO_2$) for $H_2$ or CO production from $H_2O$ or $CO_2$, respectively [Bader and Lipiński, 2016].

The process of $H_2$ production from $H_2O$ using ZnO as an intermediary will be elaborated to illustrate the overall process and constituent reactions of a thermochemical looping system. The thermochemical looping system consists of two reactions: the thermal reduction of ZnO solid into gaseous Zn and $O_2$ and oxidation of Zn with gaseous $H_2O$ yielding regenerated solid ZnO and gaseous $H_2$ [Bader and Lipiński, 2016].

$$\mathrm{ZnO} \rightarrow \mathrm{Zn} + \frac{1}{2}\mathrm{O_2} \tag{2.1}$$

$$\mathrm{Zn} + \mathrm{H_2O} \rightarrow \mathrm{H_2} + \mathrm{ZnO} \tag{2.2}$$

The overall reaction is found by adding the constituent reactions together: $H_2O$ is split into $H_2$ and $O_2$, and the two regenerated intermediaries are ZnO and Zn.

$$\mathrm{H_2O} \rightarrow \mathrm{H_2} + \frac{1}{2}\mathrm{O_2} \tag{2.3}$$

The gaseous products, $O_2$ and $H_2$ are produced in separate reactions in the cycle, making gas separation easier compared to gas separation in direct $H_2O$ thermolysis when the product gases are generated simultaneously.

In the $CO_2$ separation or production category of thermochemical looping systems, three types of reaction systems are commonly considered: metal sulfide/metal sulfate systems, metal/metal oxide systems, and metal oxide/metal carbonate systems [Fan et al., 2015]. In metal sulfide/metal sulfate and metal/metal oxide systems, a carbonaceous fuel is fully oxidized by the metal oxide or metal sulfate to $CO_2$ and $H_2O$ in one reaction, and steam or air is reduced by the metal or metal sulfide to $H_2$ or $O_2$ lean air, respectively, in the second reaction. The intermediary compounds act as oxygen carriers between the carbonaceous fuel and steam or air, and concentrated $CO_2$ only needs to be separated from $H_2O$ in the products of the fuel oxidation, rather than separated from flue gas in conventional combustion. This application of thermochemical looping is often referred to as chemical-looping combustion. An example of a chemical-looping combustion system is the nickel (Ni)/nickel oxide (NiO) system, in which natural gas or synthesis gas is oxidized by NiO and $O_2$ in air is reduced by Ni [García-Labiano et al., 2005].

Metal oxide/metal carbonate systems involving $CO_2$ are referred to as metal oxide looping systems in this work. Metal oxide looping systems feature two reactions: the thermal decomposition or calcination of the metal carbonate and the carbonation of the

metal oxide by $CO_2$ back to the metal carbonate.

$$MeCO_3 \rightarrow MeO + CO_2 \tag{2.4}$$

$$MeO + CO_2 \rightarrow MeCO_3 \tag{2.5}$$

where Me represents a bivalent metal. The overall process is the removal and release of $CO_2$ from one source to another, with metal oxide and metal carbonate as the regenerated intermediaries. Metals of interest for use in metal oxide looping systems include manganese, strontium, barium, and others [Dunstan et al., 2016]. Binary, tertiary, and perovskite mixed-metal oxide/carbonate reaction systems are also being considered [Lin et al., 2009; Dunstan et al., 2016]. The $CaO/CaCO_3$-based system, known as CaO looping, is the most widely investigated metal oxide thermochemical looping system [Stanmore and Gilot, 2005; Fennell and Anthony, 2015].

### Calcium oxide looping

CaO looping is comprised of the forward and reverse reaction of solid $CaCO_3$ decomposition.

$$CaCO_3 \rightarrow CaO + CO_2 \tag{2.6}$$

$$CaO + CO_2 \rightarrow CaCO_3 \tag{2.7}$$

Calcination and carbonation can be used to describe a family of related but distinct chemical reactions including the decomposition and regeneration of any metal carbonate, but in this work, calcination and carbonation will be used to refer to the calcination of $CaCO_3$ and the carbonation of CaO, respectively, unless otherwise noted.

A related, three step cycle has also been considered [Nikulshina et al., 2006; Phalak et al., 2013]. In place of the single carbonation reaction, it features two reactions: the hydration of CaO into calcium hydroxide ($Ca(OH)_2$) and simultaneous dehydration and carbonation of $Ca(OH)_2$ into $CaCO_3$ and $H_2O$. Carbonation in the three step cycle exhibits improved reaction rates and conversion limits compared to carbonation in the two step cycle [Nikulshina et al., 2007].

**History** Both the calcination and carbonation reactions have been widely studied individually, for their use in industrial applications. Calcination has been studied extensively for the production lime as a commodity for the cement and other chemical industries. Carbonation is relevant to the hardening of lime mortar and cement. Both the calcination and carbonation reaction are found in metallurgic refining [Oates, 1998].

CaO looping, as a reversible, two-step cycle has been considered for various applications. Early interest in the cycle was for $H_2$ production via the enhanced water gas shift reaction [Fan et al., 2015]. The cycle was first considered for $CO_2$ capture by Shimizu et al.

[1999] and has since been researched extensively for pre-, oxy-, and post-combustion $CO_2$ capture with conventional sources of process heat [Stanmore and Gilot, 2005; Blamey et al., 2010].

To implement CaO looping for $CO_2$ removal, CaO absorbs $CO_2$ from a dilute source such as flue gas in the carbonation step. Then, to implement CaO looping for $CO_2$ capture or commodity production, $CaCO_3$ is thermochemically decomposed in the calcination step into commodity grade concentrated $CO_2$, suitable for storage, sale, or further processing. Thermal energy is required to drive the calcination reaction. Conventionally, this energy is supplied by traditional fossil fuel derived sources. Conventional CaO looping is typically configured in two separate reactors for large-scale $CO_2$ capture, using particles of ground limestone as the initial feedstock material. The design goal of each reactor is to react the solid intermediaries as quickly, completely, and efficiently as possible.

For post-combustion $CO_2$ capture, $CaCO_3$ is calcined in an oxyfuel combustor, where a fuel source is combusted in a 100% oxygen environment with a near stoichiometric or rich oxygen to fuel ratio. The resulting thermal energy drives the calcination reaction. The product of both the combustion and calcination reactions is $CO_2$, resulting in a highly pure $CO_2$ product stream. Typical combustor/calciner reactors are rotary kilns or circulating fluidized beds, which use additional high purity $CO_2$ as the fluidizing gas. Fluidized and entrained bed reactors have been considered for the carbonator.

**Challenges** Challenges to the commercialization of CaO looping include conversion limitation in particles undergoing CaO looping, reactor and system optimization, and economic barriers. Carbon capture lacks sufficient economic motives for widespread implementation, and alternative means of producing $H_2$ or synthesis gas and alternative fuels to $H_2$ and synthesis gas are economically more attractive at this time [Eckaus et al., 1996]. While solutions to the economic barriers will likely be political, other challenges can be addressed with engineering solutions.

Two mechanisms limit carbonation in particles undergoing CaO looping: intra-particle mass transfer and loss of solid intermediary reactivity with cycling. The carbonation reaction is known to change suddenly from rapid to slower apparent reaction rates in particles undergoing CaO looping. The change coincides with the formation of a product layer of $CaCO_3$, both over the entire reacting particle and around individual CaO grains, which forms during calcination. It is generally agreed that this transition from rapid to slower carbonation is due to impeded mass transfer of $CO_2$ to unreacted CaO through the $CaCO_3$ product layer [Bhatia and Perlmutter, 1983; Shimizu et al., 1999; Gupta and Fan, 2002; Abanades and Alvarez, 2003; Manovic and Anthony, 2010].

Loss of reactivity with cycling in CaO looping and other heterogeneous thermochemical looping systems is primarily due to irreversible structural and chemical changes. Attrition and sintering are two irreversible structural changes known to occur in particles undergoing CaO looping [Blamey et al., 2010; Manovic and Anthony, 2010]. Attrition

leads to breakdown of solid particles and loss of reacting material as fines. Sintering results in the loss of small pores and reaction surface area, further contributing to mass transfer limitation on the carbonation reaction. Irreversible reactions with impurities and the formation of stable, unreacting compounds, similar to catalyst poisoning, are examples of irreversbile chemical changes. For example, $SO_2$ can form stable $CaSO_4$ which will not decompose back to CaO under normal CaO looping conditions, thereby deactiving the material [Anthony and Granatstein, 2001; Itskos et al., 2013].

Reactor types used for calcination and carbonation include fluidized bed and entrained bed reactors. These types of reactors have the benefit of long historical use and uniform rates of heat and mass transfer to all reacting particles, however recent analyses of thermochemical looping systems indicate that alternative reactor configurations have the potential to improve the efficiency and reaction extent achieved in both calcination and carbonation reactors [Fan et al., 2015]. Reactor design and system operation optimization are multiscale challenges. In order to design a reactor and system, understanding the effect of reactor design and system operation on conditions local to reactants as well as knowledge of the effect local conditions have on reaction rates and extents is needed.

Stoichiometry of Eqs. (2.6) and (2.7) indicates that one mole of $CaCO_3$ is theoretically needed to capture one mole of $CO_2$. However, more intermediary reactant feedstock than the stoichiometric amount is needed initially and periodically during operation, due to conversion limitations and declines in reactivity with cycling. Higher initial feedstock requirements result in higher initial plant cost, while ongoing replenishment of intermediaries results in higher operating costs. As solid intermediaries requirements increase, the capacity and energy requirements of the solid handling components of the system also increase.

**Current research** CaO looping research is currently focused on two scales: at reacting particle level and at the reactor and system level. At the reacting particle level, research is aimed at improving reactivity by (1) modifying solid intermediary materials to improve conversion limits and sustained reactivity with cycling [Liu et al., 2012; Shokrollahi Yancheshmeh et al., 2016] and (2) better understanding how intra-particle thermal transport phenomena relate to chemical kinetics and conversion. At the reactor and system level, research areas include proof of concept pilot plant demonstrations, improved reactor design and operation, and efficient integration of CaO looping into existing plants.

In thermochemical looping systems, sorbent material typically refers to the solid intermediary materials used to chemically consume and release reactants as well as any impurities or inert framework mixed with the reacting intermediaries. Research focuses on designing novel sorbent materials and maximizing sorbent reactivity with cycling. Sorbent reactivity improvement methods include manual modifications [Sayyah et al., 2013; Sánchez-Jiménez et al., 2016], particle/particulate preparation [Wang et al., 2016], inclusion of inert structures [Zhao et al., 2014], and other chemical modifications [Chen

and Khalili, 2017].

The enhancement methods and modifications just listed result in sorbent materials with conversion and cycling properties superior to unmodified $CaCO_3$. However, unmodified $CaCO_3$ is currently so abundant and cheap that the superior properties do not justify the increased cost of feedstock processing [Phalak et al., 2013]. Sorbents modified with inert structures or materials will also increase the total amount of solid material that is required and needs to be circulated [Phalak et al., 2013]. Therefore, sorbent modifications must improve properties without compromising affordability.

Intra-particle thermal transport phenomena are modeled and studied to advance the understanding of the influence of heat and mass transfer on chemical kinetics and conversion in order to guide reactor design. To the best of the author's knowledge, no numerical models of intra-particle thermal transport phenomena in single particles undergoing CaO looping have been previously reported. However, numerical models of single particles undergoing cyclic thermochemical transformations have been developed for other heterogeneous solid–gas thermochemical looping systems. Numerical models of particles undergoing either calcination or carbonation have also been reported.

Two models of single particles undergoing thermochemical looping processes that are not CaO looping have been reported. The first numerical model including intra-particle heat and mass transfer of a reacting particle coupled to chemical kinetics has been developed. The model is applied to three metal/metal oxide thermochemical looping systems, as well as three metal oxide partial reduction/oxidation systems in which the metal oxide oxidative state changes cyclicly [García-Labiano et al., 2005]. The model is used to investigate the effects of metal and reaction type, particle porosity, kinetics, external heat and mass transfer, and particle size on time to complete conversion, maximum temperature, and maximum intra-particle temperature gradient. The considered particle size range is 0.1–1.0 mm in diameter. A similar numerical model including external and intra-particle heat and mass transfer coupled to chemical kinetics has been applied to a copper/copper oxide particle (size 1 mm diameter) undergoing thermochemical cycling under a range of realistic process conditions to investigate regimes of different dominant intra-particle thermal transport phenomena [Noorman et al., 2011].

Several examples of single numerical models for particles undergoing either the calcination or carbonation reaction are reported. Three models of intra-particle phenomena developed for the calcination reaction are elaborated here. Mass transfer models including diffusion of $CO_2$ in the pore space and local morphological changes within a particle were used to extract kinetics parameters for the calcination reaction in isothermal particles [Silcox et al., 1989; García-Labiano et al., 2002]. A model including calcination kinetics, conductive heat transfer, and diffusive and advective mass transfer in the pore space has also been developed to study the relative influence of different phenomena with dimensionless numbers [Takkinen et al., 2012].

Fewer models of intra-particle phenomena exist for CaO derived from calcined $CaCO_3$

and the carbonation reaction. Generally, apparent chemical kinetic parameters are fit to experimental data without modeling intra-particle phenomena. Nikulshina et al. [2007] used experimental data specific to the experimental set up to fit apparent chemical kinetic parameters to the unreacted core model. Khinast et al. [1996] and Stendardo and Foscolo [2009] used models coupling intra-particle mass transfer to carbonation kinetics to fit intrinsic chemical kinetics parameters to experimental data.

Reactor development for CaO looping includes the study of thermal transport phenomena in reacting media, lab scale prototyping, and demonstrations [Fennell and Anthony, 2015]. Reactor modeling research include studies of calciner and carbonator reactors. For calciners, a steady-state 3-dimensional heat and mass transfer model coupled to semi-empirical calcination kinetics was developed and applied to an oxy-combustion reactor to identify optimal operating conditions [Ylätalo et al., 2013] and later used to investigation reactor performance under additional operating parameters [Parkkinen et al., 2017]. For carbonators, mass transfer of the solid and fluid phases in the fluidized bed of a 1 $MW_{th}$ reactor used for the carbonation step in a CaO looping demonstration plant was modeled in order to compare transient, 3-dimensional CFD modeling methods [Nikolopoulos et al., 2017]. A transient, 1-dimensional hydrodynamic model coupled to carbonation kinetics of a bubbling bed reactor has also been developed and used to investigate the effect of reactor size, fluidization velocity, and temperature on carbonator performance [Emad et al., 2017].

Several large-scale conventional CaO looping systems have been demonstrated. Post-combustion $CO_2$ and sulfur dioxide ($SO_2$) capturing systems, sized 1 and 2 $MW_{th}$ have been demonstrated at the Technische Universität Darmstadt, Germany [Kremer et al., 2013] and the Industrial Technology Research Institute, Taiwan [Chang et al., 2013], respectively. Post-combustion $CO_2$ capturing pilot plants, sized 0.12 and 1.7 $MW_{th}$ have been demonstrated at the Ohio State University, USA [Wang et al., 2010] and in La Pereda, Spain [Diego et al., 2014]. This second pair of plants both employed a third reactor in addition to the two reactors for carbonation and calcination in order to reactivate sorbent particles in between carbonation and calcination. Rotary kiln calciners were used in Taiwan and the USA, while fluidized bed calciners were used in Germany and Spain. Fluidized bed carbonators were used in Germany, Spain, and Taiwan while an entrained bed carbonator was used in the USA. The size range of solid particles reported in Wang et al. [2010], Chang et al. [2013], and Kremer et al. [2013] is 0.1–0.6 mm in diameter, while particles up to 0.8 mm in diameter have been used in other pilot scale CaO looping demonstrations [Lu et al., 2008]. These particle sizes are smaller than those found in metal/metal oxide and other partial metal oxide redox thermochemical looping systems or in industrial calcination processes, where particles are on the order of 1 mm or 1–100 mm in diameter, respectively.

Additional system level research includes CaO looping integration with existing processes, such as $CO_2$ capture in a cement plant [Sun et al., 2016], and system operation

optimization, such as improving process efficiency by employing strategies such as heat recovery [Matthews and Lipiński, 2012; Chacartegui et al., 2016] and optimizing the addition of fresh solid intermediary material to counteract declines in reactivity [Romeo et al., 2009].

## 2.3 Solar energy

As energy demand increases, sustainable energy sources are vital to meeting our energy needs. Just as the current energy industry is based on multiple energy sources such as coal, natural gas, and oil [International Energy Agency, 2017], a sustainable energy industry will likely need to be based on a variety of sources including wind, geothermal, and solar. Solar energy is an abundant and underutilized resource with the potential to completely change the energy industry if harnessed effectively, efficiently, and cheaply.

Two major families of solar energy technology exist, based on different fundamental physical phenomena: photovoltaic and thermal. Photovoltaic technologies utilize the photovoltaic effect of semiconductors, in which the absorption of radiation results in the excitation of electrons and the generation of electron-hole pairs in the semiconductor. Solar photovoltaic cells contain photovoltaic semiconductors and selectively separate the electron-hole pairs generated by the absorption of solar radiation. Removing the separated pairs to an external electrical circuit results in electricity. Several cells are typically packaged together in the most well known solar energy technology: a solar photovoltaic panel [Mertens, 2014].

Applications of photovoltaic technology are rapidly expanding as the technology advances and production becomes cheaper [Mertens, 2014]. Single panels range in size, efficiency, and life span, all tailored to various applications. For example, small and cheap photovoltaic panels are used to power small novelty toys; whereas robustly manufactured and efficient panels are used in spacecrafts [Mertens, 2014]. Most familiar among the general public are photovoltaic panels used to electrify buildings or in utility-scale photovoltaic power plants, in place of or in supplement to grid utility electricity. Photovoltaic panels in these applications can be mounted stationary or on one- or two-axis solar tracking systems [Mertens, 2014]. Photovoltaics that contain solar cells optimized for use with concentrated radiation and optics such as lenses or mirrors to concentrate radiation onto a smaller area are called concentrator photovoltaics. Concentrator photovoltaics yield high efficiencies and are used exclusively with tracking systems for power plant applications [Pérez-Higueras et al., 2011].

In solar thermal technologies, solar radiation is absorbed as thermal energy and the thermal energy is utilized. Solar thermal technologies are generally divided into two categories based on temperature. The categories are low- and high-temperature. Low-temperature technologies operate at temperatures near and below 100°C, with no or minimal concentrating optics. In low-temperature systems, solar radiation can

be absorbed directly by the utilizing medium or by a surface specifically design to absorb solar radiation as thermal energy, called an absorber. After radiation is absorbed by an absorber, it is transferred from the absorber to the utilizing medium. Direct absorption applications include cooking and drying processes, while processes featuring an absorber include residential or commercial hot water and desalination or other distillation processes. Absorber surfaces are more common [Duffie and Beckman, 2013].

High-temperature solar thermal technologies always feature solar tracking, concentrating optics to achieve temperatures above 100°C. High-temperature solar thermal technologies are also commonly referred to as concentrated solar thermal (CST) technologies. The ratio of the concentrator mirror area to the target or aperture area where radiation is redirected is the geometric concentration ratio. A flux-based concentration ratio is often expressed as a multiple of "suns," where one sun is equivalent to 1 kW $m^{-2}$ and the geometric concentration ratio is multiplied by one sun to yield the equivalent number of suns concentrated by the system [Weinstein et al., 2015].

Four concentrating mirror configurations for CST technology have reached commercial scale implementation: parabolic trough and linear Fresnel systems that concentrate radiation onto a line (requiring one-axis tracking) and parabolic dish and heliostat/tower systems that concentrate radiation onto a point focus (requiring two-axis tracking). For all configurations, at the aperture, the concentrated radiation is absorbed as thermal energy and transferred to water or an alternate heat transfer fluid. All current, operating, commercial CST technologies produce steam, either directly or via heat exchange with the heat transfer fluid, to generate electricity using conventional steam turbines [Weinstein et al., 2015]. This application is commonly referred to as CST electricity or concentrated solar power (CSP).

Parabolic trough systems feature a long, trough-like mirror with a truncated parabolic cross section. Each trough concentrates radiation to an absorber tube fixed at the focus of the truncated parabolic cross section, and thermal energy is transferred to a heat transfer fluid flowing through the absorber tube. Parabolic troughs achieve concentration ratios of $\sim 80$ (or 80 suns). One-axis tracking moves the parabolic trough mirror and absorber tube together. Typical operation of parabolic trough systems results in $\sim 400$°C heat transfer fluid at the absorber exit [Weinstein et al., 2015].

Linear Fresnel systems feature several long, flat, independently-tracking mirrors that reflect radiation onto a stationary absorber tube fixed above the mirrors. Concentration ratios of $\sim 80$ suns are achieved with linear Fresnel systems, and typical operation results in $\sim$ 300–400°C heat transfer fluid at the absorber exit [Weinstein et al., 2015].

Parabolic dish systems feature several small, mirror facets attached to a dish frame in the shape of a paraboloid. The mirror facets reflect radiation to a solar receiver fixed at the focus of the dish frame. Both the dish frame and receiver move together as the sun is tracked. Radiation is absorbed in the receiver by an absorber, and thermal energy is transferred to a heat transfer fluid. Concentration ratios of $\sim 1500$ suns are achieved

with parabolic dish systems, and typical operation results in $\sim$ 550–750° C heat transfer fluid at the receiver/absorber exit [Weinstein et al., 2015].

Heliostat/tower systems feature a field of two-axis, independently-tracking heliostat reflectors surrounding or adjacent to a central tower with the focus at the top. A receiver is fixed at the focus and includes an absorber surface or volume. Concentration ratios of $\sim$ 1000 suns are achieved with heliostat/tower systems, and typical operation results in $\sim$ 400–600° C heat transfer fluid at the receiver exit [Weinstein et al., 2015].

Parabolic trough systems are the most common type of realized power plants. However, most new power plants are tower systems, and current high-temperature research and design efforts are related to tower systems. These research and design efforts include reducing the cost of CST electricity by (1) improving solar receiver/absorber materials and design, (2) reducing the cost and improving the optical efficiency of the heliostat field, (3) developing higher temperature, more efficient heat transfer fluids, (4) developing novel TES materials that are cheaper, have higher energy storage density, and/or operate at higher temperatures, and (5) developing novel power block cycles [U.S. Department of Energy, 2012; Australian Solar Thermal Research Initiative, 2015].

### Solar thermochemistry

An alternative and potentially transformative application of solar energy is to use high-temperature solar thermal energy to drive thermochemical reactions [Steinfeld and Palumbo, 2003]. By replacing traditional, non-renewable sources of process heat with solar energy, energy from the sun is captured as chemical potential that can be easily stored and transported [Gray, 2009].

Solar thermochemical processes have been investigated for many different applications. Examples of solar thermochemical fuel production include fossil fuel [Hirsch et al., 2001; Dahl et al., 2004; Piatkowski and Steinfeld, 2008] or biomass [Hathaway et al., 2011] upgrading, metal-based thermochemical looping for hydrogen production [Tamaura et al., 1997; Steinfeld, 2002; Chueh and Haile, 2009; Alvani et al., 2009; Fresno et al., 2010], and direct water thermolysis [Kogan, 2000]. Synthetic liquid hydrocarbon fuels can be produced via synthesis gas derived from solar thermochemical $CO_2$ and $H_2O$ splitting cycles. Limestone [Meier et al., 2006] and ammonia [Gálvez et al., 2007] are examples of commodities produced via solar thermochemical processes. Challenges and opportunities include (1) understanding heat and mass transfer characteristics of reacting materials and chemical kinetics at high temperatures and (2) solar chemical reactor materials and design, which are topics of current research [Lipiński et al., 2013].

Thermochemical reactions involve various transient, coupled physical phenomena within a reacting medium. These phenomena present important design concerns in the realization of solar thermochemical technologies, because the phenomena within constituents of the reacting medium, such as particles, dictate macroscopic reaction behavior of the reacting medium. Reacting media may be a packed bed of particles, a

fluidized bed of particles, active material deposited on a rigid, inert framework, a porous foam made from active material, and other configurations currently being investigated. Behavior and characteristics of the bulk reacting medium then guide reactor design. Thus, successful reactor designs require a multiscale analysis.

**Solar calcium oxide looping** Solar CaO looping is being investigated for use with concentrated solar thermal energy for the applications of solar $CO_2$ capture [Reich et al., 2014b] as well as high-temperature TES [Tescari et al., 2014]. When concentrated solar thermal energy is used to drive CaO looping for $CO_2$ capture, the net result of the cycle in an input of concentrated solar energy and an output of $CO_2$ separated from a dilute source into a concentrated stream. The high-temperature capture of $CO_2$ via solar CaO looping promises high efficiencies and capture rates [Nikulshina et al., 2009].

Many of the qualities that make CaO looping well suited for solar $CO_2$ capture also make the cycle well suited for high-temperature, thermochemical TES. To implement CaO looping for TES, input thermal energy is used to calcine $CaCO_3$ into CaO and $CO_2$. The generated $CO_2$ is collected and separated from the CaO until discharge of the system is desired. When discharge is desired, CaO is exposed to the stored $CO_2$, driving exothermic carbonation. Thermal energy then is recovered from the exothermic process. The net result of the cycle is an input of thermal energy and an output of thermal energy at a later time.

A related reaction system being considered for solar thermochemical TES is the $CaO/Ca(OH)_2$ reaction system [Linder et al., 2014]. This reaction system exhibits attractive kinetics and high sorbent utilization. However, the reaction temperature are lower than CaO looping, approximately 400 to 560° C [Criado et al., 2014], making the $CaO/Ca(OH)_2$ reaction system unsuitable for high-temperature TES.

While CaO looping technologies with conventional sources of process are nearing industrial scale, solar CaO looping is relatively young. Conventional or solar CaO looping both share the benefit of extremely cheap raw material and the challenge of rapid loss of intermediary reactivity. Conventional CaO looping research areas that also apply to solar CaO looping include sorbent modification to improve sustained reactivity with cycling, the study of intra-particle thermal transport phenomena, and integration of CaO looping into existing plants. Current topics of research particular to the field of solar CaO looping include (1) system thermodynamic analyses; (2) solid intermediary interaction with concentrated solar radiation; (3) directly irradiated and indirectly heated reactor design; and (4) economic assessment.

Previous thermodynamic analyses of solar CaO looping include an analysis of a three reactor $H_2$ production system with integrated $CO_2$ capturing [Nikulshina et al., 2006] and an analysis of a two reactor system solely for $CO_2$ capture [Matthews and Lipiński, 2012]. The three reactor set up is designed to capture $CO_2$ from air and co-produce $H_2$ from methane ($CH_4$) using concentrated solar thermal energy. A thermodynamic efficiency of converting both concentrated solar and methane chemical input to the chemical energy

of $H_2$ was found to be 22.7% [Nikulshina et al., 2006].

The effect of heat recovery on required solar energy input is considered in the thermodynamic analysis of the two reactor $CO_2$ capturing system. Estimates for the solar thermal input per amount of substance of $CO_2$ captured for various heat recovery configurations and operating conditions are given. Based on the analysis, a very high theoretical minimum energy input is required to capture one mole of $CO_2$ from gas with 0.03% $CO_2$ concentration (300 ppm) [Matthews and Lipiński, 2012]. Because of the high minimum energy input required to capture from atmospheric air, only $CO_2$ capture from point sources such as flue gas will be considered in this work.

Numerical models of intra-particle thermal transport phenomena have been applied to particles that are directly irradiated with concentrated solar radiation. A heat transfer model including conduction and radiative heat transfer within a particle of $CaCO_3$ under direct high-intensity irradiation was used to investigate transient temperature and stress profiles in the particle [Dombrovsky and Lipiński, 2007]. Dombrovsky and Lipiński [2007] found intra-particle stress for the considered conditions does not cause mechanical destruction of the particles.

A model including calcination kinetics, conductive and radiative modes of heat transfer, and diffusive mass transfer in the pore space has been used to investigate radiative heat transfer modeling methods [Ebner and Lipiński, 2011], chemical reaction models [Ebner and Lipiński, 2012], and uniform versus non-uniform direct irradiation [Ebner and Lipiński, 2014]. In the radiative heat transfer modeling method investigation, results using the Rosseland diffusion approximation and Monte Carlo ray tracing method showed similar intra-particle temperature gradients and time to complete calcination. In the chemical reaction model investigation, results using the volumetric reaction model exhibited larger intra-particle temperature gradients and faster time to complete calcination compared to those using the shrinking core model. In the radiation distribution investigation, non-uniform irradiation resulted in longer time to complete calcination compared to uniform irradiation.

Two primary reactor configurations exist for solar CaO looping: a two-reactor configuration and a single reactor configuration [Reich et al., 2014b]. In a single reactor configuration, solid particles remain in one reactor, and the solar input and input gas composition change to drive either calcination and carbonation. In a two-reactor configuration, solid particles are cycled between two reactors in which separate reactions take place: a solar calciner for the calcination of $CaCO_3$ and a non-solar carbonator for the carbonation of CaO. As mentioned in Section 2.2, most conventional CaO looping systems are two-reactor configurations. Several solar reactors have been developed for the calcination of $CaCO_3$. Few single reactors have been developed for both reactions.

Several kW-scale solar reactors have been developed and demonstrated for calcining $CaCO_3$ for the production of lime [Koepf et al., 2017]. Solar lime reactors have been designed and demonstrated for processing 1–5 mm diameter $CaCO_3$ particles and showed

high conversion rates and solar to chemical efficiencies. While much of the knowledge gained from this research is applicable to solar CaO looping, solar lime reactors cannot typically be used as solar CaO looping calciners because of different design constraints. Solar calciners should be designed for calcination in high $CO_2$ concentration atmospheres for solar CaO looping for $CO_2$ capture or TES. Solar lime reactors often feature reactants open to the atmosphere or enclosed reactants in reactors designed to calcine in an air atmosphere.

Single reactor configurations that have been considered for solar CaO looping include a fluidized bed reactor and a packed bed reactor. The fluidized bed reactor has been developed and used to thermochemically cycle sorbent particles experimentally in a high-flux solar simulator [Nikulshina et al., 2009; Nikulshina and Steinfeld, 2009]. $CO_2$ was captured using the fluidized bed reactor from a gas source with a $CO_2$ concentration of 500 ppm. The packed bed reactor concept has been numerically modeled and investigated for solar $CO_2$ via CaO looping [Reich et al., 2014a, 2015]. The concept consists of dual cavities where the inner cavity serves as the solar receiver and the outer annulus region serves as the reaction zone.

Of the particle-based reactor designs being considered for solar CaO looping, convective heat and mass transfer local to reacting particles differ substantially between fluidized or packed bed reactors. Similarly, radiative heat transfer local to reacting particles differs between directly irradiated or indirectly heated reactors. When studying thermal transport phenomena at the particle level, the range of conditions to consider is determined by these design variations.

## 2.4 Summary

Thermochemical looping technologies with conventional sources of process heat have been successfully demonstrated at the pilot plant scale, proving the potential of these technologies. Because thermochemical looping processes require thermal energy, often at high temperatures, concentrated solar thermal energy is an attractive option for supplying process heat from a renewable energy resource.

Conventional and solar CaO looping share many similar benefits and challenges. The study of intra-particle thermal transport phenomena in particles undergoing CaO looping is applicable to both fields. However, conventional and solar CaO looping intra-particle thermal transport phenomena studies are distinguished by conditions surrounding particles that are related to process heat source dependent reactor designs and system configurations.

# Part I

# Numerical model formulation

Chapter 3

# Chemical thermodynamics and kinetics of calcination and carbonation

## 3.1 Introduction

When utilizing reversible reaction chemistry for engineering applications, the conditions when the forward or reverse reaction will occur must first be determined. After the direction of the reaction is determined, the rate at which the reaction will proceed must next be determined. The factors influencing both the direction and the rate that the reaction will proceed vary depending on the reaction system. For CaO looping, $CO_2$ partial pressure and temperature determine the direction the reaction will proceed, while $CO_2$ partial pressure, temperature, and reaction area determine the reaction rate.

In this chapter, the chemical thermodynamics that determine if calcination or carbonation occurs will be presented. Next a review of reaction rate forms will be presented and the reaction rate definition used in this work will be discussed. Reaction rate expressions from literature for both the calcination and carbonation reactions under conditions relevant to CaO looping are discussed, and the expressions selected for use in this work are elaborated. The reaction rate expressions for calcination and carbonation are finally combined to yield the reversible, overall reaction rate expression.

## 3.2 Thermodynamics

Calcination is an endothermic reaction that proceeds at temperatures on the order of 1000 K. Carbonation is an exothermic reaction, and under typical atmospheric conditions, the reaction rate is very slow for practical chemical engineering applications. While slow carbonation under typical atmospheric conditions is relevant to cement hardening over the life span of cement, carbonation rates relevant to CaO looping occur at elevated temperatures in the range of approximately 500–1000 K. The enthalpies of reaction at standard conditions $\Delta\bar{h}^{\circ}_{298\,\mathrm{K}}$ for calcination and carbonation are 178 kJ mol$^{-1}$ and

$-178\,\mathrm{kJ\ mol^{-1}}$, respectively.

At chemical equilibrium, the forward and reverse reactions occur at the same rate, resulting in no overall change in the concentration of either the reactants or products. For the calcination/carbonation reaction system, the equilibrium partial pressure of $CO_2$ $p_{eq}$ exponentially increases with temperature $T$ according to the following equation,

$$p_{eq} = A_{eq} \exp\left(-\frac{B_{eq}}{T}\right) \tag{3.1}$$

where $A_{eq} = 4.137 \times 10^{12}\,\mathrm{Pa}$ and $B_{eq} = 2.0474 \times 10^{4}\,\mathrm{K}$ [Barin, 1995]. Equilibrium partial pressure of $CO_2$ versus temperature is shown in Fig. 3.1 for the temperature range of interest for CaO looping.

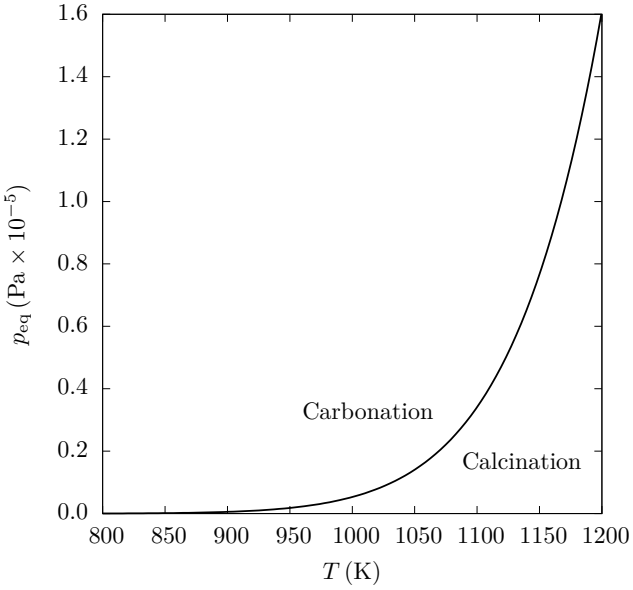


Figure 3.1: Equilibrium partial pressure of $CO_2$ versus temperature

When a system is not in equilibrium, either the calcination or carbonation reaction will be favored. $CO_2$ partial pressure and temperature conditions above and below the equilibrium line shown in Fig. 3.1 favor carbonation and calcination, respectively.

## 3.3 Kinetics

Reaction rates for calcination or carbonation have been defined and determined in a variety of ways in literature. In this section, examples of several different reaction rate expressions for calcination and carbonation are briefly discussed. Then the overall reaction rate definition and the calcination and carbonation expressions selected for use in this work is detailed. Lastly, the overall reaction rate expression is presented.

Reaction rates have been defined to describe how the mass $m$ or amount of substance $N$ of $CaCO_3$ or CaO or the molar fraction of calcium that is present as $CaCO_3$ or CaO

change per unit time $t$, reaction surface area $S$, and/or volume $V$. The fraction of calcium that is present as CaO is often referred to as conversion or reaction extent and is expressed on a molar basis.

$$X \stackrel{\text{def}}{=} \frac{N_{\text{CaO}}}{N_{0,\text{Ca}}} \tag{3.2}$$

where $N_{\text{CaO}}$ is the current amount of substance of CaO and $N_{0,\text{Ca}}$ is the initial amount of substance of calcium. When the reaction rate is defined as $\mathrm{d}X/\mathrm{d}t$, the reaction rate expression is often integrated over time to yielding an expression for reaction extent as a function of time, making this a popular definition in literature. The mathematical forms of common reaction rate definitions are shown in Table 3.1.

Table 3.1: Common reaction rate definitions

| Definition | Meaning |
|---|---|
| $\frac{\mathrm{d}m}{\mathrm{d}t}$ or $\frac{\mathrm{d}N}{\mathrm{d}t}$ | change in mass or amount of substance per unit time |
| $\frac{\mathrm{d}m}{\mathrm{d}S\mathrm{d}t}$ or $\frac{\mathrm{d}N}{\mathrm{d}S\mathrm{d}t}$ | change in mass or amount of substance per unit reaction surface area per unit time |
| $\frac{\mathrm{d}m}{\mathrm{d}V\mathrm{d}t}$ or $\frac{\mathrm{d}N}{\mathrm{d}V\mathrm{d}t}$ | change in mass or amount of substance per unit volume per unit time |
| $\frac{\mathrm{d}X}{\mathrm{d}t}$ | change in reaction extent per unit time |

In this work, a molar volumetric reaction rate is defined as

$$\bar{r}''' = -\frac{\mathrm{d}N_{\text{CaCO}_3}}{\mathrm{d}V\mathrm{d}t} = \frac{\mathrm{d}N_{\text{CaO}}}{\mathrm{d}V\mathrm{d}t} = \frac{\mathrm{d}N_{\text{CO}_2}}{\mathrm{d}V\mathrm{d}t} \tag{3.3}$$

where $N_{\text{CaCO}_3}$ and $N_{\text{CO}_2}$ are the amounts of substance of $CaCO_3$ and $CO_2$, respectively. Reaction rates, both in this work and in literature, are evaluated by equating them to an expression. The form of the expression and the parameters included in the expression for evaluating any form of reaction rate are determined by reaction models, kinetic theory, and/or inspection of experimental data trends. Constants in the expressions are then fit to match experimental data. Appropriate expressions for evaluating $\bar{r}'''$ in this work are taken from literature and elaborated below.

To evaluate reaction rate expression form and parameters for the calcination or carbonation reaction, the most commonly used technique is thermogravimetric analysis (TGA). In TGA studies, an amount of reactant is placed on a balance and is subjected to a specific environment. If the environment results in a chemical reaction, the mass of the sample will change. The transient change in sample mass is then correlated to solid composition and the rate at which the chemical reaction occurred. Several aspects of TGA studies need to be carefully considered for the study to produce accurate intrinsic chemical kinetic parameters. Such aspects include (1) understanding the environmental conditions around the reactant, (2) isolating a single chemical reaction from other chemical

reactions or transformation that cause weight change, (3) distinguishing heat and mass transfer limited reaction regimes from kinetic limited reaction regimes, and (4) selecting appropriate reaction rate expressions and parameters.

An emerging technique for studying intrinsic chemical kinetics is in-situ X-ray diffraction (XRD) analysis. In-situ XRD studies track material crystal structure changes in small, powdered samples as reactions occur. Studies of this nature have the potential to address two aspects listed above: isolating the chemical reaction and removing heat and mass transfer limitations. However, the method is still emerging. In-situ XRD studies of calcination and carbonation include Biasin et al. [2015] and Valverde and Medina [2017], respectively.

Reported reaction rate expressions for calcination and carbonation have been dependent on temperature $T$, reaction extent of the reacting medium $X$, $CO_2$ partial pressure $p_{CO_2}$, and/or reaction specific surface area, expressed as a mass-specific $s$, volume-specific $s'''$, or total $S$ quantity. Evaluated reaction rate constants can include reaction order $m$, non-Arrhenius reaction rate constant $k$, Arrhenius pre-exponential factor $k_0$, Arrhenius activation energy $\overline{E}_a$, and/or other constants.

Reaction models used to describe particles undergoing calcination or carbonation include global uniform reaction models, shrinking core models, and volumetric models such as the changing grain size model. Single global expressions assume homogeneous composition and conditions [House, 2007]. Intra-particle composition or temperature profiles are therefore not resolved. As a result, single global expressions have limited applicability as they are specific to experimental conditions and may not account for heat or mass transfer limitations [House, 2007]. The shrinking core model [House, 2007] has been used to accurately describe the calcination reaction under some conditions, however, it has not been used to accurately describe the carbonation reaction. These simpler models are generally only accurate when applied to simplified systems, for example when particles are heated at a sufficiently slow rate and/or particles are sufficiently small that heat transfer limitations do not exist [Khinast et al., 1996]. In this work, an intrinsic reaction rate expression is used to describe chemical kinetics, while a numerical model of intra-particle heat and mass transfer coupled to intrinsic kinetics presented in Chapter 4 is used to resolve spatial variations in reacting particles.

### 3.3.1 Calcination

The rate at which the calcination reaction proceeds has been extensively studied. Rate expressions typically feature a single-temperature, non-Arrhenius rate constant or a temperature-dependent Arrhenius-like rate constant. A selection of rate expressions are shown in Table 3.2. In addition to rate constants, expressions may contain morphological parameters such as reaction surface area or reaction specific surface area. Several expressions also contain functions describing the $CO_2$ partial pressure dependence $f_{CO_2}$, though the form of this function varies.

Table 3.2: Calcination reaction rate expressions, where $k$ indicates a non-Arrhenius rate contant

| Rate expression | Source |
|---|---|
| $\frac{\mathrm{d}X}{\mathrm{d}t} = k_0 \exp\left(\frac{-E_\mathrm{a}}{RT}\right)(1-X)^m$ | Gallagher and Johnson Jr. [1973] |
| $\frac{\mathrm{d}X}{\mathrm{d}t} = -kSt$ | Borgwardt [1985] |
| $\frac{\mathrm{d}N}{\mathrm{d}S\mathrm{d}t} = k f_{\mathrm{CO_2}}$ | Dennis and Hayhurst [1987]<br>Silcox et al. [1989] |
| $\frac{\mathrm{d}N}{\mathrm{d}V\mathrm{d}t} = -k s''' f_{\mathrm{CO_2}}$ | Khinast et al. [1996] |
| $\frac{\mathrm{d}N}{\mathrm{d}V\mathrm{d}t} = -k_0 \exp\left(\frac{-E_\mathrm{a}}{RT}\right) s''' f_{\mathrm{CO_2}}$ | García-Labiano et al. [2002] |
| $\frac{\mathrm{d}X}{\mathrm{d}t} = k_0 \exp\left(\frac{-E_\mathrm{a}}{RT}\right)(1-X) f_{\mathrm{CO_2}}$ | Acharya et al. [2012] |

Expressions reported by Gallagher and Johnson Jr. [1973], Borgwardt [1985], and Acharya et al. [2012] are global expressions, describing the rate of change of overall reaction extent for the considered system. Expressions reported by Dennis and Hayhurst [1987], Silcox et al. [1989], and Khinast et al. [1996] describe intrinsic chemical kinetics. While intrinsic rate constants may be specific to the experimental setup, appropriate models can result in intrinsic rate constants that apply generally to a wide variety of systems.

After a review of literature reported kinetics expressions, the expression reported by García-Labiano et al. [2002] was selected for use in this work. The expression describes intrinsic kinetics in a form that matches the rate definition in Eq. (3.3) and includes terms describing the temperature and $CO_2$ concentration dependence which are derived from data over a wide range of both parameters.

García-Labiano et al. [2002] investigated the intrinsic kinetics of the calcination of Blanca limestone at different temperatures (1048–1173 K) and under different $CO_2$ atmospheres (0–80% $CO_2$ and 0.1–1.5 MPa total pressure). Kinetic parameters describing both the temperature and $CO_2$ partial pressure dependence were fit to experimental data using a numerical model of intra-particle mass transfer in order to account for mass transfer limitations on the reaction.

The reaction rate expression is

$$\bar{r}'''_{\mathrm{calc}} = -k_{\mathrm{calc}} s'''_{\mathrm{calc}} f_{\mathrm{CO_2,calc}} \tag{3.4}$$

$$k_{\mathrm{calc}} = k_{0,\mathrm{calc}} \exp\left(-\overline{E}_{\mathrm{a,calc}} / \overline{R}T\right) \tag{3.5}$$

where $k_{\mathrm{calc}}$ is the Arrhenius-like rate constant for calcination, $s'''_{\mathrm{calc}}$ is the local, volume-

Table 3.3: Material properties of $CaCO_3$ and CaO

| Variable | Value | Unit | Source |
|---|---|---|---|
| $\rho_{CaCO_3}$ | 2730 | kg m$^{-3}$ | Oates [1998] |
| $\rho_{CaO}$ | 3350 | kg m$^{-3}$ | Oates [1998] |
| $\overline{M}_{CaCO_3}$ | 0.10009 | kg mol$^{-1}$ | Wieser [2006] |
| $\overline{M}_{CaO}$ | 0.05607 | kg mol$^{-1}$ | Wieser [2006] |
| $\phi_{0,CaCO_3}$ | 0.03 | | García-Labiano et al. [2002] |
| $s_{CaCO_3}$ | 300 | m$^2$ kg$^{-1}$ | García-Labiano et al. [2002] |
| $s_{CaO}$ | $1.9 \times 10^4$ | m$^2$ kg$^{-1}$ | García-Labiano et al. [2002] |

specific reaction surface area for calcination, $f_{CO_2,calc}$ is a function describing the calcination reaction $CO_2$ partial pressure dependence, $k_{0,calc}$ is the calcination pre-exponential factor, $\overline{E}_{a,calc}$ is the calcination activation energy, and $\overline{R}$ is the ideal gas constant and equal to 8.314 J mol$^{-1}$ K$^{-1}$.

The volume-specific reaction specific surface area for calcination is given by

$$s'''_{calc} = \frac{(1-\phi)\left[s_{CaCO_3}(1-X_{local}) + s_{CaO}X_{local}\right]}{\left[\frac{X_{local}}{\rho_{CaO}} + \frac{1-X_{local}}{\rho_{CaCO_3}}\right]} \tag{3.6}$$

where $\phi$ is the local porosity; $s_{CaCO_3}$ and $s_{CaO}$ are the mass-specific surface areas of unreacted $CaCO_3$ and CaO derived from calcined $CaCO_3$, respectively; $X_{local}$ is the reaction extent $X$ defined by Eq. (3.2) evaluated locally; and $\rho_{CaCO_3}$ and $\rho_{CaO}$ are the true densities of non-porous $CaCO_3$ and CaO, respectively.

A linear relationship between the molar fraction of CaO and the porosities of unreacted $CaCO_3$ $\phi_{0,CaCO_3}$ and completely calcined CaO $\phi_{CaO}$ is used to predict the local porosity of partially reacted solid. The linear relationship is

$$\phi = \phi_{0,CaCO_3}\left(1 - \frac{N_{CaO}}{N_{0,CaCO_3}}\right) + \phi_{CaO}\left(\frac{N_{CaO}}{N_{0,CaCO_3}}\right) \tag{3.7}$$

where $N_{0,CaCO_3}$ is the initial amount of substance of $CaCO_3$. The porosity of unreacted $CaCO_3$ can be measured or assumed; García-Labiano et al. [2002] measured the porosity of Blanca limestone, which is used in this work.

The porosity of CaO derived from calcined $CaCO_3$ $\phi_{CaO}$ can be determined from the initial porosity of $CaCO_3$ for 100% conversion:

$$\phi_{CaO} = \left[1 - \left(\frac{\rho_{CaCO_3}}{\overline{M}_{CaCO_3}} \times \frac{\overline{M}_{CaO}}{\rho_{CaO}}\right)\right] + \phi_{0,CaCO_3}\left[\left(\frac{\rho_{CaCO_3}}{\overline{M}_{CaCO_3}} \times \frac{\overline{M}_{CaO}}{\rho_{CaO}}\right)\right] \tag{3.8}$$

where $\overline{M}_{CaCO_3}$ and $\overline{M}_{CaO}$ are the molar masses of $CaCO_3$ and CaO, respectively. Using values listed in Table 3.3, the equation reduces to $\phi_{CaO} = 0.54 + 0.46\phi_{0,CaCO_3}$, meaning

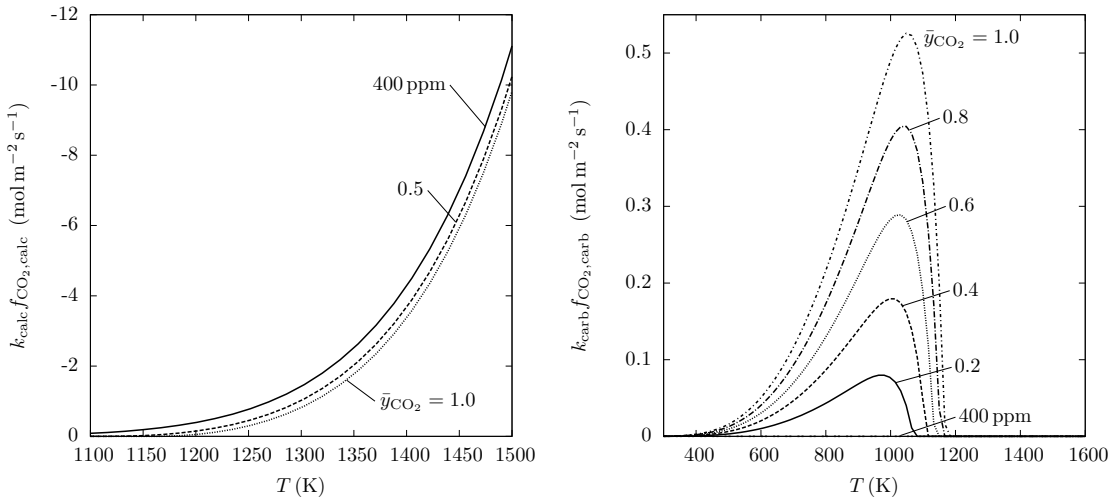


a b

Figure 3.2: Reaction rate normalized by specific surface area versus temperature for selected $CO_2$ concentrations for (a) calcination and (b) carbonation

CaO derived from calcined $CaCO_3$ will have a porosity of at least 0.54 ($\phi_{\mathrm{CaO}} \geq 0.54$). The porosity of $CaCO_3$ measured by García-Labiano et al. [2002] is given in Table 3.3, and for completely calcined CaO derived from Blanca limestone, Eq. (3.8) yields $\phi_{\mathrm{CaO}} = 0.56$.

The Langmuir–Hinshelwood mechanism model with the Freundlich isotherm was found to best predict the dependence on $CO_2$ partial pressure of experimental data for the considered conditions:

$$f_{\mathrm{CO_2,calc}} = \begin{cases} (1-\theta)\left(1 - \dfrac{p_{\mathrm{CO_2}}}{p_{\mathrm{eq}}}\right) & \text{for } p_{\mathrm{CO_2}} < p_{\mathrm{eq}} \\ 0 & \text{for } p_{\mathrm{CO_2}} \geq p_{\mathrm{eq}} \end{cases} \tag{3.9}$$

$$\theta = \begin{cases} c p_{\mathrm{CO_2}}^{1/2} & \text{for } c p_{\mathrm{CO_2}}^{1/2} < 1 \\ 1 & \text{for } c p_{\mathrm{CO_2}}^{1/2} \geq 1 \end{cases} \tag{3.10}$$

$$c = c_0 \exp\left(-\overline{E}_{\mathrm{c}} / \overline{R} T\right) \tag{3.11}$$

where $\theta$ is the fraction of active sites occupied by $CO_2$, $p_{\mathrm{CO_2}}$ is the local partial pressure of $CO_2$, $p_{\mathrm{eq}}$ is the equilibrium partial pressure of $CO_2$, evaluated using Eq. (3.1) at the local temperature, and $c$ is the adsorption constant. In this $CO_2$ dependence model, $f_{\mathrm{CO_2,calc}}$ is unitless and has been extrapolated to 1200 K and concentrations up to 100% $CO_2$ for use in this work.

Values of parameters used in Eqs. (3.5) to (3.8) and (3.11) are given in Tables 3.3 and 3.4. The calcination reaction rate normalized by reaction specific surface area for selected $CO_2$ concentrations is shown in Fig. 3.2a. Increasing temperature and decreasing $CO_2$ concentration increase the calcination rate.

Table 3.4: Reaction rate parameters

| Variable | Value | Unit | Source |
|---|---|---|---|
| $k_{0,\mathrm{calc}}$ | $6.7 \times 10^6$ | mol m$^{-2}$ s$^{-1}$ | García-Labiano et al. [2002] |
| $E_{\mathrm{a,calc}}$ | $1.66 \times 10^5$ | J mol$^{-1}$ | García-Labiano et al. [2002] |
| $c_0$ | $1.8 \times 10^{-7}$ | Pa$^{-1/2}$ | García-Labiano et al. [2002] |
| $E_{\mathrm{c}}$ | $-9.3 \times 10^4$ | J mol$^{-1}$ | García-Labiano et al. [2002] |
| $k_{0,\mathrm{carb}}$ | $1.67 \times 10^{-4}$ | mol m$^{-2}$ s$^{-1}$ kPa$^{-1}$ | Sun et al. [2008] |
| $E_{\mathrm{a,carb}}$ | $2.9 \times 10^4$ | J mol$^{-1}$ | Sun et al. [2008] |

### 3.3.2 Carbonation

Carbonation reaction rates have also been extensively studied in literature, although investigation of kinetics under conditions relevant to CaO looping is still ongoing. In particles undergoing CaO looping, mass transfer limitations on the apparent reaction rate of the particle are important to consider. Carbonating systems typically display an initial, rapid reaction rate regime followed by a slower one. The initial regime is accepted to be kinetics limited while the slower regime is generally accepted to be limited by diffusion of $CO_2$ through the dense $CaCO_3$ product layer to the unreacted CaO as discussed in Section 2.2.

A selection of carbonation rate expressions from the literature are shown in Table 3.5. Reaction rate expressions used for carbonation typically feature either a single-temperature rate constant or a temperature-dependent, Arrhenius-like rate constant. Expressions also typically feature some function related to $CO_2$ partial pressure, although the form of these functions varies greatly. In addition to rate constants and $CO_2$ partial pressure dependence functions, expressions may also contain parameters or functions related to particle morphology and diffusivity of $CO_2$ in the particle $f_{\mathrm{morph}}$.

A common morphological parameter influencing apparent carbonation kinetics is porosity, because amount, size, and connectivity of pores influence the rate of diffusion of $CO_2$ in the pore space to unreacted CaO sites. The porosity as modeled in the calcination section by Eq. (3.7) applies to the solid phase during carbonation as well as calcination. While porosity as a function of solid phase composition is used to predict the calcination reaction specific surface area in the selected calcination model above, the porosity does not appear in any apparent calcination reaction rate expressions shown in Table 3.2. Porosity influences two apparent carbonation reaction rate expressions reported by Bhatia and Perlmutter [1983] and Nikulshina et al. [2007] shown in Table 3.5 via $f_{\mathrm{morph}}$.

Expressions reported by Shimizu et al. [1999], Nikulshina et al. [2007], and Fang et al. [2009] are global expressions, describing the rate of change of overall reaction extent for the considered system. Expressions reported by Bhatia and Perlmutter [1983], Stendardo and Foscolo [2009], Symonds et al. [2009], and Li et al. [2012] describe intrinsic carbonation kinetics.

Table 3.5: Carbonation reaction rate expressions, where $k$ indicates a non-Arrhenius rate contant

| Rate expression | Source |
|---|---|
| $\frac{\mathrm{d}X}{\mathrm{d}t} = k f_{\mathrm{CO_2}} f_{\mathrm{morph}}\left(X, \phi, \text{others}\right)$ | Bhatia and Perlmutter [1983] |
| $\frac{\mathrm{d}X}{\mathrm{d}t} = -k f_{\mathrm{CO_2}} X_{\max} \exp\left(-k f_{\mathrm{CO_2}} t\right)$ | Shimizu et al. [1999] |
| $\frac{\mathrm{d}X}{\mathrm{d}t} = f_{\mathrm{morph}}\left(X, \phi, \text{others}\right)$ | Nikulshina et al. [2007] |
| $\frac{\mathrm{d}N}{\mathrm{d}V\mathrm{d}T} = k_0 \exp\left(\frac{-E_{\mathrm{a}}}{RT}\right) s''' f_{\mathrm{CO_2}}$ | Sun et al. [2008] |
| $\frac{\mathrm{d}X}{\mathrm{d}t} = k\left(1 - \frac{X}{X_{\max}}\right)^m f_{\mathrm{CO_2}}$ | Fang et al. [2009] |
| $\frac{\mathrm{d}N}{\mathrm{d}V\mathrm{d}t} = k s''' f_{\mathrm{CO_2}}$ | Stendardo and Foscolo [2009] |
| $\frac{\mathrm{d}X}{\mathrm{d}t} = k_0 \exp\left(\frac{-E_{\mathrm{a}}}{RT}\right) s''' f_{\mathrm{CO_2}} \left(1 - X\right)$ | Symonds et al. [2009] |
| $\frac{\mathrm{d}N}{\mathrm{d}t} = k f_{\mathrm{CO_2}}$ | Li et al. [2012] |

The carbonation rate expression used in this work mirrors the expression used for calcination.

$$\bar{r}'''_{\mathrm{carb}} = k_{\mathrm{carb}} s'''_{\mathrm{carb}} f_{\mathrm{CO_2,carb}} \tag{3.12}$$

$$k_{\mathrm{carb}} = k_{0,\mathrm{carb}} \exp\left(-\overline{E}_{\mathrm{a,carb}} / \overline{R}T\right) \tag{3.13}$$

where $k_{\mathrm{carb}}$ is the Arrhenius-like rate constant for carbonation, $s'''_{\mathrm{carb}}$ is the local, volume-specific reaction surface area for carbonation, $f_{\mathrm{CO_2,carb}}$ is a function describing the carbonation reaction $CO_2$ partial pressure dependence, $k_{0,\mathrm{carb}}$ is the carbonation pre-exponential function, and $\overline{E}_{\mathrm{a,carb}}$ is the carbonation activation energy. The Arrhenius-like rate constant and $CO_2$ partial pressure dependence function are taken from Sun et al. [2008], the volume-specific reaction surface area expression is taken from Stendardo and Foscolo [2009], and the morphology parameter used in the expression for evaluating the volume-specific reaction surface area is taken from García-Labiano et al. [2002].

Sun et al. [2008] studied the carbonation of fully calcined Strassburg limestone at different temperatures (1048–1173 K) and under different $CO_2$ atmospheres (0–100% $CO_2$ and 101 and 800 kPa total pressure). Very small particles in the range 38–45 μm in diameter and sample sizes less than 3 μg initially were used to minimize mass transfer limitations. The form of the $CO_2$ partial pressure dependence function was derived from a grain reaction model for a kinetically controlled solid–gas reaction expressed in the power law form. Pre-exponential factor and activation energy constants were fit to the initial, kinetics-controlled region using the grain model.

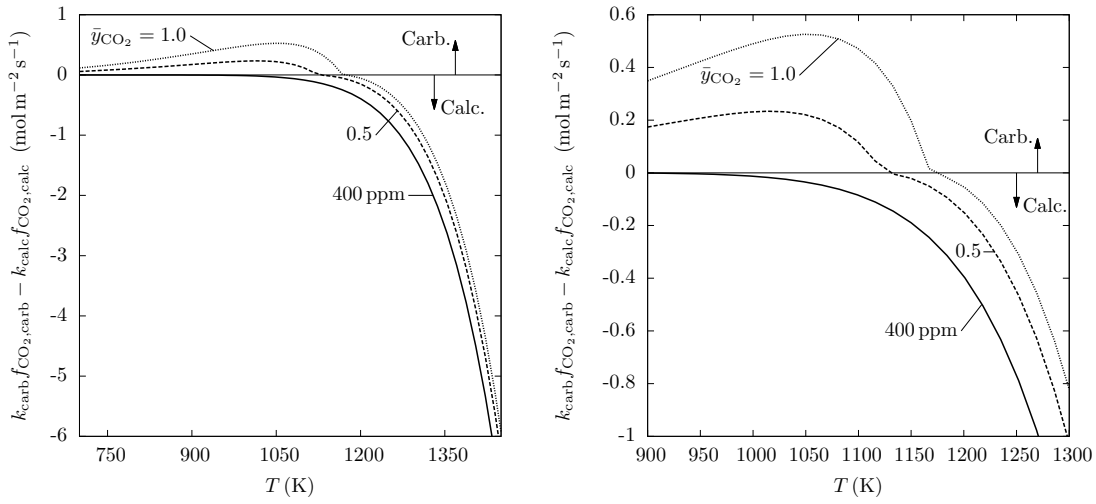


Figure 3.3: Overall reaction rate normalized by specific surface area versus temperature for selected $CO_2$ concentrations in a dry atmosphere shown for (a) all temperatures of interest for CaO looping and (b) temperatures around equilibrium: $\bar{y}_{CO_2} = 1.0$ (dotted line), 0.5 (dashed line), 400 ppm (solid line)

Values of parameters used for the carbonation reaction rate constant are given in Table 3.4. The carbonation reaction rate constant has been extrapolated to 800 K for use in this work. The $CO_2$ partial pressure dependence function for carbonation is [Sun et al., 2008]

$$f_{CO_2,carb} = \begin{cases} p_{CO_2} - p_{eq} & \text{for } p_{CO_2} > p_{eq} \\ 0 & \text{for } p_{CO_2} \leq p_{eq} \end{cases} \tag{3.14}$$

and has the units kPa. The volume-specific reaction specific surface area for carbonation is evaluated using

$$s'''_{carb} = s_{CaO} \rho_{CaO} \left(1 - \phi_{CaO}\right) X_{local}^{2/3} \tag{3.15}$$

which is adapted from Stendardo and Foscolo [2009]. The value of $s_{CaO}$ used in Eq. (3.15) in this work is the same as that used in Eq. (3.6) and is given in Table 3.3.

The carbonation reaction rate normalized by specific surface area for selected $CO_2$ concentrations is shown in Fig. 3.2b. Increasing $CO_2$ concentration results in faster kinetics. Increasing temperature results in faster kinetics until a maximum reaction rate for a given $CO_2$ concentration is reached. Further increases of temperature above the maximum reaction rate temperature results in sharply declining reaction rates until $f_{CO_2,carb} = 0$, and consequently zero carbonation reaction rate, is reached at the local equilibrium temperature.

### 3.3.3 Overall expression

The overall reaction rate expression used in this work combines the individual expressions for both reactions. This single expression indicates both the direction and magnitude of

the reaction rate:

$$\bar{r}''' = -k_{\text{calc}} s'''_{\text{calc}} f_{\text{CO}_2,\text{calc}} + k_{\text{carb}} s'''_{\text{carb}} f_{\text{CO}_2,\text{carb}} \tag{3.16}$$

The overall reaction rate is shown in Fig. 3.3 as a function of temperature for selected $CO_2$ concentrations. Negative and positive rates represent calcination and carbonation, respectively, based on the reaction rate defined by Eq. (3.3). The carbonation curve intersects the calcination curve at the equilibrium temperature for a given $CO_2$ concentration. The overall reaction rate expression is therefore continuous, however the derivative of the curve is not continuous at the transition point between calcination and carbonation.

## 3.4 Summary

In this chapter, temperature and $CO_2$ partial pressure conditions resulting in thermodynamic equilibrium of the calcination/carbonation reaction system were presented. A molar volumetric reaction rate was defined, and reaction rate expressions for calcination and carbonation, appropriate for use with the defined reaction rate, were presented. Combining the two expressions yielded an overall reaction rate expression, which is a function of temperature, $CO_2$ partial pressure, and the calcination or carbonation reaction specific surface area. The overall reaction expression is used to determine local, intrinsic reaction rates in particles undergoing CaO looping in Chapter 4.

Chapter 4

# Conservation of mass, momentum, and energy[1]

## 4.1 Introduction

In this chapter, a numerical model of heat and mass transfer coupled to chemical kinetics is presented. The model describes these thermal transport phenomena within a single, heterogeneous particle, resolving spatial variation of solid and fluid phase composition and temperature at different radial locations within the particle. Time-periodic boundary conditions drive cyclic calcination and carbonation in the particle, therefore the model is transient, and intra-particle composition and temperature gradients change with time. Numerical solution of the model results in an initial value problem which can be used to resolve concentration, pressure, and temperature gradients within a particle as it undergoes the transient transformations of CaO looping. The numerical model is presented in full in this chapter, with selected closure models elaborated in Chapter 5. The numerical model is an extended version of one developed for the transient calcination of a single particle [Yue, 2013; Yue and Lipiński, 2015b].

Intrinsic chemical kinetics is a sub-continuum phenomenon in particles of millimeter size undergoing CaO looping. In such particles, intra-particle temperature and $CO_2$ gradients can exist, resulting in non-uniform local reaction rates. Pore-level features and phenomena can be directly modeled to capture sub-continuum chemical kinetics, but for a given domain, modeling detail down to the sub-continuum level is computationally intensive. To reduce computational cost, averaging methods, models, and simplifying assumptions can be applied to a domain, which homogenize sub-continuum behavior to various extents, allowing domains to be modeled at increasing length scales. As more behavior is homogenized, less detail is preserved, but for the same domain, computational cost is reduced. Continuum scale models are only as accurate as the assumptions used to homogenize the sub-continuum phenomena. In this work, non-uniform conditions within the particle are preserved, while the method of volume averaging and closure models for selected phenomena are applied to make the problem tractable.

[1] Material in this chapter has been published in: Yue and Lipiński [2015b,c]

The analyzed system is a semitransparent, porous particle with non-uniform composition and temperature undergoing CaO looping in a reactor-like environment shown in Fig. 4.1. The analyzed system consists of two solid phase species ($CaCO_3$ and CaO), comprising the porous particle structure and two fluid phase species ($CO_2$ and an inert species), occupying the pore space. In this chapter, the equations are developed for air as the inert species, however, the equations are valid for other inert species with appropriate properties and/or equation of state as required.

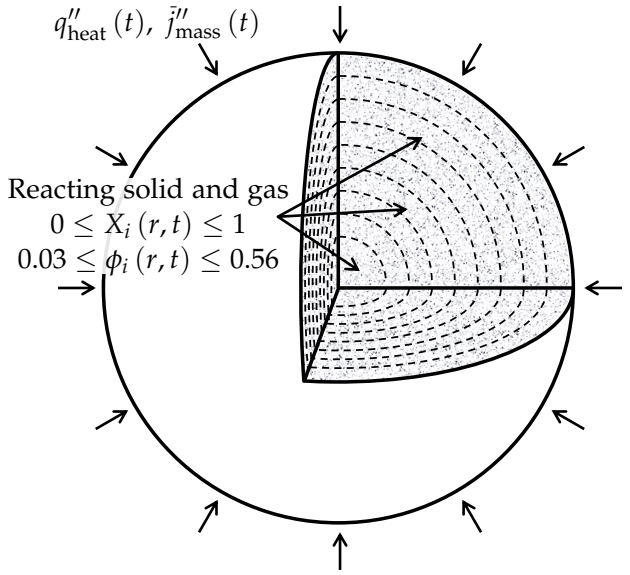


Figure 4.1: The single particle system in a reactor-like environment with non-uniform composition and temperature

In the analyzed system, the solid phase composition changes due to the calcination and carbonation reactions, while the fluid phase composition is affected by absorbed and released $CO_2$, species diffusion due to concentration gradients, and bulk advection due to pressure gradients. Convective mass transfer occurs between the fluid in the particle pore space and the ambient sweep gas surrounding the particle. Heat transfer from the surface to locations within the particle is captured in the heat transfer model. Conduction and radiation are modeled in both the solid and fluid phases. Convective heat transfer occurs between the solid and fluid phases at the particle surface and the ambient sweep gas surrounding the particle.

The model is developed with the following additional assumptions: (1) heat and mass transfer occur uniformly over the particle surface; (2) the particle radius $r_{\text{p}}$ does not change; (3) the only means of fluid mass transfer in the pore space are by diffusion and advection—fluid species do not diffuse into the solid phase; and (4) the solid and fluid phases are at local thermal equilibrium with each other. The model does not take into account particle degradation and loss of reactivity due to cycling or irreversible morphological changes such as sintering. These phenomena have been experimentally

shown to occur in particles undergoing cyclic calcination and carbonation as discussed in Section 2.2 and are important considerations for the realization of CaO looping technologies.

The model presented here is based on one developed by Keene et al. [2013] for heat and mass transfer in a reacting cerium dioxide ($CeO_2$) medium. The model of Keene et al. [2013] was developed using the method of volume-averaging [Kaviany, 1995; Whitaker, 1999] to derive continuum-level governing equations for the heterogeneous system. Following the notation established in Whitaker [1999], volume-averaged variables are denoted in this work with angle brackets. Intrinsic average variables, i.e. variables averaged over a single phase, have superscripts indicating the phase over which the variable is averaged. For example, molar density volume-averaged over the solid phase is $\langle \bar{\rho} \rangle^s$. Superficial average variables, i.e. variables averaged over the total volume, are without a superscript. For example, the superficial volume-averaged fluid velocity is denoted $\langle \vec{\mathbf{u}}_f \rangle$. Closure model properties evaluated using volume-averaged variables are not denoted with volume-averaged angle brackets.

The model consists of five volume-averaged, governing conservation equations: four conservation of mass equations for the four species of the system and one conservation of energy equation. The model also consists of two constraint equations—a simplified conservation of momentum equation and the ideal gas equation of state—and a number of closure models and equations presented in this chapter and Chapter 5. Pertinent studies [Whitaker, 1999; Ebner and Lipiński, 2011; Keene et al., 2013] and engineering intuition were used to select closure models. CaO looping is driven by time-periodic conditions interacting with the particle at the boundary via the boundary conditions, so that extra-particle conditions affect intra-particle temperature and $CO_2$ concentration which determine the reaction direction and rate.

## 4.2 Conservation equations

### 4.2.1 Mass of solid phase

The volume-averaged conservation of mass equations for $CaCO_3$ and CaO read, respectively

$$\frac{\partial \left[ (1-\phi) \left\langle \bar{\rho}_{CaCO_3} \right\rangle^s \right]}{\partial t} = -\bar{r}''' \tag{4.1}$$

$$\frac{\partial \left[ (1-\phi) \left\langle \bar{\rho}_{CaO} \right\rangle^s \right]}{\partial t} = \bar{r}''' \tag{4.2}$$

where $\bar{\rho}_{CaCO_3}$ and $\bar{\rho}_{CaO}$ are the molar densities of $CaCO_3$ and CaO, respectively, $\phi$ is the local porosity, and the reaction rate term on the right-hand side is defined by Eq. (3.3) and evaluated by Eq. (3.16) using local conditions. As the solid phase composition changes, concomitant changes in porosity $\phi$ are considered according to Eq. (3.7).

The local reaction extent $X_{\text{local}}$ is defined by expressing the reaction extent defined by Eq. (3.2) in terms of the molar densities of $CaCO_3$ and CaO,

$$X_{\text{local}} \overset{\text{def}}{=} \frac{\langle \bar{\rho}_{\text{CaO}} \rangle^{\text{s}}}{\bar{\rho}_{0,\text{CaCO}_3}} = 1 - \frac{\langle \bar{\rho}_{\text{CaCO}_3} \rangle^{\text{s}}}{\bar{\rho}_{0,\text{CaCO}_3}} \tag{4.3}$$

where $\bar{\rho}_{0,\text{CaCO}_3}$ is initial local molar density of non-porous $CaCO_3$.

### 4.2.2 Mass of fluid phase

For the fluid phase, the volume-averaged conservation of mass equations for $CO_2$ and air read, respectively

$$\frac{\partial \left( \phi \langle \bar{\rho}_{\text{CO}_2} \rangle^{\text{f}} \right)}{\partial t} + \nabla \cdot \left( \langle \bar{\rho}_{\text{CO}_2} \rangle^{\text{f}} \langle \vec{\mathbf{u}}_{\text{f}} \rangle \right) = \nabla \cdot \left( D_{\text{eff,CO}_2} \nabla \langle \bar{\rho}_{\text{CO}_2} \rangle^{\text{f}} \right) + \bar{j}''_{\text{CO}_2} s'''_{\text{phase}} \tag{4.4}$$

$$\frac{\partial \left( \phi \langle \bar{\rho}_{\text{air}} \rangle^{\text{f}} \right)}{\partial t} + \nabla \cdot \left( \langle \bar{\rho}_{\text{air}} \rangle^{\text{f}} \langle \vec{\mathbf{u}}_{\text{f}} \rangle \right) = \nabla \cdot \left( D_{\text{eff,air}} \nabla \langle \bar{\rho}_{\text{air}} \rangle^{\text{f}} \right) \tag{4.5}$$

where $\bar{\rho}_{\text{CO}_2}$ and $\bar{\rho}_{\text{air}}$ are the molar densities of $CO_2$ and air, respectively; $\langle \vec{\mathbf{u}}_{\text{f}} \rangle$ is the superficial fluid velocity; $D_{\text{eff,CO}_2}$ and $D_{\text{eff,air}}$ are the effective diffusivities of $CO_2$ and air, respectively; $\bar{j}''_{\text{CO}_2}$ is the interphase molar flux of $CO_2$ due to chemical reaction; and $s'''_{\text{phase}}$ is the volume-specific interphase surface area.

Air is modeled as a single species composed of 79% $N_2$ and 21% $O_2$. Evaluation of $\langle \vec{\mathbf{u}}_{\text{f}} \rangle$ and $D_{\text{eff}}$ for $CO_2$ and air will be discussed in the following section and in Chapter 5, respectively. The molar flux of $CO_2$ across the solid–fluid boundary $\bar{j}''_{\text{CO}_2} s'''_{\text{phase}}$ is a volumetric source term equivalent to the reaction rate $\bar{r}'''$.

### 4.2.3 Momentum of fluid phase

Darcy's law simplification of the conservation of momentum equation [Kaviany, 1995] is used to determine the fluid velocity in the pore space, where all pores are assumed active and connected to the particle exterior.

$$-\nabla \left( \phi \langle p_{\text{f}} \rangle^{\text{f}} \right) = \frac{\mu_{\text{f}}}{K_{\text{s}}} \phi \langle \vec{\mathbf{u}}_{\text{f}} \rangle \tag{4.6}$$

where $p_{\text{f}}$ is the fluid pressure, $\mu_{\text{f}}$ is the viscosity of the fluid, and $K_{\text{s}}$ is the permeability of the porous solid. Darcy's law simplification is used for its simplicity and appropriateness, because the expected fluid velocities are low enough to maintain laminar flow at all times and locations within the particle. Reynolds number analysis for representative numerical results confirms laminar flow is maintained. The analysis is elaborated for numerical results in Section 6.3.

The local fluid pressure is evaluated using the ideal gas equation, an appropriate

equation of state because $CO_2$ and air exhibit ideal gas behavior and the total fluid pressure remains low at all times and locations within the particle.

$$\langle p_{\mathrm{f}} \rangle^{\mathrm{f}} = \left( \langle \bar{\rho}_{\mathrm{CO_2}} \rangle^{\mathrm{f}} + \langle \bar{\rho}_{\mathrm{air}} \rangle^{\mathrm{f}} \right) \overline{R} \, \langle T \rangle^{\mathrm{f}} \tag{4.7}$$

where $\langle T \rangle^{\mathrm{f}}$ is the local temperature averaged over the fluid phase. The local fluid viscosity is taken as the molar average of the temperature-dependent fluid species viscosities.

$$\mu_{\mathrm{f}} = \frac{\mu_{\mathrm{CO_2}} \langle \bar{\rho}_{\mathrm{CO_2}} \rangle^{\mathrm{f}} + \mu_{\mathrm{air}} \langle \bar{\rho}_{\mathrm{air}} \rangle^{\mathrm{f}}}{\langle \bar{\rho}_{\mathrm{CO_2}} \rangle^{\mathrm{f}} + \langle \bar{\rho}_{\mathrm{air}} \rangle^{\mathrm{f}}} \tag{4.8}$$

where $\mu_{\mathrm{CO_2}}$ and $\mu_{\mathrm{air}}$ are the viscosities of $CO_2$ and air, respectively. The local permeability of the solid is taken as the molar average of the permeabilities of $CaCO_3$ and CaO derived from calcined $CaCO_3$, $K_{\mathrm{CaCO_3}}$ and $K_{\mathrm{CaO}}$, respectively.

$$K_{\mathrm{s}} = K_{\mathrm{CaCO_3}} \left(1 - X_{\mathrm{local}}\right) + K_{\mathrm{CaO}} X_{\mathrm{local}} \tag{4.9}$$

The upper bound for permeability of naturally occurring dolomite limestone and the permeability of industrial lime mortar are used for the permeabilities of $CaCO_3$ and CaO derived from calcined $CaCO_3$, respectively. Values of the parameters used in Eqs. (4.8) and (4.9) are given in Table 4.1. At temperatures above the valid temperature upper limit, the viscosity is taken as that evaluated at the valid temperature upper limit, i.e. the equations are not extrapolated beyond their reported range.

### 4.2.4 Energy

The solid and fluid phases are assumed to be at local thermal equilibrium, yielding one conservation of energy equation where latent heat changes due to bulk fluid advection, fluid species diffusion, conduction, and radiative heat transfer within the particle.

$$\begin{aligned} \frac{\partial \left\langle \bar{\rho} \overline{h} \right\rangle}{\partial t} + \nabla \cdot \left( \langle \bar{\rho}_{\mathrm{f}} \rangle^{\mathrm{f}} \, \overline{h}_{\mathrm{f}} \, \langle \vec{\mathbf{u}}_{\mathrm{f}} \rangle \right) &= \nabla \cdot \left( \overline{h}_{\mathrm{CO_2}} D_{\mathrm{eff,CO_2}} \nabla \langle \bar{\rho}_{\mathrm{CO_2}} \rangle^{\mathrm{f}} \right) \\ + \nabla \cdot \left( \overline{h}_{\mathrm{air}} D_{\mathrm{eff,air}} \nabla \langle \bar{\rho}_{\mathrm{air}} \rangle^{\mathrm{f}} \right) &+ \nabla \cdot \left( k_{\mathrm{eff}} \nabla \langle T \rangle \right) - \left\langle \nabla \cdot \vec{\mathbf{q}}''_{\mathrm{rad}} \right\rangle \end{aligned} \tag{4.10}$$

where $\overline{h}$ is specific enthalpy, $k_{\mathrm{eff}}$ is the total effective thermal conductivity of the solid and fluid phases, $\langle T \rangle$ is the temperature averaged over the total volume, and $\left\langle \nabla \cdot \vec{\mathbf{q}}''_{\mathrm{rad}} \right\rangle$ is the volume averaged divergence of the radiative heat flux. Because the solid and fluid phases are assumed to be at local thermal equilibrium the superficial average temperature is the same as the intrinsic average temperatures, $\langle T \rangle^{\mathrm{s}} = \langle T \rangle^{\mathrm{f}} = \langle T \rangle$. The time derivative term is evaluated

$$\frac{\partial \left\langle \bar{\rho} \overline{h} \right\rangle}{\partial t} = \left[ \sum_i \langle \bar{\rho}_i \rangle \, \bar{c}_{p,i} \right] \frac{\partial \langle T \rangle}{\partial t} + \left[ \sum_i \overline{h}_i \frac{\partial \langle \bar{\rho}_i \rangle}{\partial t} \right] \tag{4.11}$$

Table 4.1: Properties used in momentum conservation equation

| Variable | Value | Unit | Source |
|---|---|---|---|
| $\mu_{CO_2}$ | $1.2 \times 10^{-6} + 5 \times 10^{-8}\ T - 1.1 \times 10^{-11}\ T^2$ | N s m$^{-2}$ | Yaws [1995] |
| $\mu_{N_2}$ | $4.5 \times 10^{-7} + 6.4 \times 10^{-8}\ T - 2.7 \times 10^{-11}\ T^2 + 5.4 \times 10^{-15}\ T^3$ | N s m$^{-2}$ | Yaws [2009] |
| $\mu_{O_2}$ | $-4.9 \times 10^{-7} + 8.1 \times 10^{-8}\ T - 4.0 \times 10^{-11}\ T^2 + 1.0 \times 10^{-14}\ T^3$ | N s m$^{-2}$ | Yaws [2009] |
| $K_{CaCO_3}$ | $4.5 \times 10^{-14}$ | m$^2$ | Kaviany [1995] |
| $K_{CaO}$ | $4.37 \times 10^{-13}$ | m$^2$ | Válek et al. [2000] |

Table 4.2: Properties used in energy conservation equation

| Variable | Value | Unit | Source |
|---|---|---|---|
| $\overline{h}_{CaCO_3}$ | $1.1 \times 10^2\ T + 1.1 \times 10^{-2}\ T^2 + 2.6 \times 10^6\ T^{-1} - 1.3 \times 10^6$ | J mol$^{-1}$ | Integration of $\bar{c}_p$ |
| $\overline{h}_{CaO}$ | $50.4T + 2.1 \times 10^{-3}\ T^2 + 8.5 \times 10^5\ T^{-1} - 6.5 \times 10^5$ | J mol$^{-1}$ | Integration of $\bar{c}_p$ |
| $\overline{h}_{CO_2}$ | $51.1T + 2.2 \times 10^{-3}\ T^2 + 1.5 \times 10^6\ T^{-1} - 4.1 \times 10^5$ | J mol$^{-1}$ | Integration of $\bar{c}_p$ |
| $\overline{h}_{N_2}, \overline{h}_{O_2}$ | Linearly interpolated from tabulated data | J mol$^{-1}$ | Turns [2013] |
| $\bar{c}_{p,CaCO_3}$ | $1.1 \times 10^2 + 2.2 \times 10^{-2}\ T - 2.6 \times 10^6\ T^{-2}$ | J mol$^{-1}$ K$^{-1}$ | Binnewies and Milke [2002] |
| $\bar{c}_{p,CaO}$ | $50.4 + 4.2 \times 10^{-3}\ T - 8.5 \times 10^5\ T^{-2}$ | J mol$^{-1}$ K$^{-1}$ | Binnewies and Milke [2002] |
| $\bar{c}_{p,CO_2}$ | $51.1 + 4.4 \times 10^{-3}\ T - 1.5 \times 10^6\ T^{-2}$ | J mol$^{-1}$ K$^{-1}$ | Binnewies and Milke [2002] |
| $\bar{c}_{p,N_2}, \bar{c}_{p,O_2}$ | Linearly interpolated from tabulated data | J mol$^{-1}$ K$^{-1}$ | Turns [2013] |
| $k_{CaCO_3}$ | $\left(1.073 \times 10^3\right)\left(77 + T\right)^{-1} + 0.13$ | W m$^{-1}$ K$^{-1}$ | Zoth and Haenel [1988] |
| $k_{CaO}$ | 0.6 | W m$^{-1}$ K$^{-1}$ | Ebner and Lipiński [2011] |
| $k_{CO_2}$ | $-6.1 \times 10^{-3} + 7.5 \times 10^{-5}\ T + 9.5 \times 10^{-9}\ T^2 - 1.1 \times 10^{-11}\ T^3$ | W m$^{-1}$ K$^{-1}$ | Yaws [1995] |
| $k_{N_2}$ | $-2.3 \times 10^{-4} + 1.0 \times 10^{-4}\ T - 6.0 \times 10^{-8}\ T^2 + 2.2 \times 10^{-11}\ T^3$ | W m$^{-1}$ K$^{-1}$ | Bergman et al. [2011] |
| $k_{O_2}$ | $1.6 \times 10^{-4} + 9.4 \times 10^{-5}\ T - 2.8 \times 10^{-8}\ T^2 + 5.2 \times 10^{-12}\ T^3$ | W m$^{-1}$ K$^{-1}$ | Bergman et al. [2011] |

where $i = CaCO_3$, CaO, $CO_2$, and air and $\bar{c}_p$ is the temperature-dependent specific heat capacity. Fluid enthalpy transported due to advection is evaluated as

$$\langle \bar{\rho}_f \rangle^f \bar{h}_f = \langle \bar{\rho}_{CO_2} \rangle^f \bar{h}_{CO_2} + \langle \bar{\rho}_{air} \rangle^f \bar{h}_{air} \tag{4.12}$$

The total effective conductivity is the sum of the weighted conductivity for each species.

$$k_{eff} = (1-\phi) \left[ \frac{\langle \bar{\rho}_{CaCO_3} \rangle^s k_{CaCO_3} + \langle \bar{\rho}_{CaO} \rangle^s k_{CaO}}{\langle \bar{\rho}_{CaCO_3} \rangle^s + \langle \bar{\rho}_{CaO} \rangle^s} \right] + \phi \left[ \frac{\langle \bar{\rho}_{CO_2} \rangle^f k_{CO_2} + \langle \bar{\rho}_{air} \rangle^f k_{air}}{\langle \bar{\rho}_{CO_2} \rangle^f + \langle \bar{\rho}_{air} \rangle^f} \right] \tag{4.13}$$

Evaluation of the divergence of the radiative heat flux term $\left\langle \nabla \cdot \vec{q}''_{rad} \right\rangle$ will be discussed in Chapter 5. Values of parameters used in Eqs. (4.10) to (4.13) are given in Table 4.2. For properties used in the conservation of energy equation and associated closure models, property expressions are not extrapolated beyond their reported range and property values at temperatures greater than the valid range are taken as those evaluated at the valid temperature upper limit.

## 4.3 Initial conditions

Initial conditions are required to numerically solve the initial value problem described by the governing equations presented in Sections 4.2.1 to 4.2.4. These conditions include the molar densities of the four species of the system and temperature for the conservation of mass and energy equations, Eqs. (4.1), (4.2), (4.4), (4.5), and (4.10). Initial pressure and superficial fluid velocity in Eqs. (4.6) and (4.7) are evaluated from density and temperature initial conditions.

For the solid phase species, the solid phase is initially 100% $CaCO_3$ at all locations in the particle.

$$\langle \bar{\rho}_{CaCO_3} \rangle^s = \bar{\rho}_{0,CaCO_3}, \quad \langle \bar{\rho}_{CaO} \rangle^s = 0 \tag{4.14}$$

This condition results in $X_{local} = 0$ for all locations in the particle. The fluid in the pore space initially has the same composition as the surrounding fluid with no pressure or species concentration gradients.

$$\langle \bar{\rho}_i \rangle^f = \bar{\rho}_{\infty,i} \tag{4.15}$$

where $i = CO_2$ and air and $\bar{\rho}_\infty$ is the molar density of the ambient sweep gas. The ambient sweep gas molar densities of $CO_2$ and air are, respectively

$$\bar{\rho}_{\infty,CO_2} = \bar{y}_{\infty,CO_2} \frac{p_\infty}{\bar{R} T_\infty} \tag{4.16}$$

$$\bar{\rho}_{\infty,air} = \left(1 - \bar{y}_{\infty,CO_2}\right) \frac{p_\infty}{\bar{R} T_\infty} \tag{4.17}$$

where $\bar{y}_{\infty,CO_2}$, $p_\infty$, and $T_\infty$ are the ambient molar $CO_2$ concentration, pressure, and

temperature, respectively. In this work the ambient pressure is taken to be atmospheric pressure $p_\infty = 1.01325 \times 10^5\,\mathrm{Pa}$. The particle temperature is initially at convective equilibrium with the surroundings.

$$\langle T \rangle = T_\infty \tag{4.18}$$

These initial conditions apply for all numerical results reported in this work unless stated otherwise.

## 4.4 Boundary conditions

Two boundary conditions—one at the particle surface and one at the particle center—are required for the four conservation of mass equations and one conservation of energy equation.

### 4.4.1 For mass conservation equations

The mass flux at the center of the particle for all species is zero due to symmetry. Further, the solid phase species do not move in space, so the mass fluxes for the solid phase species at the center ($r = 0$) and surface ($r = r_\mathrm{p}$) of the particle are zero.

$$\left.\frac{\partial \langle \bar{\rho}_{\mathrm{CaCO_3}} \rangle^\mathrm{s}}{\partial r}\right|_{r=0} = \left.\frac{\partial \langle \bar{\rho}_{\mathrm{CaCO_3}} \rangle^\mathrm{s}}{\partial r}\right|_{r=r_\mathrm{p}} = 0 \tag{4.19}$$

$$\left.\frac{\partial \langle \bar{\rho}_{\mathrm{CaO}} \rangle^\mathrm{s}}{\partial r}\right|_{r=0} = \left.\frac{\partial \langle \bar{\rho}_{\mathrm{CaO}} \rangle^\mathrm{s}}{\partial r}\right|_{r=r_\mathrm{p}} = 0 \tag{4.20}$$

For the fluid species, the boundary condition at the surface is a mixed condition defined by advection and diffusion at the particle surface and convective mass transfer between fluid at the particle surface and the ambient sweep gas. Thus,

$$\left.\frac{\partial \langle \bar{\rho}_{\mathrm{CO_2}} \rangle^\mathrm{f}}{\partial r}\right|_{r=0} = 0 \tag{4.21}$$

$$\left[\langle \bar{\rho}_{\mathrm{CO_2}} \rangle^\mathrm{f} \langle u_\mathrm{f} \rangle - D_{\mathrm{eff,CO_2}} \frac{\partial \langle \bar{\rho}_{\mathrm{CO_2}} \rangle^\mathrm{f}}{\partial r}\right]_{r=r_\mathrm{p}} = h_\mathrm{m} \left( \left.\langle \bar{\rho}_{\mathrm{CO_2}} \rangle^\mathrm{f}\right|_{r=r_\mathrm{p}} - \bar{\rho}_{\infty,\mathrm{CO_2}} \right) \tag{4.22}$$

$$\left.\frac{\partial \langle \bar{\rho}_{\mathrm{air}} \rangle^\mathrm{f}}{\partial r}\right|_{r=0} = 0 \tag{4.23}$$

$$\left[\langle \bar{\rho}_{\mathrm{air}} \rangle^\mathrm{f} \langle u_\mathrm{f} \rangle - D_{\mathrm{eff,air}} \frac{\partial \langle \bar{\rho}_{\mathrm{air}} \rangle^\mathrm{f}}{\partial r}\right]_{r=r_\mathrm{p}} = h_\mathrm{m} \left( \left.\langle \bar{\rho}_{\mathrm{air}} \rangle^\mathrm{f}\right|_{r=r_\mathrm{p}} - \bar{\rho}_{\infty,\mathrm{air}} \right) \tag{4.24}$$

where $h_{\mathrm{m}}$ is the mass transfer coefficient found from the correlation for convective mass transfer for a sphere in a flow as given in Geankoplis [2003].

$$\mathrm{Sh}_d = 2 + 0.6\mathrm{Re}_{d,\infty}^{0.5}\mathrm{Sc}_{\infty}^{1/3} \tag{4.25}$$

where $\mathrm{Sh}_d$, $\mathrm{Re}_{d,\infty}$, and $\mathrm{Sc}_{\infty}$ are the Sherwood, Reynolds, and Schmidt numbers, respectively. The Sherwood and Reynolds numbers are evaluated using the diameter of the particle ($d = 2r_{\mathrm{p}}$); and the Reynolds and Schmidt numbers are evaluated at ambient conditions around the particle.

### 4.4.2 For energy conservation equation

Conservation of energy equation boundary condition at the center is

$$\left.\frac{\partial \langle T \rangle}{\partial r}\right|_{r=0} = 0 \tag{4.26}$$

due to symmetry. At the surface, the conservation of energy equation boundary condition takes two forms depending on the mode of particle heating. The two considered heating modes are (1) heating due to direct, concentrated irradiation uniformly over the particle surface and passive cooling to emulate a directly irradiated solar reactor and (2) sweep gas temperature controlled. In the sweep gas temperature controlled mode, particle heating and cooling are driven by convection between the particle surface and the ambient gas to emulate the flow of sweep gas through an indirectly or conventionally heated reactor.

**Directly irradiated surface boundary condition** If the particle is directly irradiated and passively cooled, the surface boundary condition for this mode contains terms for convective heat transfer, radiative exchange with the distant enclosure walls, and absorption of additional irradiation external to that emitted by the enclosure walls. Convective heat transfer and radiative exchange are important to consider because these phenomena result in heat loss during heating as well as drive the passive cooling.

$$\left[k_{\mathrm{eff}}\frac{\partial \langle T \rangle}{\partial r} - \langle q''_{\mathrm{rad}} \rangle\right]_{r=r_{\mathrm{p}}} = h_{\mathrm{eff}}\left(T_{\infty} - \langle T \rangle|_{r=r_{\mathrm{p}}}\right) - q''_{\mathrm{net}} \tag{4.27}$$

where $h_{\mathrm{eff}}$ is the effective surface heat transfer coefficient, $q''_{\mathrm{rad}}$ is the radiative flux from the surface into the partice, and $q''_{\mathrm{net}}$ is the net radiative flux across the particle surface. In this heating mode, the ambient temperature around the particle $T_{\infty}$ is assumed constant.

The net radiative flux into the particle is equivalent to the difference between the net absorbed (and transmitted, if applicable to the modeling method) and emitted radiation. External radiative flux incident on the particle surface $q''_{\mathrm{surf}}$ and radiative exchange with the enclosure walls are included in the evaluation of $q''_{\mathrm{net}}$. All irradiation is assumed diffuse and distributed uniformly over the particle surface, and the enclosure walls

with which the particle participates in radiative exchange are assumed black, far from the particle, and at a uniform and constant temperature $T_w$. Evaluation of $q''_{rad}$ at the surface and $q''_{net}$ depends on the method for evaluating $\langle \nabla \cdot \vec{q}''_{rad} \rangle$ and will be discussed in Chapter 5.

The effective surface heat transfer coefficient $h_{eff}$ is found from the Nusselt number correlation for surface convective heat transfer proposed by Whitaker [1972] for flow past a single particle. The Nusselt number is evaluated using the effective conductivity of the particle surface evaluated according to Eq. (4.13).

$$\mathrm{Nu}_d = 2 + \left(0.4\mathrm{Re}_{d,\infty}^{1/2} + 0.06\mathrm{Re}_{d,\infty}^{2/3}\right) \mathrm{Pr}_\infty^{0.4} \left(\frac{\mu_\infty}{\mu_f|_{r=r_p}}\right)^{1/4} \tag{4.28}$$

where $\mathrm{Nu}_d$ and $\mathrm{Pr}_\infty$ are the Nusselt and Prandtl numbers, respectively. The Nusselt number is evaluated using the particle diameter, and the Prandtl number is evaluated at the ambient conditions around the particle.

**Sweep gas controlled surface boundary condition** If particle heating is driven by the sweep gas temperature, a convective boundary condition applies at the particle surface.

$$\left[k_{eff}\frac{\partial \langle T \rangle}{\partial r} - \langle q''_{rad} \rangle\right]_{r=r_p} = h_{eff}\left(T_\infty - \langle T \rangle|_{r=r_p}\right) \tag{4.29}$$

where $T_\infty$ is replaced by a transient function representing the temperature program of the sweep gas. The temperature difference between the particle surface and surroundings is assumed negligible so radiative exchange between the particle and the enclosure walls is omitted.

If the rate of change of temperature of the sweep gas is on the order of or slower than the time scales at which convection occurs ($\mathrm{Nu}_d \leq 1$), the boundary condition can be reduced to a Dirichlet condition for particle surface temperature.

$$\langle T \rangle|_{r=r_p} = f_{T_\infty}(t) \tag{4.30}$$

where $f_{T_\infty}(t)$ is the function representing the temperature program of the reactor.

### 4.4.3 Definition of time-periodicity at the boundary

Time-periodic conditions of $q''_{surf}$ or $f_{T_\infty}(t)$ drive thermochemical cycling of the particle. Particle temperature is controlled via time-periodic irradiation $q''_{surf}$ via $q''_{net}$ in Eq. (4.27) or $f_{T_\infty}(t)$ in Eq. (4.30). Intra-particle $CO_2$ concentrations that influence chemical kinetics are also related to the surrounding $CO_2$ concentration $\bar{y}_{\infty,CO_2}$, which is treated as a time-periodic condition for $CO_2$ capture applications.

A repeating time period is defined as one thermochemical cycle. The particle is initially $CaCO_3$, so one thermochemical cycle of duration $t_{cycle}$ starts with a calcination

period of duration $t_{\text{calc}}$ followed by a carbonation period of duration $t_{\text{carb}}$. Hence, $t_{\text{cycle}} = t_{\text{calc}} + t_{\text{carb}}$. After the carbonation period ends, the next cycle begins. An arbitrary cycle $j$ begins with a calcination period at time instant $t_j$; the carbonation period for cycle $j$ begins at time instant $t_{j,\text{calc}} = t_j + t_{\text{calc}}$; and cycle $j$ ends at time instant $t_{j+1}$.

For a directly irradiated particle, high-intensity solar irradiation drives particle heating and endothermic calcination during the calcination period. During the carbonation period, the particle cools due to radiative exchange with the enclosure walls and convective heat transfer with the sweep gas to allow exothermic carbonation. The external heat flux at the particle surface $q''_{\text{surf}}$ enables this cycling by varying according to

$$q''_{\text{surf}} = \begin{cases} q''_{\text{solar}} & \text{for } 0 < t - t_j \leq t_{\text{calc}} \\ 0 & \text{for } t_{\text{calc}} < t - t_j \leq t_{\text{cycle}} \end{cases} \tag{4.31}$$

where $q''_{\text{solar}}$ is the magnitude of the concentrated solar irradiation.

The function representing the temperature program of a reactor $f_{T_\infty}(t)$ features an initial heating period of duration $t_{\text{init}}$ followed by heating and cooling cycles with optional hold periods. The initial heating period heats the particle from the initial temperature $T_0$ to the carbonation temperature $T_{\text{carb}}$ at the initial heating rate $(\mathrm{d}T/\mathrm{d}t)_0$. From there, the periodic heating and cooling cycles begin, where the calcination period includes heating to the calcination temperature as well as the calcination hold time and the carbonation period includes cooling to the carbonation temperature as well as the carbonation hold time. The duration of the initial heating period is equivalent to the start time of the first cycle, $t_{\text{init}} = t_1$.

A cycle starts with heating from $T_{\text{carb}}$ to the calcination temperature $T_{\text{calc}}$ at the heating rate $(\mathrm{d}T/\mathrm{d}t)_1$. The particle surface is held at $T_{\text{calc}}$ for the duration of the calcination hold time $t_{\text{hold,calc}}$. The particle surface is then cooled from $T_{\text{calc}}$ back to $T_{\text{carb}}$ at the cooling rate $(\mathrm{d}T/\mathrm{d}t)_2$. Finally the particle surface is held at $T_{\text{carb}}$ for the duration of the carbonation hold time $t_{\text{hold,carb}}$, and the cycle ends. The temperature program, including the initial heating period, is described by the following equation

$$f_{T_\infty}(t) = \begin{cases} T_0 + t\left(\dfrac{\mathrm{d}T}{\mathrm{d}t}\right)_0 & \text{for } 0 < t \leq t_{\text{init}} \\ T_{\text{carb}} + (t - t_j)\left(\dfrac{\mathrm{d}T}{\mathrm{d}t}\right)_1 & \text{for } t_j < t - t_j \leq t_{\text{calc}} - t_{\text{hold,calc}} \\ T_{\text{calc}} & \text{for } t_{\text{calc}} - t_{\text{hold,calc}} < t - t_j \leq t_{\text{calc}} \\ T_{\text{calc}} + (t - t_j - t_{\text{calc}})\left(\dfrac{\mathrm{d}T}{\mathrm{d}t}\right)_2 & \text{for } t_{\text{calc}} < t - t_j \leq t_{\text{cycle}} - t_{\text{hold,carb}} \\ T_{\text{carb}} & \text{for } t_{\text{cycle}} - t_{\text{hold,carb}} < t - t_j \leq t_{\text{cycle}} \end{cases} \tag{4.32}$$

There are 12 parameters in Eq. (4.32) defining the temperature program function, however only eight parameters need to be specified to fully describe the function as several

parameters are related.

$$\left(\frac{\mathrm{d}T}{\mathrm{d}t}\right)_0 = \frac{T_{\text{carb}} - T_0}{t_{\text{init}}} \tag{4.33}$$

$$\left(\frac{\mathrm{d}T}{\mathrm{d}t}\right)_1 = \frac{T_{\text{calc}} - T_{\text{carb}}}{t_{\text{calc}} - t_{\text{hold,calc}}} \tag{4.34}$$

$$\left(\frac{\mathrm{d}T}{\mathrm{d}t}\right)_2 = \frac{T_{\text{carb}} - T_{\text{calc}}}{t_{\text{carb}} - t_{\text{hold,carb}}} \tag{4.35}$$

Independent parameters include $t_{\text{hold,calc}}$ and $t_{\text{hold,carb}}$.

An example temperature program is shown in Fig. 4.2. Calcination and carbonation temperatures in Eq. (4.32) should be selected to optimize kinetics for the ambient $CO_2$ concentrations during the respective periods using thermodynamic and chemical kinetics data.

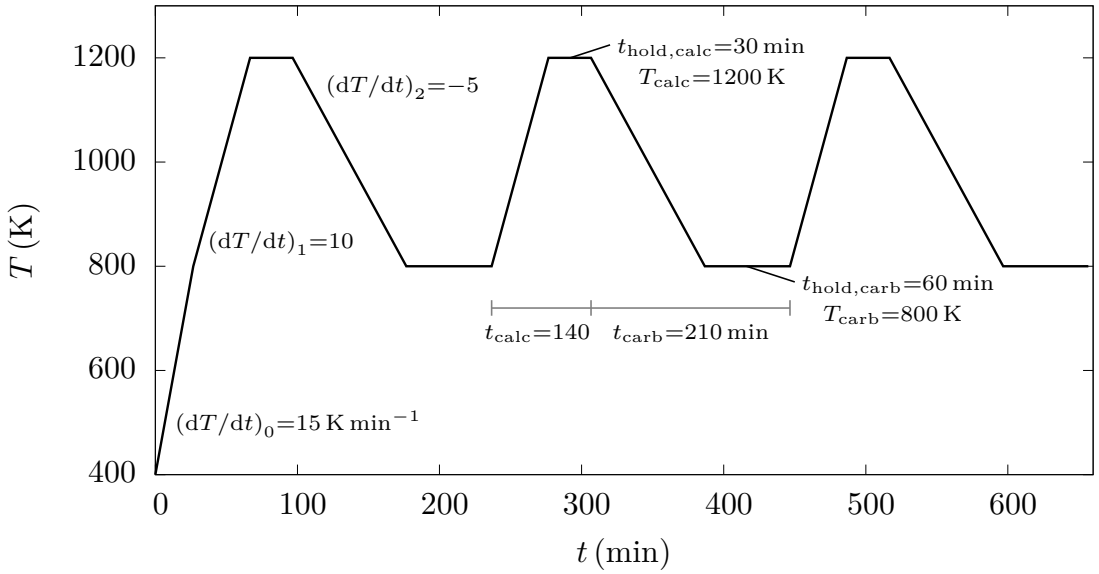


Figure 4.2: Example temperature program used with sweep gas controlled surface boundary condition: temperature $T$ is given in K, time $t$ is given in min, and heating rate $(\mathrm{d}T/\mathrm{d}t)$ is given in K $\text{min}^{-1}$

For either heating mode, if the ambient $CO_2$ concentration differs between the calcination and carbonation periods, the following time-periodic condition applies

$$\bar{y}_{\infty,\text{CO}_2} = \begin{cases} \bar{y}_{\text{CO}_2,\text{calc}} & \text{for } 0 < t - t_j \leq t_{\text{calc}} \\ \bar{y}_{\text{CO}_2,\text{carb}} & \text{for } t_{\text{calc}} < t - t_j \leq t_{\text{cycle}} \end{cases} \tag{4.36}$$

where $\bar{y}_{\text{CO}_2,\text{calc}}$ and $\bar{y}_{\text{CO}_2,\text{carb}}$ are the calcination and carbonation $CO_2$ concentrations, respectively. For $CO_2$ capture applications, $\bar{y}_{\text{CO}_2,\text{carb}}$ represents the $CO_2$ concentration of the dilute source from which $CO_2$ is being captured. The transition between values for $q''_{\text{surf}}$ and $\bar{y}_{\infty,\text{CO}_2}$ in Eqs. (4.31) and (4.36) occurs as a step change.

## 4.5 Numerical solution

The governing equations are discretized in space and time by employing the 1D finite volume method and the explicit Euler time-integration scheme. The spatial domain is discretized into $N = 30$ spherical shell elements with constant thickness $\Delta r$. The central difference scheme is used in the finite volume method to evaluate first- and second-order derivatives in Eqs. (4.4), (4.5), and (4.10), while the fluid velocity in Eq. (4.6) is evaluated at the volume element boundaries. The fluid velocity at the outer face of the outer most volume element is evaluated using the pressure gradient between the fluid pressure in the outer most volume element and the ambient pressure $p_\infty$.

Upwinding of fluid density and enthlapy is used to evaluate the advective and diffusive terms in Eqs. (4.4), (4.5), and (4.10). The effective diffusivity at the surface is taken as the average of the effective diffusivity in the outer most volume element and the binary molecular diffusivity $D_{\text{mol}}$ evaluated for the sweep gas conditions.

The discrete equations are solved using a Fortran 90 code developed for this application, and a time step of $\Delta t = 2 \times 10^{-6}$ s is used for simulations unless otherwise noted. This time step was selected based on trial and error to ensure stability of simulations with particle size $r_{\text{p}} = 2.5$ mm. A simulation of 100 min takes approximately four days to run on a desktop computer with Intel® Core™ i7-3770 4 core 3.40 GHz processor with 8 GB of memory.

Results of the model predicting calcination were previously compared to numerical results of intra-particle heat and mass transfer in a calcining particle reported in the literature [Ebner and Lipiński, 2011]. The results of this model and the one reported in literature show good agreement as reported in Yue [2013]. Grid independence was investigated by testing different numerical grids. Preliminary results were generated using a constant volume grid and grids where the thickness of the volume elements decreased linearly or exponentially from the particle surface to center. Grid independence testing shows that $N = 30$ and constant $\Delta r$ provide a good compromise between mesh resolution and modeling accuracy, and results using those parameters are in agreement with other meshing strategies.

## 4.6 Summary

In this chapter, governing equations, closure models, initial conditions, boundary conditions, and numerical solution methods were given for a numerical model of transient heat and mass transfer coupled to chemical kinetics in a single particle. Time-periodic conditions at the boundary drive CaO looping. Closure models for intra-particle radiative heat transfer and fluid diffusion in the pore space will be discussed in the next chapter.

The model is capable of predicting transient, intra-particle gradients of the following variables: reaction direction and rate, solid and fluid phase composition, temperature,

and fluid pressure and velocity in the pore space. In Part II, the numerical model will be used to investigate transient and intra-particle gradients of these variables in particles undergoing CaO looping under conditions of interest for solar $CO_2$ capture and thermochemical TES.

Chapter 5

# Closure models for intra-particle radiative transfer and mass diffusion

## 5.1 Introduction

The choice of closure models for various physical phenomena can greatly influence the accuracy of numerical model results. Calcination is generally a heat transfer limited reaction in particles undergoing CaO looping, while carbonation is generally mass transfer limited. Thus, intra-particle radiative heat transfer and diffusive mass transfer of gas species in a porous medium are selected for expanded investigation. In this chapter, the Rosseland diffusion and $P_1$ approximations for intra-particle radiative heat transfer are first elaborated and compared; and then, three models for evaluating effective diffusivity to describe binary gas diffusion in a porous medium are presented and compared.

For intra-particle radiative heat transfer, the radiative transfer equation is solved by employing approximations to obtain the divergence of the radiative flux throughout the particle. Two different approaches to solving the radiative transfer equation under the transport approximation are used: the Rosseland diffusion approximation and the lowest order approximate solution using the method of spherical harmonics, known as the $P_1$ approximation. Transport-approximate optical properties for media comprised of $CaCO_3$ and CaO are evaluated using electromagnetic wave and Mie theories, respectively.

Then, the model presented in Chapter 4 is simplified to include only heat transfer in the solid phase, and the simplified model is used to obtain temperature profiles of $CaCO_3$ and CaO particles undergoing heating or cooling using the two approximations. The temperature profiles obtained using both approximations are compared. Spectral properties of extra-particle radiative exchange and intra-particle radiative heat transfer are preserved in the $P_1$ approximation, while these details are spectrally averaged in the Rosseland diffusion approximation. However, results using both approximations are found to be in agreement. It is therefore concluded that for the considered application, the increased computational cost of the $P_1$ approximation is not justified by the preservation of spectral details.

For intra-particle binary gas diffusion in a porous medium, three models for evalu-

ating effective diffusivity are considered. Change in effective diffusivity with varying temperature and solid phase composition is predicted using each of the three considered models. The Knudsen number—the ratio of mean free path length to characteristic length—is evaluated for the considered system. Based on the Knudsen number and available knowledge of the structure of the considered particles, a baseline model is selected from the three presented models.

## 5.2 Radiative heat transfer[1]

Under high-flux irradiation and high-temperature conditions, the effects of radiative heat transfer on thermochemical behavior of reacting media can be considerable. Past studies of particles composed of $CaCO_3$ and/or CaO have neglected radiative heat transfer [Takkinen et al., 2012], used the modified differential approximation (MD$P_0$) to model radiative heat transfer [Dombrovsky and Lipiński, 2007], or used the Rosseland diffusion approximation to model radiative heat transfer [Ebner and Lipiński, 2012; Yue and Lipiński, 2015b,c]. Ebner and Lipiński [2011] evaluated thermochemical characteristics of a particle of $CaCO_3$ undergoing calcination using two intra-particle radiative heat transfer approximations in a combined heat transfer model. Good agreement was found between predictions obtained with the Rosseland diffusion approximation and those obtained using the computationally expensive Monte Carlo ray-tracing method.

In this section, optical and radiative properties of the media of the reacting particle system are first presented. The participating medium of a particle composed of $CaCO_3$, referred to as the $CaCO_3$ medium, is modeled as uniformly absorbing and non-scattering. The participating medium of a completely calcined $CaCO_3$ particle, referred to as the CaO medium, is modeled as a conglomerations of uniformly spherical, uniformly disperse grains that scatter radiation independently. Then, details of the evaluation of the divergence of the radiative heat flux term using the Rosseland diffusion and $P_1$ approximations are given. The radiative terms in the two forms of the conservation of energy equation surface boundary condition given in Section 4.4.2 are developed and presented for both approximations. Lastly, aspects of the numerical model presented in Chapter 4 describing heat transfer in the solid phase are used to model heating and cooling processes using both methods in particles with uniform composition. Temperature profiles obtained with both approximations are discussed and compared.

Two particle compositions are considered: 3% porous $CaCO_3$ and 56% porous CaO. The fluid phase composition and contribution to conduction in the conservation of energy equation are omitted to reduce computational time. Chemistry is also omitted. These omission are made to make the effect of intra-particle radiative heat transfer more pronounced. Two processes are considered: particle heating under direct, diffuse, high-flux solar irradiation, and passive particle cooling by convection and radiation to distant,

[1] Material in this section has been published in: Yue et al. [2016]

reactor-like walls. Numerical results obtained with the two methods are compared and found to be in good agreement.

### 5.2.1 Optical and radiative properties of the reacting media

The spectral extinction coefficient $\beta_\lambda$ is used in both radiative heat transfer approximations considered in this work, where $\beta_\lambda$ is the sum of the spectral absorption and scattering coefficients $\beta_\lambda = \kappa_\lambda + \sigma_{s,\lambda}$.

To evaluate the coefficients, the frequently used transport approximation is first assumed valid [Dombrovsky, 2012]. In this approach, an approximate scattering phase function is introduced leading to an equivalent and simpler radiative transfer problem of an isotropically-scattering medium with the transport-approximate scattering and extinction coefficients,

$$\sigma_{s,\lambda}^{tr} = (1 - g)\, \sigma_{s,\lambda} \tag{5.1}$$

where $g$ is the asymmetry factor. Transport-approximate coefficients are denoted by the "tr" superscript.

For simplicity, the CaO medium derived from the decomposition of $CaCO_3$ is assumed to be a conglomeration of uniformly spherical, uniformly dispersed grains that scatter radiation independently. Thus, Mie theory [Bohren and Huffman, 2004] is used to evaluate the spectral absorption coefficient $\kappa_{\lambda,CaO}$, spectral scattering coefficient $\sigma_{s,\lambda,CaO}$, and the asymmetry parameter $g_{CaO}$ for the CaO medium. A grain size of $r_{g,CaO} = 4.72 \times 10^{-7}$ m is used in this work. This average grain size is calculated assuming uniform and spherical grains for CaO derived from Blanca limestone with specific surface area $s_{CaO} = 1.9 \times 10^4\, m^2\, kg^{-1}$ as given in Table 3.3.

For the $CaCO_3$ medium, the particle is assumed large compared to the radiation wavelength and absorbing but non-scattering. Thus, $\sigma_{s,\lambda,CaCO_3} = \sigma_{s,\lambda,CaCO_3}^{tr} = 0$, and the absorption coefficient can be found from the solution for a plane wave decaying in a uniformly absorbing medium [Modest, 2013],

$$\kappa_{\lambda,CaCO_3} = \frac{4\pi k_{\lambda,CaCO_3}}{\lambda} \tag{5.2}$$

where $k_\lambda$ is the spectral imaginary part of the complex refractive index and $\lambda$ is the wavelength in a vacuum.

When the solid phase contains both $CaCO_3$ and CaO, the regions of $CaCO_3$ and CaO media are assumed optically discrete. Thus, the transport-approximate spectral extinction coefficient $\beta_\lambda^{tr}$ for the composite medium is modeled as a concentration averaged combination of the transport-approximate spectral extinction coefficients for $CaCO_3$ and CaO media.

$$\beta_\lambda^{tr} = (1 - X)\, \beta_{\lambda,CaCO_3}^{tr} + X \beta_{\lambda,CaO}^{tr}, \quad \beta_\lambda^{tr} = \kappa_\lambda + \sigma_{s,\lambda}^{tr} \tag{5.3}$$

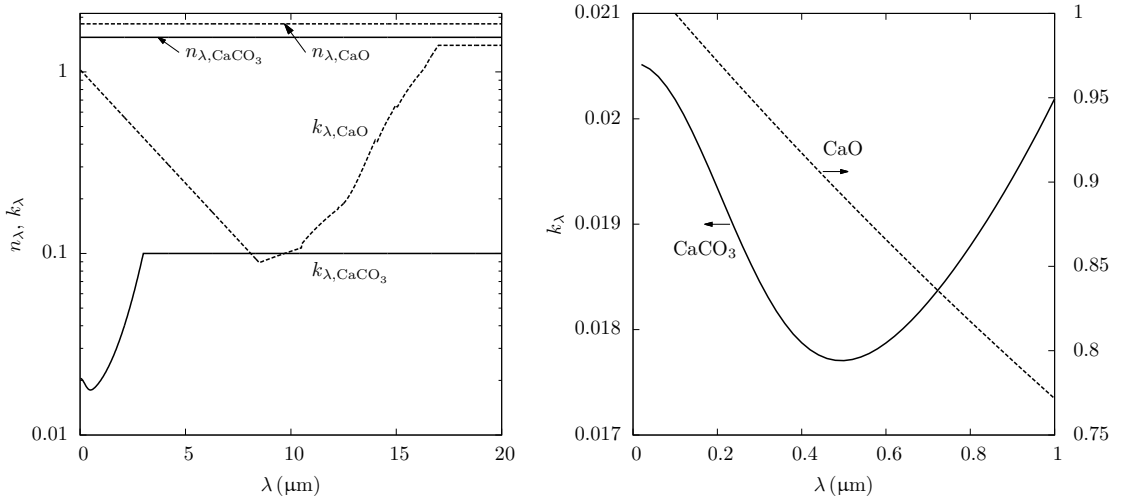


a b

Figure 5.1: Complex refractive indices for bulk $CaCO_3$ (solid lines) and CaO (dashed lines): (a) real and imaginary parts and (b) magnified view of the imaginary part in the visible wavelength range

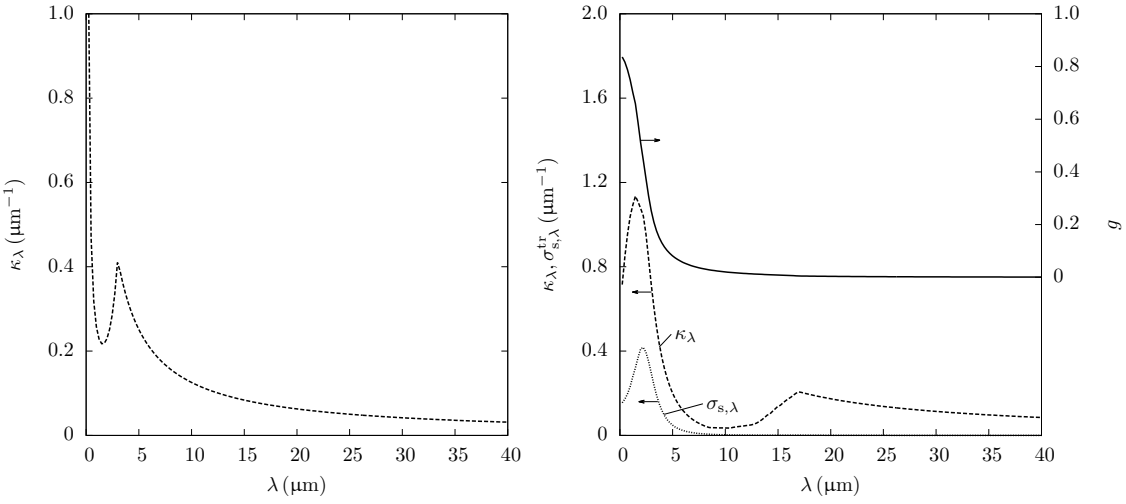


a b

Figure 5.2: Spectral absorption and scattering coefficients and the asymmetry factor for the (a) $CaCO_3$ and (b) CaO media: asymmetry factor of scattering (solid line), absorption coefficients (dashed lines), scattering coefficient (dotted line)

The real part of the refractive index $n$ for bulk $CaCO_3$ is taken from Orofino et al. [2000] and Dombrovsky and Lipiński [2007], while $n$ for bulk CaO is taken from Orofino et al. [2000]. The imaginary part of the refractive index $k$ for bulk $CaCO_3$ is taken from Brewster and Kunitomo [1984] and Dombrovsky and Lipiński [2007], while $k$ for bulk CaO is taken from Orofino et al. [2000] and Ebner and Lipiński [2011]. Spectral refractive indices for bulk $CaCO_3$ and CaO are shown in Fig. 5.1.

Piecewise mathematical expressions developed by Ebner and Lipiński [2011] approximating reported experimental curves are used in this work, resulting in the discontinuity of curves shown in Fig. 5.1a. The fluid phase is assumed to be radiatively non-participating, thus the refractive index of the fluid phase $m_\mathrm{f} = 1$.

The transport-approximate spectral absorption and scattering coefficients for the $CaCO_3$ and CaO media are shown in Fig. 5.2. The spectral asymmetry factor for scattering for the CaO medium $g_\mathrm{CaO}$ is also shown in Fig. 5.2b. The $CaCO_3$ medium is modeled as non-scattering, so $\sigma^\mathrm{tr}_{\mathrm{s},\lambda,\mathrm{CaCO_3}}$ and $g_\mathrm{CaCO_3}$ are both zero. The spectral absorption coefficient for the $CaCO_3$ medium $\kappa_{\lambda,\mathrm{CaCO_3}}$ is largest at smaller wavelengths. At wavelengths greater than $\lambda = 3\,\mu\mathrm{m}$, $\kappa_{\lambda,\mathrm{CaCO_3}}$ decreases with increasing wavelength. $\kappa_{\lambda,\mathrm{CaCO_3}}$ features a local minimum at approximately $\lambda = 1.5\,\mu\mathrm{m}$ which corresponds to a decreased value of the imaginary part of the refractive index for bulk $CaCO_3$ $k_\mathrm{CaCO_3}$ at the same wavelength. The spectral absorption and scattering coefficients for the CaO medium reach maximum values at $\lambda = 1.5$ and $1.7\,\mu\mathrm{m}$, respectively. The asymmetry factor for scattering $g_\mathrm{CaO}$ is largest at smaller wavelengths and decreases with increasing wavelengths.

### 5.2.2 Rosseland diffusion approximation

In the Rosseland diffusion approximation, the volume averaged divergence of the radiative heat flux is expressed as [Modest, 2013]

$$\langle \nabla \cdot \vec{\mathbf{q}}''_\mathrm{rad} \rangle = \nabla \cdot \left( -k_\mathrm{rad} \nabla \langle T \rangle \right) \tag{5.4}$$

and the volume averaged radiative heat flux is

$$\langle \vec{\mathbf{q}}''_\mathrm{rad} \rangle = -k_\mathrm{rad} \nabla \langle T \rangle \tag{5.5}$$

where radiative conductivity $k_\mathrm{rad}$ is a function of the effective refractive index of the porous particle, the local temperature, and the Rosseland-mean extinction coefficient [Modest, 2013],

$$k_\mathrm{rad} = \frac{16 n^2_\mathrm{eff} \sigma \langle T \rangle^3}{3 \beta^\mathrm{tr}_\mathrm{R}} \tag{5.6}$$

where $n_\mathrm{eff}$ is the effective refractive index, $\sigma = 5.6704 \times 10^{-8}\,\mathrm{W\,m^{-2}\,K^{-4}}$ and is the Stefan–Boltzmann constant, and $\beta^\mathrm{tr}_\mathrm{R}$ is the Rosseland-mean extinction coefficient. The effective refractive index is a porosity averaged combination of the real parts of the

refractive indices of the solid and fluid phases,

$$n_{\text{eff}} = (1 - \phi)\, n_{\text{s}} + \phi n_{\text{f}} \tag{5.7}$$

When the solid phase contains both $CaCO_3$ and CaO, the real part of the refractive index of the solid phase used to evaluate the radiative conductivity of the resulting participating medium is modeled as a concentration averaged combination of the real parts of the refractive indices for $CaCO_3$ and CaO.

$$n_{\text{s}} = (1 - X)\, n_{\text{CaCO}_3} + X n_{\text{CaO}} \tag{5.8}$$

The Rosseland-mean extinction coefficient is defined as [Modest, 2013]

$$\frac{1}{\beta_{\text{R}}^{\text{tr}}} = \frac{\displaystyle\int_{\lambda=0}^{\infty} \frac{1}{\beta_{\lambda}^{\text{tr}}} \frac{\mathrm{d}I_{\text{b}\lambda}}{\mathrm{d}T} \mathrm{d}\lambda}{\displaystyle\int_{\lambda=0}^{\infty} \frac{\mathrm{d}I_{\text{b}\lambda}}{\mathrm{d}T} \mathrm{d}\lambda} \tag{5.9}$$

where $I_{\text{b}\lambda}$ is the spectral blackbody intensity. The gray-band approximation of Eq. (5.9), evaluated with 120 bands, is used in Eq. (5.6) to obtain $k_{\text{rad}}$.

**Boundary conditions** At the center of the particle, the Rosseland diffusion approximation does not affect the boundary condition given by Eq. (4.26). The approximation replaces the radiative flux term $\langle q''_{\text{rad}} \rangle$ in the conservation of energy equation boundary conditions at the particle surface for either considered heating mode given by Eqs. (4.27) and (4.29) in Section 4.4.2.

$$\left[ k_{\text{eff}} \frac{\partial \langle T \rangle}{\partial r} - \langle q''_{\text{rad}} \rangle \right]_{r=r_{\text{p}}} = \left[ (k_{\text{eff}} + k_{\text{rad}}) \frac{\partial \langle T \rangle}{\partial r} \right]_{r=r_{\text{p}}} \tag{5.10}$$

No further changes to the surface boundary condition for the sweep gas controlled heating mode given by Eq. (4.29) are needed.

For the directly irradiated heating mode, the net radiative flux into the particle in Eq. (4.27) includes terms for absorbed solar irradiation, absorbed radiation emitted by the distant enclosure walls, and the radiation emitted by the particle surface.

$$q''_{\text{net}} = \alpha_{\text{eff,solar}} q''_{\text{surf}} + \alpha_{\text{eff,w}} \sigma T_{\text{w}}^4 - \varepsilon_{\text{eff,p}} \sigma \left( \langle T \rangle |_{r=r_{\text{p}}} \right)^4 \tag{5.11}$$

where $\alpha_{\text{eff,solar}}$ is the effective absorptivity for solar radiation, $q''_{\text{surf}}$ is the time-periodic radiative flux incident at the particle surface defined by Eq. (4.31), $\alpha_{\text{eff,w}}$ is the effective absorptivity for radiation emitted by the enclosure walls, $T_{\text{w}}$ is the temperature of the distant enclosure walls, and $\varepsilon_{\text{eff,p}}$ is the effective emissivity for the particle surface.

Regions of $CaCO_3$, CaO, and pore space at the surface are treated as optically discrete. Thus, the effective radiative properties of the surface are calculated from the

radiative properties of the individual species of the system. A flowchart of the process for calculating $\alpha_{\text{eff,solar}}$, $\alpha_{\text{eff,w}}$, and $\varepsilon_{\text{eff,p}}$ is shown in Fig. 5.3. The notation convention for surface radiative properties used in this work follows that of Modest [2013]. Absorptivity and emissivity variables without superscript denote quantities averaged over all incoming and outgoing directions, respectively. For reflectivity, a prime superscript denotes a directional variable, and a hemisphere superscript denotes a hemispherically averaged variable. When two superscripts are used, the first refers to incoming directions and the second refers to outgoing directions. Reflectivity variables without superscripts denote quantities averaged over all incoming and outgoing directions.

As shown in Fig. 5.3, the spectral, directional–hemispherical reflectivity $\rho'^{\frown}_{\lambda}$ of bulk $CaCO_3$, bulk CaO, and the fluid phase are first evaluated from their respective refractive indices and then combined into an effective spectral, directional–hemispherical reflectivity $\rho'^{\frown}_{\lambda,\text{eff}}$, where each constituent is treated as optically discrete. The effective spectral, directional–hemispherical reflectivity $\rho'^{\frown}_{\lambda,\text{eff}}$ is next averaged over all incident directions to yield the effective spectral, hemispherical reflectivity $\rho_{\lambda,\text{eff}}$. Finally, the total effective absorptivity $\alpha_{\text{eff}}$ and emissivity $\varepsilon_{\text{eff}}$ are calculated by averaging the effective spectral, hemispherical reflectivity over the appropriate incident or emitted spectra. For further reading on the evaluation of effective radiative properties of the surface of a CaO looping sorbent particle, the reader is directed to Yue and Lipiński [2015a].

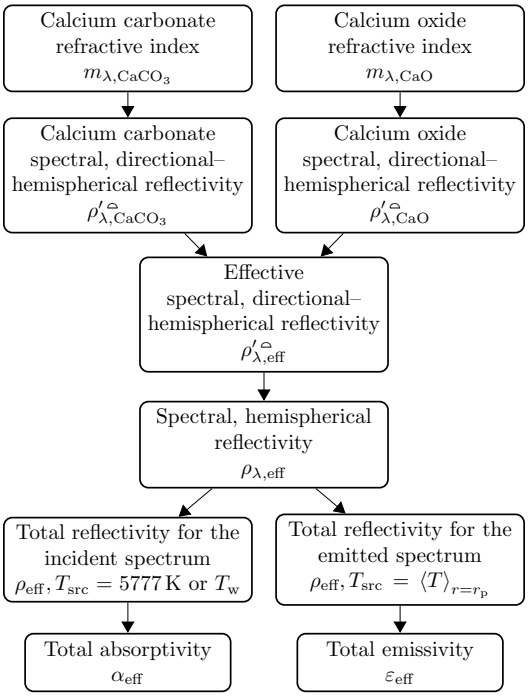


Figure 5.3: Flowchart for calculating effective absorptivity and emissivity

The complex refractive indices for bulk $CaCO_3$ and CaO are used directly in the Fresnel equations to evaluate the spectral, directional–hemispherical reflectivity $\rho'^{\frown}_{\lambda}$ for

$CaCO_3$ and CaO, respectively. The fluid phase is modeled as radiatively non-participating, thus, $\rho'^{\frown}_{\lambda,\mathrm{f}}$ is zero. The reflectivities of $CaCO_3$, CaO, and the fluid phase are combined using the local reaction extent and porosity of the surface to yield the effective spectral, directional–hemispherical reflectivity for the surface $\rho'^{\frown}_{\lambda,\mathrm{eff}}$ according to the following equation,

$$\rho'^{\frown}_{\lambda,\mathrm{eff}} = (1-\phi)\left[(1-X)\,\rho'^{\frown}_{\lambda,\mathrm{CaCO_3}} + X\rho'^{\frown}_{\lambda,\mathrm{CaO}}\right] + \phi\rho'^{\frown}_{\lambda,\mathrm{f}} \tag{5.12}$$

where $\phi$ and $X$ are the surface porosity and local reaction extent, respectively, taken as the porosity and local reaction extent of the outermost volume element, respectively.

The effective spectral, directional–hemispherical reflectivity $\rho'^{\frown}_{\lambda,\mathrm{eff}}$ is then averaged over all incident directions yielding the effective spectral, hemispherical reflectivity $\rho_{\lambda,\mathrm{eff}}$.

$$\rho_{\lambda,\mathrm{eff}} = \frac{1}{\pi}\int_{2\pi} \rho'^{\frown}_{\lambda,\mathrm{eff}} \cos\theta \mathrm{d}\Omega \tag{5.13}$$

where $\theta$ is the polar angle and $\Omega$ is the solid angle. The effective spectral, hemispherical reflectivity $\rho_{\lambda,\mathrm{eff}}$ is then averaged over a blackbody spectrum. If the spectrum represents incident irradiation, the average yields the total effective absorptivity $\alpha_{\mathrm{eff}}$ for that spectrum; if the spectrum represents emitted radiation, the average yields the total effective emissivity $\varepsilon_{\mathrm{eff}}$.

$$\alpha_{\mathrm{eff,src}} = \frac{\int_{\lambda=0}^{\infty}\left(1-\rho_{\lambda,\mathrm{eff}}\right)E_{\mathrm{b}\lambda,\mathrm{src}}\,\mathrm{d}\lambda}{\sigma T_{\mathrm{src}}^4} \tag{5.14}$$

$$\varepsilon_{\mathrm{eff,src}} = \frac{\int_{\lambda=0}^{\infty}\left(1-\rho_{\lambda,\mathrm{eff}}\right)E_{\mathrm{b}\lambda,\mathrm{src}}\,\mathrm{d}\lambda}{\sigma T_{\mathrm{src}}^4} \tag{5.15}$$

where $E_{\mathrm{b}\lambda}$ is the spectral blackbody emissive power and $T_{\mathrm{src}}$ is the temperature of the incident or emitted blackbody spectrum.

Solar irradiation, radiation emitted by the enclosure walls and incident on the particle surface, and emitted radiation from the particle surface are modeled to have the spectra of a blackbody at 5777 K, the wall temperature $T_{\mathrm{w}}$, and the surface temperature $\langle T\rangle|_{r=r_{\mathrm{p}}}$, respectively. Effective absorptivity of the particle surface therefore varies with surface composition, while effective emissivity varies with both surface composition and temperature.

### 5.2.3 Method of spherical harmonics

In the $P_1$ approximation, the divergence of the radiative heat flux is [Modest, 2013]

$$\left\langle \nabla\cdot\vec{\mathbf{q}}''_{\mathrm{rad}}\right\rangle = \int_{\lambda=0}^{\infty}\beta_{\lambda}^{\mathrm{tr}}\left(1-\omega_{\lambda}^{\mathrm{tr}}\right)\left(4\pi I_{\mathrm{b}\lambda} - \langle G_{\lambda}\rangle\right)\mathrm{d}\lambda \tag{5.16}$$

Here, $\omega_{\lambda}^{\mathrm{tr}} = \sigma_{\mathrm{s}\lambda}^{\mathrm{tr}}/\beta_{\lambda}^{\mathrm{tr}}$ and is the transport-approximate single scattering albedo and $G_{\lambda}$ is the spectral incident radiation. The spectral integration is approximated by a gray band

model with a simple midpoint rule quadrature:

$$\left\langle \nabla \cdot \vec{\mathbf{q}}''_{\mathrm{rad}} \right\rangle \approx \sum_{k=1}^{N_{\mathrm{band}}} \beta_{\lambda}^{\mathrm{tr},k} \left(1 - \omega_{\lambda}^{\mathrm{tr},k}\right) \left(4\pi I_{\mathrm{b}\lambda}^{k} - \left\langle G_{\lambda} \right\rangle^{k}\right) \Delta\lambda^{k} \tag{5.17}$$

where each gray band $k$ has a fixed band width $\Delta\lambda^k$ that has been chosen to resolve the spectral variations of the integrand. The summation is truncated at a wavelength where the contribution of further terms to the divergence of the heat flux is negligible. The incident radiation in a gray band $k$ $\left\langle G_{\lambda} \right\rangle^{k}$ is evaluated by solving a Helmholz equation [Modest, 2013]:

$$\begin{aligned} \nabla^2 \left\langle G_{\lambda} \right\rangle^{k} - \left(1 - \omega_{\lambda}^{\mathrm{tr},k}\right) \left(3 - \omega_{\lambda}^{\mathrm{tr},k}\right) \left\langle G_{\lambda} \right\rangle^{k} \\ = - \left(\beta_{\lambda}^{\mathrm{tr},k}\right)^2 \left(1 - \omega_{\lambda}^{\mathrm{tr},k}\right) \left(3 - \omega_{\lambda}^{\mathrm{tr},k}\right) 4\pi I_{\mathrm{b}\lambda}^{k} \end{aligned} \tag{5.18}$$

An alternative formulation of Eqs. (5.17) and (5.18) evaluates the total amount of radiative energy in a wavelength band $\Delta\lambda^k = \lambda_2^k - \lambda_1^k$ using the blackbody fractional function, resulting in $\left[f\left(n_{\mathrm{eff}}\lambda_2^k \left\langle T \right\rangle\right) - f\left(n_{\mathrm{eff}}\lambda_1^k \left\langle T \right\rangle\right)\right] n_{\mathrm{eff}}^2 \sigma \left\langle T \right\rangle^4$ rather than $\pi I_{\mathrm{b}\lambda}^k \Delta\lambda^k$. In this work, no difference was observed between the two approximations.

**Boundary conditions** Use of the $P_1$ approximation separates radiation at the surface from convection and conduction. The surface boundary condition for the conservation of energy equation is reformulated to contain only convection and conduction terms, while an additional set of boundary conditions for Eq. (5.18) are required to handle radiation.

When the $P_1$ approximation is employed, the boundary condition at the center of the particle for the conservation of energy equation is not affected. The boundary condition at the particle surface for either heating mode is

$$k_{\mathrm{eff}} \left.\frac{\partial \left\langle T \right\rangle}{\partial r}\right|_{r=r_{\mathrm{p}}} = h_{\mathrm{eff}} \left(T_{\infty} - \left\langle T \right\rangle|_{r=r_{\mathrm{p}}}\right) \tag{5.19}$$

The radiative heat flux terms, $q''_{\mathrm{rad}}$ at the particle surface and $q''_{\mathrm{net}}$, do not appear. These terms are now handled by the surface boundary condition for Eq. (5.18).

Equation (5.18) is solved for each gray band. Thus, boundary conditions for Eq. (5.18) are also developed for a gray band. At the center of the particle, the gradient of incident radiation for a gray band is zero due to symmetry,

$$\left.\frac{\partial \left\langle G_{\lambda} \right\rangle^{k}}{\partial r}\right|_{r=0} = 0 \tag{5.20}$$

At the surface, the following spectral boundary condition has been developed for a directly irradiated, participating medium surrounded by a non-participating medium,

$$\int_{\hat{\mathbf{s}} \cdot \hat{\mathbf{n}} > 0} I_{\lambda}\left(\hat{\mathbf{s}}\right) \hat{\mathbf{s}} \cdot \hat{\mathbf{n}} \mathrm{d}\Omega = q''_{\lambda,\mathrm{absorbed}} + \rho_{\lambda} \int_{\hat{\mathbf{s}} \cdot \hat{\mathbf{n}} < 0} I_{\lambda}\left(\hat{\mathbf{s}}\right) \hat{\mathbf{s}} \cdot \hat{\mathbf{n}} \mathrm{d}\Omega \tag{5.21}$$

where $I_\lambda(\hat{\mathbf{s}})$ is the spectral intensity in direction $\hat{\mathbf{s}}$, $\hat{\mathbf{n}}$ is the unit vector normal to the surface, $q''_{\lambda,\text{absorbed}}$ is the absorbed portion of the radiative flux incident on the outside of the particle surface, and $\rho_\lambda$ is the spectral, hemispherical reflectivity. The surface boundary condition states that the radiative flux into the particle from the particle surface (the left hand side solid angle integral) is equal to the sum of the absorbed portion of the radiative flux incident on the outside of the particle surface $q''_{\lambda,\text{absorbed}}$ and the internally reflected portion of the radiative flux incident from within the particle (the right hand side solid angle integral).

Equation (5.21) includes a term for absorbed radiative flux incident on the particle surface $q''_{\lambda,\text{absorbed}}$, while radiation emitted by the particle surface is captured by considering internally reflected radiation: that which is not internally reflected is emitted. Therefore, in order to use the $P_1$ approximation for internal radiative heat transfer in the sweep gas controlled heating mode, irradiation from the enclosure walls needs to be included in the $q''_{\lambda,\text{absorbed}}$ term in order to accurately solve for $\langle G_\lambda \rangle$ inside the particle, even if the particle surface and the enclosure walls are at radiative equilibrium.

To apply the surface boundary condition to the considered system, the $P_1$ approximation definition of intensity is used [Modest, 2013].

$$I_\lambda(\hat{\mathbf{s}}) = \frac{1}{4\pi}\left(G_\lambda + \frac{3}{\beta_\lambda(3-\omega_\lambda)}\nabla G_\lambda\right) \tag{5.22}$$

The surface boundary condition in Eq. (5.21) then becomes

$$\begin{aligned}\int_{\hat{\mathbf{s}}\cdot\hat{\mathbf{n}}>0} \frac{1}{4\pi}&\left(\langle G_\lambda\rangle^k + \frac{3}{\beta_\lambda^{\text{tr},k}\left(3-\omega_\lambda^k\right)}\frac{\partial\langle G_\lambda\rangle^k}{\partial r}\right)\Bigg|_{r=r_\text{p}} \hat{\mathbf{s}}\cdot\hat{\mathbf{n}}\,\mathrm{d}\Omega \\ &= \left(1-\rho_{\lambda,\text{eff}}^k\right)\pi I_{\lambda,\text{incident}}^k \\ &+ \rho_{\lambda,\text{eff}}^k \int_{\hat{\mathbf{s}}\cdot\hat{\mathbf{n}}<0}\left(\langle G_\lambda\rangle^k + \frac{3}{\beta_\lambda^{\text{tr},k}\left(3-\omega_\lambda^k\right)}\frac{\partial\langle G_\lambda\rangle^k}{\partial r}\right)\Bigg|_{r=r_\text{p}} \hat{\mathbf{s}}\cdot\hat{\mathbf{n}}\,\mathrm{d}\Omega\end{aligned} \tag{5.23}$$

Evaluating the integrals in Eq. (5.23) yields

$$\frac{1-\rho_{\lambda,\text{eff}}^k}{4}\left(\langle G_\lambda\rangle^k + \frac{2}{3\beta_\lambda^{\text{tr},k}\left(3-\omega_\lambda^k\right)}\frac{\partial\langle G_\lambda\rangle^k}{\partial r}\right)\Bigg|_{r=r_\text{p}} = \left(1-\rho_{\lambda,\text{eff}}^k\right)\pi I_{\lambda,\text{incident}}^k \tag{5.24}$$

Sources contributing to irradiation at the particle surface depend on the heating mode. As previously stated, boundary conditions for both heating modes must include the irradiation emitted by the enclosure walls when using the $P_1$ approximation. Irradiation from the enclosure walls is treated as diffuse with the spectral distribution of a blackbody at the temperature $T_\text{w}$. In the directly irradiated heating mode, irradiation at the particle surface includes incident solar radiation, treated as a diffuse with the spectral distribution of a blackbody at 5777 K and magnitude $q''_\text{surf}$ defined by Eq. (4.31). The effective spectral,

hemispherical reflectivities at the particle surface $\rho^k_{\lambda,\text{eff}}$ are calculated for the midpoint wavelength of each gray band using Fresnel's equations in the same manner as elaborated in the previous section, stopping at Eq. (5.13) and not averaging over wavelength.

A finer spatial mesh is used to solve for the spectral incident radiation $\langle G_\lambda \rangle$ in each wavelength band $k$ than that used to solve for other variables in order to capture the large spatial incident radiation gradients near the particle surface. The finer mesh is defined by discretizing each volume element $i$, as defined in Section 4.5, into $\alpha$ spherical shell sub-volume elements with constant thickness $\Delta r/\alpha$. Equation (5.18) is then integrated over a finite sub-volume $V_{i_{\text{sub}}}$. With the boundary conditions Eqs. (5.20) and (5.24), this yields a system of simultaneous discrete equations for $\langle G_\lambda \rangle^k$ in each sub-volume element $i_{\text{sub}}$. The system of equations is solved iteratively for each wavelength band with the Gauss-Seidel method and successive overrelaxation, with an overrelaxation coefficient $\gamma$.

The spectral incident radiation in each wavelength band $\langle G_\lambda \rangle^k$ in each sub-volume element $i_{\text{sub}}$ is used to evaluate the divergence of the radiative heat flux $\left\langle \nabla \cdot \vec{\mathbf{q}}''_{\text{rad}} \right\rangle$ using Eq. (5.17) for the sub-volume element. The divergence of the radiative heat flux is integrated over each sub-volume element $i_{\text{sub}}$ to yield the total radiative heat rate $q_{\text{rad}}$ for that sub-volume element:

$$q_{\text{rad},i_{\text{sub}}} = \int_{V_{i_{\text{sub}}}} \left\langle \nabla \cdot \vec{\mathbf{q}}''_{\text{rad}} \right\rangle_{i_{\text{sub}}} \mathrm{d}V \tag{5.25}$$

The total radiative heat rate in each volume element $i$ is the sum of the total radiative heat rate for each sub-volume element in that volume element, according to

$$q_{\text{rad},i} = \sum_{i_{\text{sub}}=1}^{\alpha} q_{\text{rad},i_{\text{sub}}} \tag{5.26}$$

The radiative heat rate in each volume element is used directly in the discrete form of the conservation of energy equation, Eq. (4.10) after applying the finite volume and explicit Euler methods as described in Section 4.5.

### 5.2.4 Heat transfer predictions using the two approximations

The spectral extinction coefficient $\beta_\lambda$ and temperature-dependent total Rosseland-mean extinction coefficient $\beta_{\text{R}}$ are calculated for the $CaCO_3$ and CaO media and shown in Fig. 5.4. As the temperature increases, both $\beta_{\text{R,CaCO}_3}$ and $\beta_{\text{R,CaO}}$ increase as shown in Fig. 5.4b. For the CaO medium, the increase is greater than for the $CaCO_3$ medium. As the temperature increases, the blackbody wavelength distribution over which $\beta_\lambda$ is averaged shifts to shorter wavelengths. Shifts to shorter wavelengths give more weight to shorter wavelength values of $\beta_\lambda$. Therefore, peaks in $\beta_\lambda$ at shorter wavelengths as shown in Fig. 5.4a result in increased $\beta_{\text{R}}$ at higher temperatures for both media. Maximum wavelength of a spectrum emitted by a blackbody versus blackbody temperature according to Wein's displacement law is shown in Fig. 5.4b along with $\beta_{\text{R}}$. When the spectrum

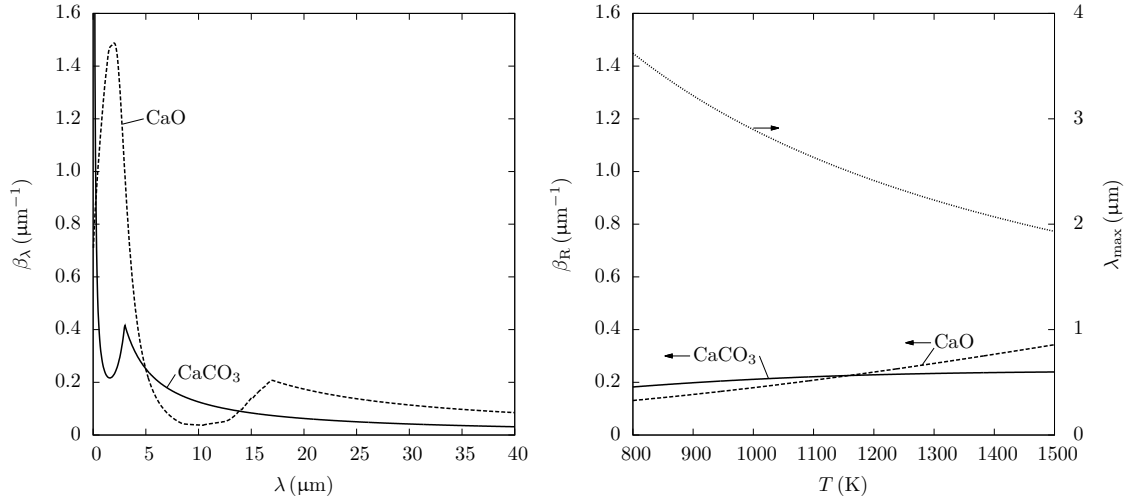


Figure 5.4: Radiative properties for the $CaCO_3$ (solid lines) and CaO (dashed lines) media, (a) spectral extinction coefficient and (b) total Rosseland-mean extinction coefficient and wavelength corresponding to maximum blackbody intensity (dotted line)

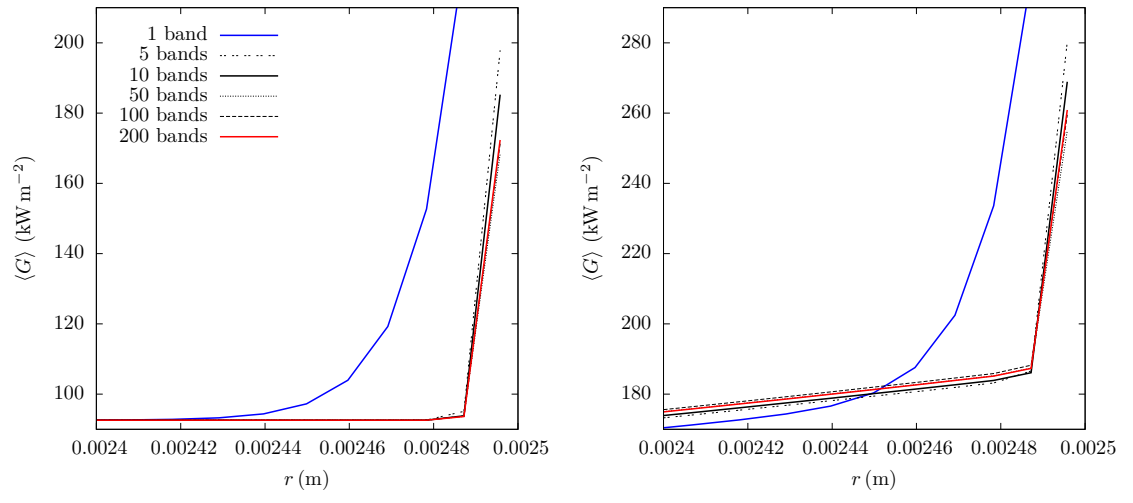


Figure 5.5: Incident radiation versus location for selected number of gray bands at time instants (a) $t = 0$ and (b) 1 s

shift such that the maximum wavelength is 2.5 μm at 1160 K, $\beta_{R,CaO}$ becomes larger than that for the $CaCO_3$ medium. For the $CaCO_3$ medium, the increase tails off because of the local trough in $\beta_\lambda$ at approximately 0.5 μm. Increased $\beta_R$ indicates decreased rates of radiative heat transfer.

To compare the two modeling methods, transient conduction–radiation heat transfer is considered in the solid phase of a particle composed of $CaCO_3$ or CaO undergoing a heating or cooling process. Conservation of energy equation solved is

$$\frac{\partial \left\langle \bar{\rho}\overline{h} \right\rangle}{\partial t} = \nabla \cdot \left( k_{\text{eff}} \nabla \left\langle T \right\rangle \right) - \left\langle \nabla \cdot \vec{\mathbf{q}}''_{\text{rad}} \right\rangle \tag{5.27}$$

where the effective thermal conductivity is

$$k_{\text{eff}} = (1 - \phi_i)\, k_i \tag{5.28}$$

where $i = CaCO_3$ or CaO. Values of parameters used in Eqs. (5.27) and (5.28) are the same as those given in Table 4.2. Particle composition does not change during the considered processes, so for $CaCO_3$ or CaO particles $\langle \bar{\rho} \rangle^{\text{s}} = \rho_{CaCO_3} / \overline{M}_{CaCO_3}$ or $\rho_{CaO} / \overline{M}_{CaO}$ and $\phi = 0.03$ or 0.56, respectively.

For the heating process, the particle temperature increases due to direct, high-flux irradiation, and for the cooling process, the particle temperature decreases due to convection and radiative exchange with the enclosure walls. Convective and radiative heat transfer occur between the particle surface and the surrounding gas and the enclosure walls, respectively, in both processes. Boundary conditions for the directly irradiated heating mode are therefore used. Values of the physical parameters used in the investigation are given in Table 5.1. The value of radiative heat flux was selected in order to achieve simulation results in which steady state is achieved in under 40 s and to produce steady state particle temperatures sufficiently high to distinguish the two radiation modeling methods. For the heating process, the particle is initially isothermal at $T = 800$ K. For the cooling process, the particle is initially isothermal at $T = 1420$ K.

Table 5.1: Physical parameters used in simulations comparing radiative heat transfer modeling methods

| Parameter | Value | Unit |
|---|---|---|
| $r_{\text{p}}$ | 0.0025 | m |
| $q''_{\text{solar}}$ | 235 | kW m$^{-2}$ |
| $T_{\text{w}}$ | 800 | K |
| $T_\infty$ | 800 | K |

Four cases are investigated using each radiative heat transfer approximation: $CaCO_3$ heating, CaO heating, $CaCO_3$ cooling, and CaO cooling. Total incident radiation $\langle G \rangle$ at time instants $t = 0$ and 1 s at locations near the particle surface is shown in Fig. 5.5 for

Table 5.2: Numerical solution parameters used in simulations comparing radiative heat transfer modeling methods

| Parameter | Value | Unit |
|---|---|---|
| $N$ | 30 | |
| $\Delta t$ | $1 \times 10^{-5}$ | s |
| $\lambda_2^{k=N_{\text{band}}}$ | 50 | μm |
| $N_{\text{band}}$ | 10 | |
| $\alpha$ | 100 | |
| $\gamma$ | 1.4 | |

$CaCO_3$ heating using the $P_1$ approximation for different numbers of gray bands $N_{\text{band}}$. Ten gray bands were determined sufficient in the $P_1$ approximation to resolve spectral variations of the surface irradiation, incident radiation, and material optical properties. The summation in Eq. (5.17) is truncated at $\lambda_2^{N_{\text{band}}} = 50\,\mu\text{m}$. All numerical solution parameters for this comparison are given in Table 5.2.

Figure 5.6 shows transient temperature profiles for all considered cases, using both the Rosseland diffusion and $P_1$ approximations. Temperature profiles are shown for the following selected locations: near the particle surface, $r/r_{\text{p}} = 0.99$; near the particle center, $r/r_{\text{p}} = 0.04$; and midway between the particle surface and center, $r/r_{\text{p}} = 0.52$.

Figures 5.6a and 5.6b show the temperature profiles during the heating of $CaCO_3$ and CaO particles, respectively. Results for both particle compositions and using both radiative heat transfer approximations show particle heating starting near the particle surface and moving into the particle. The temperature at all locations in particles of either composition in simulations employing the $P_1$ approximation increases at a marginally faster rate than in simulations employing the Rosseland diffusion approximation. The transient differences in temperatures obtained with the two radiative approximations are small for both particle compositions.

Figures 5.6c and 5.6d show the temperature profiles during the passive cooling of $CaCO_3$ and CaO particles, respectively. Temperature profiles predicted in simulations with the two radiative approximations are similar, with smaller differences between the two approximations in the cooling process than observed for the heating process.

The predicted temperature gradients in the CaO particle are larger than those in the $CaCO_3$ particle for both processes, obtained using either approximation. These larger gradients are attributed to the lower effective thermal conductivity of the CaO medium, which has higher porosity (56%) than the $CaCO_3$ medium (3%). At the same time, scattering and extinction of radiation in the CaO particle is significantly higher than in the $CaCO_3$ one, as indicated by the higher spectral extinction coefficient $\beta_\lambda$ for the CaO medium at wavelengths below $\sim 5\,\mu\text{m}$. A significant fraction of radiation (>50% for both incident and internal radiation) exists in this spectral range for all cases considered in this comparison. The intense extinction by the CaO medium leads to only

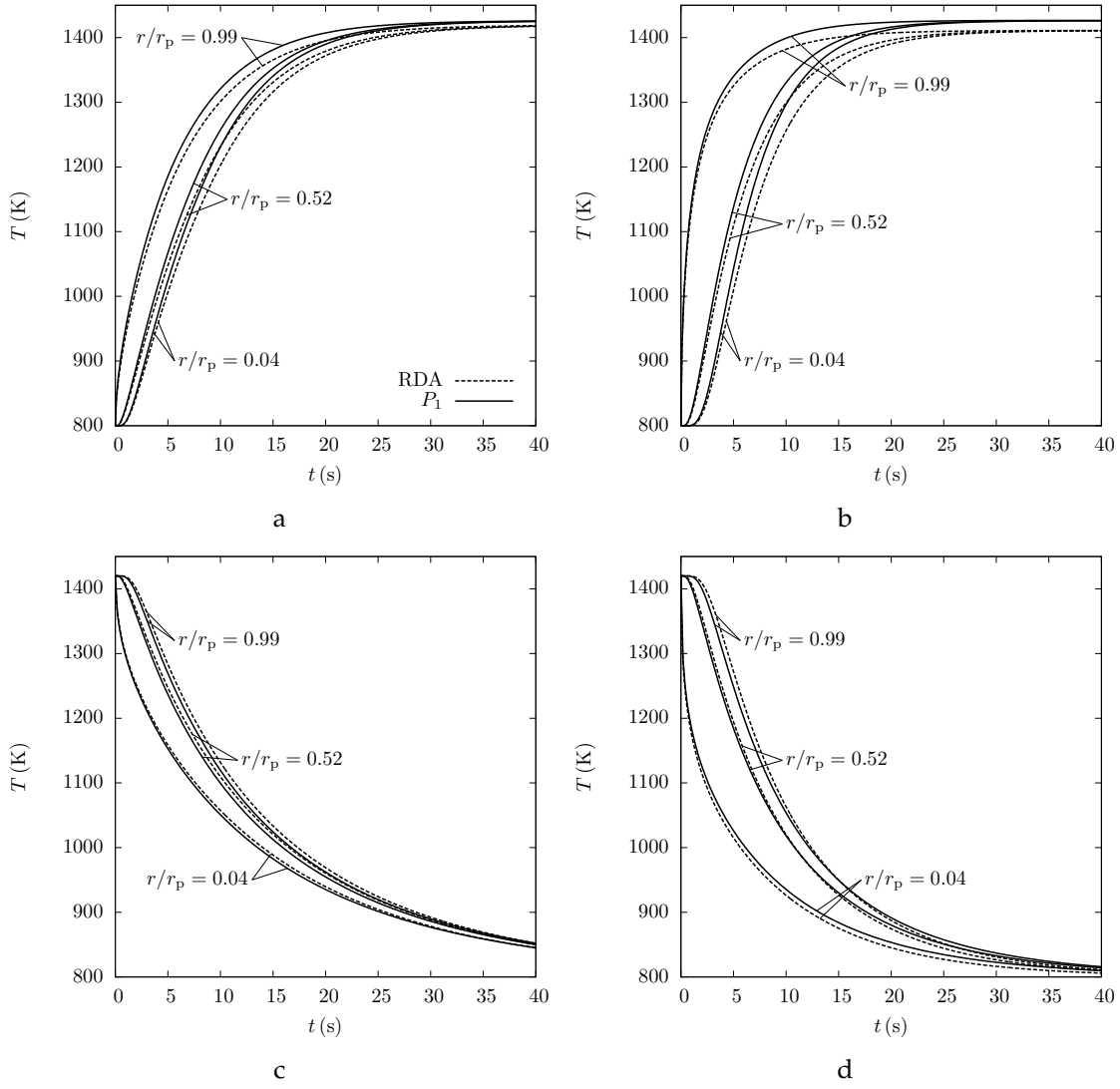


Figure 5.6: Temperature variations versus time at selected particle locations for (a) $CaCO_3$ heating, (b) CaO heating, (c) $CaCO_3$ cooling, and (d) CaO cooling: temperature variations using the Rosseland diffusion (dashed lines) or $P_1$ approximation (solid lines)

a small enhancement of the overall effective conductivity by its radiative component in the Rosseland diffusion approximation, which in turn cannot compensate for the lower ordinary thermal conductivity due to higher porosity of the CaO medium.

In the $P_1$ approximation, the intense extinction by the CaO medium directly results in significantly smaller radiative fluxes as compared to those observed in the $CaCO_3$ particle. The difference in the rates of radiative heat transfer in the $CaCO_3$ particle compared to the rates in the CaO particle are additionally magnified by the use of the $P_1$ approximation itself. The $P_1$ approximation captures these wavelength-dependent, non-local absorption and scattering effects in the optically thinner $CaCO_3$ medium while the Rosseland diffusion approximation, strictly valid for only extremely high values of the optical thickness and away from the semitransparent particle surface, does not. This also results in more rapid heating and cooling predicted with the use of the $P_1$ approximation.

To summarize, the theory and equations for the Rosseland diffusion and $P_1$ approximations for radiative heat transfer have been presented and applied to $CaCO_3$ and CaO particles. This resulted in the development of boundary conditions for the Rosseland diffusion and $P_1$ approximations for a directly-irradiated participating medium surrounded by a non-participating medium and a distant wall. These approximations and boundary conditions have been used to simulate heating by direct irradiation and passive cooling of $CaCO_3$ and CaO particles in a reactor-like environment. Temperatures predicted using a combined conductive–radiative heat transfer model incorporating the $P_1$ approximation and the developed boundary condition show an acceptable agreement to those obtained with the model incorporating the simpler and computationally less costly Rosseland diffusion approximation. For this reason, it is concluded that the increased computational cost of the $P_1$ approximation does not justify the preservation of spectral detail when compared to the Rosseland diffusion approximation in the considered application. The $P_1$ approximation is still anticipated to be a useful method for modeling radiative heat transfer in systems where preservation of spectral behavior is required.

## 5.3 Gas diffusion

Fluid diffusion in the pore space of a porous medium is a sub-continuum phenomenon driven by random molecule motion and molecule interactions with other molecules as well as interactions with the pore walls. In order to model fluid diffusion in a porous medium at the continuum level, an effective diffusivity $D_{\text{eff}}$ is used in this work to relate the molar flux of the fluid $\vec{j}''_{\text{f}}$ to the concentration gradient.

$$\vec{\mathbf{j}}''_{\text{f}} = D_{\text{eff}} \left( \nabla \bar{\rho}_{\text{f}} \right) \tag{5.29}$$

Diffusion in the pore space of the reacting particle considered in this work occurs between two gaseous species, namely $CO_2$ and the inert species. Thus, models for

evaluating effective diffusivity to describe binary gas diffusion in a porous medium, i.e. the interaction between the two gases and pore walls, are considered.

Diffusion due to gas molecule interaction with other gas molecules is called viscous diffusion, described by the binary molecular diffusivity in a two species system. Diffusion due to gas molecule interaction with the pore walls is called Knudsen diffusion, described by the Knudsen diffusivity. Three effective diffusivity models are considered in this work. The models incorporate either the binary molecular diffusivity or both the binary molecular and Knudsen diffusivities. Those diffusivities are then modified by characteristics of the porous medium to yield a continuum level effective diffusivity.

In this section, gas diffusion in a porous medium and the effective diffusivity models are discussed. The three models have been used in literature to describe gas diffusion at high temperatures in porous, reacting systems similar to the one considered in this work. Then, variations in effective diffusivity with temperature and solid phase composition predicted using each model are presented and discussed, and a model is selected to be used as the baseline model in the applications studies in Part II.

### 5.3.1 Gas diffusion in a porous medium

Binary molecular diffusion occurs in systems where concentration gradients exist between two separate species and species mixing is due to gas–gas molecular collision. The empirical relation for binary molecular diffusivity $D_{\text{mol}}$ of a dilute gas $i$ in a dilute gas $j$ was developed by Fuller et al. [1966]. The relation is used in this work with an added conversion factor for conversion to S.I. units.

$$D_{\text{mol},i} = \frac{C \langle T \rangle^{1.75} \left( \overline{M}_i^{-1} + \overline{M}_j^{-1} \right)^{0.5}}{p_{\text{f}} \left[ (\Sigma\nu)_i^{1/3} + (\Sigma\nu)_j^{1/3} \right]^2} \tag{5.30}$$

where $C$ is an S.I. unit conversion factor, $p_{\text{f}}$ is the fluid pressure, and $(\Sigma\nu)$ is the diffusion volume. The value of the constant $C$ is $1.01325 \times 10^{-2}\,\text{m}^2\,\text{kg}^{1.5}\,\text{s}^{-4}\,\text{K}^{-1.75}\,\text{mol}^{-0.5}$.

In a binary system, the binary molecular diffusivity for species $i$ in species $j$ is equivalent to the binary molecular diffusivity for species $j$ in species $i$. Thus, for $CO_2$ and air, $D_{\text{mol},CO_2} = D_{\text{mol,air}} = D_{\text{mol}}$. Molar masses $\overline{M}$ for $CO_2$ and air are 0.04401 and $0.02885\,\text{kg mol}^{-1}$, respectively [Wieser, 2006]. The fluid pressure used to evaluate binary molecular diffusivity is $\langle p_{\text{f}} \rangle^{\text{f}}$, the intrinsic volume-averaged, total fluid pressure in Eq. (4.7). The diffusion volumes $(\Sigma\nu)$ for $CO_2$ and air are 26.9 and $20.1\,\text{m}^3$, respectively [Fuller et al., 1966].

The binary molecular diffusivity describes viscous flow of gas in the pore space, however there may also be significant diffusion due to interaction between the flow and pore walls if the pores are sufficiently small. As pore size decreases, wall effects such as Knudsen diffusion, surface diffusion, and capillary condensation increase in influence and may substantially decrease rates of diffusion. The pore size relative to the mean free

path length of the gas molecules determines which type of interaction will dominate.

Knudsen diffusivity $D_K$, describing diffusion due to gas molecule collisions with the pore wall, is evaluated using the following equation [Welty et al., 2008]

$$D_{K,i} = \frac{d_{pore}}{3}\left(\frac{8\overline{R}\,\langle T\rangle}{\pi \overline{M}_i}\right)^{0.5} \tag{5.31}$$

where $i = CO_2$ and air and $d_{pore}$ is the pore diameter of the medium in which the gas is diffusing. For use in this work, the pore diameter is replaced with the characteristic length defined as $l_c = 30\phi/s'''_{phase}$ where the volume-specific interphase surface area is taken as the volume-specific reaction surface area for calcination defined by Eq. (3.6). The factor of 30 is intuitively selected to reflect the additional space between grains that exists in a conglomeration of non-spherical grains. The characteristic lengths $l_c$ for the $CaCO_3$ and CaO porous media are 11.3 and $6.00 \times 10^{-7}$ m, respectively.

To compare the mean free path length of gas molecular to characteristic length of the considered system, the mean free path length $l_{path}$ between collision of molecules can be determined from the following kinetic theory of gases equation:

$$l_{path} = \frac{k_B\,\langle T\rangle}{\sqrt{2}\pi\,\langle p_f\rangle^f\, d_{col}^2} \tag{5.32}$$

where $k_B$ is the Boltzmann constant, equal to $1.3806 \times 10^{-23}$ J K$^{-1}$ and $d_{col}$ is the collision diameter of the molecules. Gas molecules considered in this work ($CO_2$, $N_2$, and $O_2$) have collision diameters on the order of $d_{col} = 3.8 \times 10^{-10}$ m, resulting in an average mean free path length of around $l_{path} = 6.4 \times 10^{-8}$ m.

Mean free path length and characteristic length are used to evaluate the Knudsen number.

$$Kn = \frac{l_{path}}{l_c} \tag{5.33}$$

For $Kn \ll 1$, diffusion is predominantly viscous flow, while for $Kn \gg 1$, Knudsen diffusion or other smaller scale wall interaction phenomena dominate. When the Knudsen number is near unity, which is the case in this work, both viscous and Knudsen diffusive forces may act on similar orders of magnitude.

The binary molecular and Knudsen diffusivity for $CO_2$ and air are shown versus temperature in Fig. 5.7. Pressure used to evaluate $D_{mol}$ is evaluated using the ideal gas law Eq. (4.7) with the fluid molar density taken at the ambient conditions equal to the sum of the $CO_2$ and air fluid densities described by Eqs. (4.16) and (4.17).

Molecular diffusivity increases with temperature to the 0.75 power when the molar fluid density is constant and pressure is evaluated by Eq. (4.7). Knudsen diffusivity differs for $CO_2$ and air due to the difference in molar mass for $CO_2$ and air. $D_K$ increases with temperature to the 0.5 power, and increases linearly with pore size which varies non-linearly with reaction extent.

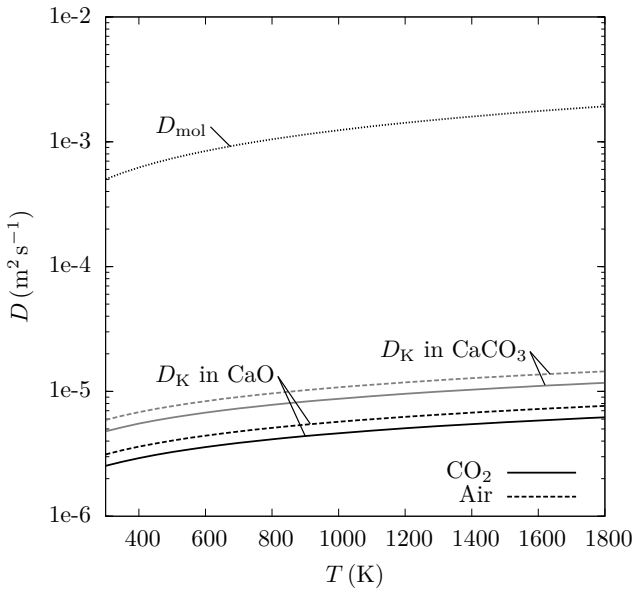


Figure 5.7: Binary molecular (dotted line) and Knudsen diffusivities versus temperature: $CO_2$ (solid lines) and air (dashed lines) in $CaCO_3$ (gray lines) and CaO (black lines)

### 5.3.2 Description of three effective diffusivity models

The models for predicting effective diffusivity, referred to as Model 1, 2, and 3, are presented in this section. Model 1 was used by Keene et al. [2013] to model argon and $O_2$ diffusion through porous $CeO_2$ undergoing thermochemical cycling driven by high-intensity solar radiation to study the effects of heat and mass transfer on the reduction kinetics of $CeO_2$. Model 2 was used by Blamey et al. [2016] to model steam and $N_2$ diffusion through a layer of porous $Ca(OH)_2$ in a particle undergoing CaO hydration to determine the intrinsic chemical kinetics reaction rate constant of CaO hydration. Model 3 was used by García-Labiano et al. [2002] to model $CO_2$ diffusion in the pore space of a $CaCO_3$ particle undergoing calcination in a furnace to study the effect of temperature, $CO_2$ partial pressure, and total pressure on calcination kinetics.

In Model 1, the binary molecular diffusivity is reduced by the porosity to yield the effective diffusivity [Cussler, 2009]:

$$D_{\mathrm{eff}} = \phi D_{\mathrm{mol}} \tag{5.34}$$

Model 1 treats diffusion in the pore space as a 1D phenomenon, where the porous media solid fraction acts as a region in which gas cannot travel but does not otherwise impede diffusion. This model is appropriate for systems with $\mathrm{Kn} \ll 1$.

Model 2 treats the binary molecular and Knudsen diffusivities as parallel diffusive resistances. Thus, the inverses of the binary molecular and Knudsen diffusivities are combined to yield the inverse of the combined diffusive resistance. The combined diffusive resistance is then reduced by the porosity and the inverse of the tortuosity $\tau$

[Cussler, 2009].

$$D_{\text{eff}} = \frac{\phi}{\tau}\left(D_{\text{mol}}^{-1} + D_{\text{K}}^{-1}\right)^{-1} \tag{5.35}$$

Tortuosity is a measure of the tortuous nature of a flow path. Larger tortuosity indicates the path through a network of pores contains many twists and turns, resulting in a longer diffusion path. Tortuosity inhibits continuum level diffusion because longer flow paths on the molecular scale result in slower linear diffusion on the continuum scale. Model 2 is appropriate for systems with Kn $\approx 1$ and the porosity and tortuosity of the medium are known.

Model 3 combines the binary molecular and Knudsen diffusivities in a similar manner to Model 2, however Model 3 takes the tortuosity to be equivalent to the inverse of porosity.

$$D_{\text{eff}} = \phi^2\left(D_{\text{mol}}^{-1} + D_{\text{K}}^{-1}\right)^{-1} \tag{5.36}$$

Model 3 is appropriate for systems with Kn $\approx 1$, and is an alternative to Model 2 when the tortuosity of the medium is unknown. Effective diffusivity predicted by all three diffusivity models is affected by properties of the fluid as well as the structure of the porous medium through which the fluid is traveling.

### 5.3.3 Predicted effective diffusivity using the three models

Effective diffusivity for the considered system is predicted using each model for a range of temperatures and solid phase composition. The range of effective diffusivity predicted with the three models spans several orders of magnitude, and the choice of effective diffusivity model is shown to significantly affect the extent of carbonation in preliminary numerical results. When tortuosity is assumed to be the inverse of porosity, $\tau_{\text{CaCO}_3} \approx 30$ and $\tau_{\text{CaO}} \approx 2$. Therefore, the following values of tortuosity are selected to encompass a potential range of effective diffusivities predicted using Model 2: $\tau = 1$, 10, and 100.

Effective diffusivity versus temperature and reaction extent are shown in Figs. 5.8 and 5.9, respectively. $D_{\text{eff}}$ values predicted using different models span several orders of magnitude. Figure 5.8 shows effective diffusivity increasing with temperature for all three models. The variation with temperature is different between Model 1 and Models 2 and 3. For all models, $D_{\text{eff}} \propto \langle T \rangle^a$, and the power $a$ varies with temperature and model. For the considered temperature range and models, the power is always less than 0.48.

In Fig. 5.9, effective diffusivity predicted with Model 1 is shown increasing monotonically with reaction extent over the entire range. Using Models 2 and 3, a minimum effective diffusivity is observed at $X = 0.03$, and then from $X = 0.03$ to 1, effective diffusivity increases with reaction extent. This local minimum is the result of the directly proportional relationship of porosity to reaction extent and the indirectly proportional relationship of characteristic length to reaction extent. From $X = 0$ to 0.03, the effect of decreasing characteristic length on $D_{\text{K}}$ is greater than the effect of increasing porosity on $D_{\text{eff}}$, resulting overall in decreasing values of $D_{\text{eff}}$. However, beyond $X = 0.03$, the effect

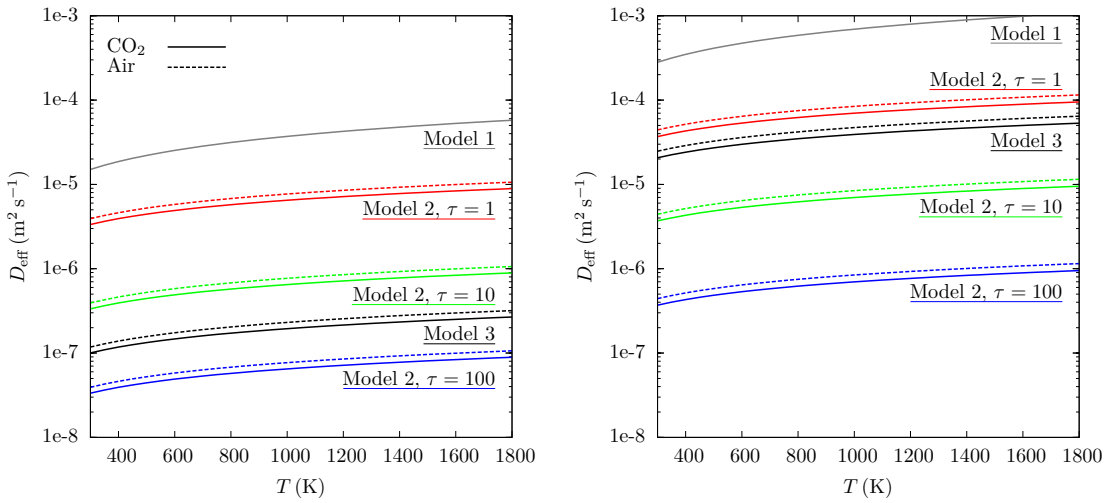


Figure 5.8: Effective diffusivity predicted by three models for $CO_2$ and air versus temperature in (a) $CaCO_3$ and (b) CaO porous media: Model 1 (solid gray line), Model 2 with $\tau = 1$ (red lines), Model 2 with $\tau = 10$ (green lines), Model 2 with $\tau = 100$, Model 3 (black lines), for $CO_2$ (solid lines) and air (dashed lines)

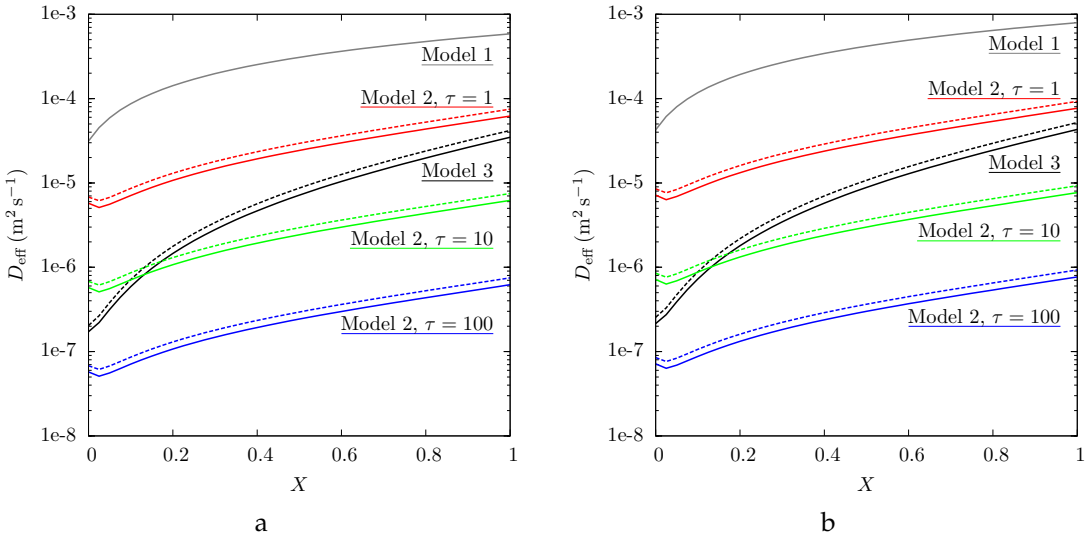


Figure 5.9: Effective diffusivity predicted by three models for $CO_2$ and air versus reaction extent at (a) $T = 800$ and (b) 1200 K: Model 1 (solid gray line), Model 2 with $\tau = 1$ (red lines), Model 2 with $\tau = 10$ (green lines), Model 2 with $\tau = 100$, Model 3 (black lines), for $CO_2$ (solid lines) and air (dashed lines)

of increasing porosity on $D_{\text{eff}}$ dominates, and $D_{\text{eff}}$ increases with reaction extent.

For all compositions, Model 1 consistently predicts the largest $D_{\text{eff}}$ for a given temperature. Models 2 and 3, which include the Knudsen diffusivity, predict much smaller values of $D_{\text{eff}}$ than Model 1, which does not include $D_{\text{K}}$. The difference between effectivity diffusivity in the $CaCO_3$ and CaO porous media is greatest in Model 3 because $D_{\text{eff}} \propto \phi^2$ in that model.

The characteristic length of the considered system is on the order of the mean free path of the gas molecules in the pore space, so Kn $\approx 1$ and viscous and Knudsen diffusion likely both occur in the particle simultaneously. Thus Model 1 likely overpredicts effective diffusivity by neglecting to account for pore wall interactions via the Knudsen diffusivity. Experimentally measured tortuosities reported in literature of porous solids similar to CaO looping sorbents span several orders of magnitude, and without specific measurement of tortuosity for the considered system, Model 2 introduced an unacceptably large amount of uncertainty. Thus, for the considered system, Model 3 is selected as the baseline model.

The Knudsen diffusivity is several orders of magnitude smaller than the binary molecular diffusivity for the conditions relevant to this work. Therefore, when treated as parallel diffusive resistances, the Knudsen diffusivity has a much greater influence on the combined diffusive resistance than the binary molecular diffusivity. In the literature, models including binary molecular diffusion or both binary molecular and Knudsen modes of diffusion have been used to model $CO_2$ transport in $CaCO_3$/CaO particles. However, if computational resources or other constraints only allow one mode of diffusion to be included, the comparison of models in this work indicates Knudsen diffusion should be included instead of binary molecular diffusion.

## 5.4 Summary

In this chapter, two modeling approximations were presented for intra-particle radiative heat transfer in particles undergoing CaO looping: the Rosseland diffusion and $P_1$ approximations. Development of the radiative terms in the directly irradiated boundary condition given by Eq. (4.27) resulted in a novel boundary condition for a directly irradiated surface surrounded by a non-participating surface for the $P_1$ approximation. The temperature profiles obtained using both approximations were compared and found to be in agreement. This agreement indicates the increased computational cost of the $P_1$ approximation is not justified by the preservation of spectral detail in the considered application.

Three models were presented for the evaluation of effective diffusivity of a two-gas system in a porous medium. Model 1 reduces the binary molecular diffusivity by porosity, while Models 2 and 3 include Knudsen diffusivity to account for molecular interactions with the reacting medium pore walls. Effective diffusivity was evaluated

using each model for a range of temperatures, including those relevant to CaO looping ($T = 300$–$1800\,\mathrm{K}$). It was also evaluated for the range of structural parameters describing a porous CaO looping sorbent associated with all values of reaction extent ($X$ =0–1). $D_{\mathrm{eff}}$ exhibited a similar relationship to temperature and reaction extent for all models, however the values of $D_{\mathrm{eff}}$ predicted with different models spanned several orders of magnitude. Based on the Knudsen number and knowledge of the structure of the considered particles, it was concluded that Model 1 is conservative and likely overpredicts diffusivity, while the parameter tortuosity, used in Model 2, cannot be accurately evaluated at this time, so the Model 3 was selected as the baseline model.

Closure models and numerical approximations can greatly influence the accuracy of modeling results. Selection of closure models and approximations should be physically motivated and justified. The impact of different applicable modeling methods should be analyzed to determine the sensitivity of numerical results to selected modeling methods. If the choice of closure model does not significantly influence numerical results, then the simplest model should be chosen. If the choice of closure model greatly influences the results, as in the case of the effective diffusivity model in the considered system, modeling methods and parameters should be reconciled with experiments as closely as possible.

In the applications studies in Part II, the Rosseland diffusion approximation is used to model intra-particle radiative heat transfer using the directly irradiated and sweep gas controlled heating modes in Chapter 6 and Chapter 7, respectively. Model 3 is used for intra-particle diffusion in Chapter 6, while an appended version Model 2 is used to evaluate tortuosity of reacting particles in Chapter 7.

# Part II

# Applications

Chapter 6

# Directly irradiated particles for carbon dioxide capture

## 6.1 Introduction

Of the reactor configurations discussed in Section 2.3 for solar thermochemistry, the directly irradiated, fluidized-bed configuration is a promising one. Directly irradiated reactors do not require a heat exchanger between the solar radiation absorber and reacting material. This has the potential to result in higher theoretical solar-to-chemical efficiency than systems requiring heat exchangers [Lipiński et al., 2013]. Moreover, fluidized-bed reactors enable efficient and uniform heat and mass transfer to the reacting material, resulting in uniform reaction extent for all material in the reactor [Levenspiel, 1999].

In this chapter, reacting particles in a directly irradiated, fluidized-bed solar thermochemical reactor are modeled as directly irradiated particles with near-uniform conditions over the particle surface. This approach resulted in good agreement between numerical and experimental temperature and conversion extent of coal particles undergoing gasification in a directly irradiated, fluidized-bed reactor [von Zedtwitz et al., 2007]. The numerical model presented in Chapter 4 with the Rosseland diffusion approximation from Section 5.2.2 and Model 3 from Section 5.3.2, is used to investigate the effect of various parameters on thermochemical conversion of particles undergoing CaO looping for solar $CO_2$ capture. For this application, $CO_2$ is absorbed from a dilute source during the carbonation period and released into a concentrated $CO_2$ stream during the calcination period.

The effect of calcination and carbonation period lengths on intra-particle temperature and composition gradients, thermochemical conversion, and solar-to-chemical efficiency is first investigated. Then, the effect of the magnitude of irradiation, particle size, and ambient gas temperature on thermochemical conversion and solar-to-chemical efficiency is investigated. Irradiation in this analysis refers to the external component of irradiation, i.e. radiation incident on the particle surface other than that emitted by the enclosure walls and quantified by $q''_{\text{solar}}$ in Eq. (4.31).

## 6.2 System description

The analyzed system is a sorbent particle as shown in Fig. 4.1 undergoing CaO looping, with calcination driven by direct irradiation during the calcination period. Convective and radiative exchange with the surroundings cools the particle during the carbonation period. Thus, the directly irradiated heating mode surface boundary conditions, Eq. (4.27) is used in this chapter. As $CO_2$ is released in a concentrated stream and absorbed from a dilute source in $CO_2$ capture applications, the surrounding fluid is modeled as a stream of commodity-grade concentrated $CO_2$ with $\bar{y}_{CO_2,calc} = 0.99$ in Eq. (4.36) and non-$CO_2$ impurities modeled as air during the calcination period. For carbonation, the surrounding fluid is modeled as a mixture of air and $CO_2$ with the $CO_2$ concentration representative of coal-fired flue gas with $\bar{y}_{CO_2,carb} = 0.15$ in Eq. (4.36). Values of the parameters used in all cases in this chapter are given in Table 6.1. The velocity of the ambient fluid surrounding the particle $u_{f,\infty}$ is used to evaluate the convective mass and heat transfer coefficients with Eqs. (4.25) and (4.28), respectively.

Table 6.1: Selected boundary and initial conditions

| Variable | Value | Unit |
|---|---|---|
| $\bar{y}_{CO_2,calc}$ | 0.99 | |
| $\bar{y}_{CO_2,carb}$ | 0.15 | |
| $T_0$ | 800 | K |
| $T_w$ | 800 | K |
| $u_{f,\infty}$ | 0.09 | m s$^{-1}$ |

To evaluate the effect of calcination and carbonation period lengths, magnitude of irradiation, particle size, and ambient gas temperature on thermochemical conversion and solar-to-chemical efficiency, the overall reaction extent of the entire particle and three evaluation metrics for each case are compared. The overall reaction extent is found by averaging $X_{local}$ over the particle volume.

$$X_{overall} \stackrel{def}{=} \frac{1}{4/3\pi r_p^3} \sum_{i=1}^{N} (X_{local,i} \Delta V_i) \tag{6.1}$$

The first evaluation metric is the sorbent utilization which compares the amount of substance of $CO_2$ captured in a thermochemical cycle $j$ to the maximum stoichiometric quantity,

$$\bar{\zeta}_j = \frac{N_{CO_2,j}}{N_{Ca,p}} \tag{6.2}$$

where $N_{CO_2,j}$ is the amount of substance of $CO_2$ absorbed by chemical reaction during the carbonation period of cycle $j$ only and $N_{Ca,p}$ is the amount of substance of calcium atoms in the particle. The amount of substance of calcium is equivalent to the maximum amount of substance of $CO_2$ that can be captured in one cycle.

The second evaluation metric is the capture capacity which compares the mass of $CO_2$ captured during cycle $j$ to the initial mass of sorbent,

$$\xi_{c,j} = \frac{m_{CO_2,j}}{m_{0,p}} \tag{6.3}$$

where $m_{CO_2,j}$ is the mass of $CO_2$ absorbed by chemical reaction during the carbonation period only, equal to $= N_{CO_2,j} \times \overline{M}_{CO_2}$ and $m_{0,p}$ is the initial mass of the particle at $t = 0\,\text{s}$. The denominator of the capture capacity is chosen to be analogous to that in the storage capacity metric for TES materials, which relates the amount of thermal energy that can be stored to the mass of storage material.

The third and final evaluation metric is the energetic efficiency, which compares the theoretical energy required for regeneration of the carbonated sorbent to the total incident energy in a cycle $j$,

$$\eta_{e,j} = \frac{N_{CO_2,j}\Delta\overline{h}^{\circ}_{298\,\text{K}}}{Q_{surf,j}} \tag{6.4}$$

where $Q_{surf,j}$ is the total amount of solar energy incident over the area $A$ of the surface of the particle during cycle $j$. $Q_{surf,j}$ is given by

$$Q_{surf,j} = \int_{t_j}^{t_{j+1}} \int_A q''_{surf}\, \mathrm{d}A\, \mathrm{d}t \tag{6.5}$$

where $q''_{surf}$ is defined by Eq. (4.31).

For the period lengths investigation, two cases with different durations of the calcination and carbonation periods are considered. For the magnitude of irradiation, particle size, and ambient gas temperature, four cases are considered for each parameter: two in which the parameter is increased from that in the baseline case and two in which the parameter is decreased. The evaluation metrics are used to compare all cases.

## 6.3 Effects of calcination and carbonation period lengths on reaction extent, temperature, and evaluation metrics[1]

To investigate the effects of calcination and carbonation period lengths, conditions driving thermochemical cycling and ambient conditions surrounding the particle remain the same, while $t_{calc}$ and $t_{carb}$, defined in Section 4.4.3, are varied. The model is used to investigate two cases: (1) with period lengths resulting in full calcination of the particle referred to as the "full-calcination case" and (2) with period lengths resulting in full carbonation of the particle referred to as the "full-carbonation case." The period length durations for both cases are identified with preliminary calculations.

For the full-calcination case, $t_{calc} = 300\,\text{s}$ and $t_{carb} = 800\,\text{s}$. The length of the calcina-

[1] Material in this section has been published in: Yue and Lipiński [2015c]

tion period is determined by the time it takes to completely calcine the particle during the first cycle. Once complete calcination is achieved, the carbonation period begins. The particle carbonates until the end of the carbonation period, at which time the cycle ends and the next cycle begins with another calcination period. In the full-calcination case, the particle does not completely carbonate during the first or subsequent carbonation periods.

For the full-carbonation case, $t_{\text{calc}} = 20\,\text{s}$ and $t_{\text{carb}} = 190\,\text{s}$. The length of the calcination period is determined by the maximum extent of calcination that subsequently allows for full carbonation during the carbonation period. The calcination period proceeds until this maximum extent of calcination is reached. Then the carbonation period begins, and the particle carbonates until full carbonation is achieved and the next cycle starts.

For the two cases considered in this section, the particle size is fixed at $r_{\text{p}} = 2.5\,\text{mm}$. The magnitude of irradiation during the carbonation period and the ambient gas temperature are also fixed for both cases, with $q''_{\text{solar}} = 235\,\text{kW m}^{-2}$ and $T_\infty = 800\,\text{K}$, respectively.

Six cycles are simulated for each case. For the full-calcination case, periodicity is achieved after two cycles, and the third and subsequent cycles are identical. For the full-carbonation case, periodicity is achieved in the first cycle, and all cycles are identical. Thus, a normalized time is defined for a cycle $j$ as $\tau = \left(t - t_j\right) / t_{\text{cycle}}$, and is used to discuss all identical cycles after periodicity is achieved. To qualitatively evaluate the effect of period time on thermochemical conversion, transient overall reaction extent profiles for each case are analyzed and compared. To quantitatively evaluate the effect of period time on thermochemical conversion and solar-to-chemical efficiency, the evaluation metrics defined above are evaluated for the fourth cycle $j = 4$ for each case and compared.

Reynolds number analysis is also conducted to confirm the validity of Darcy's law for fluid advection in the pore space, as described in Section 4.2.3. The Reynolds number is calculated from the fluid density, fluid velocity, characteristic length of the pore space, and temperature-dependent fluid viscosity for all locations in the particle during the first thermochemical cycle for both cases considered in this section. The porosity-dependent characteristic length, $l_{\text{c}}$, given in Section 5.3.1, is used. The Reynolds number is calculated for each node at 1 s intervals. For the full-calcination and full-carbonation cases, the average Reynolds numbers are $\text{Re} = 9.3 \times 10^{-5}$ and $1.0 \times 10^{-4}$, respectively. In both cases, the maximum observed Reynolds number is $\text{Re}_{\text{d}} = 1.79 \times 10^{-2}$, indicating laminar flow is maintained and Darcy's law is a valid simplification for conservation of momentum [Kaviany, 1995].

### 6.3.1 Numerical results for the full-calcination case

Overall reaction extent versus time for the full-calcination case is shown in Fig. 6.1. Figure 6.1a shows all six cycles, and Fig. 6.1b shows cycle $j = 4$. Transient variations in temperature and local reaction extent for four selected locations within the particle are shown in Figs. 6.2 and 6.3, respectively. Time and normalized time will both be given in

the initial discussion of the results for both cases in Sections 6.3.1 and 6.3.2 to compare the first cycles with subsequent, periodic cycles and to give the reader a grasp of the relevant time scales. In the remainder of the discussion of these results, only normalized time will be given.

Shown in Fig. 6.1, $X_{\text{overall}} = 0$ at $t = 0\,\text{s}$, and the cycle starts with a calcination period. The particle heats to the calcination temperature as shown in Fig. 6.2 and begins decomposing into CaO and $CO_2$ at $t = 6\,\text{s}$ for the first cycle and at $t = t_j + 4\,\text{s}$ or $\tau = 0.0036$ for subsequent cycles. Calcination continues until all $CaCO_3$ is consumed: $X_{\text{overall}} = 1$ at $t = 271\,\text{s}$ for the first cycle and $t = t_j + 59\,\text{s}$ or $\tau = 0.054$ in subsequent cycles. The calcination period ends at $t = t_{j,\text{calc}}$ or $\tau = 0.273$ for all cycles.

During the carbonation period, the particle cools until the carbonation temperature is reached as shown in Fig. 6.2, and the particle begins to carbonate at $t = t_{j,\text{calc}} + 2\,\text{s}$ or $\tau = 0.275$ for all cycles. The particle does not completely carbonate during the first or subsequent carbonation periods, reaching a minimum overall reaction extent $X_{\text{overall}} = 0.562$ at the end of each cycle at $\tau = 1$.

Two regimes are observed during the carbonation period. The distinction between the regimes is estimated based on visual inspection of $X_{\text{overall}}$ results. The regimes are shown in Fig. 6.1b and have the same duration for all cycles. The change in particle composition during the first regime, $0.275 < \tau < 0.332$, is rapid, while the change in particle composition in the second regime, $0.332 < \tau < 1$, is slower. The first regime is significantly shorter but accounts for approximately $2/3$ of the change in $X_{\text{overall}}$ during the carbonation period. The second regime comprises the majority of the time of the carbonation period but only accounts for $1/3$ of the change in $X_{\text{overall}}$.

Local reaction extents for four selected locations within the particle are shown in

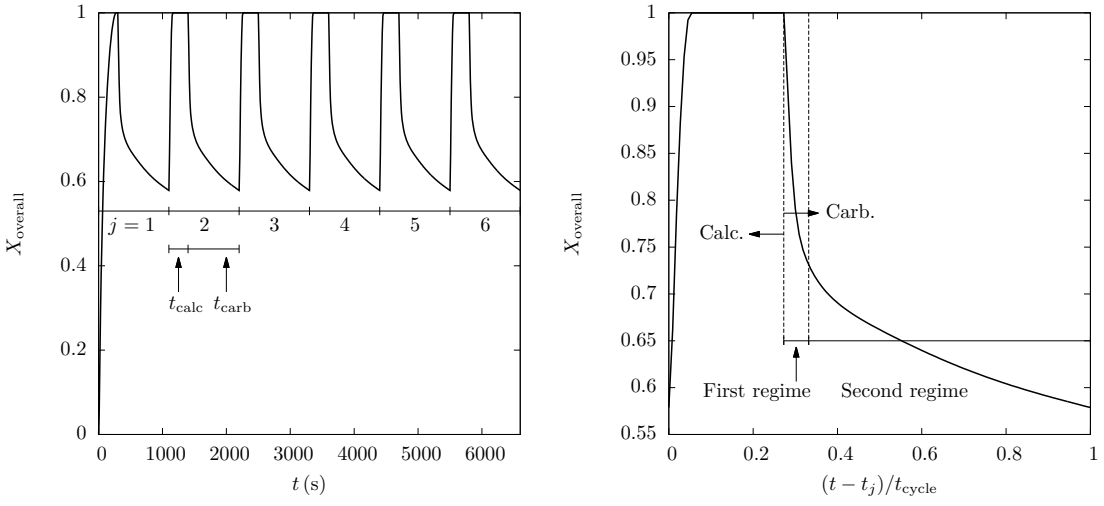


Figure 6.1: Overall reaction extent versus time for the full-calcination case with $t_{\text{calc}} = 300\,\text{s}$ and $t_{\text{carb}} = 800\,\text{s}$ (a) undergoing six cycles and (b) for cycle $j = 4$

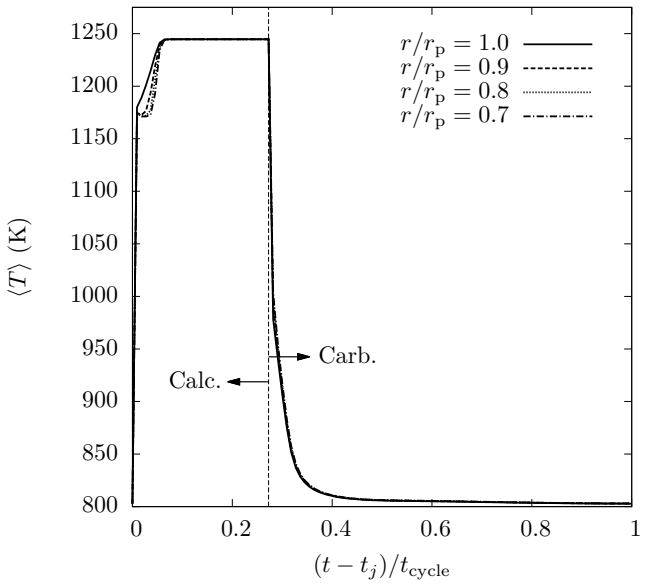


Figure 6.2: Local temperature versus time for the full-calcination case for selected locations for cycle $j = 4$: $r/r_{\text{p}} = 0.7$ (dash-dotted line), 0.8 (dotted line), 0.9 (dashed line), and 1.0 (solid line)

Fig. 6.3 for $j = 4$. The location $r/r_{\text{p}} = 1.0$ begins the cycle with a solid phase composition of pure $CaCO_3$ ($X_{\text{local}} = 0$) at $\tau = 0$ and then completely calcines to CaO ($X_{\text{local}} = 1$) at $\tau = 0.026$. Locations $r/r_{\text{p}} = 0.9$, 0.8 and 0.7 begin the same cycle with $X_{\text{local}} = 0.263$, 0.776 and 0.931, respectively and completely calcine to CaO at $\tau = 0.042$, 0.047, and 0.050, respectively.

At the beginning of the calcination period in each cycle, the particle briefly continues to carbonate before the onset of the calcination reaction. This brief amount of carbonation can be seen as a dip in reaction extent at locations $r/r_{\text{p}} = 0.8$ and 0.7 at the beginning of cycle $j$ shown in Fig. 6.3. Although not discernible due to the scale of Fig. 6.3, carbonation during the calcination period also occurs at the location $r/r_{\text{p}} = 0.9$. Carbonation during the calcination period occurs because increasing $CO_2$ concentration in the particle due to increasing ambient $CO_2$ concentration elevates the transition temperature between the calcination and carbonation reactions according to Eqs. (3.1) and (3.16). The transition temperature falls in the range 800–1200 K for $CO_2$ concentration relevant to the considered system. Increasing $CO_2$ concentration and the resulting elevated transition temperature prolongs carbonation into the calcination period. For example, at the location $r/r_{\text{p}} = 0.8$ at the beginning of cycle $j = 4$, $T = 803.0$ K and $\bar{y}_{CO_2} = 0.001$ with a transition temperature of 825.7 K according to Eq. (3.1). The transition temperature for the location $r/r_{\text{p}} = 0.8$ is reached after 6 seconds, when $T = 1184.4$ K and $\bar{y}_{CO_2} = 0.996$.

During the carbonation period, all locations return to their initial states at the beginning of the cycle, completely carbonated for $r/r_{\text{p}} = 1.0$ and partially carbonated for $r/r_{\text{p}} = 0.9$, 0.8 and 0.7. After the carbonation period begins at $\tau = 0.273$, the $r/r_{\text{p}} = 1.0$ location only exhibits a rapid carbonation regime. All other locations shown in Fig. 6.3

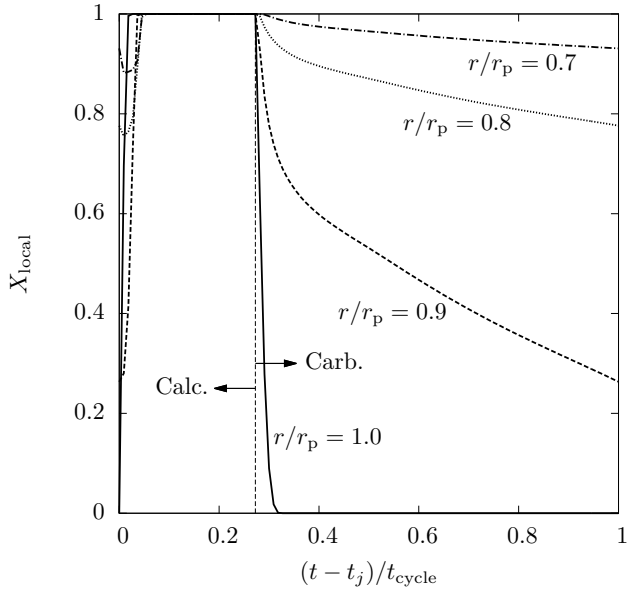


Figure 6.3: Local reaction extent versus time for the full-calcination case for selected locations for cycle $j = 4$: $r/r_{\mathrm{p}} = 0.7$ (dash-dotted line), 0.8 (dotted line), 0.9 (dashed line), and 1.0 (solid line)

exhibit both rapid and slower carbonation regimes, the second regime becoming longer with increasing distance from the particle surface.

After the calcination period, $X_{\mathrm{local}} = 1$, i.e. full calcination, at all locations in the particle. After the carbonation period, incomplete local carbonation at interior locations results in a maximum local carbonation extent and a non-uniform particle composition of a porous CaO core, a dense $CaCO_3$ outer shell, and a region of varying porosity between the two. During cycling, the particle transitions between these two states.

Figure 6.2 shows local temperature versus time for cycle $j = 4$ for four selected locations within the particle. During the calcination period, three regions are observed. First, rapid heating of all locations when no chemical reaction occurs; second, a decrease in the rate of particle heating indicative of chemical reaction; and finally, temperature stagnation of all locations. The particle heats until calcination temperature is reached, at which point the surface of the particle begins reacting. Calcination is endothermic and therefore inhibits particle heating while the reaction proceeds. Heating inside the particle proceeds after calcination of the outer regions of the particle is complete. Once all locations have completely calcined, the particle heats to the maximum stagnation temperature.

Three regions are also observed during the carbonation period. First, rapid particle cooling to the carbonation temperature; second, a decrease in the rate of particle cooling, indicative of the first, rapid carbonation regime, and finally, near-equilibrium temperature at all particle locations indicative of the second, slower carbonation regime. Carbonation is exothermic and therefore slows particle cooling while the reaction proceeds. Exterior

locations such as the particle surface reach lower temperatures earlier than interior locations. However, the differences in temperature between the locations during the carbonation period are smaller than the differences during the calcination period.

### 6.3.2 Numerical results for the full-carbonation case

Overall reaction extent versus time is shown for the full-carbonation case in Fig. 6.4. Figure 6.4a shows all six cycles, and Fig. 6.4b shows cycle $j = 4$. Transient variations in temperature and local reaction extent for four selected locations within the particle are shown in Figs. 6.5 and 6.6, respectively. All calcination periods start with particle heating to the calcination temperature as shown in Fig. 6.5. All calcination periods end at $t = t_j + 20\,\text{s}$ or $\tau = 0.095$, corresponding to $X_{\text{overall}} = 0.197$. Carbonation begins immediately in the following carbonation period and proceeds until the particle is nearly completely carbonated, $X_{\text{overall}} = 0.002$ at $t = t_{j+1}$ or $\tau = 1$. The particle fully carbonates to $X_{\text{overall}} = 0$ in the initial two seconds of the next calcination period.

During the carbonation period, rapid and slower regimes are observed and are shown in Fig. 6.4b. The rapid regime, $0.095 < \tau < 0.276$, accounts for a larger fraction of the carbonation period time in this case than the previous one: the rapid regime is 20.0% of the carbonation period for the full-carbonation case versus 8.1% for the full-calcination case. The rapid regime in this case also results in a larger fraction of carbonation: the rapid regime accounts for 80.3% of total carbonation during the carbonation period for the full-carbonation case versus 63.8% for the full-calcination case.

Local reaction extent for three selected locations in the particle for cycle $j = 4$ is shown in Fig. 6.6. At the start of the calcination period at $\tau = 0$, all locations are at $X_{\text{local}} \approx 0$. Particle heating then begins, and the particle surface $r/r_{\text{p}} = 1.0$ is

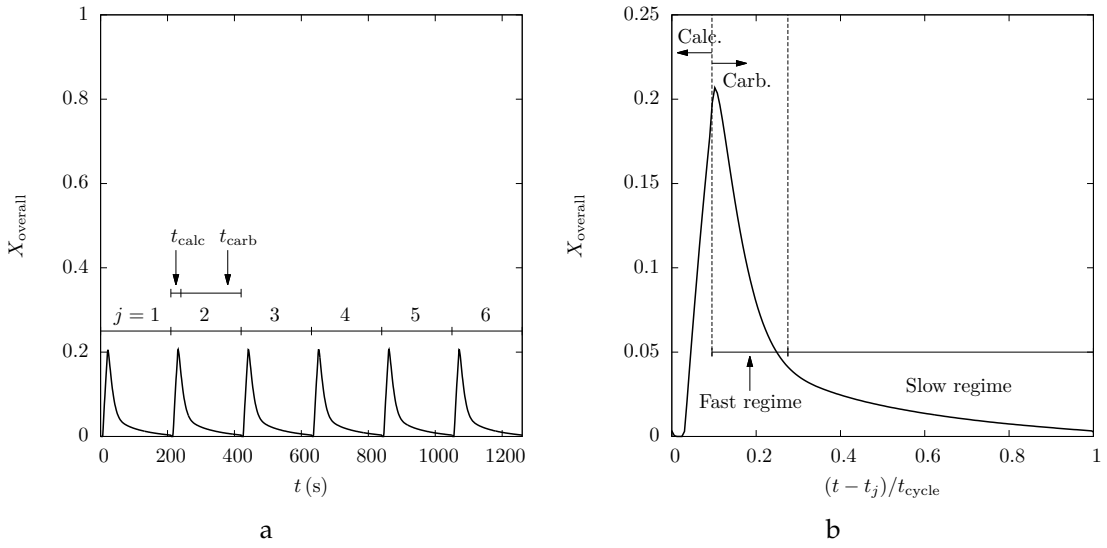


Figure 6.4: Overall reaction extent versus time for the full-carbonation case with $t_{\text{calc}} = 20\,\text{s}$ and $t_{\text{carb}} = 190\,\text{s}$ (a) undergoing six cycles and (b) cycle $j = 4$

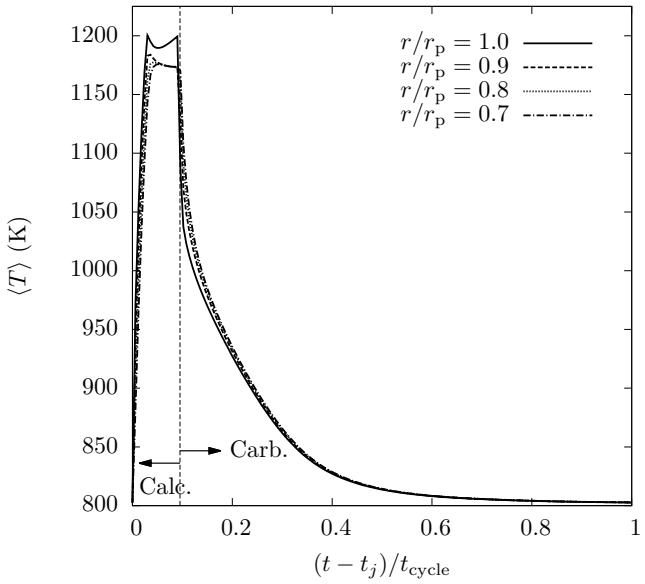


Figure 6.5: Local temperature versus time for the full-carbonation case for selected locations for cycle $j = 4$: $r/r_{\mathrm{p}} = 0.7$ (dash-dotted line), 0.8 (dotted line), 0.9 (dashed line), and 1.0 (solid line)

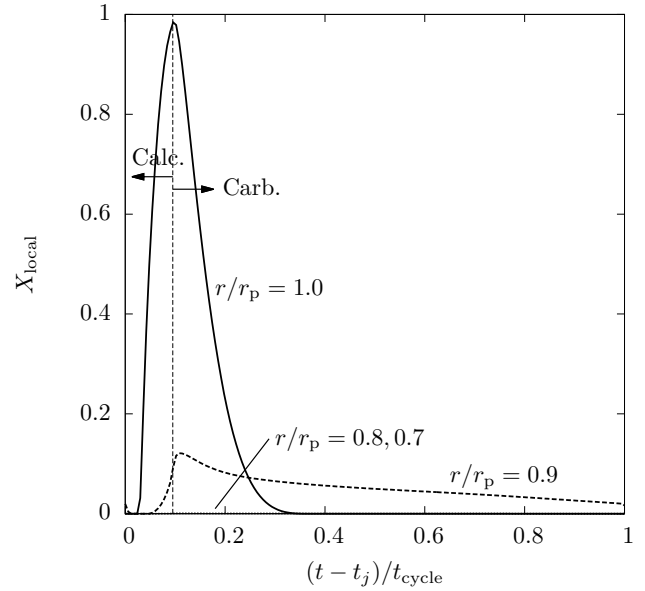


Figure 6.6: Local reaction extent versus time for the full-carbonation case for selected locations for cycle $j = 4$: $r/r_{\mathrm{p}} = 0.9$ (dashed line), 1.0 (solid line), and 0.7 and 0.8 (indistinguishable from x-axis)

the first location to reach the transition temperature and start calcining at $\tau = 0.029$. When the carbonation period starts at $\tau = 0.095$, the $r/r_p = 1.0$ location immediately begins carbonating and continues to carbonate at a nearly constant rate until nearly full carbonation ($X_{local} = 0.001$) is reached at $\tau = 0.333$. Locations near the particle surface begin calcining after the particle surface and only reach a partially calcined state. Locations $r/r_p = 0.9$ and 0.8 begin calcining at $\tau = 0.048$ and 0.071, respectively. At the end of the calcination period at $\tau = 0.095$, locations $r/r_p = 0.9$ and 0.8 calcine to $X_{local} = 0.093$ and 0.001, respectively. Locations $r/r_p < 0.8$ experience a very small amount of calcination during the calcination period with $X_{local} < 0.001$.

At the beginning of the carbonation period, all locations briefly experience calcination before carbonation starts. Residual latent heat and the decrease in the transition temperature due to decreasing $CO_2$ concentrations extend calcination into the carbonation period until the temperature decreases below the transition temperature, and carbonation begins.

Locations $r/r_p < 1.0$ only experience a small amount of calcination during the calcination period. The location $r/r_p = 0.9$ has a local reaction extent of $X_{local} = 0.093$ at the end of the calcination period, and even lower values of $X_{local}$ are observed for $r/r_p < 0.9$. After the calcination period, the particle composition is predominately a dense, unreacted $CaCO_3$ core, surrounded by a layer of porous CaO. After the carbonation period, the local reaction extent for all locations is nearly $X_{local} = 0$. During cycling, the particle transitions between these two states.

Figure 6.5 shows local temperature versus time for cycle $j = 4$ for four selected locations within the particle. During the calcination period, two regions are observed. First, a region of rapid particle heating at all locations, and then a region of decreased particle heating or no particle heating at all. All locations in the particle initially experience rapid heating without chemical reaction, then the calcination temperature is reached and chemical reaction begins, similar to the full-calcination case. Unlike the full-calcination case, the particle surface is the only location to nearly completely calcine and experience a second period of heating during the calcination period. Other interior locations either only partially calcine or do not significantly calcine at all, so the temperature of those locations remains relatively constant below the reaction temperature. The regions observed during the carbonation period of the full-carbonation case are similar to the regions observed in the full-calcination case: rapid particle cooling and periods indicative of the first, rapid and second, slower carbonation regimes.

### 6.3.3 Comparison of evaluation metrics for the considered cases

The three metrics defined in Section 6.2 are evaluated for the representative cycle $j = 4$ for each case. The metrics are given in Table 6.2 and used to compare the cases. The full-calcination case has higher sorbent utilization and capture capacity than the full-carbonation case, because the reaction intermediary compounds in the particle are used

Table 6.2: Evaluation metrics for cycle $j = 4$ from the full-calcination and full-carbonation cases

| Case | Sorbent utilization $\bar{\xi}_4$ | Capture capacity $\xi_{c,4}$ | Energetic efficiency $\eta_{e,4}$ |
|---|---|---|---|
| Full-calcination | 0.4212 | 0.1852 | 0.0234 |
| Full-carbonation | 0.1957 | 0.0860 | 0.1634 |

more extensively to capture $CO_2$ in the full-calcination case. However, the full-carbonation case has higher energetic efficiency than the full-calcination case. A longer calcination period is required to fully calcine the particle in the full-calcination case. Irradiation over a longer calcination period results in a larger amount of solar energy input, compared to the shorter calcination period and smaller amount of solar energy input in the full-carbonation case. In the full-carbonation case, more $CO_2$ is captured per energy unit than the full-calcination case for this reason. For the full-calcination case, the increase in $CO_2$ captured may not outweigh the required longer calcination period and larger solar energy input. Similarly for the full-carbonation case, the decrease in required solar energy input may not outweigh the lower utilization of the sorbent material. Larger length scale design concerns and priorities are expected to determine whether utilization of the sorbent material or energetic efficiency is more important in a given system.

## 6.4 Effects of varying irradiation, particle size, and ambient gas temperature on reaction extent and evaluation metrics

In this section, the magnitude of irradiation on the particle surface during the calcination period $q''_{solar}$, particle size $r_p$, and ambient gas temperature $T_\infty$ are independently varied from the values taken in the previous section. For the cases in this section, the calcination and carbonation periods are fixed to match the previously presented full-calcination case ($t_{calc} = 300\,s$ and $t_{carb} = 800\,s$), which is used as the baseline case for the following investigation. Three cycles are simulated for each considered case, since periodicity for the baseline case was achieved after two cycles. Sorbent utilization and energetic efficiency are evaluated for all considered cases, and metrics are used to generate metric plots. Metric plots are used to quantitatively compare the effects of varying the selected parameters on evaluation metrics.

### 6.4.1 Numerical results for cases with varying irradiation

Four cases are considered where the magnitude of the irradiation on the particle surface during the calcination period is increased to $q''_{solar} = 300$ and $500\,kW\,m^{-2}$ and decreased to 200 and $100\,kW\,m^{-2}$, from the baseline case value of $235\,kW\,m^{-2}$. The results for the four cases are shown with the baseline case in Fig. 6.7. For the cases where irradiation

is increased, complete calcination is achieved during the first and subsequent cycles, and the time to complete calcination inversely scales with the magnitude of irradiation: complete calcination is achieved at $t = 271$, 142, and 66 s in cases with $q''_{\text{solar}} = 235$, 300, and 500 kW m$^{-2}$, respectively. The carbonation profiles of these cases remain unchanged compared to the baseline case.

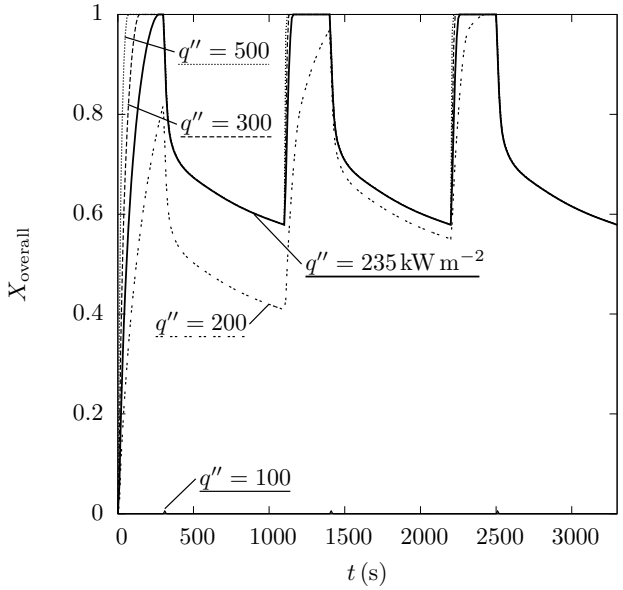


Figure 6.7: Overall reaction extent versus time for the baseline case and cases with varied irradiation: $q'' = 100$ (solid line), 200 (broken dashed line), 235 (thick solid line), 300 (dashed line), and 500 kW m$^{-2}$ (dotted line)

For the case where irradiation is decreased to $q''_{\text{solar}} = 200$ kW m$^{-2}$, complete calcination is not achieved until the third cycle and periodicity is not achieved in the three considered cycles. The particle calcines maximally to $X_{\text{overall}} = 0.823$, 0.970, and 1 during cycles $j = 1$, 2, and 3, respectively. With each subsequent carbonation period, the particle carbonates to a lesser extent corresponding to a greater overall reaction extent, approaching the baseline case carbonation profile until full calcination during the calcination period is achieved. After full calcination is achieved, the carbonation profile matches that of the baseline case and periodicity is expected in subsequent cycles. However, additional cycles were not simulated due to the high computational cost of each simulations as mentioned in Section 4.5.

For $q''_{\text{solar}} = 100$ kW m$^{-2}$, complete calcination is not achieved during any cycle. The particle calcines maximally to $X_{\text{overall}} = 0.017$. Although the magnitude of irradiation is sufficient to heat the particle to the calcination temperature, the cycle time is not long enough for a substantial amount of calcination to occur. As a result, full carbonation is rapidly achieved during the first carbonation period, and periodicity is achieved immediately, albeit to a trivially reactive cycle.

Based on the results of the considered cases, a minimum magnitude of irradiation is

required for the particle to calcine fully within the first calcination period for the baseline parameters. Cases with lower magnitudes of irradiation may achieve full calcination during later calcination periods, indicating a second minimum magnitude of irradiation is required for the particle to calcine fully during later cycles as opposed to during the first cycle.

### 6.4.2 Numerical results for cases with varying particle size

Four cases are considered where the particle size is increased to $r_p = 3.75$ and 5 mm and decreased to 1.5 and 1.25 mm, from the baseline case value of 2.5 mm. Overall reaction extent versus time for the four considered cases is shown with the baseline case in Fig. 6.8. The cases with smaller particles require a simulation time step of $\Delta t = 5 \times 10^{-7}$ s for numerical stability.

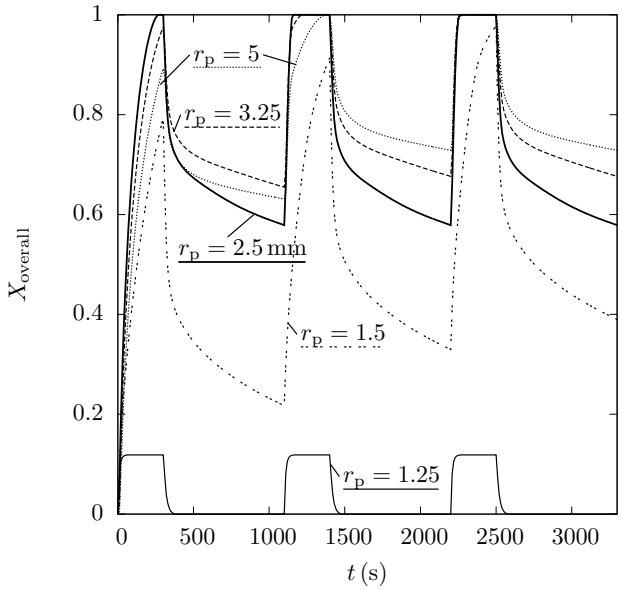


Figure 6.8: Overall reaction extent versus time for the baseline case and cases with varied particle diameter: $r/r_p = 1.25$ (solid line), 1.5 (broken dashed line), 2.5 (thick solid line), 3.25 (dashed line), and 5 mm (dotted line)

No considered cases achieve full calcination in the first cycle. For cases with larger particles, full calcination is achieved during the second cycle. The carbonation profiles of cycles $j = 2$ and 3 are identical for these cases, and periodicity is expected in subsequent cycles. During all cycles, but notably in cycles after full calcination has been achieved, the larger particles do not carbonate as extensively as the baseline case or cases with smaller particles.

For the cases with smaller particles, full calcination is not achieved in three cycles. For the case of the 1.5 mm radius particle, periodicity is also not achieved in three cycles. The 1.5 mm radius particle calcines maximally to $X_{\text{overall}} = 0.794$, 0.914, and 0.978 during cycles $j = 1$, 2, and 3, respectively. With each subsequent carbonation period, the

particle carbonates to a lesser extent corresponding to a greater overall reaction extent, approaching the baseline case carbonation profile. Periodicity with a minimum overall reaction extent less than that for the baseline case is expected with additional cycles.

For the case of the 1.25 mm radius particle, the particle exterior heats to a sufficiently high temperature to drive calcination. However, the particle interior does not heat to the calcination temperature because of convective losses. Convective losses increase after the particle exterior has calcined because calcination results in increases to the particle surface porosity, leading to increased convective losses. As a result, the calcination reaction stagnates early in the calcination period at $X_{\text{overall}} = 0.119$. Full carbonation is achieved in the first and subsequent cycles, and periodicity is achieved immediately.

### 6.4.3 Numerical results for cases with varying ambient gas temperature

To further compare the effect of convective heating relative to radiative heating, the ambient gas temperature is varied. Four cases are considered where the ambient gas temperature is increased to $T_\infty = 900$ and 1000 K and decreased to 700 and 600 K, from the baseline case value of 800 K. For these cases, the initial particle temperature remains 800 K to be consistent with the baseline case. This initial condition replaces that given by Eq. (4.18), and the particles considered in this section are not initially at thermal equilibrium with the ambient gas at $t = 0$ s.

Overall reaction extent versus time for the four cases is shown with the baseline case in Fig. 6.9. For cases where $T_\infty = 900$ and 1000 K, time to complete calcination and extent of carbonation at the end of a cycle inversely scale with ambient gas temperature. Time to complete calcination decreases with increased ambient gas temperature because the increased rates of convective heat transfer contribute to faster particle heating. Periodicity is also achieved in the second and subsequent cycles for these cases. Increases in ambient gas temperature result in higher stagnation temperatures when particle heating continues after completely calcined is achieved. For the baseline case, the stagnation temperature is 1245 K as shown in Fig. 6.2, while for the cases with $T_\infty = 900$ and 1000 K, the stagnation temperatures are 1292 and 1334 K, respectively.

Higher temperatures in the particle are also observed throughout the carbonation period, although the effect of these higher temperatures on carbonation is small. In cases with increased ambient gas temperature, particles exhibit less carbonation at the end of a cycle than that in the baseline case. The rates of change of $X_{\text{overall}}$ during the fast carbonation regime are nearly identical to that in the baseline case. The rates of change of $X_{\text{overall}}$ during the slow carbonation regime are slightly slower than that in the baseline case. The rate of change of $X_{\text{overall}}$ is the apparent reaction rate of the particle. The slow carbonation regime apparent reaction rates are determined by the rate of diffusion of $CO_2$ to unreacted CaO and the local intrinsic reaction rate.

Increased particle temperature causes increased rates of diffusion and decreased local intrinsic reaction rates at interior particle locations during slow carbonation. Effective dif-

fusivity increases with temperature as discussed in Section 5.3.3, therefore $CO_2$ diffusion occurs at a faster rate in particles with higher temperatures. However, the faster rates of diffusion are countered by decreased intrinsic reaction rates. During the slow carbonation regime, local $CO_2$ concentrations at interior particle locations are much less than the ambient carbonation concentration $\bar{y}_{\infty,CO_2} = 0.15$. At non-carbonated locations away from the particle surface, $\bar{y}_{CO_2} < 0.001$ during the slow carbonation regime. The temperature at which the maximum intrinsic carbonation rate occurs decreases with decreasing $CO_2$ concentration, as shown in Fig. 3.2b. The maximum rate occurs at temperatures below 800 K for $\bar{y}_{CO_2} < 0.001$ at atmospheric total pressure. Therefore, for the local conditions at interior particle locations during slow carbonation, increases in temperature above 800 K result in decreased intrinsic reaction rates. The decrease in intrinsic reaction rate is greater than the increased rate of $CO_2$ diffusion, resulting overall in decreased rates of change of $X_{\text{overall}}$ during slow carbonation.

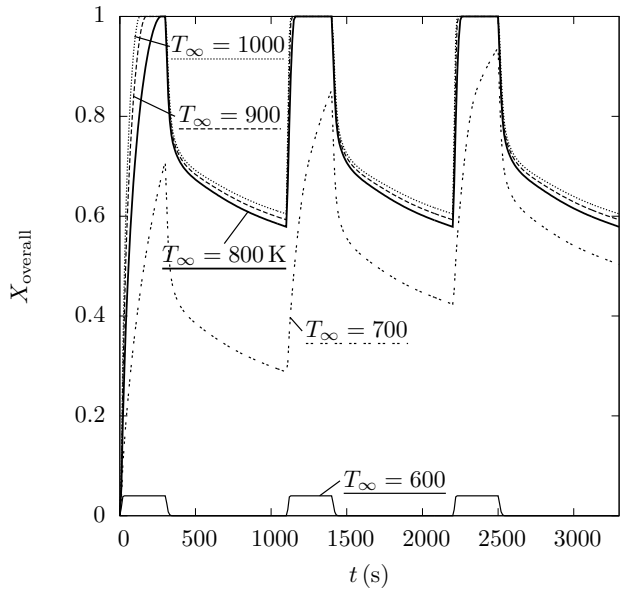


Figure 6.9: Overall reaction extent versus time for the baseline case and cases with varied ambient gas temperature: $T_\infty = 600$ (solid line), 700 (broken dashed line), 800 (thick solid line), 900 (dashed line), and 1000 K (dotted line)

For the case where $T_\infty = 700$ K, full calcination and periodicity are not achieved in the three considered cycles. The particle calcines maximally to $X_{\text{overall}} = 0.710$, 0.853, and 0.938 during cycles $j = 1$, 2, and 3, respectively. Similar to the $r_p = 1.5$ mm case, with each subsequent carbonation period, the particle carbonates to a lesser extent corresponding to a greater overall reaction extent. Periodicity with a minimum overall reaction extent slightly less than that for the baseline case is expected with additional cycles.

For the case where $T_\infty = 600$ K, convective losses prevent the interior of the particle from reaching high temperatures, inhibiting the calcination reaction in a similar manner to the case where irradiation is decreased to $q''_{\text{solar}} = 100\,\text{kW m}^{-2}$. Calcination stagnates

at $X_{\text{overall}} = 0.040$ early in the calcination period; full carbonation is achieved in the first and subsequent cycles; and periodicity is achieved immediately. Calcination stagnation in cases with reduced ambient gas temperature or irradiation indicates a minimum absorbed heat flux at the particle surface is needed to achieve full calcination during the first or subsequent cycles. The minimum heat flux can be achieved by adjusting one or both parameters.

### 6.4.4 Comparison of evaluation metrics for the considered cases

All cases are compared to the baseline case using sorbent utilization and energetic efficiency, defined by Eqs. (6.2) and (6.4), respectively. Trends in capture capacity closely follow trends in sorbent utilization, so capture capacity is not used in this comparison. Sorbent utilization and energetic efficiency are evaluated for cycle $j = 3$ for all cases, and the metrics are shown in Fig. 6.10. Sharp increases in both metrics are observed when parameters are increased and the baseline values are approached from the left.

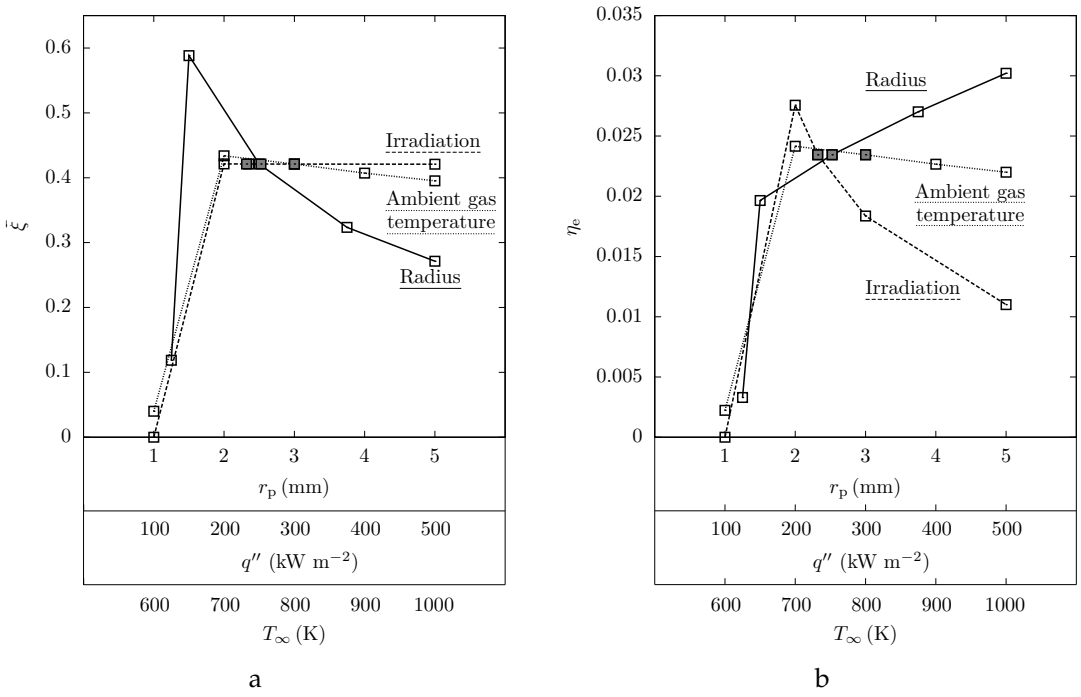


Figure 6.10: Comparison of the investigated cases (unfilled points) and the baseline case (filled points) using (a) sorbent utilization and (b) energetic efficiency: varying radius (solid line), irradiation (dashed line), and ambient gas temperature (dotted line)

Low values of both metrics for the smallest values in the considered range for each parameter are a result of calcination stagnation observed in the $q''_{\text{solar}} = 100\,\text{kW m}^{-2}$, $r_p = 1.25\,\text{mm}$, and $T_\infty = 600\,\text{K}$ cases. Once the criteria to overcome calcination stagnation are reached, both metrics increase until the metric plateaus or a local optimum is achieves and the metric starts to decrease. The only case for which this is not true is for the

energetic efficiency in cases with varying particle size. It is expected that a local optimum for energetic efficiency exists outside the considered range of particle sizes.

Increasing particle size to sizes larger than the baseline value results in increased energetic efficiency and decreased sorbent utilization. Increasing ambient gas temperature above the baseline values does not results in significant changes in either metric. Increasing irradiation above the baseline values does not result in significant changes in sorbent utilization, however it does result in decreases in energetic efficiency. Increasing irradiation and ambient gas temperature above the baseline values does not significantly change how much carbonation occurs, therefore increasing these parameters beyond a point will not change the sorbent utilization. Increasing these parameters may affect the apparent rate of calcination or carbonation, but in the considered cases the increase was small or undetectable.

A slight decrease in irradiation and ambient gas temperature to $q''_{\text{solar}} = 200\,\text{kW m}^{-2}$ and $T_\infty = 700\,\text{K}$ are expected to yield higher sorbent utilization and energetic efficiency. However, for these values, periodicity will take multiple cycles to achieve. The baseline parameter set yields a reasonable compromise between the two metrics when compared to the other cases considered and full calcination is desired in the first cycle. However, the calcination and carbonation period times are not optimized for the varied parameters, and tuning period times to specific cases is expected to increase both the sorbent utilization and energetic efficiency. The energy penalty associated with increased ambient gas temperature is also not factored into either metric but should be considered when extrapolating these results to the reactor level and selecting operating parameters.

## 6.5 Summary

Investigation of the effect of period lengths on thermochemical conversion showed that the material at the center of the particle during cycling can be either $CaCO_3$ or CaO and depending on the material, there is a trade off between maximizing the amount of $CO_2$ captured and minimizing the amount of solar energy supplied to the system. Investigation of the effect of selected parameters on thermochemical conversion showed that there are minimum requirements to achieve full calcination during the first cycle and at any point while cycling. The investigations also showed that there is a trade off between the overall reaction extent, described by the sorbent utilization metric, and thermal-to-chemical efficiency, described by the energetic efficiency metric, for the considered parameter ranges. Parametric studies that elucidate the influence of variables on evaluation metrics, like the ones presented in this chapter, are a valuable tool for selecting physical and operational parameters at the reactor scale.

Chapter 7

# Furnace heated particles for carbon dioxide capture and thermal energy storage

## 7.1 Introduction

In this chapter, thermal transport phenomena and overall reaction extent in large single particles are studied using TGA techniques and numerical modeling. Large particles, such as those considered in this work, are distinct from powdered materials typically used in TGA studies. While powdered material is appropriate for investigating chemical kinetics, large particles like those used in this study, are similar to particles found in packed and fluidized bed thermochemical reactors. Heat and mass transfer have a greater influence on apparent chemical kinetics and reaction extent in larger particles compared to beds of powder. Larger particles are used in order to investigate the influence of intra-particle mass transfer on overall reaction extent in particles of different sizes undergoing CaO looping. In this study, CaO looping is investigated for either $CO_2$ capture or thermochemical TES.

The study includes (1) characterization of the experimental sorbent material, (2) thermochemical cycling of single large particles of various sizes and in various $CO_2$ atmospheres in a furnace, (3) analysis and discussion of experimental results, (4) reproduction of experimental results via the evaluation of medium characteristics using the numerical model of Chapter 4, and (5) comparison of numerical and experimental results during the first thermochemical cycle.

This work shows that intra-particle mass transfer has a significant effect on the transient overall reaction extent of particles undergoing CaO looping. Another result of this work is a detailed numerical model reconciled with experimental data. The governing equations of the numerical model have the potential to be applied to a wide range of material morphology and experimental conditions with appropriate closure models and material properties. Such a model is capable of aiding the design, choice of particle size, and operating conditions of solar and conventional thermochemical reactors.

## 7.2 Sorbent material characterization

### 7.2.1 Methodology

Three size fractions of extruded sorbent particles are obtained from Umang Pharmatech Pvt Ltd. Based on visual inspection, particles are predominantly spherical in shape. Size fractions contain particles collected between meshes U.S. standard size 14 and 20, U.S. standard size 7 and 10, and with nominal size opening 4 and 6 mm, resulting in particles with diameter 0.84–1.41 mm, 2–2.83 mm, and 4–6 mm, respectively. These size fractions are referred to as the 1, 2.5, and 5 mm size groups, respectively.

Scanning electron microscopy with back-scattered electron detector (SEM–BSE) images of cut particle cross sections are collected using a Zeiss MA15 detector. Cut particle cross sections are washed and polished with ethanol. Images are then used to evaluate the internal morphology of samples. Energy-dispersive X-ray spectroscopy (EDX) maps of cut particle cross sections are taken using an e2v SiriusSD Silicon Drift Detector to identify the elemental composition of internal morphology features. The density of samples of whole particles is evaluated with a Quantachrome Helium Ultrapycnometer 1000 with a gas target pressure of 19 psi. Material crystalline phases are characterized by X-ray diffraction (XRD) analysis. XRD patterns of powdered particle samples are measured with an Empyrean PANalytical Diffractometer, using Cu K$\alpha$ radiation at 40 kV and 40 mA ($\lambda = 1.54178$ Å) at a scanning rate of $0.02^\circ$ s$^{-1}$. The XRD patterns are undertaken from $2\theta = 2$ to $90^\circ$. The ICDD[1] database [ICDD, 2017] is used to identify the XRD patterns of the samples. Internal morphology, density, and XRD patterns are analyzed for as-received particles from each size group. Internal morphology, density, and XRD patterns are also analyzed for a selection of particles from each size group after 20 minutes of calcination in air in a furnace at 1273 K. Samples that have undergone treatment are labeled "after-calcination."

### 7.2.2 Results

SEM–BSE images, EDX maps, density measurements, and XRD analysis are used to qualitatively compare the composition and grain structure of as-received and after-calcination particles. Results show as-received particles are composed of densely packed, larger grains consisting predominantly of $CaCO_3$. As-received particles from each size group display similar internal morphology and composition across the range of sizes. Analysis of after-calcination particles shows the particles are composed of dispersed, smaller grains consisting predominantly of CaO. After-calcination particles from each size group also display similar internal morphology and composition across the range of sizes. Thus, the material is assumed uniform for all size groups and the $CaCO_3$ particles will fully decomposed to CaO under the expected experimental conditions.

[1] International Centre for Diffraction Data

SEM–BSE images of the internal structure of six particles are obtains: one particle from each of the three size group, both as-received and after-calcination. Images from as-received particles cannot be distinguished by size group. An analogous trend is also observed in images from after-calcination particles from each size group. Therefore, SEM–BSE images for as-received and after-calcination particles from only one size group are shown, but conclusions drawn from each image are valid for all size groups. Figure 7.1 shows SEM–BSE images of the internal grain morphology of as-received and after-calcination particles from the 5 mm size group.

As-received particles display four main features: (1) light-colored grains on the order and greater than 10 μm, (2) dark-colored grains on the order and greater than 10 μm, (3) regions of fine grains, and (4) some dark pore voids. A broad distribution of grain size is observed. The light- and dark-colored grains are as large as 16.4 μm and 31 μm, respectively. The as-received particles are very compacted although some dark pore voids are discerned. The after-calcination particles show high porosity with pores varying in size from less than 1 to 19 μm. The after-calcination particles exhibit smaller grain sizes than the as-received particles: less than 1 μm grains in the after-calcination particles compared to $\sim$ 10 μm or larger grains in the as-received ones. Smaller grain size is typical of CaO derived from both naturally-occurring $CaCO_3$ from Blanca limestone [García-Labiano et al., 2002] and typical scalenohedron calcite $CaCO_3$ [Olivares-Marín et al., 2013].

Next, EDX maps of the internal structure of particles from each size group are analyzed. A selected EDX map of an as-received particle from the 1 mm size group is shown in Fig. 7.2. The as-received particle is composed mainly of calcium. The light-colored, large grains and the small fine grain regions observed in SEM–BSE images are identified as containing calcium, while the dark-colored large grains contain magnesium. A small amount of the element silicon is also observed in the EDX maps; identification of the silicon-containing compound will be discussed in the XRD analysis. EDX maps of as-received and after-calcination particles from all size groups show similar results.

Helium porosimetry results show the as-received and after-calcination particles have densities varying from $2.73 \times 10^3$ to $2.75 \times 10^3$ kg m$^{-3}$ and $3.26 \times 10^3$ to $3.27 \times 10^3$ kg m$^{-3}$, respectively. The density obtained for the as-received particles is close to bulk density of naturally occurring limestone and $\rho_{CaCO_3}$ given in Table 3.3. The values obtained for the after-calcination particles are within the experimental range obtained in previous works for pure CaO and CaO mixed with silicon and aluminum oxides [Takahashi et al., 2015], and close to $\rho_{CaO}$ given in Table 3.3.

XRD analysis is conducted with powderized as-received and after-calcination particles from each size group. Figure 7.3 shows the XRD patterns of as-received and after-calcination material from the 5 mm size group. As-received and after-calcination samples from other size groups display similar XRD patterns. From the XRD pattern for the as-received material shown in Fig. 7.3a, the as-received material contains predominantly

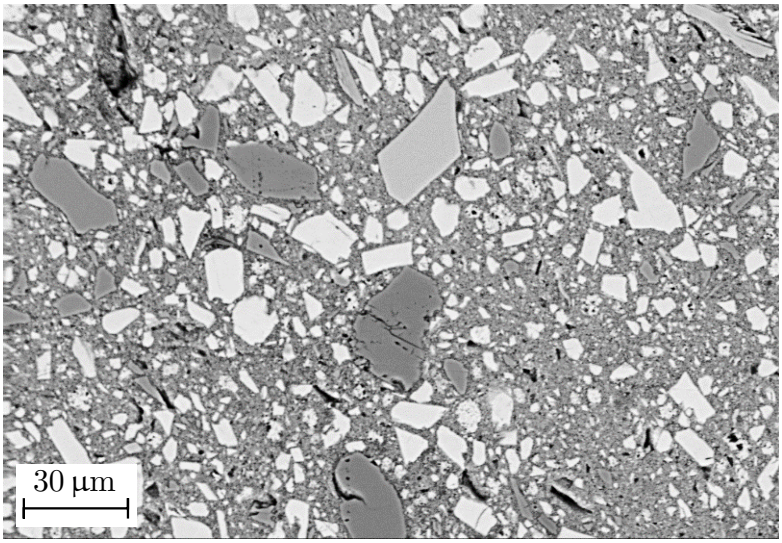


a

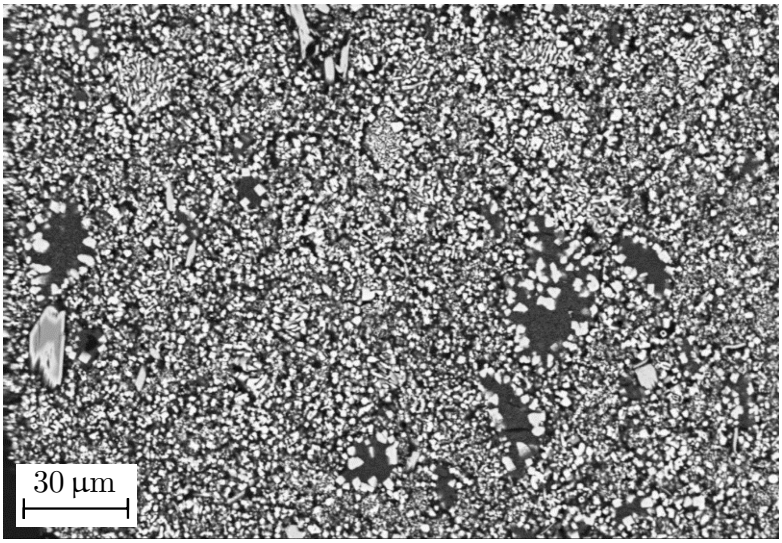


b

Figure 7.1: Grain structure of particles from the 5 mm size group (a) as-received and (b) after-calcination

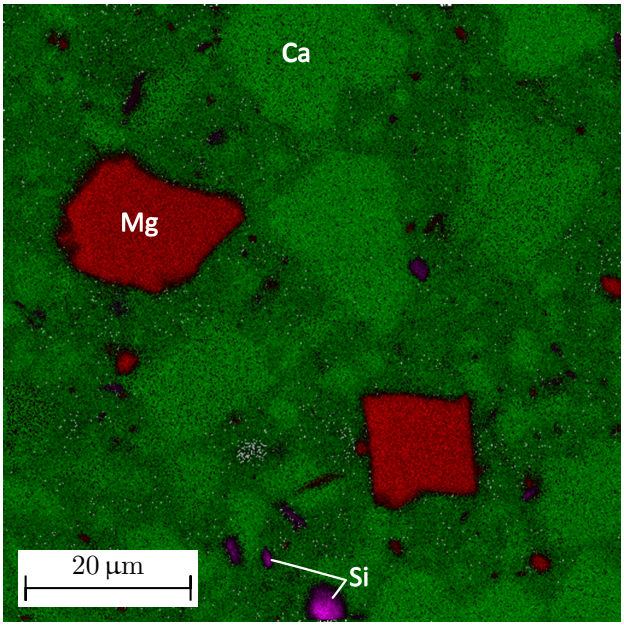


Figure 7.2: EDX map of as-received material from the 1 mm size group: calcium (green), magnesium (red), and silicon (purple)

$CaCO_3$ as calcite (JCPDS[2] 01-086-2334), with some $CaCO_3$ as aragonite (JCPDS 01-075-9984), calcium magnesium carbonate ($CaMg(CO_3)_2$) as dolomite (JCPDS 00-036-0426), and a very minor amount of silicon oxide ($SiO_2$) as quartz (JCPDS 00-046-1045). Traces of hydroxide of magnesioriebeckite ($(Na,Ca)_2(Mg,Fe)_5Si_8O_{22}(OH)_2$) (JCPDS 00-020-0656) and talc (JCPDS 04-013-2941) are also detected. Silicon previously observed in EDX maps is now identified as $SiO_2$. Based on qualitative comparison of peak intensity, impurities consist of predominantly $SiO_2$. The amount of impurities will be estimated through analysis of thermochemical cycling results in Section 7.3.2.

From the XRD pattern for the after-calcination material shown in Fig. 7.3b, the after-calcination material contains predominantly CaO as lime (JCPDS 01-077-9574), with impurities consisting mainly of magnesium oxide (MgO) as periclase, synthetic (JCPDS 00-004-0829) and $SiO_2$ as quartz (JCPDS 00-046-1045). A small amount of unreacted $CaCO_3$ as calcite (JCPDS 01-086-2334) is also detected in the after-calcination material. Magnesium, silicon, and iron impurities as well as a small amount of unreacted $CaCO_3$ are commonly found in quicklime samples obtained by calcination of limestone with contents varying from 0.3 to 2.5% of MgO and 0.2 to 1.5% of $SiO_2$ [Kogel et al., 2006].

Based on EDX and XRD results, the light-colored, large grains and regions of fine grains observed in the SEM–BSE images of as-received particles are identified as $CaCO_3$ and the dark-colored, large grains are identified as magnesium carbonate ($MgCO_3$) and/or dolomite. Based on similarity of results from all size groups, particles from all size groups have nearly identical composition. The large grains and regions of fine

[2]International Centre for Diffraction Data database standard designation

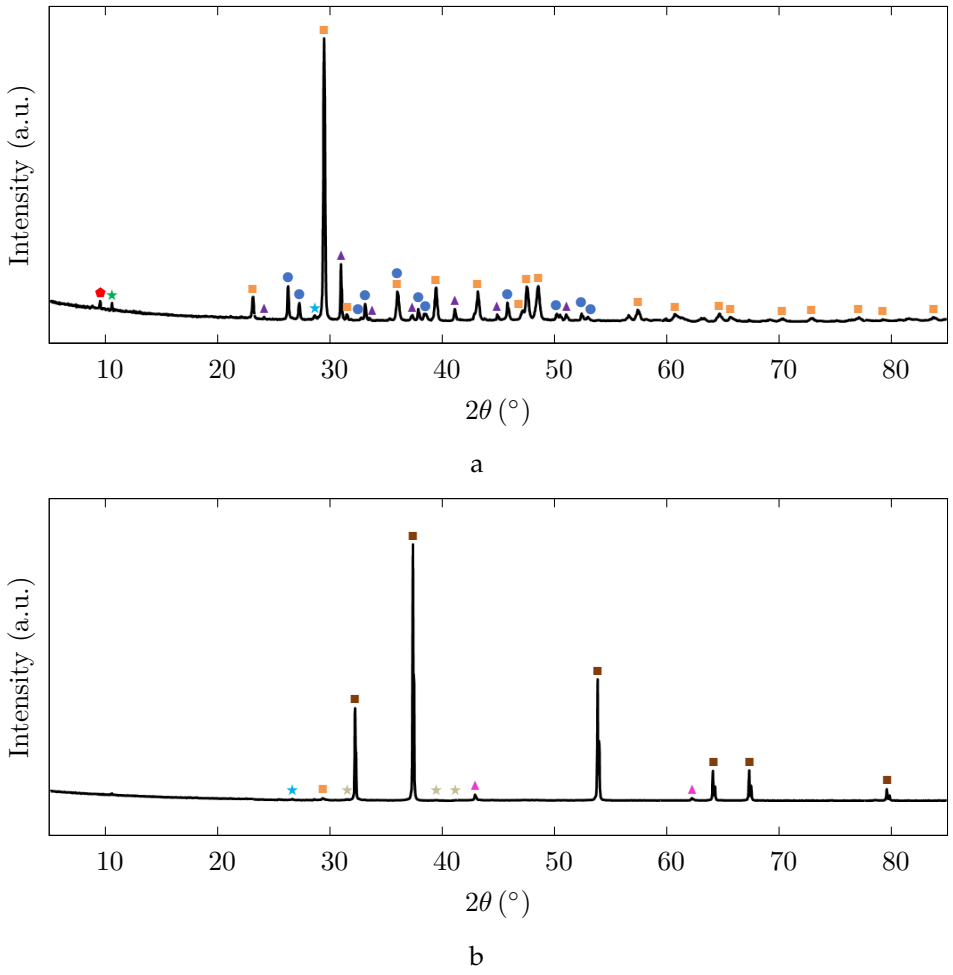


Figure 7.3: XRD patterns of (a) as-received and (b) after-calcination samples from the 5 mm size group. Intensity is expressed in arbitrary units. Symbols: ■ calcite $CaCO_3$ (JCPSD 01-086-2334), ● aragonite $CaCO_3$ (JCPDS 01-075-9984), ▲ dolomite $CaMg(CO_3)_2$ (JCPDS 00-036-0426), ★ magnesioriebeckite hydroxide $(Na,Ca)_2(Mg,Fe)_5Si_8O_{22}(OH)_2$ (JCPDS 00-020-0656), ★ quartz $SiO_2$ (JCPDS 00-046-1045), ⬟ talc 1A $Mg_3Si_4O_{10}(OH)_2$ (JCPDS 04-013-2941), ■ lime CaO (JCPDS 01-077-9574), ▲ periclase, syn MgO (JCPDS 00-004-0829), and ★ larnite $Ca_2(SiO_4)$ (JCPDS 01-080-8935)

grains of $CaCO_3$ and $MgCO_3$ decompose into fine-grained CaO and MgO, respectively, after calcination. The larger grains ($\sim 10\,\mu m$) that remain after calcination are $SiO_2$ and unreacted $CaCO_3$. Based on XRD analysis, the carbonates in the as-received material calcine almost completely to oxides after treatment.

## 7.3 Thermochemical cycling of sorbent particles in a furnace

In the following sections, the experimental methodology to study thermal transport reaction extent in single particles undergoing thermochemical cycling is elaborated. Method of analysis of the experimental data is detailed, and results are presented and discussed.

### 7.3.1 Methodology

Single particles from each size group exhibiting the highest sphericity based on visual inspection are selected for analysis. Uniformity of particle shape is prioritized over particle dimensions, resulting in a range of dimensions and initial masses for particles from a single size group.

The particles are placed in an alumina crucible. The crucible has an outer diameter of 5 mm with 1 mm thick walls and a depth of 2 mm. Particles are selected to fit laterally within the crucible, however particles from the 2.5 and 5 mm size groups extended vertically out of the top of the crucible.

Particles are thermochemically cycled in a thermogravimetric analyzer with built in differential scanning calorimetry (TGA–DSC), however the calorimetry data is not used in this work. The TGA–DSC is a SETARAM SETSYS Evolution 1750 instrument. Sample temperature readings are obtained from a thermocouple attached to the bottom of the sample holder on which the crucible sits. A mass spectrometer (MS), model Omnistar GSD 320 from Pfeiffer Vacuum, is connected to the outlet of the furnace to analyze evolved gas from the sample in the exit gas stream.

Experiments start with an initial heating period, followed by three calcination–carbonation cycles. In the calcination period, the particle is heated to the calcination temperature at a rate of $20\,K\,min^{-1}$. In the carbonation period, the sample is cooled to the carbonation temperature at a rate of $20\,K\,min^{-1}$, then held isothermally at the carbonation temperature for 30 min. Sweep gas with three different $CO_2$ concentrations is used (25, 50, and 100% $CO_2$ by volume in $N_2$), and the total sweep gas flow rate is $20\,ml\,min^{-1}$. Calcination and carbonation temperatures are evaluated for the sweep gas composition using thermodynamic data given by Eq. (3.1), and adjusted for an observed 20 to 30 K temperature difference between programmed and measured sample temperatures in preliminary experiments. Temperatures are adjusted for each $CO_2$ concentration rather than using identical temperature profiles for all cases, in order to keep intrinsic reaction

rates as uniform across cases as possible, thus allowing intra-particle mass transfer effects to be more apparent.

To investigate repeatability, one case is selected: 5 mm size group particles in 100% $CO_2$. Initial heating and the first calcination–carbonation cycle of the selected case is repeated two additional times, so three data sets are obtained for the initial heating and first calcination–carbonation cycle.

### 7.3.2 Results

Thermochemical cycling results include calcination and carbonation temperatures and the weight change of particles while undergoing cycling. Weight change is converted to overall reaction extent, and transient overall reaction extent is compared for the nine considered cases.

Table 7.1 shows the programmed furnace temperatures for calcination and carbonation for each $CO_2$ concentration. The maximum sample temperature during the first cycle and the sample temperature at the end of the first cycle for cases from the 5 mm size group, as read by the TGA–DSC thermocouple, are also given in Table 7.1. These sample temperatures are equivalent to the sample calcination and carbonation temperatures, respectively.

Table 7.1: Experimental calcination and carbonation temperatures

| $CO_2$ concentration (%) | Programmed calcination temperature (K) | Maximum sample temperature (K) | Programmed carbonation temperature (K) | End-of-cycle sample temperature (K) |
|---|---|---|---|---|
| 25 | 1253 | 1228 | 1023 | 1009 |
| 50 | 1273 | 1247 | 1093 | 1077 |
| 100 | 1302 | 1275 | 1123 | 1106 |

For the case selected to investigate repeatability (5 mm size group particle in 100% $CO_2$), the transient percent weight change is calculated for each of the three data sets. The average percent transient weight change is calculated using values from the three data sets, and the value for each data set is compared to the average at each time instant. The maximum difference is 2% and the average difference is 0.26%, confirming repeatability of that case and supporting the repeatability of all other cases.

**Initial heating and the first thermochemical cycle** Figure 7.4 shows TGA–DSC and MS results from the initial heating period as well as the first calcination–carbonation cycle of a particle from the 5 mm size group in 25% $CO_2$ atmosphere. Percent weight change of the sample, the measured sample temperature, and MS mass-to-charge ratio

$m/z$[3] signals for $m/z = 18$ and 44 are included.

Two weight changes, beginning at $t = 38$ and 74 min, are observed during initial heating. The onset of these weight changes is marked with a dashed line in Fig. 7.4b. These initial heating period weight changes are not observed in subsequent cycles and are attributed to the release of $H_2O$ and the decomposition of $MgCO_3$ in the dolomite identified in the XRD analysis in Section 7.2.2.

For the first initial heating weight change, the weight of the particle decreases by 2% when heating from $T = 319$ to 1048 K. These temperatures are also marked with dashed lines in Fig. 7.4b. The MS signal peak for $m/z = 18$ indicates the release of $H_2O$ during this period. The $H_2O$ is attributed to the release of $H_2O$ bound in the natural carbonate crystals at the lower temperatures [L'vov, 1997; Gunasekaran and Anbalagan, 2007] and the decomposition of hydroxide impurities at the higher temperatures [Kashcheev et al., 2016].

A second weight loss of another 3% starts at 1048 K and corresponds to an MS $m/z$ signal peak for $m/z = 44$. This weight loss is attributed to the decomposition of $MgCO_3$ in the dolomite. Dolomite decomposition consists of two steps, one at a lower temperature ($\sim$ 1050 K in $N_2$) associated with the calcination of $MgCO_3$ and one at a higher temperature ($\sim$ 1107 K in $N_2$) associated with the calcination of $CaCO_3$ [Gunasekaran and Anbalagan, 2007]. The first decomposition step results in the release of $CO_2$ according to the following reaction

$$\mathrm{CaMg\,(CO_3)_2} \rightarrow \mathrm{CaCO_3 + MgO + CO_2} \tag{7.1}$$

The $CaCO_3$ remaining in the dolomite after the first decomposition reaction of $MgCO_3$ calcines in the same manner as pure $CaCO_3$ according to Eq. (2.6).

The temperature of the second observed weight loss ($T = 1048$ K) agrees with the temperature at which the first dolomite decomposition step occurs ($T = 1050$ K). The corresponding MS $m/z$ signal peak for $m/z = 44$ therefore indicates $CO_2$ released by the chemical reaction given by Eq. (7.1). These two weight changes during the initial heating are observed to some degree in experiments with particles from all size groups and in all $CO_2$ atmospheres.

After initial heating, a rapid weight loss occurs, followed by a period of no weight change, and then a weight increase, as shown in Fig. 7.4a. The onsets of the rapid weight loss and weight increase occur at 1092 and 1047 K, respectively. The weight loss and increase correspond to an MS $m/z$ signal peak and trough, respectively, for $m/z = 44$. The rapid weight loss is the calcination of $CaCO_3$; the weight increase is the carbonation of CaO. The MS $m/z$ signal peak is $CO_2$ released by the calcination reaction given by Eq. (2.6); the MS $m/z$ signal trough is due to the uptake of $CO_2$ by the carbonation reaction given by Eq. (2.7). Subsequent thermochemical cycles show similar weight

[3]This usage and notation follows the *Compendium of Chemical Terminology* [IUPAC, 1997] definition of mass-to-charge ratio in mass spectrometry.

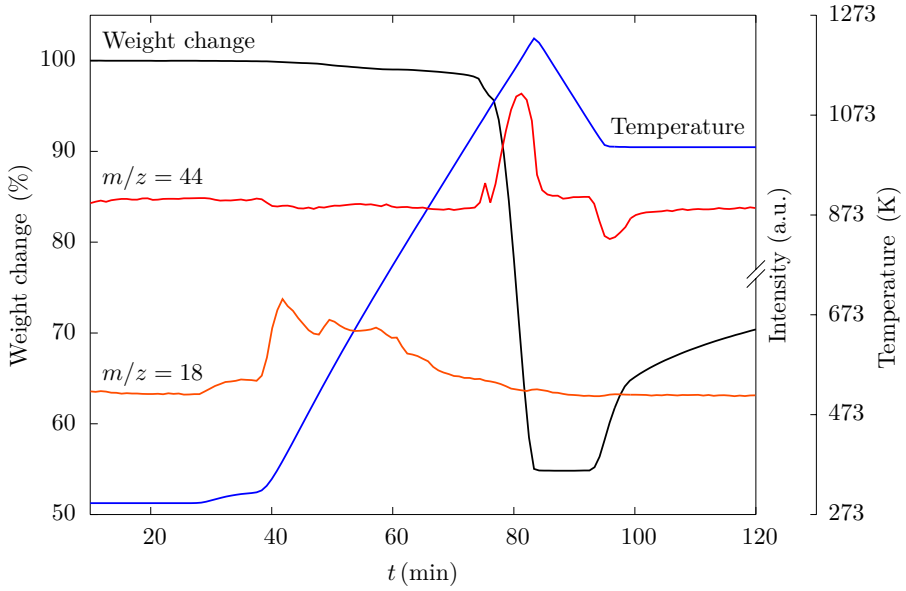


a

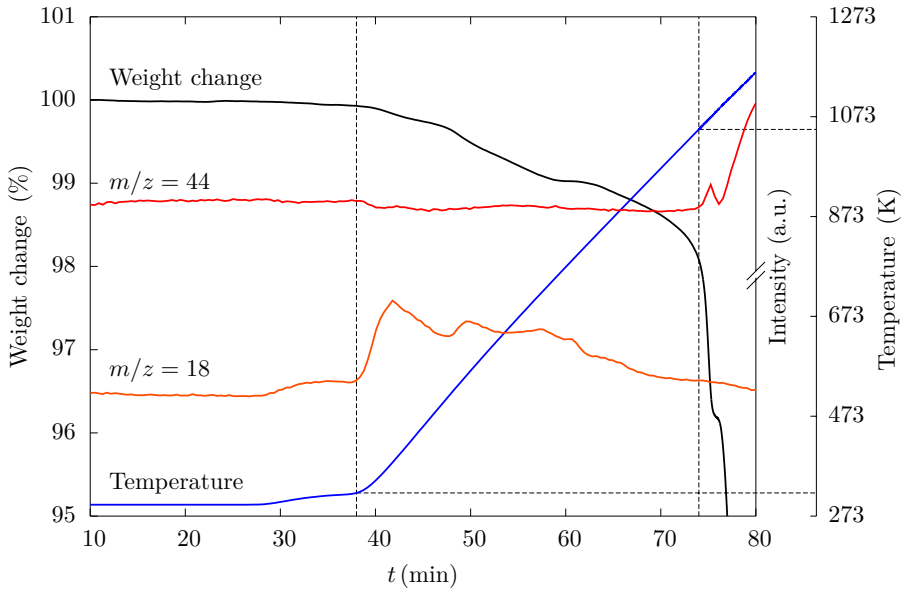


b

Figure 7.4: Initial heating and the first calcination–carbonation cycle of a particle from the 5 mm size group in 25% $CO_2$ atmosphere, for (a) $t = 10$ to 120 min and (b) a magnified view of $t = 10$ to 80 min: percent weight change (black line), temperature (blue line), MS $m/z = 18$ signal (orange line), and MS $m/z = 44$ signal (red line), MS $m/z$ signals are represented in arbitrary units on a logarithmic scale

changes and MS $m/z$ signals for $m/z = 44$, indicating cyclic calcination and carbonation and thus, CaO looping.

A small fraction of the weight increase and decrease during cycling could be due to the cyclic carbonation and calcination of MgO and $MgCO_3$, respectively. However, MgO carbonation has been shown to require higher $CO_2$ partial pressures to proceed at appreciable rates [Fagerlund et al., 2012], therefore any weight changes due to MgO carbonation or subsequent $MgCO_3$ calcination are assumed small enough to be neglected.

**Evaluating overall reaction extent from experimental data** To compare cases with different initial masses, overall reaction extent for experimental results is found from the mass of the sample measured by TGA–DSC according to the following equation

$$X_{\text{overall}} = \left(1 - \frac{m - m_{\text{impurities}}}{m_0 - m_{\text{impurities}}}\right)\left(\frac{\overline{M}_{\text{CaCO}_3}}{\overline{M}_{\text{CaCO}_3} - \overline{M}_{\text{CaO}}}\right) \tag{7.2}$$

where $m$, $m_{\text{impurities}}$, and $m_0$ are the actual mass of the sample, the mass of the impurities, and the initial mass of the sample, respectively. Overall reaction extent for experimental results is distinct from theoretical weight change for full conversion because overall reaction extent is evaluated on a molar basis rather than a mass basis. The overall reaction extent defined by Eq. (7.2) is analogous to the overall reaction extent for numerical results defined by Eq. (6.1).

The initial mass of the sample $m_0$ for calculating $X_{\text{overall}}$ is taken as the mass of the sample after the initial heating period changes described above (dehydration, hydroxide decomposition, and the first dolomite decomposition step). For example, for the 5 mm size group particle in 25% $CO_2$ shown in Fig. 7.4, $m_0$ is taken as the mass at $t = 76$ min.

The mass of the impurities $m_{\text{impurities}}$ for calculating $X_{\text{overall}}$ is estimated by assuming 100% calcination of $CaCO_3$ in a particle. This is accomplished by setting the overall reaction extent in Eq. (7.2) to $X_{\text{overall}} = 1$ for the minimum mass achieved during the first cycle, and then solving for $m_{\text{impurities}}$. The mass of the impurities therefore includes species that do not react during cycling such as $SiO_2$ and MgO, while species lost during the initial heating such as $H_2O$ and $CO_2$ released during dolomite decomposition are deducted from the initial mass. Initial mass, the calculated mass of the impurities, and the ratio of calculated impurities to initial mass are given in Table 7.2 for each case.

Based on the material characterization in Section 7.2.2, particles from all size groups are assumed to have roughly the same composition. Therefore it follows that the fraction of impurities in each particle selected for cycling is uniform. The average percentage of impurities is 6.75%, and the values range from 6.17 to 7.77% showing good agreement with the average, with two exceptions. The two outlying cases are the 2.5 mm size group particle in 50% $CO_2$ and the 5 mm size group particle in 25% $CO_2$.

Particles from the 2.5 and 5 mm size group cycled in 50% and 25% $CO_2$ exhibit larger and smaller fractions of impurities, respectively than the rest of the considered particles. A hypothesized explanation for these two outlying particles is the variation in grain sizes

observed in SEM–BSE images in Section 7.2.2. As particles are extruded, the presence or absence of large grains of impurities have the potential to result in particles with larger and smaller amounts of impurities, respectively.

Table 7.2: Initial mass and mass of impurities used for calculating overall reaction extent

| Case | $m_0$ (mg) | $m_{\text{impurities}}$ (mg) | $m_{\text{impurities}}/m_0 \times 100\%$ (%) |
|---|---|---|---|
| 1 mm 25% $CO_2$ | 2.93 | 0.20 | 6.83 |
| 1 mm 50% $CO_2$ | 2.43 | 0.15 | 6.17 |
| 1 mm 100% $CO_2$ | 3.49 | 0.25 | 7.16 |
| 2.5 mm 25% $CO_2$ | 12.34 | 0.83 | 6.73 |
| 2.5 mm 50% $CO_2$ | 9.07 | 1.08 | 11.91 |
| 2.5 mm 100% $CO_2$ | 10.37 | 0.79 | 7.62 |
| 5 mm 25% $CO_2$ | 56.34 | 0.01 | 0.02 |
| 5 mm 50% $CO_2$ | 47.73 | 3.71 | 7.77 |
| 5 mm 100% $CO_2$ | 52.90 | 3.46 | 6.54 |

**Trends observed in results for all considered cases** Overall reaction extent is shown versus time in Figs. 7.5 and 7.6 for particles from the 1, 2.5, and 5 mm size groups in 25, 50, and 100% $CO_2$ atmospheres. Figure 7.5 compares overall reaction extent versus time for different $CO_2$ atmospheres, while Fig. 7.6 compares overall reaction extent versus time for particles from different size groups. Initially, particles consist of predominantly $CaCO_3$ and $X_{\text{overall}} = 0$. Once the calcination temperature (given in Table 7.1 for each case) is reached, particles calcine rapidly to completion and $X_{\text{overall}} \approx 1$.

Calcination occurs rapidly, and complete calcination is achieved in under 10 minutes for all cases. As particles calcine, the product layer of CaO becomes very porous allowing for unimpeded diffusion of product $CO_2$ away from the reaction area. Ambient $CO_2$ concentration affects intrinsic chemical kinetics, but the experimental temperature program is adjusted specifically to each $CO_2$ concentration to compensate for the dependence of calcination kinetics on $CO_2$ concentration. As a result, the effect of ambient $CO_2$ concentration on the rate of change of overall reaction extent during calcination is not apparent in the overall reaction extent results shown in Figs. 7.5 and 7.6.

During the carbonation period, the temperature decreases to the carbonation temperature (given in Table 7.1 for each case). Particles begin to carbonate, and $X_{\text{overall}}$ decreases. Two regimes are observed during all carbonation periods: an initial regime with rates of change of overall reaction extent on the order of the observed calcination rates and a second regime with rates of change 1–2 orders of magnitude slower than the rates of change during the initial carbonation regime. The initial and second regimes will be herein referred to as the fast and slow regimes, respectively.

The fast regime spans the first 5–10 min of the carbonation period, while the slow regime spans the remaining 25–30 min of the carbonation period. The rate of change of the overall reaction extent during carbonation in the fast regime is fairly uniform for all

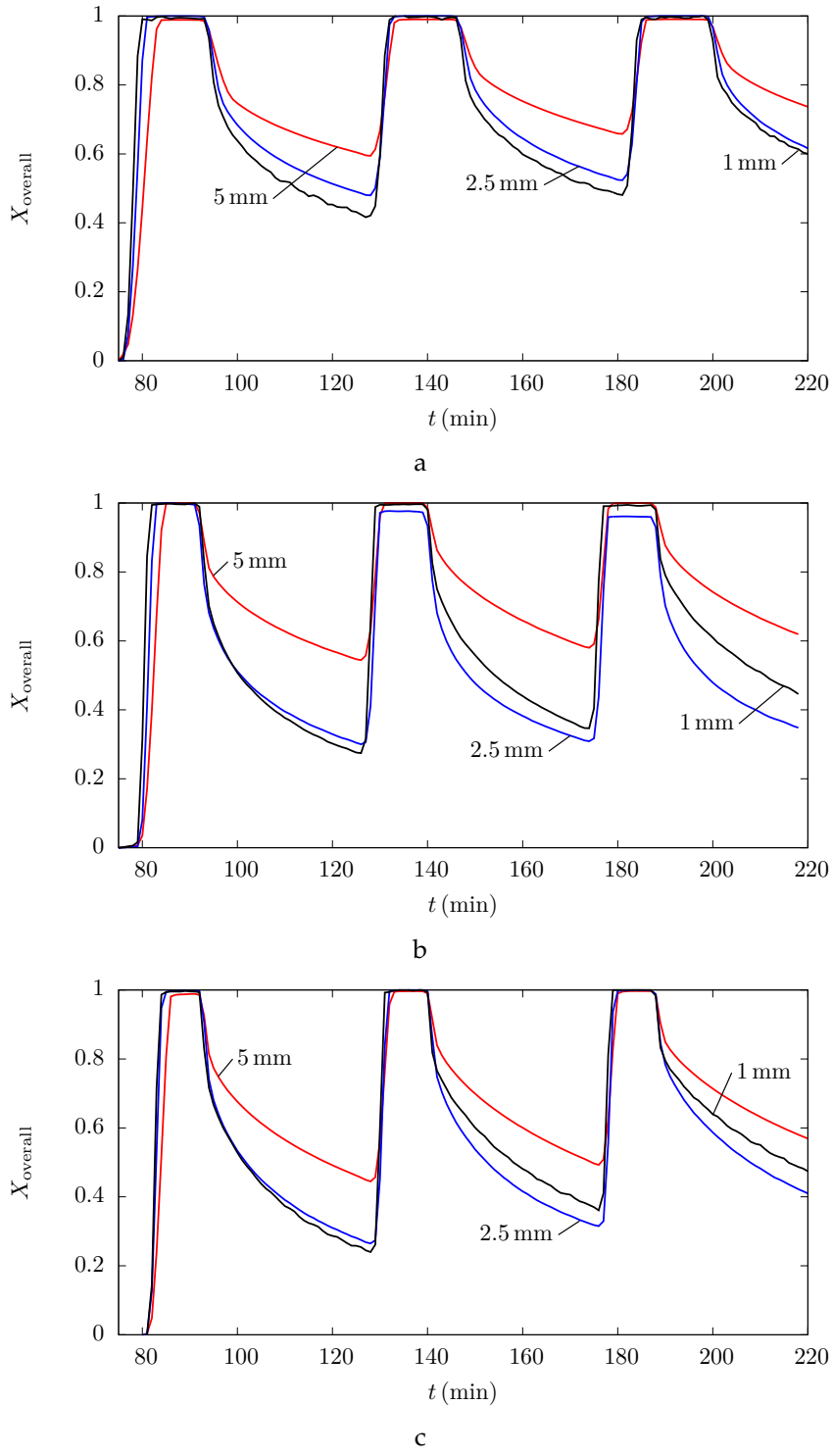


Figure 7.5: Overall reaction extent versus time for particles from the 1 (black lines), 2.5 (blue lines), and 5 mm (red lines) size groups cycled in (a) 25, (b) 50, and (c) 100% $CO_2$ atmospheres

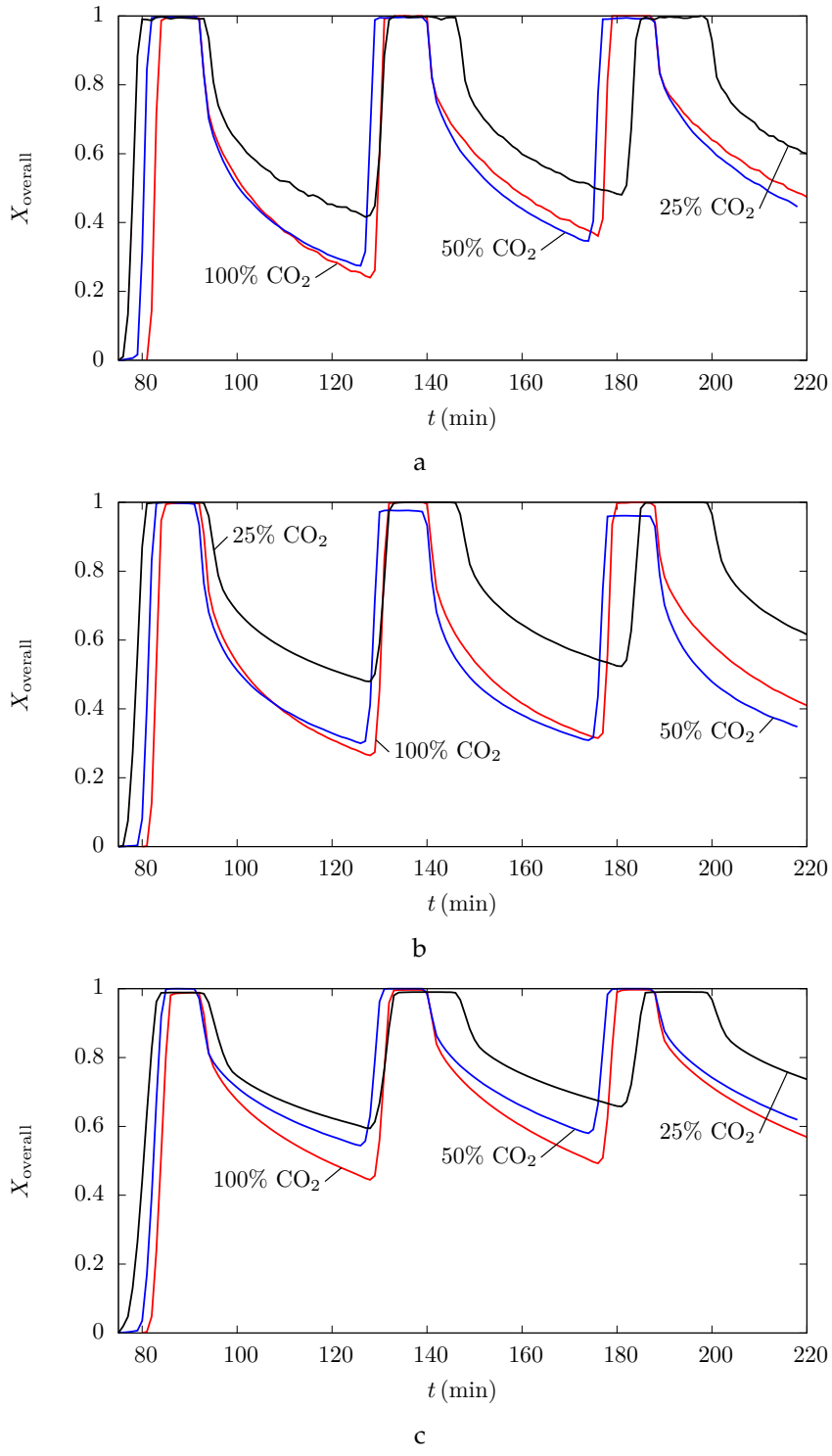


Figure 7.6: Overall reaction extent versus time for particles from the (a) 1, (b) 2.5, and (c) 5 mm size groups cycled in 25 (black lines), 50 (blue lines), and 100% $CO_2$ (red lines) atmospheres

cases, while a range of rates during the slow regime are observed. None of the particles completely carbonate during the carbonation period, but 30 minutes is sufficient for particles from all cases to exhibit both fast and slow carbonation regimes.

Each case reaches a maximum state of carbonation and therefore a minimum value for $X_{\text{overall}}$ for each cycle. When the carbonation period ends, the next calcination period begins from this minimum $X_{\text{overall}}$ state. Particles begin calcining again with $X_{\text{overall}}$ increasing from the minimum $X_{\text{overall}}$ in the previous cycle to $X_{\text{overall}} = 1$ at the end of the calcination period.

During the carbonation period, the fast regime is limited by chemical kinetics, while the slow regime is limited by diffusion of $CO_2$ to unreacted CaO through the dense $CaCO_3$ product layer [Alvarez and Abanades, 2005]. SEM–BSE images taken of cross sections of two selected particles that have been cycled three times show inhomogeneity and support the conclusion that slow carbonation is diffusion limited.

Images of cross sections are taken of particles from the 5 mm size group after three thermochemical cycles in 50 and 100% $CO_2$. The images are shown in Fig. 7.7; an image of the 5 mm size group particle cycled in 25% $CO_2$ was not be obtained. A distinct boundary between a porous, inner core material (CaO) and a dense, outer shell material ($CaCO_3$) is apparent. Large black voids in the cross section images may be due to material being washed away when the samples are polished for SEM–BSE imaging but may also be artifacts of the manufacturing process. Similar large black voids are also observed in cross section images taken of as-received particles that have not been thermochemically cycled.

The instantaneous rates of change of the overall reaction extent observed in Figs. 7.5 and 7.6 are equivalent to volume-weighted averages of local reaction rate at all locations within the particle. This rate of change is referred to as the instantaneous apparent reaction rate. To estimate the instantaneous apparent reaction rate, transient overall reaction extent data is reduced to one data point per second. Then, the instantaneous apparent reaction rate is approximated for each second $i$ by the following equation

$$\left(\frac{\mathrm{d}X_{\text{overall}}}{\mathrm{d}t}\right)_i \approx \frac{X_{\text{overall},i} - X_{\text{overall},i-1}}{\Delta t} \tag{7.3}$$

where $\Delta t = 1\,\text{s}$. Three time intervals are defined over which instantaneous apparent reaction rates are then time-averaged: (1) for calcination, from the onset to conclusion of the calcination reaction, (2) for fast carbonation, from the onset of carbonation to the transition from fast to slow carbonation, and (3) for slow carbonation, from the transition from fast to slow carbonation to the end of the carbonation period. The transition between fast and slow carbonation is defined based on visual inspection of transient overall reaction extent and instantaneous apparent reaction rate curves.

The instantaneous apparent reaction rate during calcination, fast carbonation, and slow carbonation is averaged to yield an average apparent reaction rate for each time

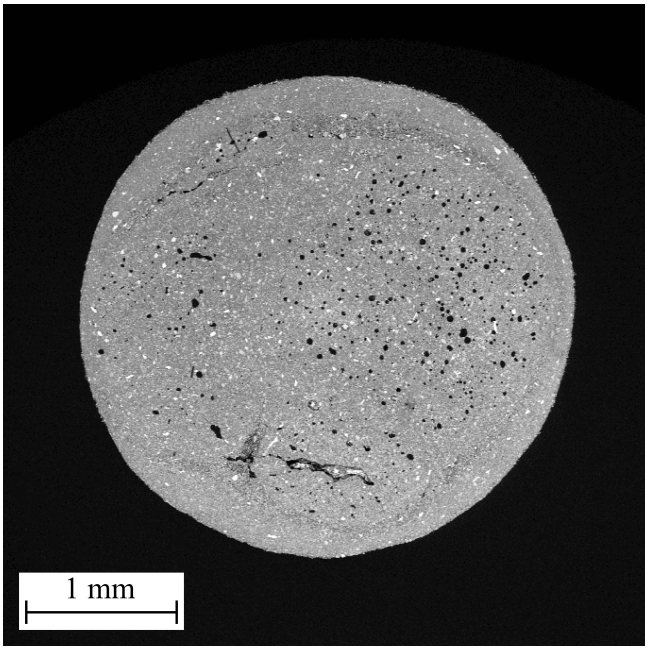


a

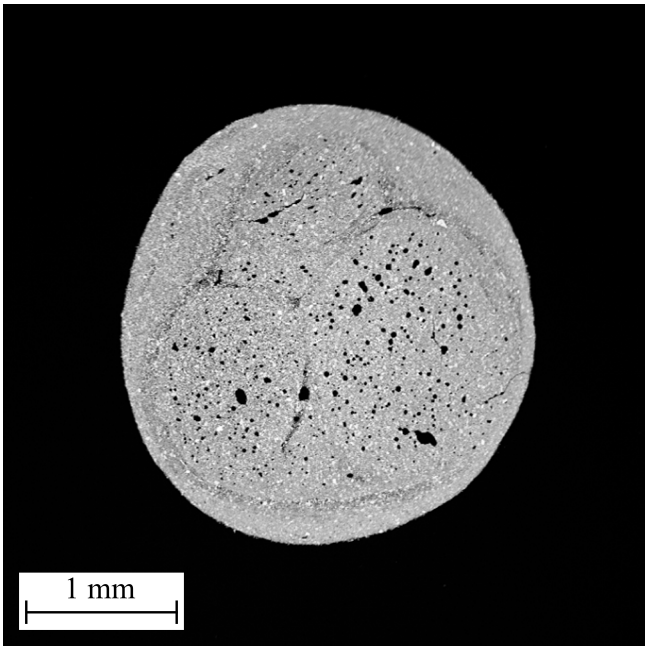


b

Figure 7.7: SEM–BSE images of 5 mm size group particle cross sections after thermochemical cycling in (a) 50 and (b) 100% $CO_2$ atmospheres

interval according to

$$\left(\frac{\mathrm{d}X_{\text{overall}}}{\mathrm{d}t}\right)_{\text{average}} = \frac{\sum_{i=t_{\text{start}}}^{t_{\text{end}}} \left(\frac{\mathrm{d}X_{\text{overall}}}{\mathrm{d}t}\right)_i}{t_{\text{end}} - t_{\text{start}}} \tag{7.4}$$

where the time intervals over which the instantaneous apparent reaction rates are averaged start at $t_{\text{start}}$ and end at $t_{\text{end}}$. The average apparent reaction rates for calcination, fast carbonation, and slow carbonation during the first cycle are shown for all considered cases in Table 7.3, expressed in $\text{min}^{-1}$ to agree the x-axis units in Figs. 7.5 and 7.6.

Table 7.3: Average apparent reaction rates ($\text{min}^{-1}$) during calcination, fast carbonation, and slow carbonation

| Case | $\left(\frac{\mathrm{d}X_{\text{overall}}}{\mathrm{d}t}\right)_{\text{calc}}$ | $\left(\frac{\mathrm{d}X_{\text{overall}}}{\mathrm{d}t}\right)_{\text{carb,fast}}$ | $\left(\frac{\mathrm{d}X_{\text{overall}}}{\mathrm{d}t}\right)_{\text{carb,slow}}$ |
|---|---|---|---|
| 1 mm 25% $CO_2$ | $24.61\times10^{-2}$ | $-9.96\times10^{-2}$ | $-1.09\times10^{-2}$ |
| 1 mm 50% $CO_2$ | $30.66\times10^{-2}$ | $-12.38\times10^{-2}$ | $-1.42\times10^{-2}$ |
| 1 mm 100% $CO_2$ | $34.66\times10^{-2}$ | $-12.48\times10^{-2}$ | $-1.45\times10^{-2}$ |
| 2.5 mm 25% $CO_2$ | $17.68\times10^{-2}$ | $-5.54\times10^{-2}$ | $-0.87\times10^{-2}$ |
| 2.5 mm 50% $CO_2$ | $25.38\times10^{-2}$ | $-10.11\times10^{-2}$ | $-1.21\times10^{-2}$ |
| 2.5 mm 100% $CO_2$ | $25.75\times10^{-2}$ | $-11.79\times10^{-2}$ | $-1.43\times10^{-2}$ |
| 5 mm 25% $CO_2$ | $12.09\times10^{-2}$ | $-3.26\times10^{-2}$ | $-0.58\times10^{-2}$ |
| 5 mm 50% $CO_2$ | $16.71\times10^{-2}$ | $-5.38\times10^{-2}$ | $-0.83\times10^{-2}$ |
| 5 mm 100% $CO_2$ | $19.21\times10^{-2}$ | $-6.64\times10^{-2}$ | $-1.04\times10^{-2}$ |

Average apparent reaction rates for the same size group and time interval are expected to be similar regardless of $CO_2$ concentration, because TGA–DSC temperature programs have been adjusted for each $CO_2$ concentration in an attempt to produce uniform reaction rates for all $CO_2$ concentration. However, the average apparent reaction rates for each time intervals decrease slightly with $CO_2$ concentration within a size group. Normalized intrinsic calcination reaction rates shown in Fig. 3.2a can vary by up to $0.2\,\text{mol}_{CO_2}\,\text{m}^{-2}\,\text{s}^{-1}$ or approximately $500\,\text{g}_{CO_2}\,\text{m}^{-2}\,\text{min}^{-1}$ with varying $CO_2$ concentration, for a fixed reaction surface area and temperature in the range relevant to the experimental results presented in this section. Considering this potential span of rates, the variation in reaction rate with $CO_2$ concentration observed in Table 7.3 is considered small.

Apparent reaction rates for the same $CO_2$ concentration are expected to decrease with increasing particle size because the apparent reaction rates are volume-weighted, averages of the intrinsic reaction rates. For example, if particles from the 1 and 5 mm size groups experience the same intrinsic reaction rate over the same depth into the particle from the particle surface, then the volume exhibiting that intrinsic reaction rate will be a larger fraction of the 1 mm size group particle than the 5 mm one. The larger volume

fraction in the smaller particle leads to a larger apparent reaction rate than that for the larger particle. This trend of decreasing average apparent reaction rate with particle size for the same $CO_2$ is observed over the considered particle size range in all $CO_2$ concentrations for calcination, fast carbonation, and slow carbonation.

**Comparison of results for particles from different size groups and carbon dioxide atmospheres** Two trends are observed when comparing cases with particles from the 2.5 and 5 mm size groups cases: (1) $X_{\text{overall}}$ when the carbonation reaction transitions from the fast to slow regime in the first cycle decreases with decreasing particle size and (2) $X_{\text{overall}}$ at the end of the first and subsequent cycles decreases with decreasing particle size. One additional trend is observed when comparing cases with different $CO_2$ concentrations: the rate of the slow carbonation regime decreases with decreasing $CO_2$ concentration.

Overall reaction extent results for particles from the 1 mm size group do not follow the observed trends. It is not apparent why results for particles from this size group are inconsistent with observed and expected trends. The 1 mm size group cases can be distinguished from the other cases by comparing average apparent reaction rates. However, the difference between the average apparent reaction rates between some cases is insignificant when compared to the uncertainty in calculating the overall reaction extent and the ratio of TGA–DSC measurement noise to sample size.

Possible reasons the 1 mm size group particles do not exhibit the expected trends include different flow pattern of the sweep gas and faster densification of smaller particles. Particles from the 1 mm size group are completely submerged in the crucible, whereas a portion of particles from the larger size groups protrudes above the top of the crucible. Flow patterns of sweep gas in and around the crucible have the potential to differ between particles that protrude above the crucible (those from the 2.5 and 5 mm size groups) and particles that do not (those from the 1 mm size group). Small particles may also experience different rates of densification of the $CaCO_3$ product layer. Due to their smaller size, the 1 mm size group particles have the potential to experienced faster local heating rates, resulting in a denser and/or more sintered product layer. However, without additional information, these hypotheses cannot be confirmed, warranting further investigation of the 1 mm size group cases.

For cases with particles from the 2.5 and 5 mm size groups, overall reaction extent when the carbonation reaction transitions from the fast to slow regime in the first cycle decreases with decreasing particle size. As previously stated, the transition point is estimated by visual inspection of overall reaction extent and instantaneous apparent reaction rate results. Overall reaction extent at the transition point is given for all cases in Table 7.4. Decreasing $X_{\text{overall}}$ at the transition point with decreasing particle size can be observed most clearly in Fig. 7.5a. This trend also results in decreasing values of $X_{\text{overall}}$ at the end of the first and subsequent cycles with decreasing particle size. The differences in $X_{\text{overall}}$ at the transition point between 2.5 and 5 mm size group particle

Table 7.4: Overall reaction extent at the transition from fast to slow carbonation during the first cycle

| Case | $X_{\text{overall}}$ |
|---|---|
| 1 mm 25% $CO_2$ | 0.734 |
| 1 mm 50% $CO_2$ | 0.697 |
| 1 mm 100% $CO_2$ | 0.724 |
| 2.5 mm 25% $CO_2$ | 0.736 |
| 2.5 mm 50% $CO_2$ | 0.680 |
| 2.5 mm 100% $CO_2$ | 0.730 |
| 5 mm 25% $CO_2$ | 0.754 |
| 5 mm 50% $CO_2$ | 0.802 |
| 5 mm 100% $CO_2$ | 0.786 |

cases are smaller than the differences in $X_{\text{overall}}$ at the end of the cycle.

Decreasing overall reaction extent at the transition and at the end of the cycle is related to the critical product layer thickness. A critical thickness of the dense $CaCO_3$ outer layer marks the point when the carbonation reaction switches from the fast to slow regime. This critical thickness is associated with the switch from a kinetics limited reaction to a mass transfer limited one as discussed in Section 2.2. For product layer thicknesses greater than the critical thickness, $CO_2$ diffusion through the $CaCO_3$ layer is sufficiently slow to limit the carbonation reaction.

Critical thickness is expected to be independent of particle size, because diffusion of $CO_2$ through the outer layer of $CaCO_3$ is predominantly a 1D phenomenon. Anisotropy of intra-particle properties or nonuniformity of conditions at the particle surface have the potential to result in more complex directional dependence. However, for the considered cases, the particles are assumed sufficiently isotropic and the conditions sufficiently uniform that the particles react uniformly for all polar and azimuthal angles. With these assumptions, the concentration gradient of $CO_2$ driving diffusion only exists radially from one side of the outer $CaCO_3$ layer (the particle surface) to the other (adjacent to the unreacted CaO). If the ambient conditions remain the same, the thickness at which radial $CO_2$ diffusion becomes sufficiently impeded to impede carbonation will be the same, regardless of particle size, as long as the particle radii are larger than the critical thickness. Critical thickness is expected to increase with increasing $CO_2$ concentration, because the $CO_2$ concentration gradient across the $CaCO_3$ layer increases with increasing ambient $CO_2$ concentration. The larger gradient results in a stronger driving force for $CO_2$ diffusion.

Critical thickness describes spatial variation of composition within a particle, and therefore cannot be directly extracted from $X_{\text{overall}}$, which is spatially averaged. For a given critical thickness, the size of the outer $CaCO_3$ region relative to total particle size decreases with increasing particle size. Conversely, the larger the particle, the more CaO

is located in the center of the particle and surrounded by the $CaCO_3$ when the critical thickness is reached. Therefore, for the same critical thickness, larger particles exhibit less carbonation and a larger $X_{\text{overall}}$ when the carbonation reaction switches from the fast to slow regime.

Cases with different $CO_2$ concentrations are compared to investigate the effect of $CO_2$ concentration on overall reaction extent. Calcination behavior and the rate and duration of the fast carbonation regime remain roughly the same with changing $CO_2$ concentration, due to the adjusted temperature programs as previously discussed. For particles from the 2.5 and 5 mm size group, the rate of the slow carbonation regime decreases with decreasing $CO_2$ concentration, as shown in Table 7.3. The trend can also be observed in Figs. 7.5 and 7.6; and it is most apparent in Fig. 7.6c. Decreasing $CO_2$ concentration is expected to result in slower apparent reaction rates during slow carbonation, because decreased $CO_2$ concentration yields slower rates of diffusion of $CO_2$ through the outer product layer. Slower diffusion rates, in turn, result in slower carbonation reaction rates in the slow regime and decreased conversion back to $CaCO_3$ (i.e. increased $X_{\text{overall}}$) at the end of each cycle.

All cases show the effects of intra-particle mass transfer on the apparent reaction rate during carbonation, because all cases exhibit both fast and slow carbonation. The effect of particle size and $CO_2$ concentration on overall reaction extent when the carbonation reaction transitions from fast to slow can be observed in some of the considered cases (those with particles from the 2.5 and 5 mm size groups), but not all (those with particles from the 1 mm size group). Thermochemical cycling of particles from the 1 mm size group warrants further investigation.

## 7.4 Reproduction of experimental results using the numerical model

In this section, the numerical model presented in Chapter 4 is used to determine medium characteristics of the sample material and reproduce the experimental results. Characteristics are evaluated by adjusting model parameters. Numerically predicted overall reaction extent using tuned medium characteristic values is compared to that obtained experimentally.

Practical considerations and limitations of the TGA–DSC setup presented in Section 7.3.1 likely result in some nonuniform conditions around particles. As previously discussed in Section 7.3.2, the nonuniformity of the conditions is assumed small, so the 1D model is used. To emulate the TGA–DSC setup the following conditions are used. The inert fluid species is $N_2$. The molar mass and diffusion volume for $N_2$ are $\overline{M}_{N_2} = 0.02801\,\text{kg mol}^{-1}$ [Wieser, 2006] and $(\Sigma\nu)_{N_2} = 17.9\,\text{m}^3$ [Fuller et al., 1966], respectively. In the surface boundary conditions for the fluid-phase mass conservation equations, Eqs. (4.22) and (4.24), the convective mass transfer coefficient between fluid

at the particle surface and ambient conditions is evaluated for a sphere in a flow with velocity $u_{f,\infty} = 0.002\,\mathrm{m\,s^{-1}}$. This velocity emulates the $20\,\mathrm{ml\,min^{-1}}$ flow rate of sweep gas through the furnace with diameter $d = 18\,\mathrm{mm}$.

For the energy conservation equation, the surface boundary condition for sweep gas controlled temperature given by Eq. (4.30) is used. The temperature profile of the sweep gas used for the particle surface temperature $f_{T_\infty}(t)$ emulates the experimental temperature protocol for each $CO_2$ concentration. The surface temperature used in the model during the calcination period is assumed to be 20 K less than the sample temperature read by the TGA–DSC. This assumption is made to model an estimated difference between the temperature shown by the sample thermocouple and the actual sample temperature during heating.

### 7.4.1 Evaluation of medium characteristic of the particles and other considerations to improve numerical model fitness

Overall reaction extent predicted using the original model with the updated boundary conditions just described is first compared to experimental overall reaction extent for the 2.5 and 5 mm size groups. Lack of preliminary agreement between the numerical and experimental results motivates the identification of medium characteristics that need to be adjusted or included in the model. Adjusted medium characteristics improve the agreement, and overall reaction extent predicted using the adjusted medium characteristics is compared to experimental overall reaction extent with good agreement.

Overall reaction extent for one cycle predicted using the model with the updated boundary conditions for a 5 mm diameter particle in 25% $CO_2$ is shown in Fig. 7.8 with the corresponding experimentally measured results. Preliminary numerical results obtained with the original model compare similarly to experimental results, irrespective of the considered particle size (2.5 or 5 mm) and $CO_2$ concentration (25, 50, or 100% $CO_2$). Therefore, the following conclusions drawn from comparing numerical results for a particle from the 5 mm size group in 25% $CO_2$ to experimentally measured results are applicable to all considered particle sizes and $CO_2$ concentrations.

The rate of calcination predicted by the model agrees with the rate of calcination observed experimentally. Thus, no properties or characteristics related to the rate of calcination are selected for adjustment. During the carbonation period, however, the rate and duration of both the fast and slow carbonation regimes predicted by the model do not agree with those observed in the experimental results. The numerically predicted rates of the fast and slow carbonation regimes are higher than the corresponding measured ones; and the predicted duration of the fast carbonation regime is longer than the measured one.

Medium-specific quantities in the model that determine the rate and duration of the fast and slow carbonation regimes include carbonation reaction specific surface area $s'''_{\mathrm{carb}}$ and effective diffusivity of fluid in the pore space $D_{\mathrm{eff}}$. A reduction in $s'''_{\mathrm{carb}}$ will result

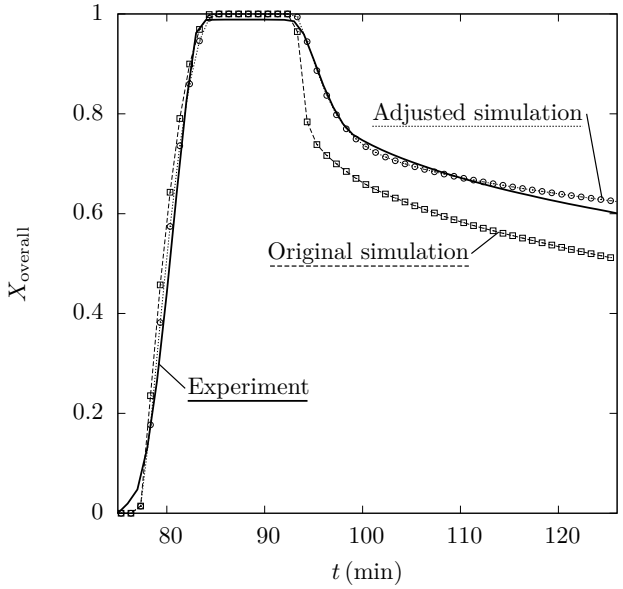


Figure 7.8: Overall reaction extent versus time for a particle from the 5 mm size group undergoing the first calcination–carbonation cycle in 25% $CO_2$ atmosphere: experimental results (solid line), numerical results using the original model with modified boundary conditions (square points, dashed line), numerical results using the adjusted model with modified boundary conditions (round points, dotted line)

in a reduction in reaction rate during the fast carbonation regime. A reduction in $D_{\text{eff}}$ will result in reductions of the duration of the fast carbonation regime and the reaction rate during the slow carbonation regime. Modifications to either quantity will not affect calcination or the onset of carbonation. Therefore, $s'''_{\text{carb}}$ and medium characteristics influencing $D_{\text{eff}}$ are selected as the characteristics to scrutinize for the sample material.

The following equation is introduced to evaluate the mass-specific surface area of CaO, $s_{\text{CaO}}$ based on the average CaO grain size $r_{\text{g,CaO}}$, adapted from Stendardo and Foscolo [2009]

$$s_{\text{CaO}} = \frac{6\bar{\rho}_{0,\text{Ca}}\overline{M}_{\text{CaO}}}{r_{\text{g,CaO}}\left(\rho_{\text{CaO}}\right)^2\left(1-\phi_{\text{CaO}}\right)^2} \tag{7.5}$$

where $\bar{\rho}_{0,\text{Ca}}$ is the initial molar density of calcium. Mass-specific surface area of CaO from Eq. (7.5) is then used in Eq. (3.15) to evaluate the volume-specific carbonation reaction specific surface area $s'''_{\text{carb}}$ instead of the measured value of $s_{\text{CaO}}$ reported in Table 3.3 which was used to evaluate carbonation kinetics in Chapter 6.

A value of $r_{\text{g,CaO}} = 1.84 \times 10^{-6}$ m results in good agreement between predicted rates of carbonation during the fast carbonation regime and the corresponding measured rates. The tuned value for $r_{\text{g,CaO}}$ results in $s_{\text{CaO}} = 2.2 \times 10^3\,\text{m}^2\,\text{kg}^{-1}$, which is a decrease from the value of $s_{\text{CaO}} = 1.9 \times 10^4\,\text{m}^2\,\text{kg}^{-1}$ used previously. The tuned value of $r_{\text{g,CaO}}$ is also an order of magnitude larger than the average grain size calculated assuming uniformly spherical grains in Section 5.2.1, $r_{\text{g,CaO}} = 4.72 \times 10^{-7}$ m. However, the tuned value for $r_{\text{g,CaO}}$ is in qualitative agreement with CaO grain sizes observed in SEM–BSE images (in

this work and in literature) and is on the same order of magnitude as values reported in literature [García-Labiano et al., 2002; Stendardo and Foscolo, 2009].

Model 3 was used to evaluated effective diffusivity in the preliminary numerical results using the original model with modified boundary conditions, shown in Fig. 7.8. However, in order to accurately model the slow carbonation regime, Model 2 is adopted to evaluate $D_{\text{eff}}$ for $CO_2$ and $N_2$.

$$D_{\text{eff},i} = \frac{\phi}{\tau}\left(D_{\text{mol}}^{-1} + D_{\text{K},i}^{-1}\right)^{-1} \tag{7.6}$$

where $i = CO_2$ and $N_2$ and $\tau$ is the tortuosity of the solid phase. The solid phase tortuosity is taken as the molar weighted combination of the tortuosities of $CaCO_3$ and CaO.

$$\tau = (1 - X_{\text{local}})\,\tau_{CaCO_3} + X_{\text{local}}\tau_{CaO} \tag{7.7}$$

Tortuosity of the pore network within the particle is related to the diffusion path. An increases in tortuosity results in an increase in the length of the diffusion path and a decrease in the rate of apparent linear diffusion. This diffusivity model is used because it introduces the medium characteristics of $\tau_{CaCO_3}$ and $\tau_{CaO}$ not included in Model 3, and the inclusion of these characteristics also results in the reduction of $D_{\text{eff}}$.

Tuning tortuosity for the sample material yields 200 and 1.8 for $\tau_{CaCO_3}$ and $\tau_{CaO}$, respectively. While tortuosity is often equated to the inverse of porosity as discussed in Section 5.3.2 and as is assumed in Model 3, tuned tortuosity values for the sorbent material do not agree with this assumption, hence, supporting the use of an alternative effective diffusivity model. The tortuosity for CaO, $\tau_{CaO} = 1.8$, is approximately equal to the inverse of the $\phi_{CaO}$ used in this work. However, the inverse of porosity for $CaCO_3$ used in this work is $\phi_{CaCO_3}^{-1} = 33$, which is an order of magnitude smaller than the tuned value, $\tau_{CaCO_3} = 200$.

Simulations using the tuned tortuosities feature transitions between the fast and slow carbonation regimes closer to those observed experimentally. Rates of carbonation during the slow regime are also closer to experimentally observed rates. No experimental data could be found for the tortuosity of CaO for comparison. However, $\tau_{CaO}$ is of a similar order of magnitude as values reported in literature for $CaCO_3$ [Laudone et al., 2015; Levy et al., 2015] and other similar materials [Cussler, 2009].

However, $\tau_{CaCO_3}$ is substantially higher than reported values by approximately two orders of magnitude [Laudone et al., 2015; Levy et al., 2015]. This higher value of $\tau_{CaCO_3}$ suggests that there may be some other mechanism inhibiting diffusion of $CO_2$ through $CaCO_3$ that is not accounted for by the model such as sintering. Sintering of CaO grains is well documented, and the amount of sintering increases with higher temperatures, longer exposure to high temperatures, higher partial pressure of $CO_2$, and larger amount of impurities [Blamey et al., 2010]. The tuned value of $\tau_{CaCO_3}$ is likely increased in order to account for additional mass transfer inhibiting phenomena such as sintering and the

loss of micropores with cycling that are not accounted for in the model.

While adjusting $\tau_{CaCO_3}$ and $\tau_{CaO}$, it was observed that the predicted transition between the fast and slow regimes and the rate of carbonation during the slow regime could be closely matched to corresponding experimental results for cases with a single $CO_2$ concentration. However, experimental results could not be matched for all cases with different $CO_2$ concentrations simultaneously. The empirical function $f_{CO_2,\text{diff}}$ is therefore included in the diffusivity model because the experimental results could not be well predicted by the numerical model for all considered $CO_2$ concentrations without a parameter varying with ambient $CO_2$ concentration. Thus, the effective diffusivity is

$$D_{\text{eff},i} = \frac{\phi \times f_{CO_2,\text{diff}}}{(1 - X_{\text{local}})\,\tau_{CaCO_3} + X_{\text{local}}\tau_{CaO}} \left(D_{\text{mol}}^{-1} + D_{\text{K},i}^{-1}\right)^{-1} \tag{7.8}$$

The following values of $f_{CO_2,\text{diff}}$ are used: 1, 0.9, and 0.1 for 25, 50, and 100% $CO_2$ atmospheres, respectively. To illustrate the effect the model adjustments have on overall reaction extent, numerical results using the adjusted model with boundary conditions modified to emulate the TGA are shown in Fig. 7.8. The adjusted model results show a marked improvement over the preliminary numerical results.

The values of $f_{CO_2,\text{diff}}$ imply a inverse dependence between ambient $CO_2$ concentration and effective diffusivity of fluid in the pore space of $CaCO_3$, but more evidence is needed to support this hypothesis. Possible physical explanations for the dependence of $D_{\text{eff},CO_2}$ on ambient $CO_2$ concentration include different micro-grain growth patterns and extent of loss of micro-grains due to sintering with different ambient $CO_2$ concentrations.

### 7.4.2 Results

In the following section, numerical results for overall reaction extent of 2.5 and 5 mm diameter particles are compared to analogous experimental results of particles from the 2.5 and 5 mm size groups, respectively. Similar trends and differences between experimental and numerical results are discussed. Time and sharpness of transitions are compared; and then the average apparent reaction rate during calcination and the fast and slow carbonation regimes are compared. Lastly, the average percent relative error (PRE) between experimental and numerical overall reaction extent for the first cycle of each case are compared.

Numerical results for 1 mm diameter particles have not been obtained due to the high computational cost of those simulations. The explicit Euler method used for time integration in the numerical model requires an increasingly smaller time step with decreasing mesh size. Simulations of 1 mm diameter particles result in very small mesh sizes. Thus, the time step required for stability is prohibitively small; simulation times have been estimated to be longer than two months, as compared to the simulations for 2.5 and 5 mm particles which took approximately three weeks to complete.

**Comparison of numerical and experimental overall reaction extent** Numerically predicted overall reaction extent for 2.5 and 5 mm diameter particles for all considered $CO_2$ concentrations are shown in Fig. 7.9, along with the corresponding measured values. The numerical results show good agreement with the experimental ones during the first cycle. Five transitions can be observed in both numerical and experimental overall reaction extent results: (1) onset of calcination, (2) conclusion of calcination, (3) onset of carbonation, (4) switch from fast to slow carbonation, and (5) switch from carbonation to calcination at the end of the cycle. All transitions are sharper in the numerical results than the experimental ones. In the calcination period, the onset and rate of calcination match well based on visual inspection for all cases considered, particularly in the first cycle. In the carbonation period, the differences between the numerical and experimental results are larger than to the differences between results in the calcination period. The differences in the carbonation period become larger with increased cycle number.

The numerically predicted instantaneous apparent reaction rates during the fast carbonation regime closely match those measured experimentally for all cases. However, the numerically predicted durations of the fast carbonation regime are longer than those measured experimentally for all cases. Of all considered cases, the numerically predicted duration of fast carbonation for a 5 mm particle in 25% $CO_2$ matches that measured experimentally the closest. The numerically predicted apparent reaction rates during the slow carbonation regime are smaller than those measured experimentally. The difference in both rates and durations between numerical and experimental results increase with increasing $CO_2$ concentration and cycle number. These differences suggest the diffusion model or the dependence of carbonation kinetics on local $CO_2$ concentration in the numerical model should be investigated further and possibly improved upon in order to predict carbonation behavior with more accuracy. Suggestions for potential improvements are given in Sections 7.5 and 8.2.

Average apparent reaction rates are calculated from numerical results for the first cycle of the six cases, using Eqs. (7.3) and (7.4) and the methodology given in Section 7.3.2. The time intervals used to calculate the average values for numerical results are defined using the same convention as those for the experimental results. However, the onset and conclusion of reactions occur at different times in numerical and experimental results. Thus, the time intervals for calculating numerical and experimental average apparent reaction rates are different.

Average apparent reaction rates from experimental and numerical results for calcination, fast carbonation, and slow carbonation are given in Table 7.5. The numerically predicted average apparent reaction rates are in good agreement with those observed experimentally. The largest disagreement between numerically and experimentally observed average apparent reaction rates is for the 2.5 mm size group particle in 100% $CO_2$ case. The best agreement between numerically and experimentally observed average apparent reaction rates is for the 2.5 and 5 mm size group particles in 25% $CO_2$ case.

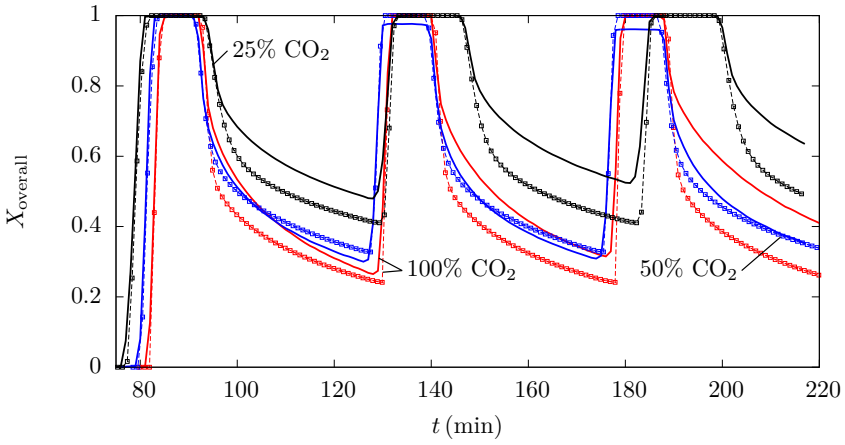


a

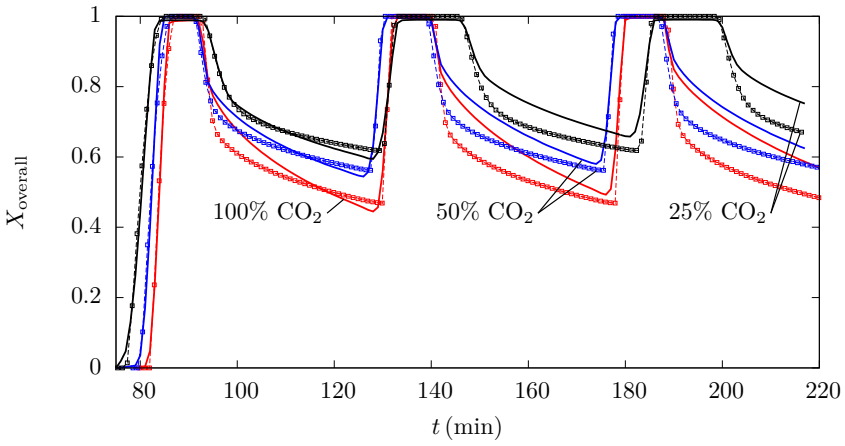


b

Figure 7.9: Numerical and experimental overall reaction extent versus time for particles from the (a) 2.5 and (b) 5 mm size groups cycled in 25 (black lines and points), 50 (blue lines and points), and 100% $CO_2$ (red lines and points) atmospheres: experimental results (solid lines) and numerical results (square points, dashed lines)

Table 7.5: Experimental and numerical average apparent reaction rates ($\text{min}^{-1}$) during calcination, fast carbonation, and slow carbonation

| Case | $\left(\frac{\mathrm{d}X_{\text{overall}}}{\mathrm{d}t}\right)_{\text{calc}}$ | $\left(\frac{\mathrm{d}X_{\text{overall}}}{\mathrm{d}t}\right)_{\text{carb,fast}}$ | $\left(\frac{\mathrm{d}X_{\text{overall}}}{\mathrm{d}t}\right)_{\text{carb,slow}}$ |
|---|---|---|---|
| Exp. 2.5 mm 25% $CO_2$ | $17.675\times10^{-2}$ | $-5.536\times10^{-2}$ | $-0.870\times10^{-2}$ |
| Num. 2.5 mm 25% $CO_2$ | $18.233\times10^{-2}$ | $-5.743\times10^{-2}$ | $-0.734\times10^{-2}$ |
| Exp. 2.5 mm 50% $CO_2$ | $25.377\times10^{-2}$ | $-9.865\times10^{-2}$ | $-1.189\times10^{-2}$ |
| Num. 2.5 mm 50% $CO_2$ | $26.383\times10^{-2}$ | $-8.776\times10^{-2}$ | $-0.818\times10^{-2}$ |
| Exp. 2.5 mm 100% $CO_2$ | $25.745\times10^{-2}$ | $-11.785\times10^{-2}$ | $-1.425\times10^{-2}$ |
| Num. 2.5 mm 100% $CO_2$ | $37.267\times10^{-2}$ | $-15.384\times10^{-2}$ | $-0.874\times10^{-2}$ |
| Exp. 5 mm 25% $CO_2$ | $12.089\times10^{-2}$ | $-3.256\times10^{-2}$ | $-0.576\times10^{-2}$ |
| Num. 5 mm 25% $CO_2$ | $12.096\times10^{-2}$ | $-3.793\times10^{-2}$ | $-0.460\times10^{-2}$ |
| Exp. 5 mm 50% $CO_2$ | $16.707\times10^{-2}$ | $-5.375\times10^{-2}$ | $-0.826\times10^{-2}$ |
| Num. 5 mm 50% $CO_2$ | $14.851\times10^{-2}$ | $-6.206\times10^{-2}$ | $-0.563\times10^{-2}$ |
| Exp. 5 mm 100% $CO_2$ | $19.213\times10^{-2}$ | $-6.643\times10^{-2}$ | $-1.042\times10^{-2}$ |
| Num. 5 mm 100% $CO_2$ | $20.339\times10^{-2}$ | $-10.173\times10^{-2}$ | $-0.630\times10^{-2}$ |

The 2.5 mm size group particle in 25% $CO_2$ exhibits the smallest percent difference between numerical and experimental average apparent reaction rates, while the 5 mm size group particle in 25% $CO_2$ exhibits the smallest total difference between numerical and experimental average apparent reaction rates.

Visualizations of numerical results of 5 mm particles for all considered $CO_2$ atmospheres are shown in Fig. 7.10. The visualizations show spatial variations in solid phase composition and porosity of partially-carbonated particles at the end of three cycles. The overall reaction extents and average porosities are $X_{\text{overall}} = 0.623$, 0.556, and 0.475 and $\phi = 0.36$, 0.33, and 0.28 for 5 mm diameter particles cycled in 25, 50, and 100% $CO_2$ atmospheres, respectively. Overall reaction extent values indicate the particles are approximately equal parts $CaCO_3$ and CaO, but these values do not relay information about the spatial distribution of $CaCO_3$ and CaO. Figure 7.10 shows that porous CaO occupies the core of all particles, while $CaCO_3$ forms a shell surrounding the CaO core. A sharp gradient separates the two regions, and the gradient between the two regions is largest in the particle cycled in 100% $CO_2$ and decreases with decreasing $CO_2$ concentration.

Visualizations in Fig. 7.10 can be compared to the SEM–BSE images of cross sections of cycled particles show in Fig. 7.7. Cross sections of experimentally cycled particles also show distinct regions of $CaCO_3$ and CaO separated by a sharp gradient. Overall reaction extent is $X_{\text{overall}} = 0.72$ and 0.36 for the 5 mm size group particles cycled in 50 and 100% $CO_2$ shown in Fig. 7.7, respectively. While the predicted and observed overall reaction extent values are not in agreement, both the predicted and observed particles display similar spatial variation trends: two distinct regions of material separated by a sharp gradient.

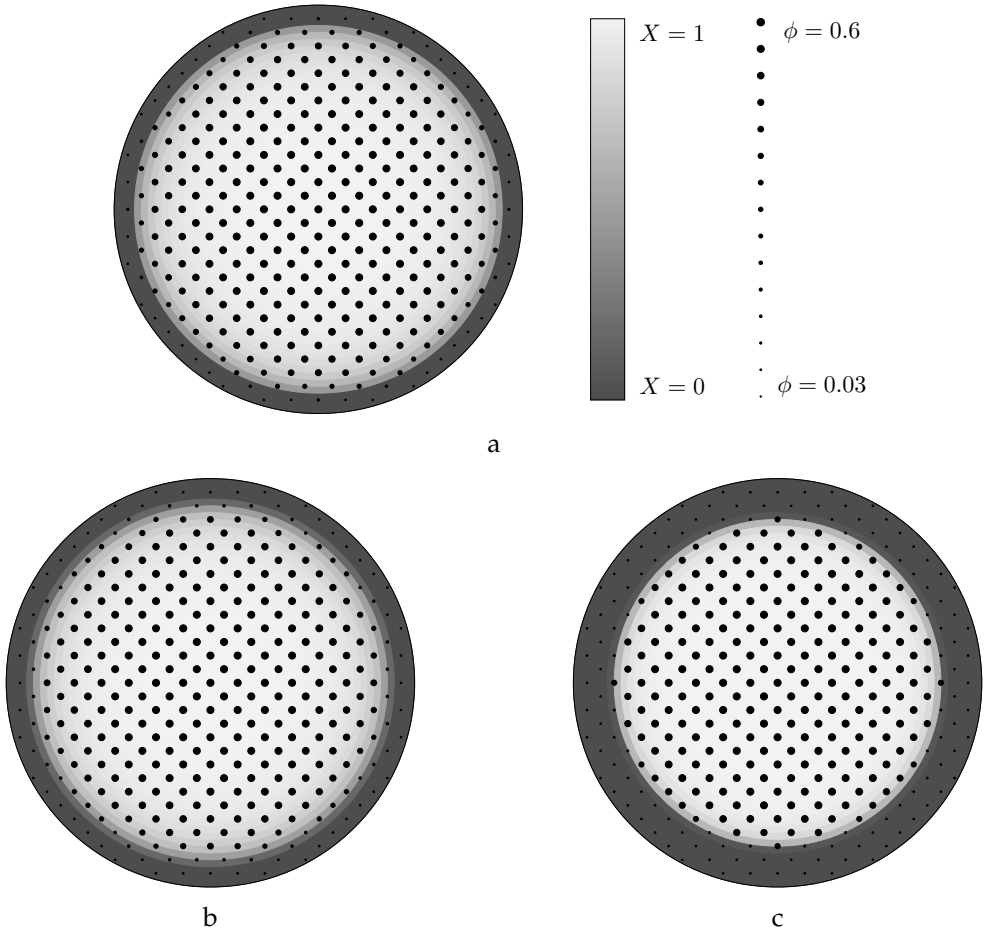


Figure 7.10: Numerically predicted spatial variation in composition and porosity for particles from the 5 mm size group after cycling in (a) 25, (b) 50, and (c) 100% $CO_2$ atmospheres: solid phase composition (color) and porosity (dot size)

The PRE between the experimental and numerical overall reaction extent $\delta$ is calculated for each time instance $i$ at a frequency of one second for the first cycle, according to the following equation

$$\delta_i = 100\% \times \left| \frac{X_{\text{overall,num},i} - X_{\text{overall,exp},i}}{X_{\text{overall,exp},i}} \right| \tag{7.9}$$

where the "num" and "exp" subscripts indicate numerical and experimental values, respectively. Instantaneous PRE values are then averaged over time intervals according to

$$\bar{\delta} = \frac{\sum_{i=t_{\text{start}}}^{t_{\text{end}}} \delta_i}{t_{\text{end}} - t_{\text{start}}} \tag{7.10}$$

where $\bar{\delta}$ is the average PRE. Four averaging time intervals are defined: calcination, fast carbonation, slow carbonation, and the entire first cycle. Average PRE during calcination,

fast carbonation, and slow carbonation are calculated using time intervals that combine those used to calculate the average apparent reaction rates for experimental and numerical results. The longest possible time interval is used for calculating the average PRE using the minimum lower and maximum upper average apparent reaction rate time interval bounds.

Average PRE for all considered numerical cases and time intervals is given in Table 7.6. Comparing average PRE during the different reaction regimes, average PRE during fast carbonation is the smallest, followed by the average PRE during the slow carbonation, while average PRE during calcination is the largest. Average PRE for the calcination is larger than that for either other periods even though visual inspection of transient curves in Fig. 7.9 suggests results show good agreement.

Table 7.6: Average percent relative error between experimental and numerical overall reaction extent for the entire first cycle and during calcination, fast carbonation, and slow carbonation

| Case | $\bar{\delta}_1$ (%) | $\bar{\delta}_{\text{calc}}$ (%) | $\bar{\delta}_{\text{carb,fast}}$ (%) | $\bar{\delta}_{\text{carb,slow}}$ (%) |
|---|---|---|---|---|
| 2.5 mm 25% $CO_2$ | 12.35 | 44.51 | 1.70 | 12.98 |
| 2.5 mm 50% $CO_2$ | 6.45 | 35.58 | 1.83 | 5.04 |
| 2.5 mm 100% $CO_2$ | 13.36 | 44.74 | 7.81 | 13.75 |
| 5 mm 25% $CO_2$ | 4.97 | 28.85 | 0.50 | 1.58 |
| 5 mm 50% $CO_2$ | 5.60 | 24.68 | 2.90 | 2.91 |
| 5 mm 100% $CO_2$ | 7.42 | 28.24 | 3.09 | 5.08 |

Two factors contribute to larger average PRE during calcination: the range of values being compared and the magnitude of apparent reaction rate. The range of values being compared during calcination is larger than that in other time intervals. $X_{\text{overall}}$ during calcination ranges from 0 to 1, whereas $X_{\text{overall}}$ during fast and slow carbonation spans only a fraction of that range, around 30%. Calcination apparent reaction rates are also larger than those during carbonation. Fast apparent reaction rates over the full range of overall reaction extents result in larger relative errors between experimental and numerical results during calcination compared to carbonation, even though numerical and experimental calcination results visually appears to agree as well as or better than those during carbonation.

The lowest average PRE for the entire first cycle is for the 5 mm 25% $CO_2$ case with $\bar{\delta} = 4.97\%$, followed closely by the 5 mm 50% $CO_2$ case with $\bar{\delta}_1 = 5.60\%$. Although the 2.5 mm 50% $CO_2$ case has $\bar{\delta}_1$ in the range of those for the 5 mm cases, the average PREs for all 5 mm cases are generally lower than those for all 2.5 mm cases.

**Discussion of differences between numerical and experimental results** Experimental particles have the potential to react non-uniformly, resulting in differences between numerical and experimental results as discussed in Section 7.3.2. The numerical model assumes homogeneous initial composition of the particle and uniform ambient conditions

around the particle. However, the experimental sorbent particles are made by extrusion and have the potential to feature some non-uniformity in the orientation of grains due to the manufacturing method. Particles in the TGA–DSC also rest in a crucible, and conditions have the potential to vary across the particle surface. If conditions varied substantially, the assumptions of uniform ambient conditions would be invalid. These conditions could account for some of the differences between numerical and experimental results, however the particles react relatively uniformly in the radial direction as observed by particle cross sections in Fig. 7.7, so it is assumed that differences due to non-uniformity of reaction in experimental particles are small enough to be neglected.

Size difference between numerically and experimentally investigated particles has the potential to contribute to differences between numerical and experimental results. Shape uniformity was prioritized over particle size when selecting particles for thermochemical cycling. Therefore, the size of experimentally investigated particles is possibly different from those investigated numerically. This size difference then has the potential to contribute to differences between numerical and experimental overall reaction extent results. However, in the data sets used to investigate repeatability, variability in the initial mass of particles from a single size group has been shown to have a small effect on percent weight change during thermochemical cycling. This will be explained further in the following paragraph. Based on the small effect of the variability of initial mass, numerical results for 2.5 and 5 mm diameter particles are hypothesized to well-represent most particles from their equivalent experimental size groups.

The data sets used to investigate repeatability, as discussed in Section 7.3.2, are used here to support the hypothesis that numerical results for 2.5 and 5 mm diameter particles well-represent most particles from their equivalent experimental size groups. Three data sets exist for the first calcination–carbonation cycle of particles from the 5 mm size group in 100% $CO_2$. The transient percent weight change results ($m/m_0$) from the data set for the particle with the largest initial mass ($m_0 = 81.8$ mg) and that for the particle with the smallest initial mass ($m_0 = 52.1$ mg) are compared. The average and maximum differences between the two sets are 0.5 and 4.2%. These small differences indicate transient percent weight change results for the two data sets are very similar. If percent weight change is similar, overall reaction extent will also be similar, because percent weight change offset by the amount of impurities is directly related to overall reaction extent as shown in Eq. (7.2). Thus, initial mass in the range considered for repeatability does not substantially affect percent weight change results. Based on that conclusion, it is assumed the variability of overall reaction extent results with size of particle from a single size group is sufficiently small that representative numerical results accurately represent their equivalent size group. However, future work should include additional numerical results to further interrogate the validity of this assumption.

The loss of reactivity with cycling observed in experimental results is not observed in numerical ones. The loss of reactivity is most predominant in the shortening of the

fast carbonation regime with increasing cycle number. The well-documented irreversible morphological changes that occur in the particles due to cycling, such as sintering, as discussed in Section 2.2 are not accounted for in the numerical model. This is an acknowledged shortcoming of the presented numerical model, and suggestions for improvements to the model to account for sintering are given in Section 8.2.

## 7.5 Summary

The effect of particle size and ambient $CO_2$ concentration on overall reaction extent in large particles was investigated. In the experimental part of the study, material characterization prior to thermochemical cycling identified the sorbent material as predominantly $CaCO_3$ and confirmed the $CaCO_3$ in the obtained sorbent material can be decomposed to CaO under the expected experimental conditions. Particles of three different sizes were then thermochemically cycled in a TGA–DSC in three different $CO_2$ atmospheres.

In the numerical part of the study, the numerical model of thermal transport phenomena was used to adjust selected medium characteristics. The selected parameters of carbonation reaction specific surface area and the tortuosities of $CaCO_3$ and CaO were adjusted, resulting in agreement between numerical and experimental transient overall reaction extent for the first cycle. In the cases considered in Section 7.4, morphology-related adjustments to the carbonation reaction specific surface area and the diffusivity model resulted in changes in overall reaction extent of up to 20% in order to achieve agreement. Morphology-related adjustments to the model illustrate the influence material properties and morphology can have on thermal transport phenomena in porous reacting systems, and this motivates further research on the interaction between morphology, apparent material properties, and thermal transport phenomena in porous reacting systems.

Experimental and numerical results showed both particle size and ambient $CO_2$ concentration affect average apparent reaction rates and the value of overall reaction extent when transitioning between fast and slow carbonation in particles from the 2.5 and 5 mm size groups. The effect of particle size and $CO_2$ concentration on overall reaction extent was most pronounced during the carbonation period. During the calcination period, the TGA–DSC was able to supply heat to all particle sizes at a sufficient rate to drive rapid calcination. During the carbonation period, the reaction was initially chemical kinetics limited and then switched to a mass diffusion limited regime. This slower, diffusion limited regime corresponds to a region of diminishing returns when this reaction cycle is used in an application.

The numerical model well predicted temperature dependent kinetics, illustrated by the onset of reactions and partially by the rates of calcination and carbonation. One quantity not consistently predicted with accuracy was the overall reaction extent at the end of one thermochemical cycle. For the model to be used specifically to estimate overall reaction extent at the end of one cycle (equivalent to the maximum material utilization),

further modifications to the model are recommended, including parameter tuning for specific $CO_2$ concentrations of interest to yield accurate overall reaction extents at the end of one cycle.

The carbonation extent of larger particles and particles in lower $CO_2$ concentration atmospheres was lower than smaller particles and particles in higher $CO_2$ concentration atmospheres. This implies the smallest particles and highest $CO_2$ concentrations are ideal in order to utilize the reacting material to the highest extent. However, results shown in Chapter 6 identified a trade off between sorbent utilization and energetic efficiency. Small particles and high $CO_2$ concentrations may not be desired if the increase in sorbent utilization comes at an unacceptably high penalty in energetic efficiency. For thermochemical TES, the highest purity $CO_2$ possible should be used for both calcination and carbonation to maximize material utilization and thus, energy storage capacity of the material. For $CO_2$ capture on the other hand, most common $CO_2$ point sources, such as flue gas contain up to 15% $CO_2$. Thus, carbonation under lower $CO_2$ concentrations is still important to consider.

Chapter 8

# Conclusions and outlook

Solar thermochemical processes featuring particulate media are an attractive and emerging field of study. The research presented in this work aimed to advance the field of solar thermochemistry by advancing understanding of the transient and coupled nature of chemistry, heat transfer, and mass transfer occurring in particles undergoing CaO looping. Intra-particle phenomena determine macroscopic reaction rates and chemical transformations in particles, which in turn determine conversion and efficiency in reactors and processes. Understanding transient thermal transport phenomena at the intra-particle level and thermal transport response to high-intensity solar irradiation can be used to improve the efficiency of solar thermochemical process technology, thereby increasing commercial viability and bringing the technology closer to industrial scale implementation.

In summary, the work presented in this thesis included a review of chemical kinetics and the development of a reaction rate expression describing the two reactions of CaO looping in Chapter 3. A numerical model and modeling methods linking chemical kinetics to intra-particle heat and mass transfer were presented in Chapters 4 and 5. The developed model was then used in two application investigations. In the first investigation presented in Chapter 6, directly irradiated particles were configured for $CO_2$ capture. Cycle time, magnitude of irradiation, particle size, and ambient gas temperature were varied, and evaluation metrics were used to compare the effect of varying each parameter. In the second investigation presented in Chapter 7, furnace heated particles were configured for $CO_2$ capture and thermochemical TES. Experimental results were obtained by thermochemically cycling single sorbent particles of varying sizes in a furnace in different $CO_2$ atmospheres. Adjustments to the numerical model produced numerical results in agreement with experimental data for the first thermochemical cycle.

## 8.1 Conclusions

Major conclusions from this work are (1) an intra-particle thermal transport model describing both calcination and carbonation provides information that models for only one reaction do not; (2) the detail and fidelity of an intra-particle thermal transport

model determine the accuracy of numerical results in particles undergoing CaO looping, particularly with regard to diffusive mass transfer; and (3) trade offs exist between sorbent utilization and energetic efficiency for some operational and system parameters relevant to particles undergoing CaO looping.

In this work, the utility of and requirements for an advanced numerical model of thermal transport phenomena describing both calcination and carbonation were shown. Two occurrences were observed in numerical results using the developed model that would not be seen in models for only one reaction. In Section 6.3, carbonation at the start of the calcination period was observed in the full-calcination case. In Section 6.4, overall reaction extent behavior during the second and third cycles was observed in five cases where full calcination and periodicity were not achieved in the first cycle ($q'' = 200\,\mathrm{kW\,m^{-2}}$; $r_\mathrm{p} = 1.5$, 3.25, and 5 mm; and $T_\infty = 700\,\mathrm{K}$). Carbonation during the calcination period and overall reaction extent behavior when full calcination is not achieved in the first cycle would not be discernible in results using numerical models for only calcination or carbonation. These cycling results are crucial to single-reactor configuration reactor development.

For a single intra-particle thermal transport model to describe both reactions, the following elements are required: (1) a chemistry closure model that describes the direction of the reversible reaction system and magnitude of the reaction rate, (2) the inclusion of pertinent heat and mass transfer phenomena, and (3) novel time-periodic boundary conditions. All of these elements have been implemented in this work. The chemistry closure model for the reaction rate term in the governing equations must accurately capture the rate of both reactions. In studies of reacting in particles in Chapters 6 and 7 and in literature, reacting particles have exhibited solid phase composition gradients. The gradients influence rates of intra-particle heat and mass transfer, which in turn determine the apparent reaction rate of the particle. In this work, the volumetric reaction model was applied to discrete volume elements within the particle, enabling the resolution of intra-particle composition gradients. The developed reaction rate expression is compatible with the volumetric reaction model and describes reversible chemical kinetics. The expression is dependent on local temperature and $CO_2$ concentration, motivating resolution of those gradients within the particle as well. This closure model and reaction rate expression were necessary to accurately simulate both reactions in a particle using a single numerical model, as demonstrated by the reconciliation of experimental and numerical results in Chapter 7.

Using a single numerical model to describe both calcination and carbonation also required novel and dynamic boundary conditions, distinct from those used in literature for single reaction models. In single reaction models, constant boundary conditions were typically sufficient to drive the chemical reaction. However, in this work, boundary conditions that change with time were developed in Chapter 4 and implemented in Chapters 6 and 7 to drive both reactions in turn. The conditions approximately emulate a

reactor environment, and they are periodic, so multiple cycles can be simulated as shown in Chapters 6 and 7. These time-periodic conditions were necessary for the model to capture cyclic thermochemical transformations in a particle.

In reacting particles, calcination is generally a heat transfer limited reaction, while carbonation is generally a mass transfer limited one. Therefore, both heat and mass transfer phenomena are important for studying the range of particle sizes considered in this work, and both phenomena need to be accurately modeled to produce meaningful results. The model presented in this work includes physical phenomena often disregarded in other studies in literature, such as advective mass transfer and radiative heat transfer. Agreement between intra-particle radiative heat transfer modeling methods in Section 5.2 and numerical and experimental results during calcination in Section 7.4 supports the accuracy of heat transfer aspects of the numerical model.

Two findings indicate model accuracy is sensitive to fluid diffusion: (1) the range of effective diffusivities predicted by different models in Section 5.3 spans several orders of magnitude and (2) adjustments to diffusive mass transfer aspects of the model were required for agreement between numerical and experimental results during slow carbonation in Section 7.4. Investigation into binary molecular and Knudsen diffusion phenomena in Section 5.3 showed that, when combined as parallel resistances, Knudsen diffusivity is the dominant factor over binary molecular diffusivity in determining effective diffusivity. In literature, if diffusion is considered, binary molecular diffusivity or combined binary molecular and Knudsen diffusivities are typically considered. However, this work showed that if computational resources do not allow the inclusion of both modes of diffusion, then Knudsen diffusion should be included rather than binary molecular.

Adjustments to the diffusion closure model and related material properties produced numerical results reconciled with those obtained experimentally in Section 7.4. To the best of the author's knowledge, this is the first time a numerical model of thermal transport phenomena with such high fidelity has been reconciled with experiments involving individual reacting particles. However, the modifications to the diffusion closure model indicate more research investigating diffusion phenomena in porous sorbent particles for CaO looping is warranted. Internal particle morphology and properties were shown in this work to significantly influence thermal transport phenomena in the porous reacting system, illustrating the importance of research focused on the relationship between morphology and thermal transport phenomena in heterogeneous reacting systems.

Investigations in Chapter 6 revealed trade offs between sorbent utilization and energetic efficiency for certain investigated parameter ranges. A trade off between the two metrics was most apparent for the range of particle sizes considered in this work, as show in the metric plots in Fig. 6.10. Appropriate evaluation metrics are needed to fully assess and describe the relative influence of parameters on thermochemical transformations and other aspects of particles undergoing CaO looping. The trade offs identified in this work

show the importance of using multiple evaluation metrics and defining those metrics deliberately.

Knowledge of the relative magnitude of evaluation metric trade offs for controllable parameters can be extrapolated for use in aiding system and component design at the next length scale. The next larger length scale for reacting particles is groups of reacting particles in a reactor or a reacting medium. This length scale introduces practical considerations and constraints that may prioritize one evaluation metric or design concern over other factors. Evaluation metrics can be extrapolated and used to aid in addressing reacting medium level design concerns and priorities.

Larger particles and particles in lower $CO_2$ concentrations carbonate less than smaller particles and particles in higher $CO_2$ concentrations, respectively. This implies the smallest particles and highest $CO_2$ concentrations are ideal to maximum sorbent utilization, because under those conditions, the reacting material is utilized to the furthest extent. However, practical constraints and particle strength against attrition are more likely to determine the lower limit on particles size. For thermochemical TES, the highest purity $CO_2$ possible should be used for both calcination and carbonation to maximize material utilization and thus, energy storage capacity of the material. For $CO_2$ capture on the other hand, most common point sources, such as flue gas, are only maximally 15% $CO_2$, so carbonation under lower concentrations is still important to consider.

Results presented in this work have been used to guide the selection of operational parameters of a laboratory solar thermochemical reactor. A 1 $kW_{th}$ solar-driven packed bed thermochemical reactor prototype has been designed and built in the Research School of Engineering at the Australian National University [Reich et al., 2015, 2017]. The reactor features a packed bed of spherical sorbent particles, contained in an annular reaction zone surrounding a solar cavity receiver. The reactor was designed to investigate solar CaO looping for $CO_2$ capture and is appropriate for investigating other promising reaction systems for $CO_2$ capture and other applications. Numerical model results presented in Chapters 6 and 7 have been used to recommend an 800 K target temperature of the sweep gas through the packed bed and 5 mm diameter particles for initial reactor testing. Numerical model results from this work will contribute to the selection of additional operational parameters as reactor commissioning and testing proceeds.

Studying intra-particle thermal transport phenomena in reacting particles provides useful information that can be extrapolated to the reactor level and used for making reactor design and operation decisions. However, practical consequences exist when studying only single reacting particles, due to the limitations of accurately extrapolating particle level studies to the reactor level. Particle–particle interactions, reactor wall effects, non-uniform heat and mass transfer within particle-based reacting media, and non-uniform conversion of particles are some phenomena that are important to consider when developing reactors, and analysis of single particles does not provide information about such phenomena. Non-uniformity of temperature and fluid phase concentration across

the reacting medium is particularly pronounced in packed bed reactors. While analysis of thermal transport phenomena at the intra-particle level constitutes an important component, multi-scale hierarchical studies are important for optimizing particle–gas reacting systems encountered in solar thermochemical processes.

## 8.2 Outlook

Areas of opportunity in the fields of thermochemical looping and solar thermochemistry related to the work presented here include (1) improvements to the numerical model, (2) extension of the model to other thermochemical looping systems, and (3) guiding reactor design and operation.

The most significant shortcoming of the numerical model developed in this work is the model's inability to predict loss of reactivity with cycling. Future work could include the addition of sintering and/or other mechanisms that result in loss of reactivity with cycling to the model. As the rate and extent of sintering are related to temperature and exposure duration [Blamey et al., 2010], sintering models could decrease maximum reaction specific surface area by a factor proportional to both local temperatures above the sintering threshold and the duration of exposure.

The model could also be expanded to 3D in order to include non-uniform conditions at the particle surface. Non-uniformity of conditions around reacting particles is expected to be more significant in packed bed reactors compared to fluidized bed reactors. Knowledge of the effect of uniform and non-uniform conditions on intra-particle thermal transport phenomena and evaluation metrics would aid in the choice between packed bed and fluidized bed reactor designs.

The experimental and numerical methods of the investigation presented in Chapter 7 for examining intra-particle and system characteristics and connecting those characteristics to apparent reaction rates of reacting particles are suitable for application to other reacting particulate systems, such as hercynite ($(FeAl)_2O_4$) reduction/oxidation cycling being investigated for solar $H_2$ production via water splitting [Muhich et al., 2016] or strontium carbonate ($SrCO_3$)/strontium oxide (SrO) calcination/carbonation cycling being investigated for high-temperature TES [Bagherisereshki et al., 2018].

The presented model could be used as a tool for guiding particle-based reactor design and operation. Solar reactor realization avenues include designing reactors specifically to receive and utilize concentrated solar energy or integrating high-temperature solar energy into existing conventional CaO looping pilot scale demonstrations. The flexibility of the boundary conditions for the model presented in this work makes this model applicable to both avenues and heating modes.

# References


Abanades, J. and Alvarez, D., 2003. Conversion limits in the reaction of $CO_2$ with lime. *Energy and Fuels*, 17, 2 (2003), 308–315. doi:10.1021/ef020152a. (cited on page 12)

Acharya, B.; Dutta, A.; and Basu, P., 2012. Circulating-fluidized-bed-based calcium-looping gasifier: Experimental studies on the calcination–carbonation cycle. *Industrial and Engineering Chemistry Research*, 51, 25 (2012), 8652–8660. doi:10.1021/ie300629a. (cited on page 27)

Ahn, Y.; Bae, S.; Kim, M.; Cho, S.; Baik, S.; Lee, J.; and Cha, J., 2015. Review of supercritical $CO_2$ power cycle technology and current status of research development. *Nuclear Engineering and Technology*, 47, 6 (2015), 647–661. doi:10.1016/j.net.2015.06.009. (cited on page 5)

Alvani, C.; Bellusci, M.; La Barbera, A.; Padella, F.; Pentimalli, M.; Seralessandri, L.; and Varsano, F., 2009. Reactive pellets for improved solar hydrogen production based on sodium manganese ferrite thermochemical cycle. *Journal of Solar Energy Engineering*, 131, 3 (2009), 031015-1–5. doi:10.1115/1.3142723. (cited on page 18)

Alvarez, D. and Abanades, J., 2005. Determination of the critical product layer thickness in the reaction of CaO with $CO_2$. *Industrial and Engineering Chemistry Research*, 44, 15 (2005), 5608–5615. doi:10.1021/ie050305s. (cited on page 103)

Anthony, E. and Granatstein, D., 2001. Sulfation phenomena in fluidized bed combustion systems. *Progress in Energy and Combustion Science*, 27, 2 (2001), 215–236. doi:10.1016/s0360-1285(00)00021-6. (cited on page 13)

Australian Solar Thermal Research Initiative, 2015. *ASTRI Annual Report*. Technical report. Retrieved from http://www.astri.org.au/wp-content/uploads/2014/11/ASTRI_Annual_Report_2015-v5-20160428.pdf. (cited on page 18)

Bader, R. and Lipiński, W., 2016. *Solar Thermochemical Processes*, chap. 9, 345–394. World Scientific, Hackensack, New Jersey. doi:10.1142/9789814689502_0009. (cited on pages 3 and 10)

Bagherisereshki, E.; Tran, J.; Lei, F.; and AuYeung, N., 2018. Investigation into SrO/$SrCO_3$ for high temperature thermochemical energy storage. *Solar Energy*, 160 (2018), 85–93. doi:10.1016/j.solener.2017.11.073. (cited on page 125)

Barin, I., 1995. *Thermochemical Data of Pure Substances*. Wiley-VCH Verlag GmbH, Weinheim, Germany, 3rd edn. doi:10.1002/9783527619825. (cited on page 24)

Bergman, T.; Lavine, A.; Incropera, F.; and Dewitt, D., 2011. *Fundamentals of Heat and Mass Transfer*. John Wiley and Sons, Inc., Hoboken, New Jersey USA, 7th edn. ISBN 9780470917855. (cited on page 39)

Bhatia, S. and Perlmutter, D., 1983. Effect of the product layer on the kinetics of the $CO_2$–lime reaction. *AIChE Journal*, 29, 1 (1983), 79–86. doi:10.1002/aic.690290111. (cited on pages 12, 30, and 31)

Biasin, A.; Segre, C.; Salviulo, G.; Zorzi, F.; and Strumendo, M., 2015. Investigation of CaO–$CO_2$ reaction kinetics by in-situ XRD using synchrotron radiation. *Chemical Engineering Science*, 127 (2015), 13–24. doi:10.1016/j.ces.2014.12.058. (cited on page 26)

Binnewies, M. and Milke, E., 2002. *Thermochemical Data of Elements and Compounds*. Wiley-VCH Verlag GmbH, Weinheim, Germany, 2nd edn. doi:10.1002/9783527618347. (cited on page 39)

Blamey, J.; Anthony, E.; Wang, J.; and Fennell, P., 2010. The calcium looping cycle for large-scale $CO_2$ capture. *Progress in Energy and Combustion Science*, 36, 2 (2010), 260–279. doi:10.1016/j.pecs.2009.10.001. (cited on pages 12, 111, and 125)

Blamey, J.; Zhao, M.; Manovic, V.; Anthony, E.; Dugwell, D.; and Fennell, P., 2016. A shrinking core model for steam hydration of CaO-based sorbents cycled for $CO_2$ capture. *Chemical Engineering Journal*, 291 (2016), 298–305. doi:10.1016/j.cej.2016.01.086. (cited on page 66)

Bohren, C. and Huffman, D., 2004. *Absorption and Scattering of Light by Small Particles*. Wiley-VCH Verlag GmbH, Weinheim, Germany. doi:10.1002/9783527618156. (cited on page 50)

Borgwardt, R., 1985. Calcination kinetics and surface area of dispersed limestone particles. *AIChE Journal*, 31, 1 (1985), 103–111. doi:10.1002/aic.690310112. (cited on page 27)

Brewster, M. and Kunitomo, T., 1984. The optical constants of coal, char, and limestone. *Journal of Heat Transfer*, 106, 4 (1984), 678–683. doi:10.1115/1.3246738. (cited on page 52)

Burgaleta, J.; Arias, S.; and Ramirez, D., 2011. Gemasolar, the first tower thermosolar commercial plant with molten salt storage. *Proceedings of the SolarPACES 2011 Conference*, Granada, Spain, September 20–23 (2011). (cited on page 5)

Chacartegui, R.; Alovisio, A.; Ortiz, C.; Valverde, J.; Verda, V.; and Becerra, J., 2016. Thermochemical energy storage of concentrated solar power by integration of the calcium looping process and a $CO_2$ power cycle. *Applied Energy*, 173 (2016), 589–605. doi:10.1016/j.apenergy.2016.04.053. (cited on page 16)

Chang, M.; Huang, C.; Liu, W.; Chen, W.; Cheng, J.; Chen, W.; Wen, T.; Ouyang, S.; Shen, C.; and Hsu, H., 2013. Design and experimental investigation of the calcium looping process for 3-$kW_{th}$ and 1.9-$MW_{th}$ facilities. *Chemical Engineering and Technology*, 36, 9 (2013), 1525–1532. doi:10.1002/ceat.201300081. (cited on page 15)

Chen, H. and Khalili, N., 2017. Fly-ash-modified calcium-based sorbents tailored to $CO_2$ capture. *Industrial and Engineering Chemistry Research*, 56, 7 (2017), 1888–1894. doi:10.1021/acs.iecr.6b04234. (cited on page 13)

Chueh, W. and Haile, S., 2009. Ceria as a thermochemical reaction medium for selectively generating syngas or methane from $H_2O$ and $CO_2$. *ChemSusChem*, 2, 8 (2009), 735–739. doi:10.1002/cssc.200900138. (cited on page 18)

Cottrell, A., 1997. *An Introduction to Metallurgy*. CRC Press, Taylor and Francis Group, Boca Raton, Florida USA, 2nd edn. ISBN 9780901716934. (cited on page 2)

Criado, Y.; Alonso, M.; and Abanades, J., 2014. Kinetics of the CaO/Ca(OH)$_2$ hydration/dehydration reaction for thermochemical energy storage applications. *Industrial and Engineering Chemistry Research*, 53, 32 (2014), 12594–12601. doi:10.1021/ie404246p. (cited on page 19)

Cussler, E., 2009. *Diffusion: Mass transfer in fluid systems*. Cambridge University Press, Cambridge, United Kingdom, 3rd edn. doi:10.1017/cbo9780511805134. (cited on pages 66, 67, and 111)

Dahl, J.; Weimer, A.; Lewandowski, A.; Bingham, C.; Bruetsch, F.; and Steinfeld, A., 2004. Dry reforming of methane using a solar-thermal aerosol flow reactor. *Industrial and Engineering Chemistry Research*, 43, 18 (2004), 5489–5495. doi:10.1021/ie030307h. (cited on page 18)

Dennis, J. and Hayhurst, A., 1987. The effect of $CO_2$ on kinetics and extent of calcination of limestone and dolomite particles in fluidised beds. *Chemical Engineering Science*, 42, 10 (1987), 2361–2372. doi:10.1016/0009-2509(87)80110-0. (cited on page 27)

Diego, M.; Arias, B.; Grasa, G.; Abanades, J.; Díaz, L.; Lorenzo, M.; and Sánchez-Biezma, A., 2014. Calcium looping with enhanced sorbent performance: Experiemental testing in a large pilot plant. *Energy Procedia*, 63 (2014), 2060–2069. doi:10.1016/j.egypro.2014.11.222. (cited on page 15)

Dombrovsky, L., 2012. The use of transport approximation and diffusion-based models in radiative transfer calculations. *Computational Thermal Sciences*, 4, 4 (2012), 297–315. doi:10.1615/computthermalscien.2012005050. (cited on page 50)

Dombrovsky, L. and Lipiński, W., 2007. Transient temperature and thermal stress profiles in semi-transparent particles under high-flux irradiation. *International Journal of Heat and Mass Transfer*, 50, 11–12 (2007), 2117–2123. doi:10.1016/j.ijheatmasstransfer.2006.11.008. (cited on pages 20, 49, and 52)

Duffie, J. and Beckman, W., 2013. *Solar Engineering of Thermal Processes*. John Wiley and Sons, Inc., Hoboken, New Jersey USA, 4th edn. ISBN 9780470873663. (cited on page 17)

Dunstan, M.; Jain, A.; Liu, W.; Ong, S.; Liu, T.; Lee, J.; Persson, K.; Scott, S.; Dennis, J.; and Grey, C., 2016. Large scale computational screening and experimental discovery of novel materials for high temperature $CO_2$ capture. *Energy and Environmental Science*, 9, 4 (2016), 1346–1360. doi:10.1039/c5ee03253a. (cited on page 11)

Dutcher, B.; Fan, M.; and Russell, A., 2015. Amine-based $CO_2$ capture technology development from the beginning of 2013—A review. *ACS Applied Materials and Interfaces*, 7, 4 (2015), 2137–2148. doi:10.1021/am507465f. (cited on page 4)

Ebner, P. and Lipiński, W., 2011. Heterogeneous thermochemical decomposition of a semi-transparent particle under direct irradiation. *Chemical Engineering Science*, 66, 12 (2011), 2677–2689. doi:10.1016/j.ces.2011.03.028. (cited on pages 20, 36, 39, 46, 49, and 52)

Ebner, P. and Lipiński, W., 2012. Heterogeneous thermochemical decomposition of a semi-transparent particle under high-flux irradiation—Changing grain size versus shrinking core models. *Numerical Heat Transfer, Part A: Applications*, 62, 5 (2012), 412–431. doi:10.1080/10407782.2012.703466. (cited on pages 20 and 49)

Ebner, P. and Lipiński, W., 2014. Heterogeneous thermochemical decomposition of a semi-transparent particle under high-flux irradiation: Uniform versus non-uniform irradiation. *Heat and Mass Transfer*, 50, 7 (2014), 1031–1036. doi:10.1007/s00231-014-1311-7. (cited on page 20)

Eckaus, R.; Jacoby, H.; Ellerman, A.; Leung, W.; and Yang, Z., 1996. *Economic Assessment of $CO_2$ Capture and Disposal*, Joint Program Report Series Report 15. Technical report, MIT Joint Program on the Science and Policy of Global Change. Retrieved from http://globalchange.mit.edu/publication/13893. (cited on pages 5 and 12)

Emad, S.; Hegazi, A.; El-Eman, S.; and Okasha, F., 2017. Dynamic model of calcium looping carbonator using alternating bubbling beds with gas switching. *Fuel*, 208 (2017), 522–534. doi:10.1016/j.fuel.2017.07.049. (cited on page 15)

Ervin, G., 1977. Solar heat storage using chemical reactions. *Journal of Solid State Chemistry*, 22, 1 (1977), 51–61. doi:10.1016/0022-4596(77)90188-8. (cited on page 6)

Fagerlund, J.; Highfield, J.; and Zevenhoven, R., 2012. Kinetics studies on wet and dry gas–solid carbonation of MgO and $Mg(OH)_2$ for $CO_2$ sequestration. *RSC Advances*, 2, 27 (2012), 10380–10393. doi:10.1039/c2ra21428h. (cited on page 99)

Fan, L., 2010. *Chemical Looping Systems for Fossil Energy Conversions*. AIChE–John Wiley and Sons, Inc, Hoboken, New Jersey USA. doi:10.1002/9780470872888. (cited on pages 2 and 3)

Fan, L.; Zeng, L.; and Luo, S., 2015. Chemical-looping technology platform. *AIChE Journal*, 61, 1 (2015), 2–22. doi:10.1002/aic.14695. (cited on pages 1, 2, 3, 9, 10, 11, and 13)

Fang, F.; Li, Z.; and Cai, N., 2009. Experiment and modeling of $CO_2$ capture from flue gases at high temperature in a fluidized bed reactor with Ca-based sorbents. *Energy and Fuels*, 23, 1 (2009), 207–216. doi:10.1021/ef800474n. (cited on pages 30 and 31)

Fennell, P. and Anthony, B., 2015. *Calcium and Chemical Looping Technology for Power Generation and Carbon Dioxide ($CO_2$) Capture*. Woodhead Publishing, Cambridge, United Kingdom. ISBN 9780857092434. (cited on pages 11 and 15)

Fresno, F.; Yoshida, T.; Gokon, N.; Fernández-Saavedra, R.; and Kodama, T., 2010. Comparative study of the activity of nickel ferrites for solar hydrogen production by two-step thermochemical cycles. *International Journal of Hydrogen Energy*, 35, 16 (2010), 8503–8510. doi:10.1016/j.ijhydene.2010.05.032. (cited on page 18)

Fuller, E.; Schettler, P.; and Giddings, J., 1966. A new method for prediction of binary gas-phase diffusion coefficients. *Industrial and Engineering Chemistry*, 58, 5 (1966), 18–27. doi:10.1021/ie50677a007. (cited on pages 64 and 108)

Gallagher, P. and Johnson Jr., D., 1973. The effect of sample size and heating rate on the kinetics of the thermal decomposition of $CaCO_3$. *Thermochimica Acta*, 6, 1 (1973), 67–83. doi:10.1016/0040-6031(73)80007-3. (cited on page 27)

Gálvez, M.; Frei, A.; Halmann, M.; and Steinfeld, A., 2007. Ammonia production via a two-step $Al_2O_3$/AlN thermochemical cycle. 2. Kinetic analysis. *Industrial and Engineering Chemistry Research*, 46, 7 (2007), 2047–2053. doi:10.1021/ie061551m. (cited on page 18)

García-Labiano, F.; Abad, A.; de Diego, L.; Gayán, P.; and Adánez, J., 2002. Calcination of calcium-based sorbents at pressure in a broad range of $CO_2$ concentrations. *Chemical Engineering Science*, 57, 13 (2002), 2381–2393. doi:10.1016/s0009-2509(02)00137-9. (cited on pages 14, 27, 28, 29, 30, 31, 66, 91, and 111)

García-Labiano, F.; de Diego, L.; Adánez, J.; Abad, A.; and Gayán, P., 2005. Temperature variations in the oxygen carrier particles during their reduction and oxidation in a chemical-looping combustion system. *Chemical Engineering Science*, 60, 3 (2005), 851–862. doi:10.1016/j.ces.2004.09.049. (cited on pages 10 and 14)

Geankoplis, C., 2003. *Transport Processes and Separation Process Principles*. Pearson Prentice Hall, Upper Saddle River, New Jersey USA, 4th edn. ISBN 9780131018143. (cited on page 42)

Gray, H., 2009. Powering the planet with solar fuel. *Nature Chemistry*, 1, 7 (2009). doi:10.1038/nchem.141. (cited on pages 4 and 18)

Guédez, R.; Spelling, J.; Laumert, B.; and Fransson, T., 2014. Optimization of thermal energy storage integration strategies for peak power production by concentrating solar power plants. *Energy Procedia*, 49 (2014), 1642–1651. doi:10.1016/j.egypro.2014.03.173. (cited on page 5)

Gunasekaran, S. and Anbalagan, G., 2007. Thermal decomposition of natural dolomite. *Bulletin of Materials Science*, 30, 4 (2007), 339–344. doi:10.1007/s12034-007-0056-z. (cited on page 97)

Gupta, H. and Fan, L., 2002. Carbonation–calcination cycle using high reactivity calcium oxide for carbon dioxide separation from flue gas. *Industrial and Engineering Chemistry Research*, 41, 16 (2002), 4035–4042. doi:10.1021/ie010867l. (cited on page 12)

Hathaway, B.; Davidson, J.; and Kittelson, D., 2011. Solar gasification of biomass: Kinetics of pyrolysis and steam gasification in molten salt. *Journal of Solar Energy Engineering*, 133, 2 (2011), 021011-1–9. doi:10.1115/1.4003680. (cited on page 18)

Herzog, H., 2009. *Carbon Dioxide Capture and Storage*, chap. 13. Oxford University Press, New York, New York USA. doi:10.1093/acprof:osobl/9780199573288.003.0013. (cited on page 4)

Hirsch, D.; Epstein, M.; and Steinfeld, A., 2001. The solar thermal decarbonization of natural gas. *International Journal of Hydrogen Energy*, 26, 10 (2001), 1023–1033. doi:10.1016/s0360-3199(01)00040-4. (cited on page 18)

Ho, C. and Iverson, B., 2014. Review of high-temperature central receiver designs for concentrating solar power. *Renewable and Sustainable Energy Reviews*, 29 (2014), 835–846. doi:10.1016/j.rser.2013.08.099. (cited on page 5)

House, J., 2007. *Principles of Chemical Kinetics*. Elsevier Inc., Oxford, UK, 2nd edn. ISBN 9780123567871. (cited on pages 2 and 26)

ICDD, 2017. *Powder Diffraction File Inorganic and Organic Data Book*. International Centre for Diffraction Data, Newtown Square, Pennsylvania USA. (cited on page 90)

International Energy Agency, 2017. *Key World Energy Statistics*. Technical report. Retrieved from http://www.iea.org/publications/freepublications/publication/KeyWorld2017.pdf. (cited on pages 3 and 16)

Itskos, G.; Grammelis, P.; Scala, F.; Pawlak-Kruczek, H.; Coppola, A.; Salatino, P.; and Kakaras, E., 2013. A comparative characterization study of Ca-looping natural sorbents. *Applied Energy*, 108 (2013), 373–382. doi:10.1016/j.apenergy.2013.03.009. (cited on page 13)

IUPAC, 1997. *Compendium of Chemical Terminology, (the "Gold Book")*. Compiled by A. McNaught and A. Wilkinson. Blackwell Scientific Publications, Oxford, 2nd edn. XML on-line corrected version: http://goldbook.iupac.org (2006–) created by M. Nic, J. Jirat, B. Kostata; updates compiled by A. Jenkins. doi:10.1351/goldbook. (cited on page 97)

Iverson, B.; Conboy, T.; Pasch, J.; and Kruizenga, A., 2013. Supercritical $CO_2$ Brayton cycles for solar-thermal energy. *Applied Energy*, 111 (2013), 957–970. doi:10.1016/j.apenergy.2013.06.020. (cited on page 5)

Jakobsen, H., 2014. *Chemical Reactor Modeling: Multiphase Reactive Flows*. Springer, Cham, Switzerland, 2nd edn. doi:10.1007/978-3-540-68622-4. (cited on pages 1, 2, and 3)

Kalafati, D., 1991. Diffusion entropy and theoretical separative work for gas mixtures with variable concentration. *Journal of Engineering Physics*, 61, 4 (1991), 1234–1240. doi:10.1007/bf00872591. (cited on page 4)

Kashcheev, I.; Zemlyanoi, K.; Ust'yantsev, V.; and Voskretsova, E., 2016. Study of thermal decomposition of natural and synthetic magnesium compounds. *Refractories and Industrial Ceramics*, 56, 5 (2016), 522–529. doi:10.1007/s11148-016-9880-2. (cited on page 97)

Kaviany, M., 1995. *Principles of Heat Transfer in Porous Media*. Springer-Verlag New York, Inc, New York, New York USA, 2nd edn. doi:10.1007/978-1-4612-4254-3. (cited on pages 36, 37, 39, and 75)

Keene, D.; Davidson, J.; and Lipiński, W., 2013. A model of transient heat and mass transfer in a heterogeneous medium of ceria undergoing nonstoichiometric reduction. *Journal of Heat Transfer*, 135, 5 (2013), 052701-1–9. doi:10.1115/1.4023494. (cited on pages 36 and 66)

Khinast, J.; Krammer, G.; Brunner, C.; and Staudinger, G., 1996. Decomposition of limestone: The influence of $CO_2$ and particle size on the reaction rate. *Chemical Engineering Science*, 51, 4 (1996), 623–634. doi:10.1016/0009-2509(95)00302-9. (cited on pages 15, 26, and 27)

Kim, J.; Johnson, T.; Miller, J.; Stechel, E.; and Maravelias, C., 2012. Fuel production from $CO_2$ using solar-thermal energy: System level analysis. *Energy and Environmental Science*, 5, 9 (2012), 8417–8429. doi:10.1039/c2ee21798h. (cited on page 4)

Kim, J.; Miller, J.; Maravelias, C.; and Stechel, E., 2013. Comparative analysis of environmental impact of S2P (Sunshine to Petrol) system for transportation fuel

production. *Applied Energy*, 111 (2013), 1089–1098. doi:10.1016/j.apenergy.2013.06.035. (cited on pages 3 and 4)

Koepf, E.; Alxneit, I.; Wieckert, C.; and Meier, A., 2017. A review of high temperature solar driven reactor technology: 25 years of experience in research and development at the Paul Scherrer Institute. *Applied Energy*, 188 (2017), 620–651. doi:10.1016/j.apenergy.2016.11.088. (cited on page 20)

Kogan, A., 2000. Direct solar thermal splitting of water and on-site separation of the products—IV. Development of porous ceramic membranes for a solar thermal water-splitting reactor. *International Journal of Hydrogen Energy*, 25, 11 (2000), 1043–1050. doi:10.1016/s0360-3199(00)00024-0. (cited on page 18)

Kogel, J.; Trivedi, N.; Barker, J.; and Krukowski, S., 2006. *Industrial Minerals & Rocks: Commodities, Markets and Uses*. Society for Mining, Mettalurgy, and Exploration, Inc., Littleton, Colorado USA, 7th edn. ISBN 9780873352499. (cited on page 93)

Kolb, C. and Worsnop, D., 2012. Chemistry and composition of atmospheric aerosol particles. *Annual Review of Physical Chemistry*, 63, 1 (2012), 471–491. doi:10.1146/annurev-physchem-032511-143706. (cited on page 2)

Kremer, J.; Galloy, A.; Ströhle, J.; and Epple, B., 2013. Continuous $CO_2$ capture in a 1-$MW_{th}$ carbonate looping pilot plant. *Chemical Engineering and Technology*, 36, 9 (2013), 1518–1524. doi:10.1002/ceat.201300084. (cited on page 15)

Kuravi, S.; Trahan, J.; Goswami, D.; Rahman, M.; and Stefanakos, E., 2013. Thermal energy storage technologies and systems for concentrating solar power plants. *Progress in Energy and Combustion Science*, 39, 4 (2013), 285–319. doi:10.1016/j.pecs.2013.02.001. (cited on page 5)

Laudone, G.; Gribble, C.; Jones, K.; Collier, H.; and Matthews, G., 2015. Validated *a priori* calculation of tortuosity in porous materials including sandstone and limestone. *Chemical Engineering Science*, 131 (2015), 109–117. doi:10.1016/j.ces.2015.03.043. (cited on page 111)

Levenspiel, O., 1999. *Chemical Reaction Engineering*. John Wiley and Sons, Inc., Hoboken, New Jersey USA, 3rd edn. ISBN 9780471254249. (cited on pages 2 and 72)

Levy, C.; Matthews, G.; Laudone, G.; Gribble, C.; Turner, A.; Ridgway, C.; Gerard, D.; Schoelkopf, J.; and Gane, P., 2015. Diffusion and tortuosity in porous functionalized calcium carbonate. *Industrial and Engineering Chemistry Research*, 54, 41 (2015), 9938–9947. doi:10.1021/acs.iecr.5b02362. (cited on page 111)

Li, Z.; Sun, H.; and Cai, N., 2012. Rate equation theory for the carbonation reaction of CaO with $CO_2$. *Energy and Fuels*, 26, 7 (2012), 4607–4616. doi:10.1021/ef300607z. (cited on pages 30 and 31)

Lin, Y.; Yang, Q.; and Ida, J., 2009. High temperature sorption of carbon dioxide on perovskite-type metal oxides. *Journal of the Taiwan Institute of Chemical Engineers*, 40, 3 (2009), 276–280. doi:10.1016/j.jtice.2008.12.010. (cited on page 11)

Linder, M.; Roßkopf, C.; Schmidt, M.; and Wörner, A., 2014. Thermochemical energy storage in kW-scale based on $CaO/Ca(OH)_2$. *Energy Procedia*, 49 (2014), 888–897. doi:10.1016/j.egypro.2014.03.096. (cited on page 19)

Lipiński, W.; Davidson, J.; Haussener, S.; Klausner, J.; Mehdizadeh, A.; Petrasch, J.; Steinfeld, A.; and Venstrom, L., 2013. Review of heat transfer research for solar thermochemical applications. *Journal of Thermal Science and Engineering Applications*, 5, 2 (2013), 021005-1–14. doi:10.1115/1.4024088. (cited on pages 18 and 72)

Liu, W.; An, H.; Qin, C.; Yin, J.; Wang, G.; Feng, B.; and Xu, M., 2012. Performance enhancement of calcium oxide sorbents for cyclic $CO_2$ capture—A review. *Energy and Fuels*, 26, 5 (2012), 2751–2767. doi:10.1021/ef300220x. (cited on page 13)

Lu, D.; Hughes, R.; and Anthony, E., 2008. Ca-based sorbent looping combustion for $CO_2$ capture in pilot-scale dual fluidized beds. *Fuel Processing Technology*, 89, 12 (2008), 1386–1395. doi:10.1016/j.fuproc.2008.06.011. (cited on page 15)

L'vov, B., 1997. Mechanism of thermal decomposition of alkaline-earth carbonates. *Thermochimica Acta*, 303, 2 (1997), 161–170. doi:10.1016/s0040-6031(97)00261-x. (cited on page 97)

Ma, Z. and Turchi, C., 2011. Advanced supercritical carbon dioxide power cycle configurations for use in concentrating solar power systems. *Proceeding of the Supercritical $CO_2$ Power Cycle Symposium*, Boulder, Colorado USA, May 24–25 (2011). (cited on page 5)

Manovic, V. and Anthony, E., 2010. Sintering and formation of a nonporous carbonate shell at the surface of CaO-based sorbent particles during $CO_2$-capture cycles. *Energy and Fuels*, 24, 10 (2010), 5790–5796. doi:10.1021/ef100931v. (cited on page 12)

Matthews, L. and Lipiński, W., 2012. Thermodynamic analysis of solar thermochemical $CO_2$ capture via carbonation/calcination cycle with heat recovery. *Energy*, 45, 1 (2012), 900–907. doi:10.1016/j.energy.2012.06.072. (cited on pages 16, 19, and 20)

Meier, A.; Bonaldi, E.; Cella, G.; Lipiński, W.; and Wuillemin, D., 2006. Solar chemical reactor technology for industrial production of lime. *Solar Energy*, 80, 10 (2006), 1355–1362. doi:10.1016/j.solener.2005.05.017. (cited on page 18)

Mertens, K., 2014. *Photovoltaics: Fundamentals, Technology and Practice*. John Wiley and Sons, Ltd., West Sussex, United Kingdom. ISBN 9781118634165. (cited on page 16)

Modest, M., 2013. *Radiative Heat Transfer*. Academic Press, Oxford, United Kingdom, 3rd edn. ISBN 9780123869449. (cited on pages 50, 52, 53, 54, 55, 56, and 57)

Muhich, C.; Ehrhart, B.; Al-Shankiti, I.; Ward, B.; Musgrave, C.; and Weimer, A., 2016. A review and perspective of efficient hydrogen generation via solar thermal water splitting. *WIREs Energy and Environment*, 5, 3 (2016), 261–287. doi:10.1002/wene.174. (cited on page 125)

Müller-Steinhagen, H. and Trieb, F., 2004. Concentrating solar power: A review of the technology. *Ingenia*, 18 (2004), 43–50. Retrieved from https://www.ingenia.org.uk/Ingenia/Articles/cb679c4f-9298-44aa-8356-ca9bff45704c. (cited on page 6)

Nikolopoulos, A.; Stroh, A.; Zeneli, M.; Alobaid, F.; Nikolopoulos, N.; Ströhle, J.; Karellas, S.; Epple, B.; and Grammelis, P., 2017. Numerical investigation and comparison of coarse grain CFD–DEM and TFM in the case of a 1 $MW_{th}$ fluidized bed carbonator simulation. *Chemical Engineering Science*, 163 (2017), 189–205. doi:10.1016/j.ces.2017.01.052. (cited on page 15)

Nikulshina, V.; Gálvez, M.; and Steinfeld, A., 2007. Kinetic analysis of the carbonation reactions for the capture of $CO_2$ from air via the $Ca(OH)_2$–$CaCO_3$–CaO solar thermochemical cycle. *Chemical Engineering Journal*, 129, 1–3 (2007), 75–83. doi:10.1016/j.cej.2006.11.003. (cited on pages 11, 15, 30, and 31)

Nikulshina, V.; Gebald, C.; and Steinfeld, A., 2009. $CO_2$ capture from atmospheric air via consecutive CaO-carbonation and $CaCO_3$-calcination cycles in a fluidized-bed solar reactor. *Chemical Engineering Journal*, 146, 2 (2009), 244–248. doi:10.1016/j.cej.2008.06.005. (cited on pages 19 and 21)

Nikulshina, V.; Hirsch, D.; Mazzotti, M.; and Steinfeld, A., 2006. $CO_2$ capture from air and co-production of $H_2$ via the $Ca(OH)_2$–$CaCO_3$ cycle using concentrated solar power—Thermodynamic analysis. *Energy*, 31, 12 (2006), 1715–1725. doi:10.1016/j.energy.2005.09.014. (cited on pages 11, 19, and 20)

Nikulshina, V. and Steinfeld, A., 2009. $CO_2$ capture from air via CaO-carbonation using a solar-driven fluidized bed reactor—Effect of temperature and water vapor concentration. *Chemical Engineering Journal*, 155, 3 (2009), 867–873. doi:10.1016/j.cej.2009.10.004. (cited on page 21)

Noorman, S.; Gallucci, F.; van Sint Annaland, M.; and Kuipers, J., 2011. A theoretical investigation of CLC in packed beds. Part 1: Particle model. *Chemical Engineering Journal*, 167, 1 (2011), 297–307. doi:10.1016/j.cej.2010.12.068. (cited on page 14)

Oates, J., 1998. *Lime and Limestone: Chemistry and Technology, Production and Uses*. Wiley-VCH Verlag GmbH, Weinheim, Germany. doi:10.1002/9783527612024. (cited on pages 2, 11, and 28)

Olivares-Marín, M.; Cuerda-Correa, E.; Nieto-Sánchez, A.; García, S.; Pevida, C.; and Román, S., 2013. Influence of morphology, porosity and crystal structure of $CaCO_3$ precursors on the $CO_2$ capture performance of CaO-derived sorbents. *Chemical Engineering Journal*, 217 (2013), 71–81. doi:10.1016/j.cej.2012.11.083. (cited on page 91)

Orofino, V.; Blanco, A.; Blecka, M.; Fonti, S.; and Jurewicz, A., 2000. Carbonates and coated particles on Mars. *Planetary and Space Science*, 48, 12–14 (2000), 1341–1347. doi:10.1016/s0032-0633(00)00114-8. (cited on page 52)

Palumbo, R.; Keunecke, M.; Möller, S.; and Steinfeld, A., 2004. Reflections on the design of solar thermal chemical reactors: Thoughts in transformation. *Energy*, 29, 5–6 (2004), 727–744. doi:10.1016/s0360-5442(03)00180-4. (cited on page 6)

Pardo, P.; Deydier, A.; Anxionnaz-Minvielle, Z.; Rougé, S.; Cabassud, M.; and Cognet, P., 2014. A review on high temperature thermochemical heat energy storage. *Renewable and Sustainable Energy Reviews*, 32 (2014), 591–610. doi:10.1016/j.rser.2013.12.014. (cited on pages 2 and 5)

Parkkinen, J.; Myöhänen, K.; Abanades, J.; Arias, B.; and Hyppänen, T., 2017. Modelling a calciner with high inlet oxygen concentration for a calcium looping process. *Energy Procedia*, 114 (2017), 242–249. doi:10.1016/j.egypro.2017.03.1166. (cited on page 15)

Pérez-Higueras, P.; Muñoz, E.; Almonacid, G.; and Vidal, P., 2011. High concentrator photovoltaics efficiencies: Present status and forecast. *Renewable and Sustainable Energy Reviews*, 15, 4 (2011), 1810–1815. doi:10.1016/j.rser.2010.11.046. (cited on page 16)

Phalak, N.; Wang, W.; and Fan, L., 2013. $Ca(OH)_2$-based calcium looping process development at the Ohio State University. *Chemical Engineering and Technology*, 36, 9 (2013), 1451–1459. doi:10.1002/ceat.201200707. (cited on pages 3, 11, and 14)

Piatkowski, N. and Steinfeld, A., 2008. Solar-driven coal gasification in a thermally irradiated packed-bed reactor. *Energy and Fuels*, 22, 3 (2008), 2043–2052. doi:10.1021/ef800027c. (cited on page 18)

Pierantozzi, R., 2003. *Kirk-Othmer Encyclopedia of Chemical Technology*, chap. Carbon dioxide. John Wiley and Sons, Inc., Hoboken, New Jersey USA, 5th edn. doi:10.1002/0471238961.0301180216090518.a01.pub2. (cited on page 4)

Rackley, S., 2010. *Carbon Capture and Storage*. Butterworth-Heinemann, Burlington, Massachusetts USA, 1st edn. ISBN 9781856176361. (cited on page 4)

Reich, L.; Bader, R.; Simon, T.; and Lipiński, W., 2014a. Heat and mass transfer model of a packed-bed reactor for solar thermochemical $CO_2$ capture. In *Proceedings of the 15th International Heat Transfer Conference*, vol. IHTC15-8893, 6541–6553. doi:10.1615/ihtc15.pmd.008893. (cited on page 21)

Reich, L.; Bader, R.; Simon, T.; and Lipiński, W., 2015. Thermal transport model of a packed-bed reactor for solar thermochemical $CO_2$ capture. *Special Topics and Reviews in Porous Media*, 6, 2 (2015), 197–209. doi:10.1615/.2015012344. (cited on pages 21 and 124)

Reich, L.; Melmoth, L.; Yue, L.; Bader, R.; Gresham, R.; Simon, T.; and Lipiński, W., 2017. A solar reactor design for research on calcium oxide-based carbon dioxide capture. *Journal of Solar Energy Engineering*, 139, 5 (2017), 054501-1–4. doi:10.1115/1.4037089. (cited on page 124)

Reich, L.; Yue, L.; Bader, R.; and Lipiński, W., 2014b. Towards solar thermochemical carbon dioxide capture via calcium oxide looping: A review. *Aerosol and Air Quality Research*, 14, 2 (2014), 500–514. doi:10.4209/aaqr.2013.05.0169. (cited on pages 19 and 20)

Rochelle, G., 2009. Amine scrubbing for $CO_2$ capture. *Science*, 325, 5948 (2009), 1652–1654. doi:10.1126/science.1176731. (cited on page 4)

Romeo, L.; Lara, Y.; Lisbona, P.; and Escosa, J., 2009. Optimizing make-up flow in a $CO_2$ capture system using CaO. *Chemical Engineering Journal*, 147, 2–3 (2009), 252–258. doi:10.1016/j.cej.2008.07.010. (cited on page 16)

Sánchez-Jiménez, P.; Valverde, J.; Perejón, A.; de la Calle, A.; Medina, S.; and Pérez-Maqueda, L., 2016. Influence of ball milling on CaO crystal growth during limestone and dolomite calcination: Effect of $CO_2$ capture at calcium looping conditions. *Crystal Growth and Design*, 16, 12 (2016), 7025–7036. doi:10.1021/acs.cgd.6b01228. (cited on page 13)

Sayyah, M.; Lu, Y.; Masel, R.; and Suslick, K., 2013. Mechanical activation of CaO-based adsorbents for $CO_2$ capture. *ChemSusChem*, 6, 1 (2013), 193–198. doi:10.1002/cssc.201200454. (cited on page 13)

Shimizu, T.; Hirama, T.; Hosoda, H.; Kitano, K.; Inagaki, M.; and Tejima, K., 1999. A twin fluid-bed reactor for removal of $CO_2$ from combustion processes. *Chemical Engineering Research and Design*, 77, 1 (1999), 62–68. doi:10.1205/026387699525882. (cited on pages 11, 12, 30, and 31)

Shokrollahi Yancheshmeh, M.; Radfarnia, H.; and Iliuta, M., 2016. High temperature $CO_2$ sorbents and their application for hydrogen production by sorption enhanced steam reforming process. *Chemical Engineering Journal*, 283 (2016), 420–444. doi:10.1016/j.cej.2015.06.060. (cited on page 13)

Silcox, G.; Kramlich, J.; and Pershing, D., 1989. A mathematical model for the flash calcination of dispersed $CaCO_3$ and $Ca(OH)_2$ particles. *Industrial and Engineering Chemistry Research*, 28, 2 (1989), 155–160. doi:10.1021/ie00086a005. (cited on pages 14 and 27)

Stalkup, F., 1978. Carbon dioxide miscible flooding: Past, present, and outlook for the future. *Journal of Petroleum Technology*, 30, 8 (1978), 1102–1112. doi:10.2118/7042-pa. (cited on page 4)

Stanmore, B. and Gilot, P., 2005. Review—Calcination and carbonation of limestone during thermal cycling for $CO_2$ sequestration. *Fuel Processing Technology*, 86, 16 (2005), 1707–1743. doi:10.1016/j.fuproc.2005.01.023. (cited on pages 11 and 12)

Steinfeld, A., 2002. Solar hydrogen production via a two-step water-splitting thermochemical cycle based on Zn/ZnO redox reactions. *International Journal of Hydrogen Energy*, 27, 6 (2002), 611–619. doi:10.1016/s0360-3199(01)00177-x. (cited on page 18)

Steinfeld, A. and Palumbo, R., 2003. Solar thermochemical process technology. In *Encyclopedia of Physical Science and Technology* (Ed. R. Meyers), 237–256. Academic Press, Cambridge, Massachusetts USA, 3rd edn. doi:10.1016/b0-12-227410-5/00698-0. (cited on page 18)

Stendardo, S. and Foscolo, P., 2009. Carbon dioxide capture with dolomite: A model for gas–solid reaction within the grains of a particulate sorbent. *Chemical Engineering Science*, 64, 10 (2009), 2343–2352. doi:10.1016/j.ces.2009.02.009. (cited on pages 15, 30, 31, 32, 110, and 111)

Steynberg, A., 2004. *Introduction to Fischer–Tropsh Techonology*, chap. 1, 1–63. Elsevier B. V., Amsterdam, The Netherlands. doi:10.1016/S0167-2991(04)80458-0. (cited on page 3)

Sun, J.; Liu, W.; Wang, W.; Hu, Y.; Yang, X.; Chen, H.; Zhang, Y.; Li, X.; and Xu, M., 2016. Optimizing synergy between phosphogypsum disposal and cement plant $CO_2$ capture by the calcium looping process. *Energy and Fuels*, 30, 2 (2016), 1256–1265. doi:10.1021/acs.energyfuels.5b02786. (cited on page 15)

Sun, P.; Grace, J.; Lim, C.; and Anthony, E., 2008. Determination of intrinsic rate constants of the CaO–$CO_2$ reaction. *Chemical Engineering Science*, 63, 1 (2008), 47–56. doi:10.1016/j.ces.2007.08.055. (cited on pages 30, 31, and 32)

Symonds, R.; Lu, D.; Macchi, A.; Hughes, R.; and Anthony, E., 2009. $CO_2$ capture from syngas via cyclic carbonation/calcination for a naturally occurring limestone: Modelling and bench-scale testing. *Chemical Engineering Science*, 64, 15 (2009), 3536–3543. doi:10.1016/j.ces.2009.04.043. (cited on pages 30 and 31)

Takahashi, S.; Neuville, D.; and Takebe, H., 2015. Thermal properties, density and structure of percalcic and peraluminus CaO–$Al_2O_3$–$SiO_2$ glasses. *Journal of Non-Crystalline Solids*, 411 (2015), 5–12. doi:10.1016/j.jnoncrysol.2014.12.019. (cited on page 91)

Takkinen, S.; Saastamoinen, J.; and Hyppänen, T., 2012. Heat and mass transfer in calcination of limestone particles. *AIChE Journal*, 58, 8 (2012), 2563–2572. doi:10.1002/aic.12774. (cited on pages 14 and 49)

Tamaura, Y.; Kojima, M.; Hasegawa, N.; Tsuji, M.; Ehrensberger, K.; and Steinfeld, A., 1997. Solar energy conversion into $H_2$ energy using ferrites. *Journal de Physique IV*, 7, C1 (1997), 673–674. doi:10.1051/jp4:19971275. (cited on page 18)

Tescari, S.; Agrafiotis, C.; Breuer, S.; de Oliveira, L.; Neises-von Puttkamer, M.; Roeb, M.; and Sattler, C., 2014. Thermochemical solar energy storage via redox oxides: Materials and reactor/heat exchanger concepts. *Energy Procedia*, 49 (2014), 1034–1043. doi:10.1016/j.egypro.2014.03.111. (cited on page 19)

Turns, S., 2013. *An Introduction to Combustion*. McGraw–Hill Education, New York, New York USA, 3rd edn. ISBN 9780073380193. (cited on page 39)

U.S. Department of Energy, 2012. *SunShot Vision Study*. Technical report. Retrieved from https://energy.gov/sites/prod/files/2014/01/f7/47927.pdf. (cited on page 18)

U.S. Department of Energy, 2014. *2014: The Year of Concentrating Solar Power*. Technical report. Retrieved from https://energy.gov/sites/prod/files/2014/10/f18/CSP-report-final-web.pdf. (cited on page 5)

Válek, J.; Hughes, J.; and Bartos, P., 2000. *Gas Permeability, Porosity and Carbonation of Modern Conservation Lime Mortar Mix*. Wiley-VCH Verlag GmbH, Weinheim, Germany. doi:10.1002/3527606211.ch30. (cited on page 39)

Valverde, J. and Medina, S., 2017. Limestone calcination under calcium-looping conditions for $CO_2$ capture and thermochemical energy storage in the presence of $H_2O$: An *in situ* XRD analysis. *Physical Chemistry Chemical Physics*, 19, 11 (2017), 7587–7596. doi:10.1039/c7cp00260b. (cited on page 26)

von Zedtwitz, P.; Lipiński, W.; and Steinfeld, A., 2007. Numerical and experimental study of gas–particle radiative heat exchange in a fluidized-bed reactor for steam-gasification of coal. *Chemical Engineering Science*, 62, 1–2 (2007), 599–607. doi:10.1016/j.ces.2006.09.027. (cited on page 72)

Wang, K.; Hu, X.; Zhao, P.; and Yin, Z., 2016. Natural dolomite modified with carbon coating for cyclic high-temperature $CO_2$ capture. *Applied Energy*, 165 (2016), 14–21. doi:10.1016/j.apenergy.2015.12.071. (cited on page 13)

Wang, W.; Ramkumar, S.; Li, S.; Wong, D.; Iyer, M.; Sakadjian, B.; Statnick, R.; and Fan, L., 2010. Subpilot demonstration of the carbonation–calcination reaction (CCR) process: High-temperature $CO_2$ and sulfur capture from coal-fired power plants. *Industrial and Engineering Chemistry Research*, 49, 11 (2010), 5094–5101. doi:10.1021/ie901509k. (cited on page 15)

Weinstein, L.; Loomis, J.; Bhatia, B.; Bierman, D.; Wang, E.; and Chen, G., 2015. Concentrating solar power. *Chemical Reviews*, 115, 23 (2015), 12797–12838. doi:10.1021/acs.chemrev.5b00397. (cited on pages 17 and 18)

Welty, J.; Wicks, C.; Wilson, R.; and Rorrer, G., 2008. *Fundamentals of Momentum, Heat, and Mass Transfer*. John Wiley and Sons, Inc., Hoboken, New Jersey USA, 5th edn. ISBN 9780470128688. (cited on page 65)

Wentworth, W. and Chen, E., 1976. Simple thermal decomposition reactions for storage of solar thermal energy. *Solar Energy*, 18, 3 (1976), 205–214. doi:10.1016/0038-092x(76)90019-0. (cited on page 6)

Whitaker, S., 1972. Forced convection heat transfer correlations for flow in pipes, past flat plates, single cylinders, single spheres, and for flow in packed beds and tube bundles. *AIChE Journal*, 18, 2 (1972), 361–371. doi:10.1002/aic.690180219. (cited on page 43)

Whitaker, S., 1999. *The Method of Volume Averaging*. Kluwer Academic, Dordrecht, the Netherlands. doi:10.1007/978-94-017-3389-2. (cited on page 36)

Wieser, M., 2006. Atomic weights of the elements 2005. *Pure and Applied Chemistry*, 78, 11 (2006), 2051–2066. doi:10.1351/pac200678112051. (cited on pages 28, 64, and 108)

Wilcox, J., 2012. *Carbon Capture*. Springer, New York, New York USA. doi:10.1007/978-1-4614-2215-0. (cited on page 4)

Yaws, C., 1995. *Handbook of Transport Property Data: Viscosity, Thermal Conductivity, and Diffusion Coefficients of Liquids and Gases*. Gulf Publishing, Houston, Texas USA. ISBN 9780884153924. (cited on page 39)

Yaws, C., 2009. *Transport Properties of Chemicals and Hydrocarbons*. William Andrews, Norwich, New York USA. ISBN 9780815520399. (cited on page 39)

Ylätalo, J.; Parkkinen, J.; Ritvanen, J.; Tynjälä, T.; and Hyppänen, T., 2013. Modeling of the oxy-combustion calciner in the post-combustion calcium looping process. *Fuel*, 113 (2013), 770–779. doi:10.1016/j.fuel.2012.11.041. (cited on page 15)

Yue, L., 2013. *A numerical model of transient thermal transport phenomena in a high-temperature solid–gas reacting system for $CO_2$ capture applications*. Master's thesis, University of Minnesota, Minneapolis, MN. (cited on pages 34 and 46)

Yue, L. and Lipiński, W., 2015a. Effect of surface radiative properties of a $CO_2$ sorbent particle on its interactions with high-flux solar irradiaiton. *Optics Express*, 23 (2015), A752–A763. doi:10.1364/oe.23.00a752. (cited on page 54)

Yue, L. and Lipiński, W., 2015b. A numerical model of transient thermal transport phenomena in a high-temperature solid–gas reacting system for $CO_2$ capture applications. *International Journal of Heat and Mass Transfer*, 85 (2015), 1058–1068. doi:10.1016/j.ijheatmasstransfer.2015.01.124. (cited on pages 34 and 49)

Yue, L. and Lipiński, W., 2015c. Thermal transport model of a sorbent particle undergoing calcination–carbonation cycling. *AIChE Journal*, 61, 8 (2015), 2647–2656. doi:10.1002/aic.14840. (cited on pages 34, 49, and 74)

Yue, L.; Wheeler, V.; and Lipiński, W., 2016. Combined heat transfer in a directly irradiated optically-large heterogeneous spherical particle. In *Proceedings of the 8th International Symposium on Radiative Transfer, RAD-16*, 310–317. (cited on page 49)

Zhao, M.; Shi, J.; Zhong, X.; Tian, S.; Blamey, J.; Jiang, J.; and Fennell, P., 2014. A novel calcium looping absorbent incorporated with polymorphic spacers for hydrogen production and $CO_2$ capture. *Energy and Environmental Science*, 7, 10 (2014), 3291–3295. doi:10.1039/c4ee01281j. (cited on page 13)

Zoth, G. and Haenel, R., 1988. *Appendix*, 449–468. Kluwer Academic, Dordrecht, the Netherlands. doi:10.1007/978-94-009-2847-3_10. (cited on page 39)